

Synthesis, Structuring and Surface Charge - An Investigation of the Use of Polymeric Materials as Antibiofouling Surfaces

Meabh Kennedy BSc. (Hons)

This thesis is submitted to Dublin City University, in fulfilment of the requirements for the degree of Doctor of Philosophy in Chemistry

Principal Supervisor: Dr Susan Kelleher

Secondary Supervisor: Dr Ruairí Brannigan

School of Chemical Sciences

May 2026

Declaration

Dearbhaím leis seo gurb é mo shaothar féin amháin an t-ábhar seo atá á leagan isteach agam i gcomhair measúnaithe ar an gclár staidéir le haghaidh na dámhachtana dochtúireacht agus go bhfuil gach cúram réasúnach glactha agam a dheimhniú, agus tá na rialacháin agus dearbhú a bhaineann le hIntleacht Shaorga Ghiniúnach comhlíonta agam, ar feadh m'eolais, gur saothar bunaidh é seo nach sáraíonn aon dlí cóipchirt, agus nár baineadh as saothar aon duine eile é ach amháin agus a mhéid go luaitear agus go n-aithnítear an saothar sin laistigh de théacs mo shaothairse.

I hereby certify that this material, which I now submit for assessment on the programme of study leading to the award of Doctorate of Philosophy (PhD) is entirely my own work, and that I have exercised reasonable care to ensure that the work is original and have conformed to the regulations on the use and declaration of Generative AI, and does not to the best of my knowledge, breach any law of copyright, and has not been taken from the work of others save and to the extent that such work has been cited and acknowledged within the text of my work.

Signed: Meabh Kennedy

ID No.: 21269900

Date: 26th May 2026

Declaration of Generative AI Tools

Tools: Clearly indicate the tool name and model (or version) you used and the date(s) of use. If you used a tool multiple times, provide the range of dates over which the tool was used and the model/versions used.	*Illustrae.ai, used to create illustration from images taken. 1/9/2025-31/10/2025*	*Imagine.art.ai, used to add colour to SEM images, 1/11/2025-16/11/2025*
Outputs: Specify what tool outputs were generated and used by you and for what purpose.	*Illustration of TLC plates in Chapter 4 of this thesis.*	*SEM images with bacteria on them that have colour, in Chapter 5.*
Prompts: Provide a record of the prompts you used here or link to an appendix where the prompts used are listed.	*Images of the TLC plates from the lab were taken and illustration of said plates were created with the AI tool.*	*Add colour to the bacterial cells present in these images without changing the background of the image.*
Iterations: Provide some commentary on the number and type of iterations. This can be linked to your report on prompts and outputs above.	N/A	N/A
Critical Reflection: If Gen AI tools have been used minimally, a very brief critical reflection on its role in the research submitted for examination can be included here. Otherwise, specify the parts of the thesis where critical reflection on the use and role of Gen AI tools is included.	This tool was used for one image only. It was used to make the images input to program uniform without changing the observations and results ascertained.	This tool was used as it was not changing the content of the image or for any data analysis purposes but adding colour to aid the reader to easily visualise the bacteria.

Table of Contents

DECLARATION ..... **II**

DECLARATION OF GENERATIVE AI TOOLS ..... **III**

TABLE OF CONTENTS ..... **IV**

LIST OF FIGURES ..... **VII**

LIST OF TABLES ..... **XVII**

ABBREVIATIONS ..... **XVIII**

ABSTRACT ..... **XXI**

ACKNOWLEDGEMENTS ..... **XXII**

PUBLICATIONS AND CONFERENCES ..... **XXIV**

PREFACE ..... **XXV**

CHAPTER 1 INTRODUCTION **1**

1.1 POLYMERS 1

1.1.1 Fundamentals of Polymers *1*

1.1.2 Polycaprolactone (PCL) *4*

1.1.3 Poly(2-allyloxymethyl-2-ethyl-trimethylene carbonate) (PAOMEC) *6*

1.2 BIODEGRADABLE POLYMERS AND THEIR APPLICATIONS 9

1.2.1 Overview of Biodegradable Polymers *9*

1.2.2 PCL and its Applications *12*

1.2.3 Polycarbonates and their Applications *16*

1.3 ANTIBIOFOULING SURFACES 20

1.3.1 Antifouling Overview *20*

1.3.2 Surface modifications of biomaterials *23*

1.3.3 Influence of Surface Charge *25*

1.3.4 Influence of Surface Topography *27*

1.4 PROJECT AIMS 30

CHAPTER 2 MATERIALS AND METHODS **32**

2.1 MATERIALS 32

2.2 INSTRUMENTATION 33

2.3 METHODS 35

2.3.1 Synthesis, Fabrication and Crosslinking *35*

2.3.2 Cell Testing *40*

2.3.3 Analysis Techniques *48*

CHAPTER 3 SYNTHESIS AND MODIFICATION OF OLIGOMERS 52

3.1 PCLDMA 52
3.1.1 Introduction 52
3.1.2 Methacrylation of PCL Diol (M_n 1250 g/mol) 52
3.1.3 Methacrylation of PCL Diol (M_n 530 g/mol) 62
3.2 PAOMEC 66
3.2.1 Introduction 66
3.2.2 Synthesis of Reagents for Polymerisation 66
3.2.3 Polymerisation of AOMEC 68
3.3 Conclusions 79

CHAPTER 4 CROSSLINKING, STRUCTURING AND FUNCTIONALISATION 82

4.1 Introduction to Crosslinking and Patterning 82
4.2 Crosslinking and Patterning of PCLDMA 84
4.2.1 Crosslinking of PCLDMA 84
4.2.2 Crosslinking Structured Samples of PCLDMA 92
4.3 Crosslinking, Functionalisation and Structuring of PAOMEC 103
4.3.1 Preliminary Crosslinking and Functionalisation of PAOMEC 103
4.3.2 Structuring and Analysis of Crosslinked PAOMEC 114
4.4 Conclusions 127

CHAPTER 5 CELL TESTING 129

5.1 Introduction to Antibiofouling Surfaces of Biomaterials 129
5.2 Bacterial Cell Testing of PAOMEC 133
5.2.1 Preparation of a Cell Testing Protocol 134
5.2.2 Cell Testing Protocol Refinement 143
5.2.3 Static Antibiofouling Cell Testing – The Results 152
5.3 Introduction to the Influence of Surface Topography on Endothelial Cells 159
5.4 Cell Testing of Structured PCLDMA with HAECs 162
5.4.1 Preliminary Cell Viability Analysis 163
5.4.2 Preliminary Cell Proliferation Analysis 169
5.5 Conclusions 171

CHAPTER 6 CONCLUSIONS AND FUTURE WORK 173

6.1 Chapter 3: Synthesis and Modification of Oligomers 173
6.2 Chapter 4: Crosslinking, Structuring and Functionalisation 174
6.3 Chapter 5: Cell Testing 175

BIBLIOGRAPHY 178

APPENDICES 1

Appendix A 1

APPENDIX B 8
APPENDIX C 12

List of Figures

Figure 1.1: Illustration of monomer, oligomer and polymers as well as the ordering of polymers..... 1
Figure 1.2: Schematic of general examples of addition and condensation polymerisation reactions.[10] 3
Figure 1.3: General reactive scheme for chain-growth polymerisation, where * represents the radical generated.[12] 4
Figure 1.4: General reaction scheme for ROP of ε-caprolactone to PCL. 5
Figure 1.5: ROP of PCL, adapted from Chen et al.[28] 5
Figure 1.6: Biodegradation pathway of PCL.[30] 6
Figure 1.7: Reaction scheme of first reported synthesis of PAOMEC, adapted from Kühling et al.[34]; examples of catalyst used in AOMEC polymerisation, namely 1,5,7-triazabicyclo[4.4.0]dec-5-ene (left) and 1,8-diazabicyclo[5.4.0]undec-7-ene (DBU) (right).[35–38] 7
Figure 1.8: General reaction scheme for; AOMEC polymerisation with dual catalytic system (top), and post-polymerisation functionalisation via UV-initiated thiol-ene chemistry (bottom), adapted from Thomas et al.[39] 8
Figure 1.9: Scheme of polymer biodegradation, inspired by work published by Lucas et al.[47]..... 10
Figure 1.10: Summary of some common applications of biodegradable polymers across many fields.[50] 11
Figure 1.11: (1) Column chart of published research in Web of Science database from 2016 to 2024 analysed on the database and searched using the keywords; “polymer”, ”biomedical” and “applications” as topics (title, abstract and index)(top); schematic overview of various medical applications of biodegradable polymers (bottom).[52] 12
Figure 1.12: Overview of research completed by Zhao et al. involving the electrospinning, mechanical and antimicrobial testing and food packaging capabilities of PCL, chitosan blended films.[59]..... 14
Figure 1.13: Image of Norplant with ruler for scale (left) [64]; Scanning electron microscopy (SEM) of electrospun PCL loaded with zinc oxide nanoparticles

(middle)[65]; and preparation of and light microscope images of PCL scaffold (right).[66] 16
Figure 1.14: 3D computer aided design (CAD) model and 3D printed PMAC with scale bars representing 2.5 mm (left) and 3D print of PAOMEC sample place on a 5 pence coin to show scale. 17
Figure 1.15: Reaction scheme for pizoelectronic inkjet printing process.[68] 17
Figure 1.16: Illustration of studies performed by Zong et al. (top)[70] and Zhang et al.(bottom).[71] 19
Figure 1.17: Illustration of the 5 stages of biofilm formation.[74] 21
Figure 1.18: Breakdown of microbiology infections on implantable cardiac devices.[86] 22
Figure 1.19: SEM images of different medical devices with biofilms: (a) ventilation tube; (b) needleless connector; (c) pacemaker wire (top).[80] SEM images of biofilm development on titanium over a 48 hour period, to mimic that of a dental implant.[90] 23
Figure 1.20: Three mechanisms by which antibiofouling surfaces work and the surface modification completed to create such surfaces adapted from Durand et al.[97] The thickness of the links are estimations of the amount of research articles on the topics. 24
Figure 1.21: Illustration of conversion of zwitterionic surface to cationic surface due to bacteria induced acidic environment.[105] 26
Figure 1.22: Confocal microscopy images of different biofilms formed on various surfaces using Pseudomonas aeruginosa, adapted from Rzhepishevska et al. The samples named SPM and MEDSAH are the anionic and zwitterionic samples, respectively. METAC is the cationic sample (left)[108] and illustration for click-reactions used for post-polymerisation functionalisation (right).[112] 27
Figure 1.23: Water contact angles and roll off angles of different topographical shapes (top)[123]; SEM images of different nano- and microstructures including hierarchical templates (middle); photos taken of E. coli, a gram-negative strain, and S. aureus, a gram-positive strain and their respective responses to nanostructures and hierarchical templates with nanostructures at the base of the micropillars.[126] ... 29
Figure 3.1: Curly arrow reaction mechanism for methacrylation of PCL Diol. 53
Figure 3.2: ^{1}H NMR spectra of starting materials including (left to right); PCL diol (blue), methacryloyl chloride (red) and PCLDMA-1350 (green). The peaks highlighted and outlined represent the acrylate protons of MAC and the alcohol

proton of PCL Diol (top to bottom). The dotted purple outlines represent the CH_2 group of the repeating unit in both PCL diol and PCLDMA. 55
Figure 3.3: Percentage methacrylation versus time in hours calculated by ^{1}H NMR integration, graphed using R. 57
Figure 3.4: FTIR spectra of PCL Diol (black) and PCLDMA-1350 (red). 59
Figure 3.5: GPC spectrum of dW/dLogM versus the calculated M_w on the Log scale of PCLDMA-1350 60
Figure 3.6: DSC of PCLDMA-1350 elucidating the T_g, T_{m1} and T_{m2}. 61
Figure 3.7: Methacrylation of PCLDMA-630 measured over 7 days, analysis was completed using R..... 62
Figure 3.8: GPC spectrum of dW/dLogM versus the calculated M_w on the Log scale of PCLDMA-630. 64
Figure 3.9: DSC of PCLDMA-630 elucidating the T_g, T_{cc}, T_{m1} and T_{m2}..... 65
Figure 3.10: ^{1}H NMR (600 MHz, $CDCl_3$) spectrum of purified AOMEC. 67
Figure 3.11: ^{1}H NMR (600 MHz, $CDCl_3$) spectrum of purified TU co-catalyst..... 68
Figure 3.12: Reaction Scheme for both monomer and polymer synthesis. 69
Figure 3.13: Proposed reaction scheme for ROP of AOMEC with TU catalyst and DBU..... 70
Figure 3.14: ^{1}H NMR spectrum of polymerisation reaction after 3 days, red outlined ^{1}H NMR spectrum is the zoomed in area (top) of the section of the full spectrum (middle) outlined and highlighted in red. Graph of percentage monomer conversion after daily sampling over a 96-hour period (bottom left) and equation used to calculate monomer conversion (%) (bottom right) from integration of ^{1}H NMR spectrum. 71
Figure 3.15: ^{1}H NMR spectra of purified PAOMEC using hexane (bottom, blue spectrum) and methanol (top, red spectrum). The blue highlighted and outlined at peaks at 7.76 ppm and 4.33 ppm highlight the presence of the TU catalyst (dashed outline) and AOMEC monomer (full outline), respectively, when hexane was used in the purification process. 73
Figure 3.16: TLC plate of different fractions from the column separation of an impure PAOMEC sample. Fractions 2 to 8 were UV active as demonstrated by the pencil marks circling the UV active spots while fraction 9 only showed activity in the permanganate stain (left); TLC plates post staining with different solvent ratios of

ethyl acetate and hexane, respectively (outlined, right). Rendering of TLC plates was completed using AI Illustrae.co. 74
Figure 3.17: FTIR spectra of AOMEC (red, top) and PAOMEC (navy, bottom) with key peak differences outlined with boxes. 76
Figure 3.18: GPC spectrum of dW/dLogM versus calculated M_w on the Log scale of PAOMEC. 77
Figure 3.19: GPC of PAOMEC samples from syntheses with (black, line spectrum) and without (blue, dashed spectrum) 1,4-butane diol used as the initiator. 78
Figure 3.20: DSC analysis of amorphous PAOMEC. 79
Figure 4.1: General photopolymerisation crosslinking scheme, illustrated using Biorender.com 82
Figure 4.2: Reaction scheme of excitation of Irgacure-2959 to triplet excited state by UV light followed by α-cleavage. Example of how the radicals formed from this cleavage can interact with the acrylate terminal group of PCLDMA forming activated radical centres to enable photopolymerisation to continue between PCLDMA and HDDA, alike. 83
Figure 4.3: Free radical crosslinking example involving Irgacure-2959 as the PI, a thiol functionality and PAOMEC. 84
Figure 4.4: Reactants used for the fabrication of PCLDMA-based crosslinked materials, including short chain monomer HDDA and photoinitiators Irgacure-2959 and PBPO. 85
Figure 4.5: Reaction scheme for the crosslinking of PCLDMA with HDDA. 86
Figure 4.6: Illustration of components of the crosslinking chamber and crosslinking process (top) and images of the crosslinking chamber including grip clips used to secure the PDMS spacers between the glass slides as well as the resulting crosslinked samples. 87
Figure 4.7: FTIR spectra of neat HDDA and PCLDMA-1350: HDDA 1:9 and 1:4 blends pre- and post-crosslinking for 120 minutes. 89
Figure 4.8: 1:9 (top) and 1:4 (bottom) FTIR spectra comparing exposure of samples to UV-light for 60 and 120 minutes. 90
Figure 4.9: Viscosity (mPa.sec) measurements taken of both PCLDMA-630 and PCLDMA-1350 with different ratios of HDDA pre-crosslinking (top left); WCA measurements of planar, crosslinked samples using PCLDMA-1350 (top right); images taken from WCA measurements showing water droplets on each planar

sample type demonstrating similarity across all three samples, with red lines illustrating the angles measured (bottom) and illustration of surface wetting characterisation between the vapour, liquid and solid interface giving the WCA, θ_{Young}, adapted from Huhtamäki et al. Error bars on both column charts represent the standard deviation.[190] 92
Figure 4.10: Illustration of side on view of the replica moulding process used to create structured, crosslinked materials (top); and the parameters of the structured materials that can be altered. 93
Figure 4.11: Image of Tosena splendida blue cicada with zoomed in image of FESEM images taken from top-down and at a tilt (top); schematic of replica moulding process (bottom). 94
Figure 4.12: FESEM image of Tosena splendida blue wing (top left), PPGDA primary mould with nanoholes (top right), PEGDA secondary mould with nanopillars (bottom left) and column chart of height, pitch and diameter measurements made. Error bars represent the standard deviation. All tilted FESEM images were taken at 40 º tilts and scale bars are all 0.2 µm. 95
Figure 4.13: Illustration adapted from of NIL process to create T1 (top); image of iridescent, patterned 10 mm x 10 mm, T1 silicon template (bottom left); FESEM image of lined structure with 1 µm scale bar (bottom centre); FESEM image with 2 µm scale bar (bottom right). 97
Figure 4.14: Image of 1:4 mould from T1 taken by AFM (a); graph of the peaks measured by AFM below images of the crosslinked sample with light used to elucidate the iridescence (b); top down FESEM images taken of 1:4 samples (c and d); table of the averages and standard deviations of the measurements of T1 (provided by ThunderNil) and of PCLDMA:HDDA from the analysis completed. Scale bars for all images are 1 µm. 100
Figure 4.15: Scatter plot for percentage mass loss of 1:9 samples at three times points (left). The error bars are representative of the standard deviation. Image of one example of each sample at each time point showing yellowing as degradation continues (right). 102
Figure 4.16: Equations used to calculate the moles of allyl groups present followed by moles of SHX required (top) and crosslinking reaction of PAOMEC and SHX (bottom). 104

Figure 4.17: FTIR analysis of crosslinking process showing of reactants in the pre-crosslinking blend separately and combined and the post-crosslinking PAOMEC sample..... 106
Figure 4.18: Reactants planned for use in crosslinking of PAOMEC and functionalisation of the crosslinked networks. 107
Figure 4.19: General reaction for reversible disulfide exchange adapted from Davis et al. and image of pre-crosslinking blend containing cystamine dihydrochloride that has undergone uncontrolled gelation.[219] 108
Figure 4.20: Viscosity analysis of PAOMEC, SHX and pre-crosslinking blend for PAO_X (top). Standard deviation is represented by error bars. Swelling studies and images of each sample type used in the studies (bottom)..... 110
Figure 4.21: Reaction scheme for cystamine dihydrochloride desalting and images of the salt and resulting viscous, yellow liquid of cystamine. Image of glass vial containing pre-crosslinking blend after instantaneous precipitation of reactants.... 112
Figure 4.22: Reaction of ninhydrin with cystamine that results in purple colour (left); images of samples before and after ninhydrin exposure and the vials in which the qualitative analysis was carried out (right)..... 113
Figure 4.23: FESEM image of 2-photon polymerisation template (top) and SEM image of replica moulded PAO_X, inset picture of moulded PDMS where bubbles are visible, as outline in purple. 115
Figure 4.24: FESEM images of PAO_COOH samples of three different ratios of SHX:COOH, 3:2, 7:3 and 2:1 that were replica moulded from PEG primary mould from the T1 template. 116
Figure 4.25: Schematic of 3D-printed PLA template with measurements (a); 3D digital replica of 3D-printed PLA mould (b); image of 3D-printed PLA mould and PDMS replica mould (c); images of pre-crosslinking blend, crosslinking chamber and 10 mm diameter PAO_X sample post-crosslinking (d). 118
Figure 4.26: Images of structured PEGDA, PAO_X and PAO_COOH samples, examples of FESEM and AFM images and a table of the resulting measurements of the various structure parameters compared to the T1 silicon template. 119
Figure 4.27: WCA measurements and images of each sample type with a water droplet (a); illustration of nanoindentation process,[249] and calculation used to find Young's modulus (b); hardness, reduced elastic and Young's moduli of each sample (c). 122

Figure 4.28: DSC analysis of purified PAOMEC and crosslinked samples PAO_X and PAO_COOH. 123
Figure 4.29: Mass loss analysis of degraded samples after 2, 30 and 60 days and images of these samples at said time points. The error bars represent the standard deviations. 124
Figure 4.30: DSC analysis of PAO_X and PAO_COOH samples after degradation over 2, 30, 60 days and table of the corresponding T_gs. 125
Figure 4.31: FTIR spectra of PAO_X and PAO_COOH samples at each time point of the degradation study; full spectrum (a) and zoomed in to between the wavenumbers of 2500 cm^{-1} and 4000 cm^{-1} 126
Figure 5.1: Confocal microscopy images of stained samples (a); post-microscopy image analysis with ImageJ (b); and CFU counting utilised to support the results obtained through staining studies.[268] 131
Figure 5.2: Quantitative analysis of adhesion of bacteria based on the CFU of the petri dishes imaged.[271] 132
Figure 5.3: Illustration of DDM procedure (top); results of PAOMEC sample, blank disk (negative control) and ampicillin loaded disc (positive control) on agar plates with a lawn of bacteria, namely S. epidermidis (left) and E. coli (right). Table of the zone of inhibition around the positive control (bottom). 136
Figure 5.4: Illustration of MTS assay procedure, created with BioRender.com 137
Figure 5.5: Absorbances measured for PAO_X samples not yet exposed to MTS solution, with no cells presence (top); and absorbances measured for fixatives planned for use in testing (bottom). Graphs made by Dr Graham Reid. 138
Figure 5.6: Direct assay absorbances measured after 3 hours (top left) and 20 hours (bottom left) soaking in LB with no cells present; photograph of 48-well plate with circle of the PAO_X samples soaked in LB for 3 hours and exposed to MTS solution; and column chart comparing absorbances measured from negative control (LB with no cells or sample present) and PAO_X sample at the 60-minute time point (t_{60}) (bottom right). Standard deviations are represented by the error bars. Graphs were made by Dr Graham Reid. 140
Figure 5.7: Absorbances measured from indirect MTS assay with inset images of petri dishes used to confirm no cells were present in the LB negative control, at three different timepoints. Graphs were made by Dr Graham Reid. 141

Figure 5.8: Column chart of absorbances measured from from crystal violet assay performed where the erro bars represent standard deviation (left); chemical structure of crystal violet showing positive charge (top right); colour change of PAO_COOH sample due to non-specific binding of the crystal violet stain to the crosslinked network..... 143
Figure 5.9: SEM image of PAO_COOH planar sample, with scale bar of 20 μm. .. 144
Figure 5.10: Process for percentage area coverage by bacteria on PAOMEC samples using Trainable Weka Segmentation plugin in Fiji ImageJ software. 145
Figure 5.11: Cell testing protocol in preparation for SEM imaging for quantitative analysis of biofouling. 147
Figure 5.12: Growth curve of P. fluorescens at three different temperatures 25 ºC, 30 ºC and 37 ºC. 149
Figure 5.13: Comparative column chart showing percentage area coverage of each sample type by P. fluorescens at 37 ºC and 30 ºC (top right) where error bar represent standard deviation; equation used to calculate coefficient of variation demonstrating the variability of data collected at 30 ºC (top right); and SEM images of PAO_X at 37 ºC (bottom left) and 30 ºC (bottom right) highlighting the difference observed in percentage coverage of samples by bacteria. 150
Figure 5.14: SEM images of planar and structured sample demonstrating less visible bacteria and structures - as circled, with 20 μm scale bar (top); SEM of full sample (bottom left) with 400 μm scale bar; and photograph of the same sample showing the polymerised, gel-like substance observed..... 152
Figure 5.15: Box plot of the percentage area coverage of the crosslinked surfaces with P. fluorescens. The maximal and minimal data point of each dataset were displayed with crosses with a dash; the mean of each dataset is represented by a black square. The statistical analysis, specifically Kruskal–Wallis H test, and a Dunn post-hoc test with a Bonferroni correction showed statistical significance between samples where **** is noted where $p \leq 0.0001$. 153
Figure 5.16: FESEM images of PAO_X and PAO_COOH structured and planar samples to highlight the difference in bacterial cell coverage of the surfaces as well as the different types of biofilms observed. Colour added using AI-assisted image editor.[309] 155

Figure 5.17: FESEM images which elucidate the bending of structures. The zoomed in area (bottom) of one of the FESEM images highlights the possibility of some bacteria cells falling between the lined ridges into the channels. 158
Figure 5.18: Influence of micropillars on cell morphology demonstrated with SEM and fluorescent confocal microscopy (top)[328]; and SEM images of different structured surfaces investigated for effects on ECs (bottom).[329] 162
Figure 5.19: FESEM image of 1:4 PCLDMA:HDDA and side on illustration of the measured parameter of the structures; images of planar (top right) and structured (bottom right) PCLDMA:HDDA samples cut to 6 mm circles. 164
Figure 5.20: Reduction of MTT by enzymes to give purple formazan.[334] 164
Figure 5.21: Results from MTT assay of positive and negative controls and planar and structured PCLDMA:HDDA samples at three time-points. Error bars represent standard deviation. A p-value of < 0.05, signifying statistical significance, is represented using an *. 165
Figure 5.22: LDH assay mechanism of action via two-step enzymatic process, as illustrated by Khalef et al.[334] 167
Figure 5.23: LDH production represented by; fold change relative to the control (top); and percentage released relative to the top standard (bottom). Error bars represent standard deviation. A p-value of < 0.05, signifying statistical significance, is represented using an *. 168
Figure 5.24: Scatter plot of proliferation MTT assay performed over 4 timepoints, with measurements relative to T_0 of the control. Error bars represent standard deviation. A p-value of < 0.05, signifying statistical significance, is represented using an *..... 170
Figure A.1: ^{1}H NMR (600 MHz, $CDCl_3$) spectrum of MAC with most common impurity. Protons H_a and H_c utilised to find the percentage of impurity present. 1
Figure A.2: ^{1}H NMR (600 MHz, $CDCl_3$) spectrum of PCLDMA-1350 with labels denoting each proton on the PCLDMA structure. 2
Figure A.3: Stacked ^{1}H NMR (600 MHz, $CDCl_3$) spectra of each stage of the purification process (left to right) to give purified PCLDMA-630. 3
Figure A.4: Annotated ^{1}H NMR (600 MHz, $CDCl_3$) spectrum of PCLDMA-630..... 4
Figure A.5: Annotated ^{13}C NMR (150 MHz, $CDCl_3$) spectrum of AOMEC post-distillation under vacuum. 5
Figure A.6: Annotated ^{13}C NMR (150 MHz, $CDCl_3$) spectrum of TU cocatalyst..... 6

Figure A.7: Annotated ^{1}H NMR (600 MHz, $CDCl_3$) spectrum of fully purified PAOMEC. 7
Figure B.1: Comparative FTIR spectra of PCL diol-530, PCLDMA-630 and PCLDMA-630:HDDA (1:4 ratio) pre- and post-crosslinking for 60 minutes (top). Peaks representing the alkene stretch (bottom left) and bend (bottom right) of the terminal alkene groups on pure PCLDMA_630 and PCLDMA:HDDA (1:4) pre- and post-crosslinking. 8
Figure B.2: FESEM image of PCLDMA:HDDA 1:9 secondary mould top down (top left) and tilted (top right) with nanopillars. Column chart of height, pitch and diameter measurements made comparing fidelity of 1:9 and PEGDA secondary moulds. Error bars represent the standard deviation. FESEM image of PCLDMA:HDDA 1:4 secondary mould top down (bottom left) and tilted (bottom right) showing collapse of nanopillars. All tilted FESEM images were taken at 40 º. 9
Figure B.3: FTIR (left) and DSC (right) spectra from degraded samples at each time point displayed in the spectra. 10
Figure B.4: ^{1}H NMR (600 MHz, $CDCl_3$) spectra of swelling studies of PAO_X samples at four timepoints soaked in deionised water showing the leaching of propylene carbonate from PAO_X sample. 10
Figure B.5: ^{1}H NMR (600 MHz, $CDCl_3$) spectra of PAO_X (a) and PAO_COOH (b) samples post soaking in PBS buffer at three time points. 11

List of Tables

Table 1: Methacrylation of PCLDMA using different ratios of reactants and reaction durations. Percentage methacrylation of PCLDMA was calculated by integration using H^1 NMR spectra of samples from the crude reaction mixture at the end of the reaction time. The percentage yield and percentage methacrylation were used to ascertain the success of each reaction. 56
Table C.1: Data from Ray-Scheirer statistical test showing the degrees of freedom (Df), sum of the squares (Sum Sq) H and p-values. The statistically significant data are outlined in green using results collected from planar, uncharged as samples, PAO_X, as the baseline for comparison. 12
Table C.2: Results from Dunn post-hoc test with a Bonferroni correction with the statistically significant results outlined in green. 12

Abbreviations

AFM	Atomic force microscopy
ANOVA	Analysis of variance
AOMEC	2-allyloxymethyl-2-ethyltrimethylene carbonate
APCs	Aliphatic polycarbonates
BSC	Biological safety cabinet
CAD	Computer aided design
CFU	Colony-forming unit
CV	Crystal violet
Đ	Dispersity
DBU	1,8-Diazabicyclo[5.4.0]undec-7-ene
DCM	Dichloromethane
DDM	Disc diffusion method
DNA	Deoxyribonucleic acid
DP	Degree of polymerisation
DSC	Differential scanning calorimetry
ECs	Endothelial cells
EPS	Extracellular polymer substance
FESEM	Field-emission scanning electron microscopy
FTIR	Fourier Transform Infrared
GPC	Gel permeation chromatography
H_2O_2	Hydrogen peroxide
HACC	Hydroxypropyltrimethyl ammonium chloride chitosan
HAECs	Human Aortic Endothelial Cells
HCl	Hydrochloric Acid
HDDA	1,6-hexanediol diacrylate
Irgacure-2959	2-hydroxy-4’-(2-hydroxyethoxy)-2-methylpropiophenone
ISO	International Organization for Standardization
LB	Lysogeny broth
LDH	Lactate dehydrogenase
MAC	Methacryloyl chloride
M_n	Number average molecular weight

M_p	Molecular weight of the highest peak
MRSA	Methicillin-resistant Staphylococcus aureus
MTS	3-(4,5-dimethylthiazol-2-yl)-5-(3-carboxymethoxyphenyl)-2-(4-sulfophenyl)-2H-tetrazolium salt
MTT	3-(4,dimethylthiazolyl-2)-2, 5-diphenyltetrazolium bromide
M_w	Weight average molecular weight
NADH	Nicotinamide adenine dinucleotide
NMR	Nuclear Magnetic Resonance
OD_{600}	Optical density at 600 nm
PAOMEC	Poly(2-allyloxymethyl-2-ethyltrimethylene carbonate)
PBPO	Phenylbis(2,4,6-trimethylbenzoyl) phosphine oxide
PBS	Phosphate-buffered saline
PCL	Polycaprolactone
PCLDMA	Polycaprolactone dimethacrylate
PDMS	Polydimethylsiloxane
PEGDA	Polyethylene glycol diacrylate
PHC	Poly(1,6-hexamethylene carbonate)
PI	Photoinitiator
PLA	Poly(lactic acid)
PMAC	poly(5-methyl-5-allyloxycarbonyl-1,3-dioxan-2-one)
PPGDA	Polypropylene glycol diacrylate
ROP	Ring opening polymerisation
rpm	Revolutions per minute
SEM	Scanning electron microscopy
SHX	pentaerythritol tetrakis(3-mercaptopropionate)
SKN	Shikonin
T_c	Crystallisation temperature
T_{cc}	Cold crystallisation
T_g	Glass transition
THF	Tetrahydrofuran
TLC	Thin Layer Chromatography
T_m	Melting temperature
TMAD	Trimethylolpropane allyl ether diol

TU	1-(3,5-bis(trifluoromethyl)phenyl)-3-cyclohexylthiourea
UN	United Nations
UV	Ultraviolet
VEGF	Vascular Endothelial Growth Factor
WCA	Water Contact Angle
WHO	World Health Organisation

Abstract

Thesis Title: Synthesis, Structuring and Surface Charge - An Investigation of the Use of Polymeric Materials as Antibiofouling Surfaces

Name: Meabh Áine Kennedy BSc. (Hons)

Post-operative infection is a significant issue in the healthcare sector. Approximately 2-10% of patients contract infections upon medical device implantation. This is largely due to biofilm formation.[1] Antibiotics are oftentimes unable to penetrate said biofilms, thus rendering them ineffective.[2] This research aimed to create crosslinked, polymeric materials that are biodegradable and prevent bacterial adhesion. The antibiofouling properties of the materials' surface and the influence of surface topography and charge on said properties were to be investigated.

Polymers offer many properties that make them ideal for this area of research, such as their ability to be tailored for purpose.[3] Polycaprolactone (PCL) and poly(2-allyloxymethy-2-ethyltrimethylene) carbonate (PAOMEC) were selected for this work due to their biocompatibility and capacity to be crosslinked via photo-initiated free radical polymerisation.

PCL diol was methacrylated with yields of 81-89% and PAOMEC was synthesised with yields of 80-89% with 85% purity. These materials were then mixed with solvents and short chain chemicals and then crosslinked via UV-initiated processes.

Inspired by naturally occurring structured surfaces that repel bacteria, a replica moulding technique was utilised to introduce sub-micron surface topography to the crosslinked PCL and PAOMEC materials. In the case of PAOMEC, functionalisation of the material was also attempted with different functional groups to create cationic and anionic surfaces. The degradability of the crosslinked materials was assessed by *in vitro* testing under biological conditions.

Bacterial cell testing was performed to understand the influence of surface topography and functionalisation on surface biofouling. The sub-micron surface topography significantly reduced biofouling while surface functionalisation was found to have no significant influence.

Mammalian endothelial cell testing was performed with PCL materials. No adverse cellular interactions were observed due to the presence of sub-micron structures. Significantly higher cell proliferation was measured on the structured surfaces, elucidating potential benefits of introducing structured surfaces to biomedical devices.

Acknowledgements

Thank you to the organisations that funded this research, Dublin City University and the Irish Research Council. I have had the privilege of spending the last four years livening interests in areas I never knew existed, developing lifelong skills and growing as a researcher. Thank you also to the examiners, Prof. Clare Mahon and Dr Hasim Ibrahim for taking the time to read this thesis and Dr Darren Fayne for chairing the examination.

To my primary supervisor Dr Susan Kelleher. There are so many things that I have learned throughout my time in DCU, many of which are from you. Your perseverance, persistent love of the work, despite its challenges, and the ardent care you have for our group and research as a whole, is truly energising to be around. Thank you for your advice and support, not only in relation to this research but also on my career – and sometimes life! I feel extremely fortunate to have worked for you and learned from you.

To my secondary supervisor Dr Ruairí Brannigan, thank you for your time, energy and expertise. Your patience with your explanations, and willingness to help in the lab and the general kindness you provided were so appreciated.

To the Kelleher Nanostructured Materials group members past and present, Graham, Urbain, Ana, Purabi, Clare, Ciara, Emma, Dylan, Laura, Hannah, with honorary mentions to Aisha and Lele, thank you for making coming to work such a joy. To Niamh and Jess for taking the time to welcome me into the group when they were in the throes of writing their own theses. To Aisha, for being my lab mother when I was a new first year researcher and taking the time to share all of your experience and care with me. To Graham, for the numerous lunch time chats in the early days and indulging my seemingly never-ending list of questions, you are a wealth of both scientific and musical knowledge, and I can’t thank you enough for sharing both with me! To Purabi, for your warmth, unwavering kindness, guidance and friendship. To Ciara, Emma, Dylan, Laura and the honorary Kelleher Rebecca, thank you all for giving me the perfect excuse to try every restaurant in Dublin that I wanted to. Seeing you all at lunchtime was often a highlight on the days when I needed it most.

Thank you for becoming so much more than colleagues, even if Rebecca doesn't think so.

To the great many colleagues I have met, outside of the Kelleher Research group, in DCU and beyond. To Dr. Keith Rochfort for your extreme generosity of time and skills, thank you. Special mentions of course must also go to the members of the DCU School of Chemical Sciences department. It has been a joy to work in an environment in which research, innovation and collaboration are so heavily celebrated. There are too many to name but thank you to all of those in the technical team, postgraduate and postdoctoral researchers alike and the academic staff, all of whom were so welcoming from day one. The kindness and support that is seemingly a prerequisite to becoming a member of this department, is something I never take for granted.

To my friends outside of the DCU research bubble who act as a reminder of life beyond the PhD. If I start listing, I will most definitely forget someone. Instead, I promise to finally plan the well-needed catch ups and phone calls, reply to messages, and take the trips or organise the visits that have acted as the light at the end of the tunnel. Thank you all for your understanding, gentle and persistent check-ins and continuing friendship.

To my family. To my mam and dad, Geraldine and Eddie. There are not enough words, and I am not a talented enough writer to truly express how grateful I am for all that you have both done for me, but I will continue to remind you at every opportunity I get. Thank you both so much for the life you have given me and for the love you shown me. To my sister Aoife, my self-appointed future maid of honour and business partner. Thank you for the phone calls even when I forget, for all of the words of encouragement and for being my best friend.

Finally, to the soon-to-be Dr Khatie Lau. The real Dunboyne Diana. Thank you for everything. Thank you for listening to my ramblings, sitting with me through all of the late nights and to both you and Emi for providing a home for me, in Dunboyne of all places! You are a constant source of wonder and awe. It's been a crazy few years and there is no one I would rather have lived them with than you. I can't wait to celebrate with you when you finally catch up with me.

Go raibh mile maith agaibh. Nílim ach i mo thús.

Publications and Conferences

Publication: Controlled degradation of polycaprolactone-based micropillar arrays. Niamh Geoghegan, Mark O'Loughlin, Colm Delaney, Keith D. Rochfort, **Meabh Kennedy**, Srikanth Kolagatla, Lucia Podhorska, Brian J. Rodriguez, Larisa Florea and Susan M. Kelleher. *Biomaterials Science*, 2023, **11**, 3077–3091.

Publication: “Surface topography versus Surface Functionalisation: Investigating the Drivers of Antibiofouling Behaviour with poly(2-allyloxymethyl-2-ethyltrimethylene) (PAOMEC)”, **Meabh Kennedy**, Graham Reid, Ciara Tobin, Ruairí Brannigan, Susan M. Kelleher. (to be submitted)

Poster Presentation: **“**Mechanobactericidal polymer surfaces – Refining the Synthesis and Structuring of Polycaprolactone Materials”, DCU Chemical Sciences Department “Chemistry Day”, Dublin, Ireland, May 2023.

Oral Presentation: “Little needles, big job: how we plan to destroy antibiotic-resistant bacteria”, Oral presentation competition, “Tell it Straight”, DCU, Dublin, Ireland, May 2023.

Poster Presentation: “Mechanobactericidal polymer surfaces for Medical Devices – Refining the Synthesis and Structuring of Polycaprolactone Materials”, Young Researchers Meeting, Warwick University, Warwick, UK, July 2023.

Poster Presentation: “Mechanobactericidal Polymer Surfaces for Medical Devices – Synthesis and functionalisation of poly(2-allyloxymethyl-2-ethyltrimethylene carbonate) (PAOMEC)”, ICI Chemistry Colloquium, Dublin, Ireland, June 2024.

Poster Presentation: “Mechanobactericidal Polymer Surfaces for Medical Devices - Investigating the Influence of Short Chain Functional Groups on the Bactericidal Abilities of Nanostructured pAOMEC”, IUPAC MACRO 2024 the 50th World Polymer Congress", Warwick University, Warwick, UK, July 2024.

Oral Presentation: “Little needles, big job: how we plan to destroy antibiotic-resistant bacteria”, National oral presentation competition, “Thesis in Three”, Royal Irish Academy, Dublin, Ireland, November 2024.

Oral Presentation; “Charged Up and Rough Around the Edges: Synthesis, Structures and Anionic Surfaces for Antibiofouling”, DCU Chemical Sciences Department “Chemistry Day”, Dublin, Ireland, May 2025.

Oral Presentation: “Microscale, Macro Effect? The Influence of Surface Charge and Topography on Biofilm Formation”, MRS Fall Meeting and Exhibit, Hyne Convention Centre, Boston, USA, November 2025

Preface

Chapter 1: Introduction

Chapter 2: Materials and Methods

Chapter 3: Synthesis and Modification of Oligomers

Chapter 4: Crosslinking, Structuring and Functionalisation

Chapter 5: Cell Testing

Chapter 6: Conclusions and Future Work

This research project was undertaken to gain further understanding of factors that influence the antibiofouling properties of the surfaces of biomaterials. Specifically, this work focussed on the fabrication of oligomer based, degradable materials and how altering the surface properties of these materials, including surface charge and topography, changes how bacteria interact with the surface.

Chapter 1 is a literature review which introduces the topics discussed in more depth throughout this thesis including, polymers as materials, biodegradable polymers and the potential applications associated with them and biofouling. A specific focus was given to antibiofouling surfaces and current research on how surface topography and surface charge can influence how bacteria interact with a surface. Materials and methods including experimental procedures and use of instruments are detailed in **Chapter 2**. The synthesis and preparation of all materials involved in the work as well as the associated analysis completed is discussed in **Chapter 3**. This included the methacrylation of polycaprolactone diol, the synthesis of the monomer 2-allyloxymethyl-2-ethyl-trimethylene carbonate, cocatalyst 1-(3,5-bis(trifluoromethyl)phenyl)-3-cyclohexylthiourea and oligomer poly(2-allyloxymethyl-2-ethyl-trimethylene carbonate). **Chapter 4** reported on the crosslinking of the synthesised materials through the replica moulding process. Novel studies focussed on the introduction of different functionalities or topographies to the crosslinked materials were also performed. Polycaprolactone dimethacrylate was crosslinked with short chain monomer 1,6-hexanediol diacrylate at different ratios and then structures on the sub-micron scale were introduced. Poly(2-allyloxymethyl-2-ethyl-trimethylene carbonate) was mixed with pentaerythritol tetrakis(3-mercaptopropionate) and crosslinked though similar replica moulding processes. Once completed, the introduction of different short chain chemicals, namely 3-mercaptopropionic acid and cystamine dihydrochloride, as well as sub-micron surface topography, which had not yet been previously explored or reported, was performed. The antibiofouling properties of the new crosslinked materials, structured and non-structured, functionalised and non-functionalised, were analysed as reported in **Chapter 5**. Static cell testing was performed with different poly(2-allyloxymethyl-2-ethyl-trimethylene carbonate) based materials to enable a direct comparison between samples, to further our understanding of the influence of surface structures and surface functionalisation, on antibiofouling properties.

Mammalian cell testing was also performed with the sub-micron structured polycaprolactone-based materials to investigate the biocompatibility of this surface topography. The final summary of conclusions and future work are discussed in **Chapter 6**.

Chapter 1 Introduction

1.1 Polymers

1.1.1 Fundamentals of Polymers

Polymers are macromolecules made up of single molecules called monomers. An oligomer is a low molecular weight polymer. There is no strict minimum molecular weight of a macromolecule to designate it an oligomer or polymer. Generally, a polymer has a greater molecular weight than 5000 g/mol. An oligomer must have at least two monomer units and, as defined by IUPAC, must have its properties affected by the removal of one or a few repeating units.[4,5]

Polymer chains can be organised in a neat, orderly manner or can be packed randomly. These polymers are defined as crystalline or amorphous, respectively. A polymer that has aspects of ordered and disordered packing are generally defined as semi-crystalline, as illustrated in **Figure 1.1**. The order of the system can, in turn, affect the properties of that system.[6]

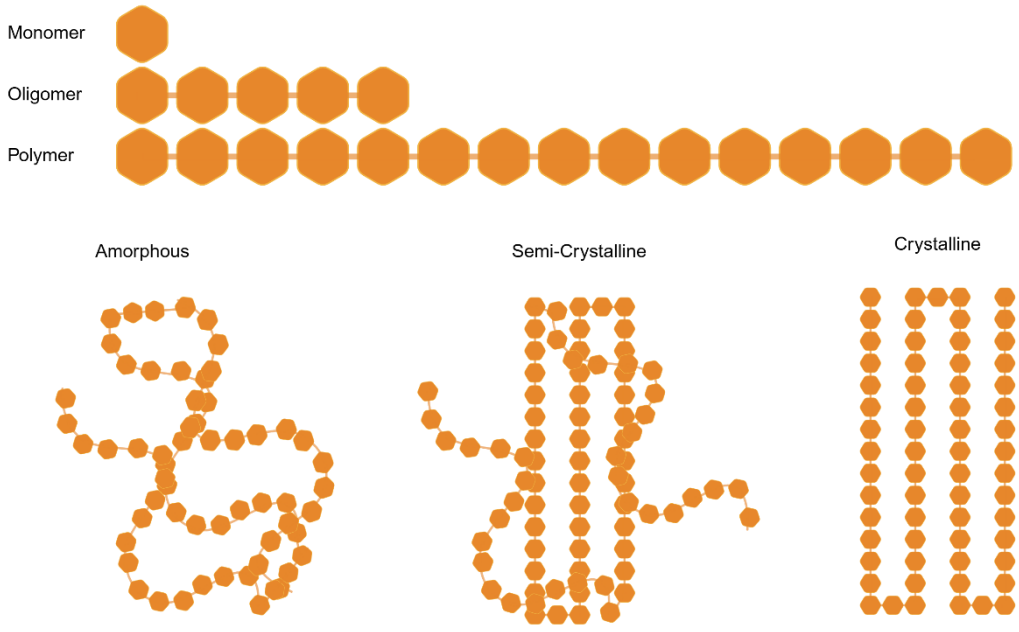


Figure 1.1: Illustration of monomer, oligomer and polymers as well as the ordering of polymers.

Polymers are often only associated with materials like rubbers and plastics. However, these are only two categories of polymers and there are very many more. Polymers

can occur naturally such as cellulose in plants or polynucleotides in deoxyribonucleic acid (DNA), while other polymers can be made synthetically.[7,8]

Synthetic polymers are made by polymerisation reactions, involving the linking of monomer units into a chain- or network-like fashion. The monomer units can be all the same, resulting in a homopolymer or they can represent two or more units, which then form a co-polymer. The amount and type of monomer units that connect to each other can then vary the properties of the resulting polymer. The covalent bonding of monomer units that occurs in polymerisation is generally defined by one of two categories of polymerisation: condensation or addition. Condensation polymerisation is a reaction that results in the formation of a byproduct, often water, and can occur between two or more different monomers. Conversely, addition polymerisations generally involve the reaction of at least one type of monomer without the formation of condensate by-products. Both types of synthetic polymerisation reactions are depicted in **Figure 1.2**.[9]

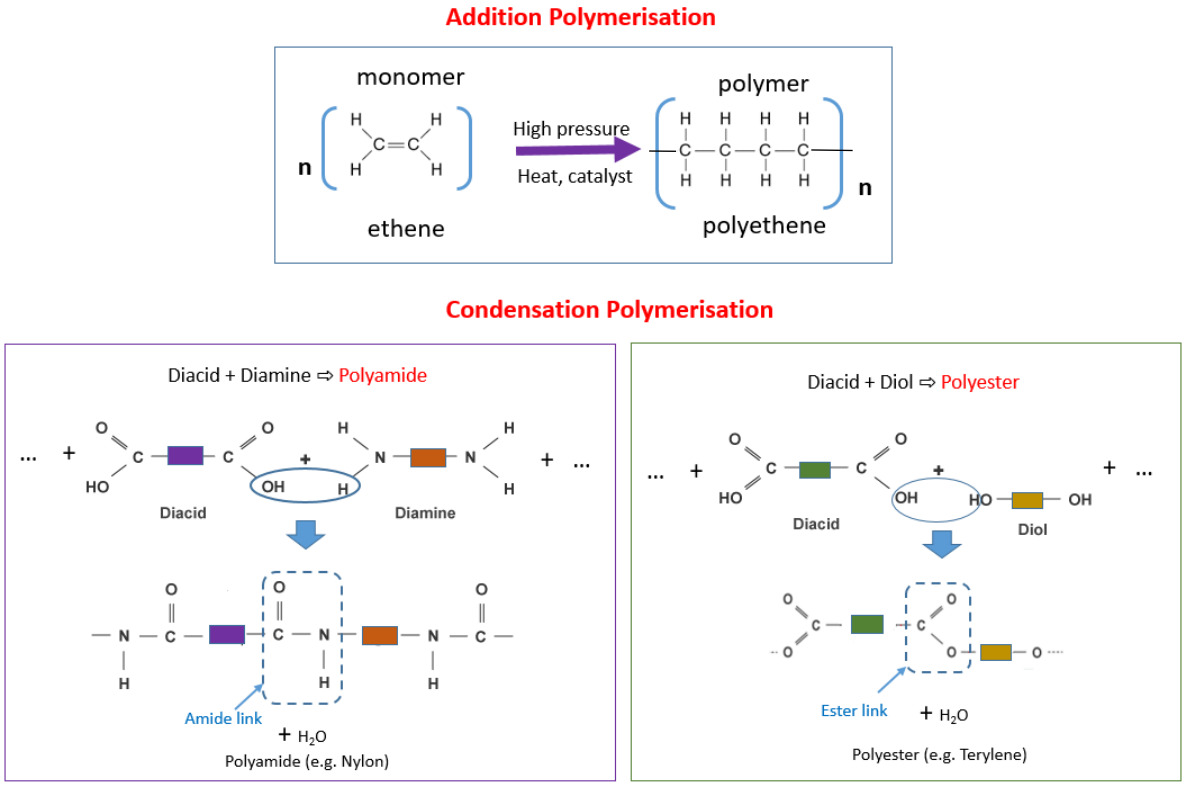


Figure 1.2: Schematic of general examples of addition and condensation polymerisation reactions.[10]

Condensation, also known as step-growth, polymerisations involve a single monomer unit or more with complimentary end groups capable of reacting with one another to form a chain and eliminating a small molecule. This type of reaction results in a variety of polymers including polyesters and polyamides.[11]

Addition or chain-growth polymerisation is a three-step reaction involving initiation, propagation and termination. As no elimination occurs, the repeating unit of resulting polymers maintain the same chemical structure as the monomers they were derived from. This type of polymerisation generally requires an initiator which has a cation, anion, organometallic complex or free radical, known as a reactive centre. Once the reactive centre is activated the propagation occurs, whereby many monomers can rapidly add to the initiator in a short space of time. The type of reactive centre, monomer and temperature as well as any other reaction conditions can affect the rate of propagation. The most well-known functional group found in this type of polymerisation is the carbon-carbon double bond as can be seen in **Figure 1.3**. The polymerisation is complete upon termination of the reactive centre. A key difference between the chain-growth reactions and step-growth reactions is the molecular weight

of the polymer and percent conversion as chain-growth reactions show high molecular weight polymers at all percentage conversions.[12]

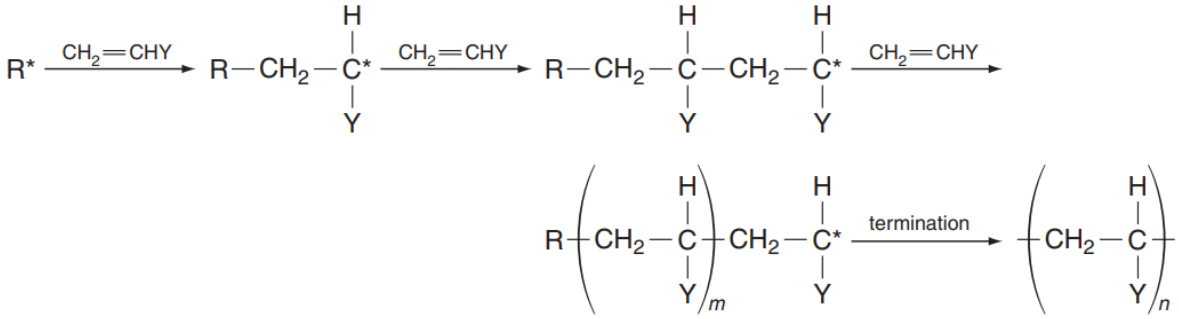


*Figure 1.3: General reactive scheme for chain-growth polymerisation, where * represents the radical generated.*[12]

Ring opening polymerisation (ROP) is generally considered to be a form of chain growth polymerisation.[13] ROP reactions involve the conversion of the ring monomer unit to an acyclic or shorter cyclic monomeric unit.[14] There are various pathways through which ROP can proceed including, but not exclusive to, cationic ROP, anionic ROP, radical ROP and monomer activated ROP. The ring strain of the monomer units can often be a driving force behind ROP.[15] This type of chain growth polymerisation can be used to synthesise a variety of polymers including polynorbornene, polysiloxane, polyethyleneimines as well as polyesters such as polycaprolactone (PCL) and polycarbonates like poly(2-allyloxymethyl-2-ethyltrimethylene carbonate) (PAOMEC), as discussed in this research.[15–17]

1.1.2 Polycaprolactone (PCL)

PCL is a well-known polyester and has found many uses in industry due to its various advantageous properties. It is a semi-crystalline polymer that generally sees an increase in crystallinity with a decrease in molecular weight.[18] The thermal properties, degradation profile and permeability are just some properties which can be affected by the degree of crystallinity.[19] It is soluble in a variety of organic solvents whilst remaining insoluble in water.[20,21] PCL can also be copolymerised with various polymers including polyethylene glycol (PEG), poly(ethylene oxide) and poly(lactic acid) (PLA) to name a few. These copolymers can therefore be tailored to refine polymer properties for the desired application.[22–25]

Labet and Thielemans have reviewed the various approaches taken to synthesise PCL in detail.[21] In short, polycondensation of 6-hydroxyhexanoic acid is one

approach. This is a less commonly used approach due to the low molecular weights and high dispersity recorded. The second more common approach is ROP, as in **Figure 1.4**. The first reported synthesis of PCL was in 1934 by Natta et al. Since then, various procedures have been designed expanding on the types of ROP that can be used to synthesise PCL.[21,26,27]

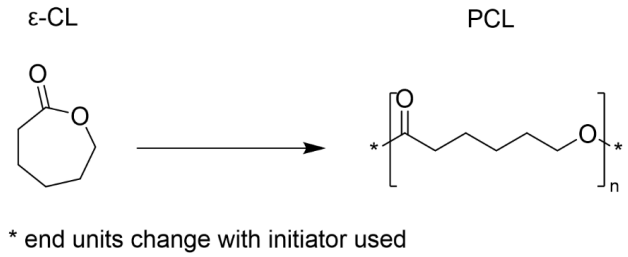


Figure 1.4: General reaction scheme for ROP of ε-caprolactone to PCL.

Depending on the type of reaction and the initiator selected, the end group functionality of the PCL chain can be altered. In this research, PCL diol was reacted with methacrylate groups to introduce the acrylate functionality necessary for crosslinking of the material. An example of PCL diol synthesis was reported by Chen et al. and proceeded via a monomer activated ROP approach. Diethylene glycol utilised as the initiator and was activated by tin catalyst stannous octoate, as in the scheme in **Figure 1.5**.[28] Further functionalisation of the alcohol termini can be performed, as is discussed in **Chapter 3**.

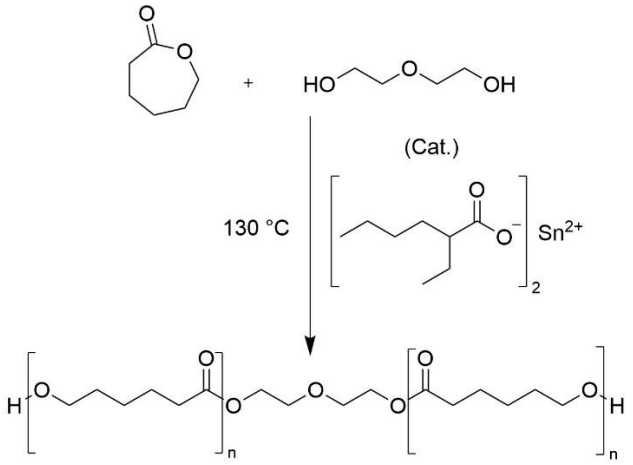


Figure 1.5: ROP of PCL, adapted from Chen et al.[28]

Arguably, one of the most advantageous properties of PCL is its biodegradability and biocompatibility. Biodegradation involves the breaking down polymers into smaller units by biological processes or under biological conditions. Due to the presence of

the ester bonds within the linear chain, PCL can undergo ester hydrolysis. Within the body, the degradation of PCL has been found to involves two stages; the first is the aforementioned hydrolysis and the second is the enzymatic breakdown of PCL when it is of a low enough molecular weight.[29] As in **Figure 1.6**, it is first hydrolytically degraded to form 6-hydroxycaproic acid. It can then undergo ω- and β-oxidation which generally involves the breaking down of acids, like fatty acids, into acetyl-CoA. Finally, it can at this stage enter the citric acid cycle to be safely removed from the body.[20,30]

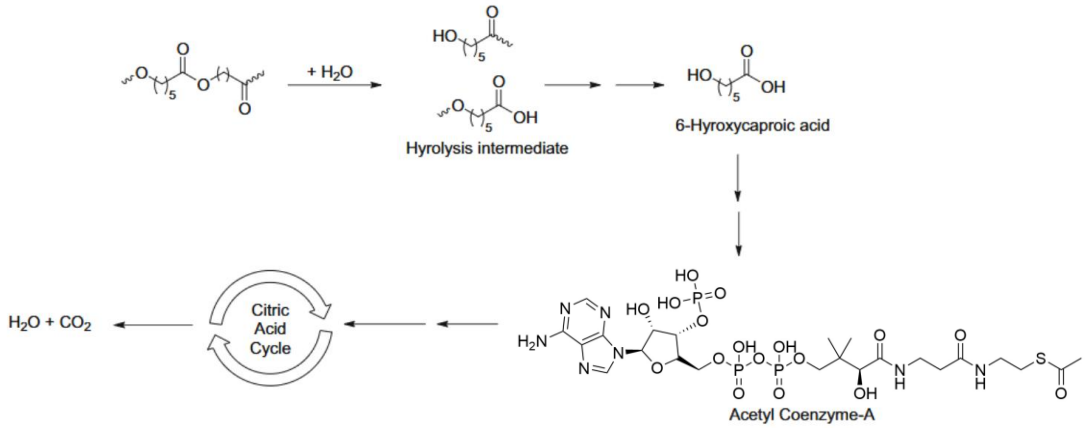


Figure 1.6: Biodegradation pathway of PCL.[30]

As a result of the biodegradable and biocompatible properties of PCL, extensive research has been completed and use of PCL materials in biomedical applications is widespread. This is discussed in more detail in **Section 1.2**.

1.1.3 Poly(2-allyloxymethyl-2-ethyl-trimethylene carbonate) (PAOMEC)

PAOMEC, is another polymer that is made by ROP. It is an aliphatic polycarbonate, which are another group of polymers that have been extensively investigated in literature due to their biodegradable carbonate group. They are most commonly synthesised from 5- or 6-membered cyclic monomers via various ROP routes and have the additional advantage of side chains that can undergo further functionalisation.[31–33]

The monomer, 2-allyloxymethyl-2-ethyl-trimethylene carbonate (AOMEC) is an example of a 6-membered ring that can be polymerised via ROP. It is a type of 2,2-disubstituted trimethylene carbonate that has a side chain with a free alkene group which provides opportunity for post-polymerisation functionalisation. Kühling et al. first reported the anionic ROP of AOMEC with butyllithium as an initiator in 1989 to

form poly(2-allyloxymethyl-2-ethyl-trimethylene carbonate) (PAOMEC), as in **Figure 1.7**. This research also reported early crosslinking studies utilising the alkene functionality present. 2,2'-azoisobutyronitrile or di-tert-butyl peroxide were used as thermally activated radical initiators for said crosslinking studies.[34]

Further research by Olsén et al. focussed on a ring closing depolymerisation approach to isolate the AOMEC monomer.[35] The thermodynamic behaviour of the polymerisation depolymerisation was performed with a tin catalyst, stannous octoate, due to high temperatures of 200 ºC being required. However, organic catalyst 1,5,7-triazabicyclo[4.4.0]dec-5-ene, was used for the polymerisation of AOMEC. Previous use of this type of catalyst has been demonstrated to catalyse the reaction through hydrogen bonding of the initiator and monomer enabling a pseudo-anionic ROP to proceed.[36] Further studies were completed using another organic catalyst 1,8-diazabicyclo[5.4.0]undec-7-ene (DBU), to understand the influence of different solvent and temperature on AOMEC polymerisation versus depolymerisation. Additionally, the importance of initial monomer concentration was investigated with lower AOMEC concentrations found at reaction equilibrium due to higher initial monomer concentrations. Of particular interest for this research was the approximate 10% AOMEC concentration remaining when the initial monomer concentration of 2.0 M was used in dichloromethane (DCM) at 30 ºC, as discussed in more detail in **Chapter 3**.[37,38]

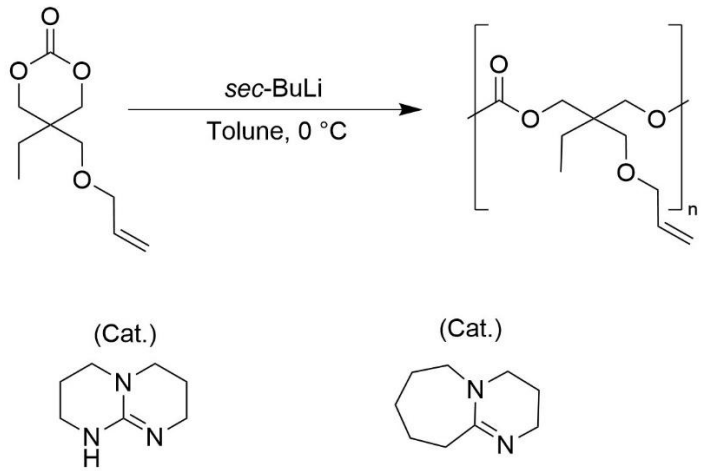


Figure 1.7: Reaction scheme of first reported synthesis of PAOMEC, adapted from Kühling et al.[34]; examples of catalyst used in AOMEC polymerisation, namely 1,5,7-triazabicyclo[4.4.0]dec-5-ene (left) and 1,8-diazabicyclo[5.4.0]undec-7-ene (DBU) (right).[35–38]

The additional advantage of polycarbonates, such as PAOMEC, is the side chains on the repeating unit of the polymer that enable further functionality. Olsén et al. reported an example of post-polymerisation functionalisation via UV-initiated thiol-ene chemistry using 1-dodecanethiol.[35] More recently, research completed by Thomas et al. investigated the functionalisation of PAOMEC with UV-initiated thiol-ene chemistry utilising 1-dodecanethiol, benzyl mercaptan and 3-mercaptopropionic acid. The same group also demonstrated the advantages of a dual catalytic system involving DBU and thiourea co-catalyst, 1-(3,5-bis(trifluoromethyl)phenyl)-3-cyclohexylthiourea (TU) for this ROP, as shown in **Figure 1.8**.[39] As with Olsén et al., high percentage monomer conversion was reported when an initial monomer concentration of 2.0 M was utilised.[37,39]

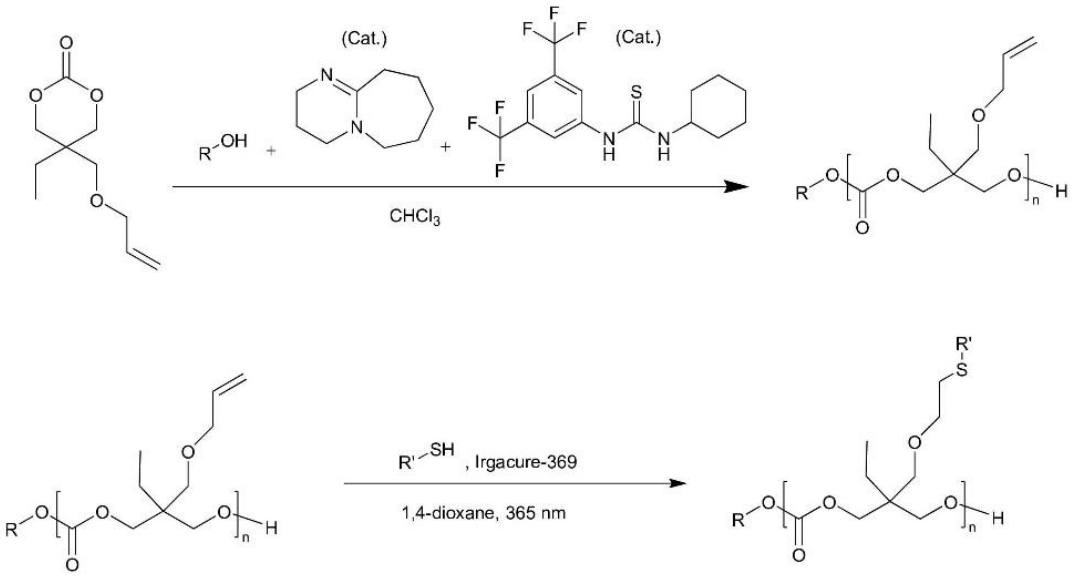


Figure 1.8: General reaction scheme for; AOMEC polymerisation with dual catalytic system (top), and post-polymerisation functionalisation via UV-initiated thiol-ene chemistry (bottom), adapted from Thomas et al.[39]

Copolymerisation of PAOMEC has also demonstrated the potential applications and variability of this polymer. Thiol functionalised polyethylene glycol (PEG) chains were introduced to PAOMEC to create thermo-responsive polymers. When in water the different hydrophilic PEG chain lengths resulted in precipitation of the PEG-grafted PAOMEC at varying temperature. This design was reported to be of interest for potential applications in thermally responsive drug delivery due to the biodegradability of the materials and the tuneability.[39] Temperature controlled co-polymerisation of AOMEC with ε-caprolactone was also reported by the same

research group, further demonstrating the variety of potential materials offered with these monomers.[40] It was this early work, demonstrating the facile ROP synthesis and advantages of post-polymerisation functionalisation that inspired the use of PAOMEC in this research.

Like PCL, PAOMEC has been demonstrated to degrade hydrolytically.[41] There are no specific studies demonstrating the degraded products as PAOMEC is less extensively studied in literature. That being said, aliphatic polycarbonates have been reported to degrade in the body enzymatically and bacterial strains such as *Pseudomonas* and *Variovorax*, were demonstrated to be capable of degrading polycarbonates like poly(hexamethylene carbonate).[42,43] Şucu and Shaver reviewed a series of degradable polyester and polycarbonate crosslinked materials. The synthesis types, co-polymerisation approaches and crosslinking properties were some of the points of discussion surrounding how the biodegradability of said materials could be tailored. This review emphasised the importance of these polymer types in the creation of degradable crosslinked thermoset materials with endless potential.[44]

PAOMEC, unlike PCL, does not have a long history of use in biomaterials or widespread research for applications: however, research of aliphatic polycarbonates elucidating their potential as biodegradable polymers for biomaterials is discussed in further **Section 1.2**.

1.2 Biodegradable polymers and their applications

1.2.1 Overview of Biodegradable Polymers

Biodegradable polymers can be classed by their synthesis or structure. They can be sourced synthetically and can be made from renewable or non-renewable, fossil fuel sources. Alternatively, they can be sourced solely from naturally occurring materials such as biomass.[45,46]

To be classified as biodegradable, historically materials had to decompose by microorganisms. In more recent times, biodegradation is considered to be a three-step process involving biodeterioration, biofragmentation and assimilation, as in **Figure 1.9**. Biodeterioration sees microorganisms and other abiotic factors break down the biodegradable polymers. These abiotic factors initiate degradation once

surpassing the activation energy of the chemical bonds of the polymer. For the purpose of this research, the biodeterioration of the polymers used must occur through factors such as body temperature, pH in the body and chemical attack by enzymes. This ensures their ability to break down in the body when used in medical devices. Microorganisms can also secrete enzymes or free radicals which enable depolymerisation, the fragmenting of biodegradable polymers progressively lowering their molecular weight. Assimilation sees the polymers' degradation products be absorbed into some aspect of microbial metabolic pathways. Other small fragments may be simultaneously excreted from the organism and salts as well as molecules like carbon dioxide, nitrogen, water or methane can be excreted to the environment through the mineralisation process.[47,48]

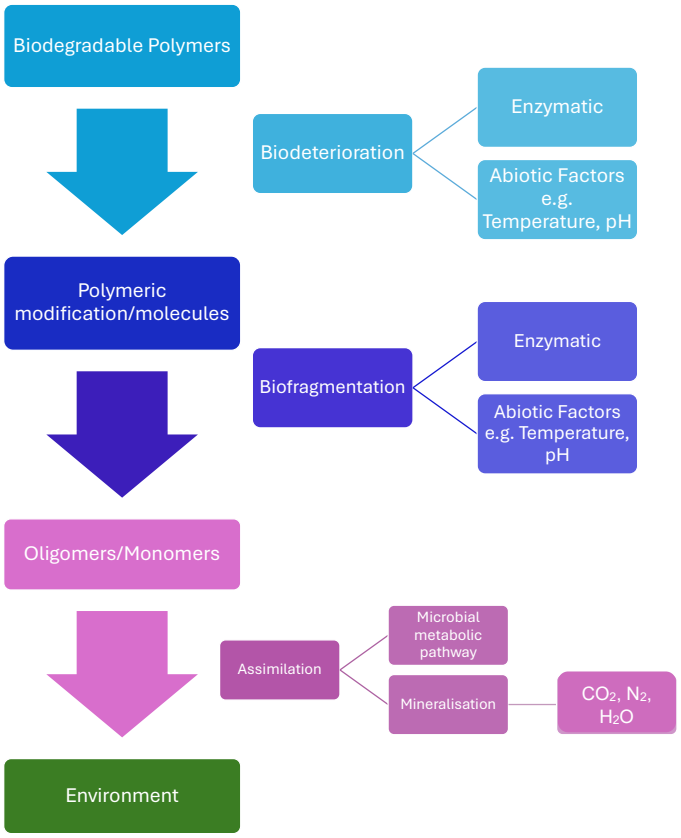


Figure 1.9: Scheme of polymer biodegradation, inspired by work published by Lucas et al.[47]

Research and creation of materials that have biodegradable properties has become an ever-expanding area of focus. The negative environmental implications of non-degradable materials make their mass production and end of life treatment highly

unsustainable. A fundamental requirement of such materials is their capacity to work for a finite amount of time before breaking down into environmentally and biologically friendly materials.[49] As a result, these materials have found use across a variety of industries as summarised in **Figure 1.10,** one of which is the medical industry.[50]

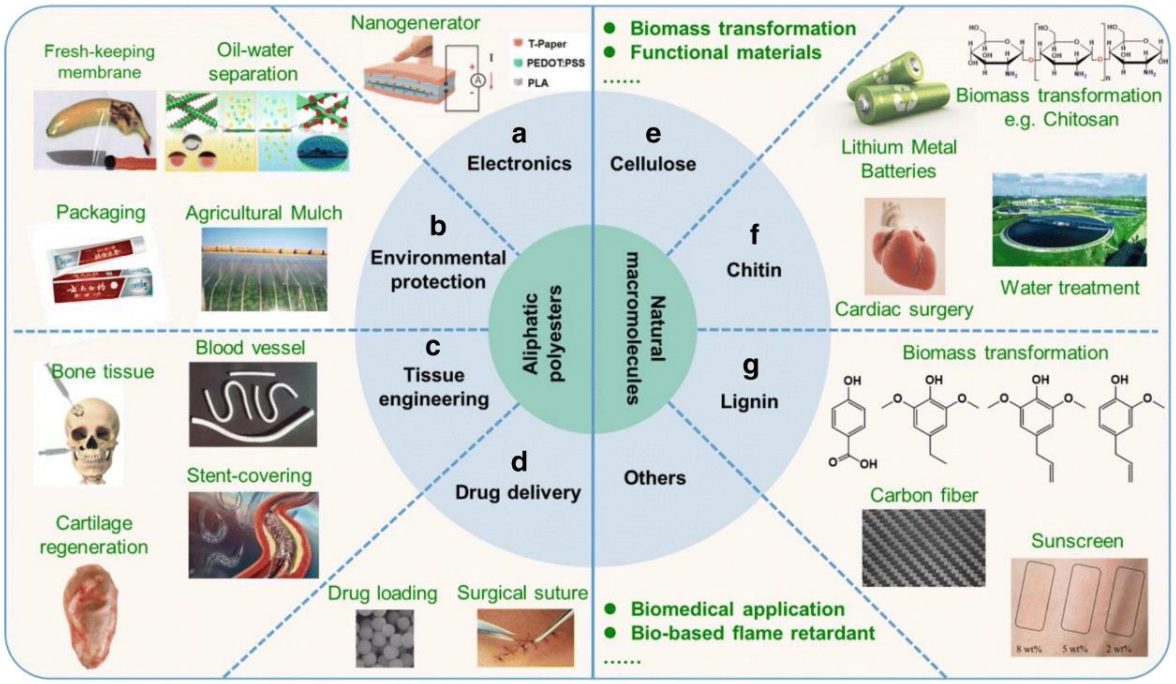


Figure 1.10: Summary of some common applications of biodegradable polymers across many fields.[50]

Over the last ten years, the amount of published research associated with polymers for biomedical applications has continued to grow annually, as in **Figure 1.11**.[51] Aside from environmental advantages, biodegradable polymers are also often more biocompatible and have tuneable properties compared to some traditional metallic or ceramic implants. Increased biocompatibility gives a reduction in cellular inflammation, infection, cytotoxicity and eventual implant rejection. Tuneability means that the type of biodegradable polymer, and by extension the type of implant, used can be refined by the desired application and timeline required. The implant-organism interaction is divided into three separate time periods: instantaneous, up to 60 minutes; short-term contact, up to 30 days; long-term contact, more than 30 days.[52] As a result, polymers have found many uses in biomedical settings across an array of fields including in cardiology[53], urology[54], dentistry[55], tissue regeneration[56] and drug delivery[57], demonstrated in **Figure 1.11**.

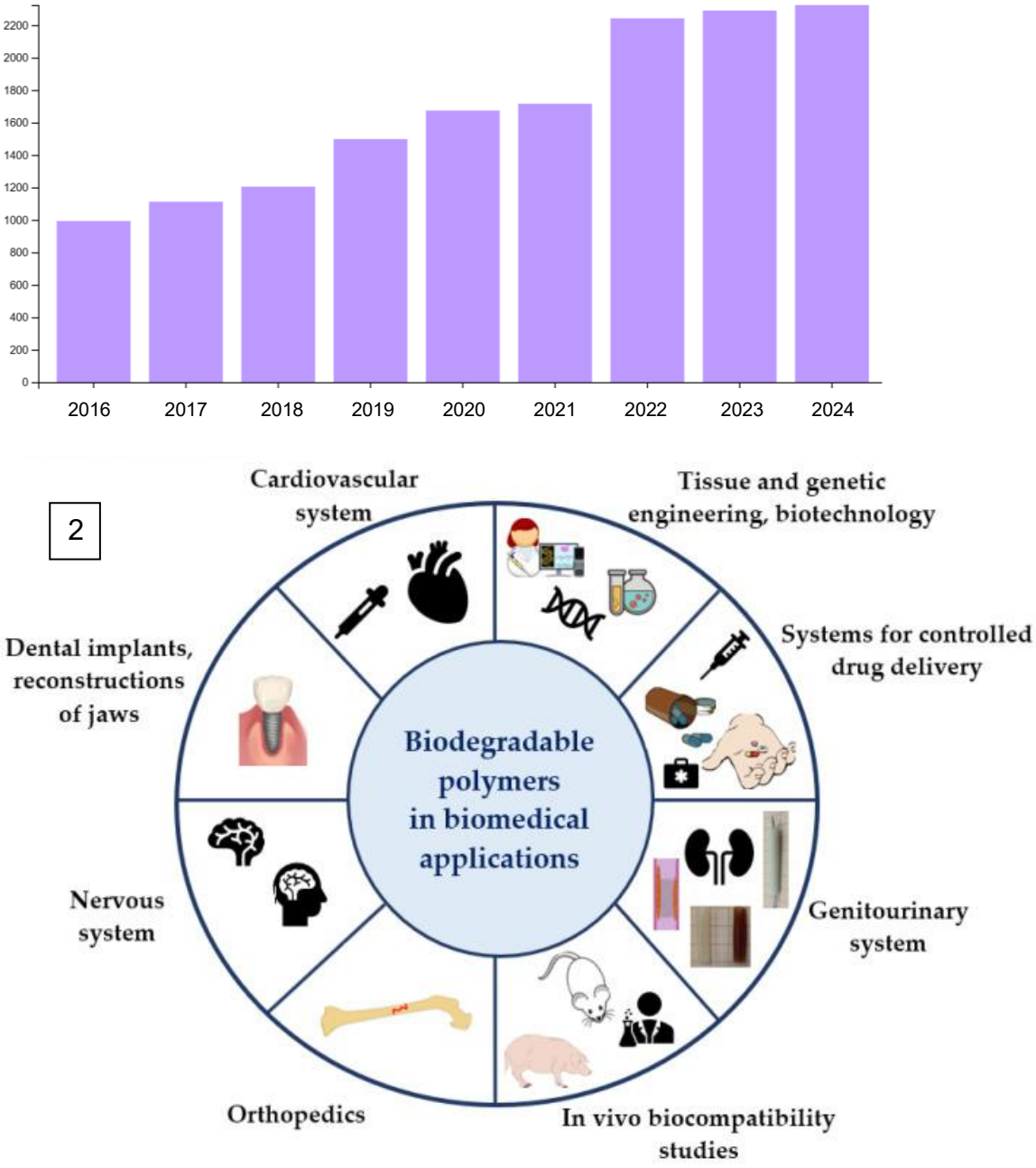


Figure 1.11: (1) Column chart of published research in Web of Science database from 2016 to 2024 analysed on the database and searched using the keywords; "polymer", "biomedical" and "applications" as topics (title, abstract and index)(top); schematic overview of various medical applications of biodegradable polymers (bottom).[52]

1.2.2 PCL and its Applications

Outside of the medical industry, the degradable nature of PCL, combined with the other properties mentioned above, has resulted in its use as a sustainable alternative in food science, agriculture and textiles. Research into its use in the food packaging industry has also been completed.

Zou et al. and Zhao et al. both reported on the blending of PCL with varying chitosan concentrations. These polymer blends were used to make films for food packaging purposes by electrospinning.[58,59] Zhao et al. reported on the advantages of the mixing of PCL with chitosan which gave improved surface roughness, increased antibacterial properties and higher hydrophobicity when compared to pure PCL electrospun fibres, as in **Figure 1.12**. Testing was completed comparing the electrospun PCL/chitosan films to standard polyethylene film and a 10% lower decay rate of fruit was observed with the chitosan blended PCL.[59]

Zou et al. blended hydroxypropyltrimethyl ammonium chloride chitosan (HACC), a quaternised version of chitosan, with PCL. The blend was loaded with Shikonin (SKN), a naphthoquinone found in certain plant roots, and electrospun to fabricate nanofibrous films. Both HACC and SKN have antibacterial properties, and the PCL/HACC/SKN film was found to have improved hydrophobicity and tensile strength. Additionally, SKN is pH-reactive therefore the researchers suggested potential use of the film as a form of “intelligent packaging”. Colour change, due to the presence of the SKN, could be observed based on the pH of food samples relative to their freshness. This property was tested by storing shrimp at different temperatures over a number of days, and visually analysing the change in colour of the PCL/HACC/SKN membrane, demonstrating the exciting versatility and potential of such materials.[58]

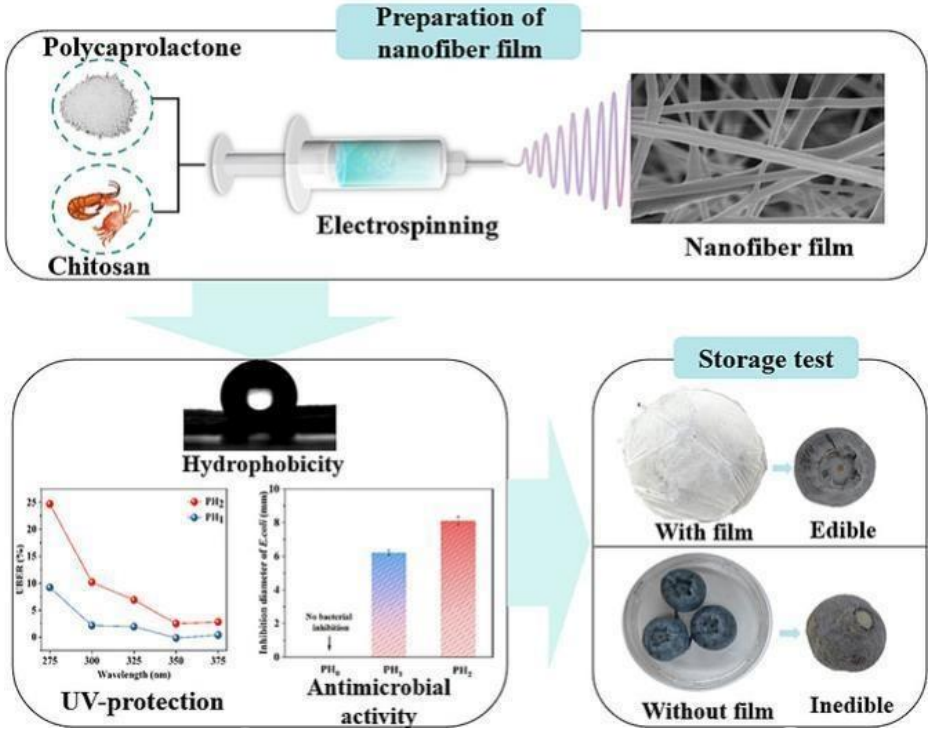


Figure 1.12: Overview of research completed by Zhao et al. involving the electrospinning, mechanical and antimicrobial testing and food packaging capabilities of PCL, chitosan blended films.[59]

The loading of PCL has also been studied for use in the food industry. El-Messery et al. completed research which saw the microencapsulation of polyphenols, extracted from olive leaves, into PCL-microcapsules through the double emulsion technique. This enabled the loading of these polyphenol dense microspheres into yoghurt without causing colour, acidity or viscosity change compared to the control. The research also noted the advantage of the PCL-microcapsule as a protective layer for the olive leaves. Digestion studies elucidated a greater release of the polyphenols in the intestinal fluid as opposed to the gastric and oral stages of digestion. The protective layer of the PCL was thus additionally desirable as it resulted in controlled release enabling the use of the polyphenols as antioxidants in the more effective location while avoiding degradation at oral and gastric stages of digestion.[60] Microencapsulation techniques involving PCL were also utilised to allow for the controlled release of citric acid and naringin which aim to increase plant growth promoter bacteria. Cesari et al. found potential use of PCL as an alternative to available chemical fertilisers.[61]

The capacity of PCL to be spun and sprayed has also seen it emerge in textile research. Chen et al. studied the loading of PCL with ciprofloxacin, an antibiotic. It was electrosprayed onto cotton alongside polyurethane loaded with zinc oxide nanoparticles. The resulting textile was covered in Janus nanoparticles, nanoparticles with two distinct phases or chemical and physical properties on opposite sides of the nanoparticle. This gave the clothing increased antibacterial activity and UV protection properties.[62] These are just some examples of the array of possible applications of PCL outside of its use in healthcare.

In the healthcare sector, as was briefly mentioned above, PCL has become a well-known polymer. It is FDA-approved and as such, has grown in popularity for use in a variety of healthcare associated materials. Perhaps the most commonly referenced example of this is the PCL hormonal bar. Capronor, first developed in the 1980s by Pitt et al., was a PCL capsule containing levonorgestrel to prevent ovulation.[63] Since then more device variations have built on this early work aiming to improve issues faced. More recently, a PCL based bar named Norplant, as imaged in **Figure 1.13**, was reported. It contained pluronic F68, a medium used to solubilise the PCL and drug levonorgestrel and enhance drug release, was used. It is FDA-approved and removed the early problems faced with ethyl oleate leaching from the Capronor.[64]

Other research has built on the drug delivery and structural capabilities of PCL. Augustine et al., electrospun PCL loaded with zinc oxide nanoparticles, as imaged in **Figure 1.13**, which have antibacterial properties by creating reactive oxygen species. They demonstrated the wound healing capacity of the membrane which promoted cell migration and proliferation.[65] PCL has also been 3D printed to form scaffolds for cellular regeneration, as in **Figure 1.13**. Lei et al. performed a type of 3D printing called fused deposition modelling with PCL. Magnesium phosphate pentahydrate was added to the PCL to aid the bone regeneration process. *In vitro* and *in vivo* studies were completed demonstrating the repair of defects in the tibia and maxillofacial bones of rabbits.[66]

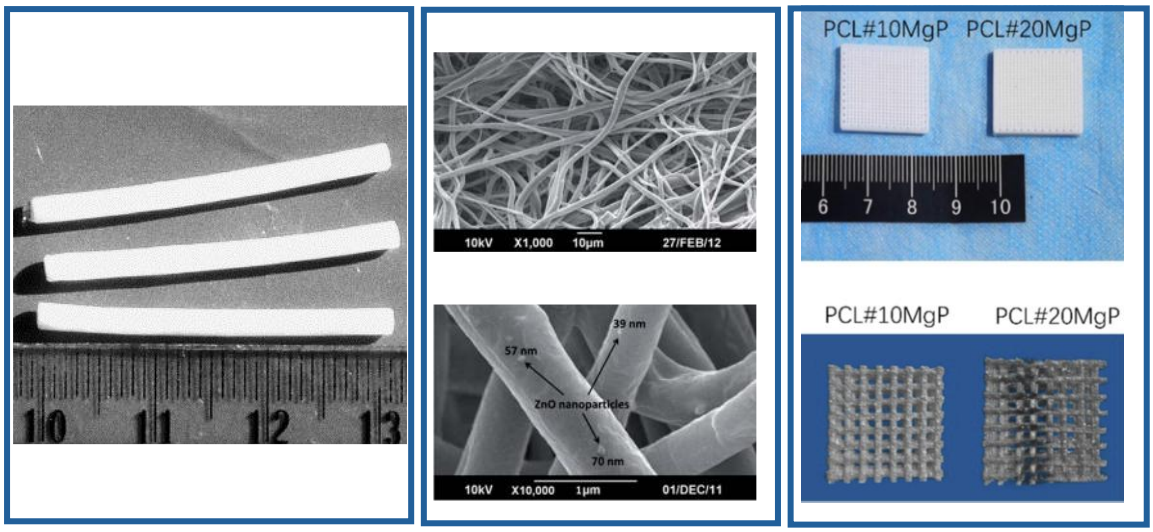


Figure 1.13: Image of Norplant with ruler for scale (left) [64]; Scanning electron microscopy (SEM) of electrospun PCL loaded with zinc oxide nanoparticles (middle)[65]; and preparation of and light microscope images of PCL scaffold (right).[66]

These are just a few examples of the existing and potential uses of PCL in biomaterials. As such, the extensive research completed in this area was another reason for the selection of PCL as one of the polymers of focus for this research.

1.2.3 Polycarbonates and their Applications

Unlike PCL, PAOMEC does not have a long history of use in biomaterials or widespread research for applications, as was previously mentioned. Research by the Dove Research Group involved investigations into the 3D printing of allyl functionalised polycarbonates. Thomas et al. and Barker et al. specifically focussed on PAOMEC and similarly structured poly(5-methyl-5-allyloxycarbonyl-1,3-dioxan-2-one) (PMAC). Microstereolithography is a type of 3D printing method based on stereolithography, wherein a photopolymerisable resin is exposed to UV-light to allow for layer-by-layer crosslinking on the sub-micron and microscale. The major advantage provided by these materials was that acrylate based photopolymerisation, which can be toxic, could be avoided. Examples of the resulting printed structures can be seen in **Figure 1.14**.[41,67] Barker et al. performed Bovine intervertebral disc cell studies to confirm the cytocompatibility of the material.

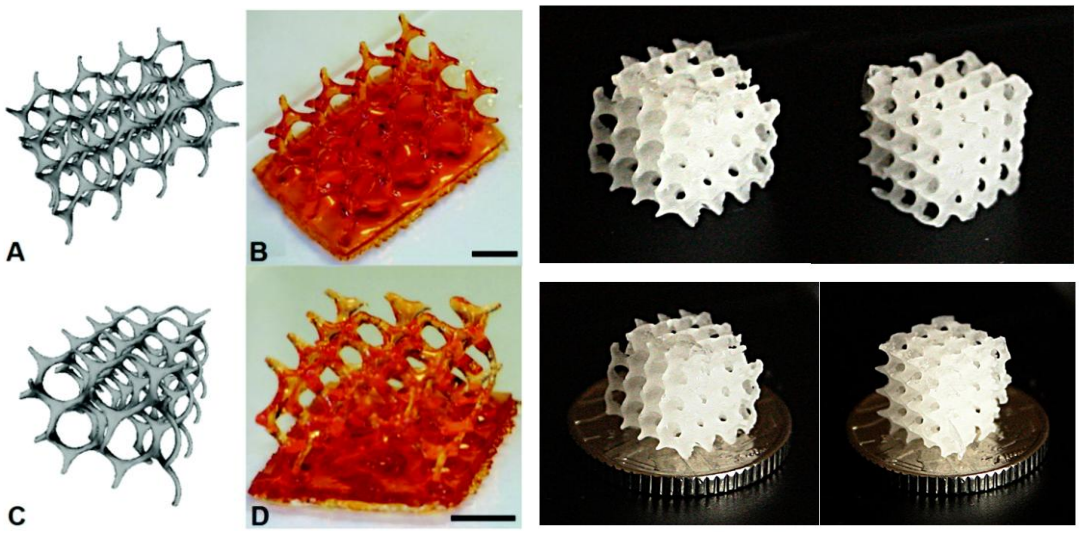


Figure 1.14: 3D computer aided design (CAD) model and 3D printed PMAC with scale bars representing 2.5 mm (left) and 3D print of PAOMEC sample place on a 5 pence coin to show scale.

Outside of PAOMEC, various other aliphatic carbonates have been researched for use in a wide array of applications and industries. Due to the added functionality provided by aliphatic polycarbonates (APCs), they have found use in 3D printing techniques like microlithography, as mentioned above. They have also been researched in piezoelectric ink jet printing, as illustrated in **Figure 1.15**. This is a form of printing whereby the polymer material is deposited in the form of droplets and crosslinked via UV-initiated reactions. This process used thiol crosslinker chemicals which could be activated by UV light, thus forming bonds between alkenes and thiol groups, which is also known as thiol-ene click chemistry. With this printing process, microscale dots can be printed with different properties depending on the blend of polymers used.[68]

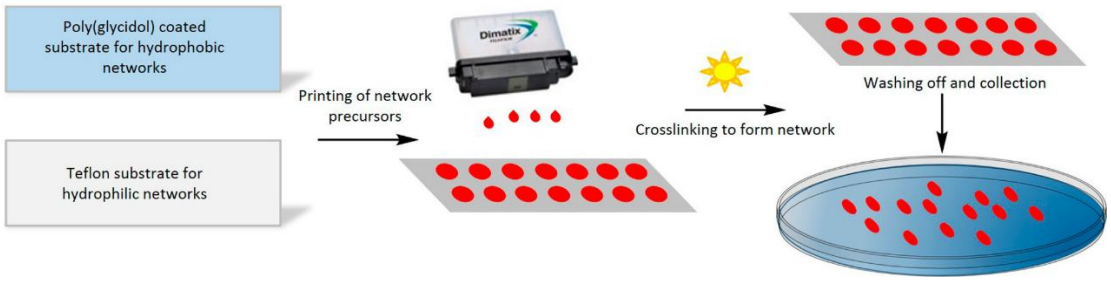


Figure 1.15: Reaction scheme for pizoelectronic inkjet printing process.[68]

Early studies have also commenced into the use of APCs in carbon dioxide gas separation. The presence of the carbonate groups in APCs result in increased affinity for carbon dioxide. Carbon capture technologies are of interest for the removal of excess carbon dioxide from the atmosphere and its isolation for use as a carbon

source. The APCs tested were analysed on their permeability to nitrogen and carbon dioxide and their selectivity of carbon dioxide over nitrogen for better carbon capture. Comparison between poly(1,4-butylene carbonate), poly(1,5-pentamethylene carbonate), and poly(1,6-hexamethylene carbonate) (PHC) membranes was performed. The results demonstrated that the longer chain diol of PHC gave more ordered packing and higher rigidity of the membrane leading to higher carbon dioxide selectivity. These materials all showed promise with PHC being deemed to have the most potential for use as a sustainable approach to carbon dioxide capture.[69]

In medicine, there has been interest in polycarbonates for various applications. Zong et al. completed a study involving the synthesis of a polycarbonate-based hydrogel used for the promotion of epithelial cell regeneration, as illustrated in **Figure 1.16**. A cyclic carbonate monomer was functionalised with an aldehyde and polymerised with PEG used as the initiator and to increase hydrophilicity. Adipic acid dihydrazide was reacted with the free aldehydes to crosslink the hydrogel in water through the formation of acyl hydrazone bonds. Drug release behaviour was studied using curcumin as a model and *in vitro* and *in vivo* studies performed on mouse models. This demonstrated the cell regenerative power of the hydrogel with and without the drug present, thereby highlighting the benefit of the presence of the hydrogel alone. The biodegradation of the gel was also confirmed via both hydrolytic pathways in phosphate saline buffer (PBS), with and without the presence of lipase, which is known to aid ester hydrolysis.[70]

Like PCL, drug loading of aliphatic polycarbonates and their drug release capabilities has been of interest in the literature. An example of such research was reported by Zhang et al., wherein a functionalised polycarbonate was loaded with simvastatin, a statin used to increase bone regeneration, as seen in **Figure 1.16**. The functionalities, namely imidazole and phenyl azido side groups were used as chelating agents to enable the polycarbonate to coat the zinc lithium alloy via photo-crosslinking methods. The aim of the coating was to slow the release of Zn^{2+} cations from the alloy which reduced the excessive early release of Zn^{2+} cations which had been observed to cause cytotoxic responses. At controlled rates however, the Zn^{2+} and simvastatin release promoted new bone growth in rabbit models. Additionally, of

benefit was the antibacterial effects shown by the combined efforts of the Zn^{2+} cations and simvastatin.[71]

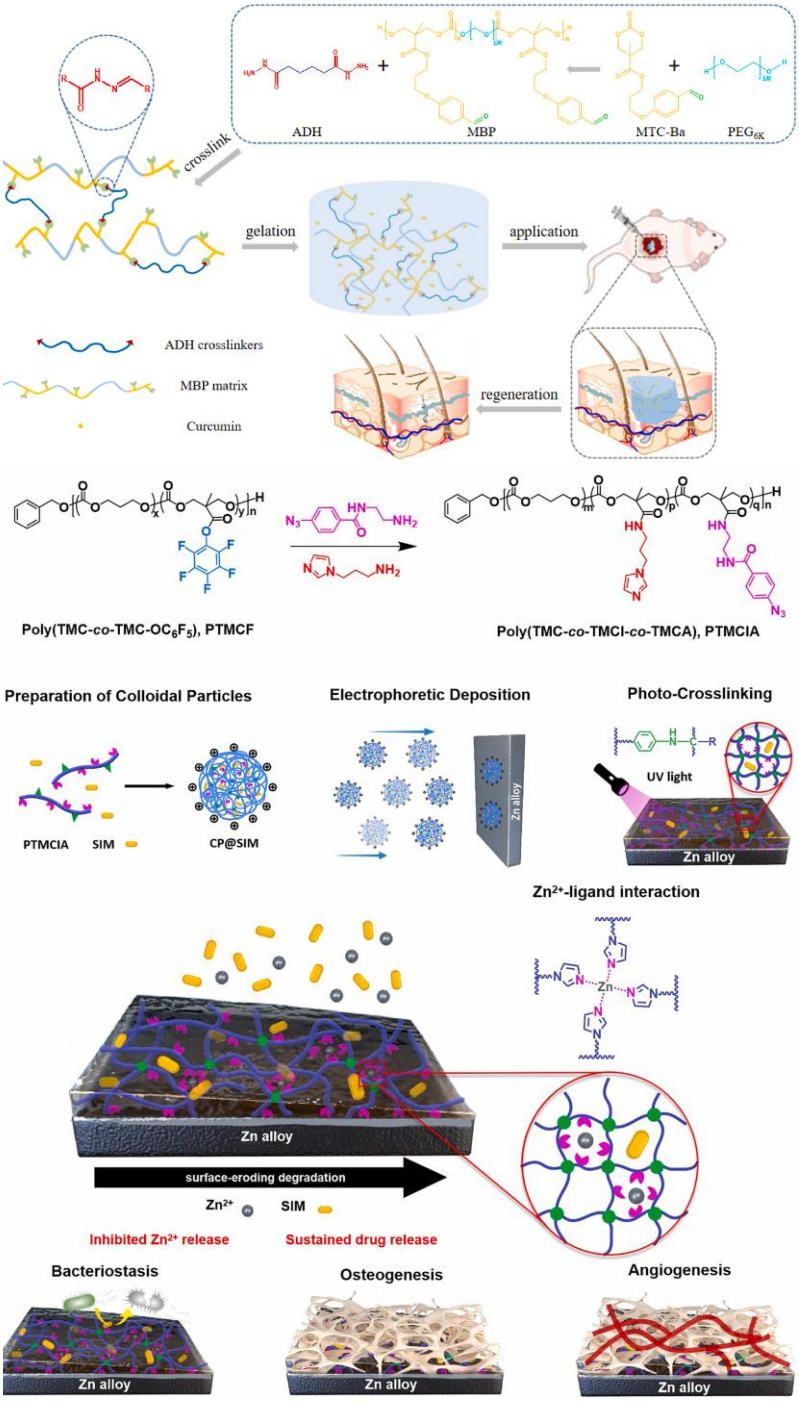


Figure 1.16: Illustration of studies performed by Zong et al. (top)[70] and Zhang et al.(bottom).[71]

Despite not being studied as extensively as PCL, the early research mentioned above elucidates the exciting potential of polycarbonates, such as PAOMEC, due to their biocompatibility, degradation profile and functionalisation possibilities. Both PCL and PAOMEC, were therefore selected for this research to further investigate their potential

as biomaterials. A specific focus was placed on the use of these polymers to create materials that are not only biocompatible and degradable but also materials that prevent biofouling.

1.3 Antibiofouling Surfaces

1.3.1 Antifouling Overview

Fouling, in general, is the attachment of unwanted materials to a surface. Biofouling is specific to the attachment of microbes such as bacteria.[72] Bacteria that are free flowing are often classified to be in the planktonic state; however, their build up on surfaces has been observed as a common occurrence.[73] The accumulation of bacteria and resulting biofouling of a surface can lead to biofilm formation, as illustrated in **Figure 1.17**.[74] A biofilm is defined as group of bacteria in a matrix, generally attached to or associated with a surface. Biofilm formation is generally broken up into a five step process. These bacteria often attach to a surface, initially in a reversible manner. This first stage is followed by stage two, irreversible attachment resulting in microcolony growth. It is during this stage that the point of attachment of the bacterial cell to the surface transitions from the cell pole or flagella to the entire cell attaching longitudinally. The next two stages are denoted maturation-I and maturation-II. These stages involve the attached bacteria forming cell clusters that are within the extracellular polymeric substances (EPS) matrix followed by the growing of these clusters from a few cells in thickness to matured microcolonies. The final stage involves detachment or dispersion of cells from the EPS matrix back into the free flowing, planktonic state.[75,76]

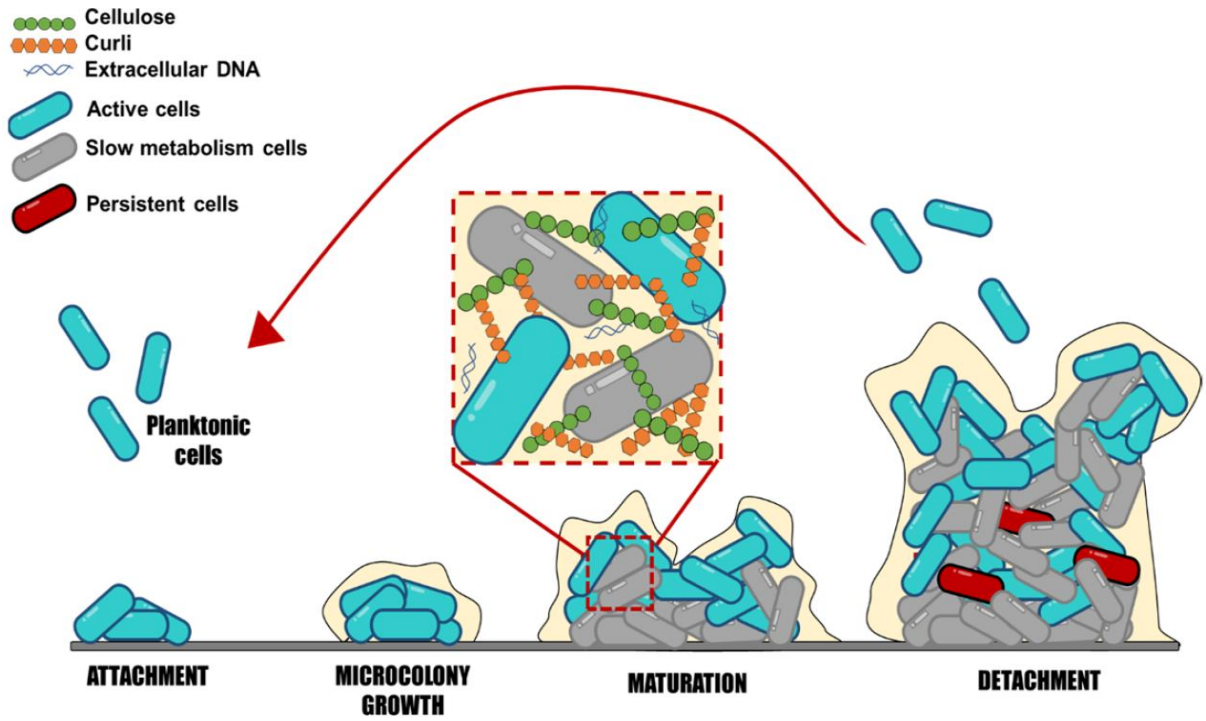


Figure 1.17: Illustration of the 5 stages of biofilm formation.[74]

Fouling is a problem in many industries including medicine. Implants and other biomaterials used vary across different specialties; however, post operative infection remains a common threat. Bacterial colonisation at the implantation site and implant-cell interface can cause a variety of infections or lead to biofilm formation thus causing a variety of post operative complications.[77] Bacterial infections associated with biomaterial or medical device implantation is estimated to affect 2 to 10% of all patients but can be as high as 35% which has been reported in some fields like breast augmentation.[1,77–80]

The most common bacteria that cause post-operative infections are *Staphylococcus, Streptococcus, and Pseudomonas*.[81] *Staphylococcus aureus* (*S. aureus*) and *S. epidermidis*, two strains of gram-positive bacteria, make up two of three implant-related infections in orthopaedics.[82] *Staphylococci* infections also especially common in dental and cardiovascular implants, as in **Figure 1.18**.[83–85]

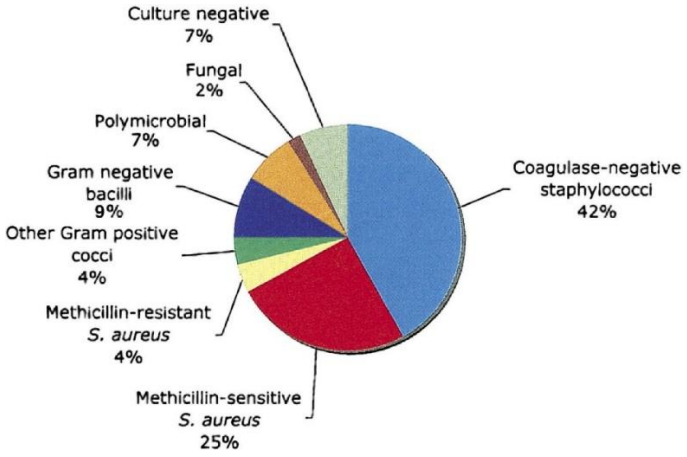


Figure 1.18: Breakdown of microbiology infections on implantable cardiac devices.[86]

It is common practice to give prophylactic antibiotics pre-surgery to prevent bacterial infections when implanting medical devices. Broad spectrum antibiotics or intravenous antibiotics can also be given post-surgery to suppress the possibility of contracting a bacterial infection. There is evidence to suggest provision of antibiotics for an extended period of time post-surgery does reduce infections occurring but this protocol is case-, surgery- and patient-based.[87] There has also been research showing that antibiotic prescriptions vary across the globe. There is no set standard of care which results in variance in the care of patients post-operatively, simply due to the country in which they are treated.[88] This lack of consistency can result in over-prescription and misuse of antibiotics, which can in turn lead to antibiotic resistance.

Metal implants are commonly used in a variety of fields, including but not exclusive to dental and orthopaedic fields. Titanium and its alloys are some of the most commonly used metals due to their biocompatibility and high mechanical strength. Despite the advantages of titanium, biofouling is a commonly reported issue. For example, imaging of titanium dental implants elucidated the adhesion of *S. aureus* to the surface which can lead to biofilm formation, as seen in the SEM images in **Figure 1.19**.[89]

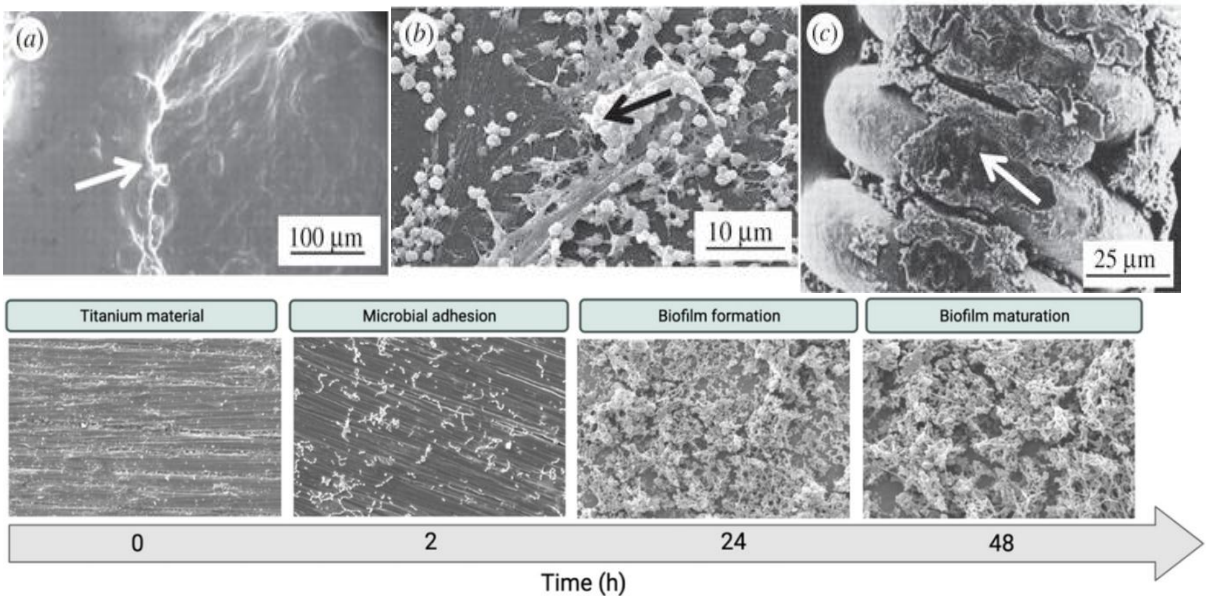


Figure 1.19: SEM images of different medical devices with biofilms: (a) ventilation tube; (b) needleless connector; (c) pacemaker wire (top).[80] SEM images of biofilm development on titanium over a 48 hour period, to mimic that of a dental implant.[90]

Due to the biofouling issues commonly observed, many approaches have been taken to limit implant associated infections. Tardelli et al. and Villegas et al. comprehensively summarised many approaches taken to enhance the antibiofouling properties of titanium based surfaces, including changing surface chemistry through anti-adhesion surface coating and bactericidal surface coating as well as changing the surface topography.[91,92]

As current materials have been shown to be susceptible to bacteria and the standard of care and provision of antibiotics is not always consistent or effective, material and surface modification of medical devices has been deemed a possible solution. The aim of such modifications is to provide alternatives to the provision of systemic antibiotic treatments and fight bacteria in a more targeted manner.[93]

1.3.2 Surface modifications of biomaterials

Biofilms, as mentioned above, are defined as a colony or community of bacteria that adhere to surfaces within an EPS matrix. They have been found to be antibiotic-resistant in many cases. There are many contributing factors that result in the lower efficacy of antibiotics when treating biofilms including the inability of the antibiotics to effectively penetrate though the matrix that surrounds bacteria. The EPS matrix contains many other chemicals outside of bacterial cells including eDNA,

polysaccharides and proteins. These chemicals can interact with antibiotics thereby interrupting interaction with bacteria.[94] The National Institute of Health in the United States estimates that up to 80% of bacterial infections can be attributed to biofilms.[95] It is therefore theorised that creating surfaces that are inherently antibiofouling, i.e. surfaces that prevent the first stage of biofilm formation, the adhesion of bacteria, could decrease the risk of biofilm formation. In literature, there are generally three main categories of approaches taken to create antibiofouling surfaces; active molecule release from the surface; killing microorganisms that come in contact with the surface; and by having antiadhesive surface properties, as summarised in **Figure 1.20**.[96]

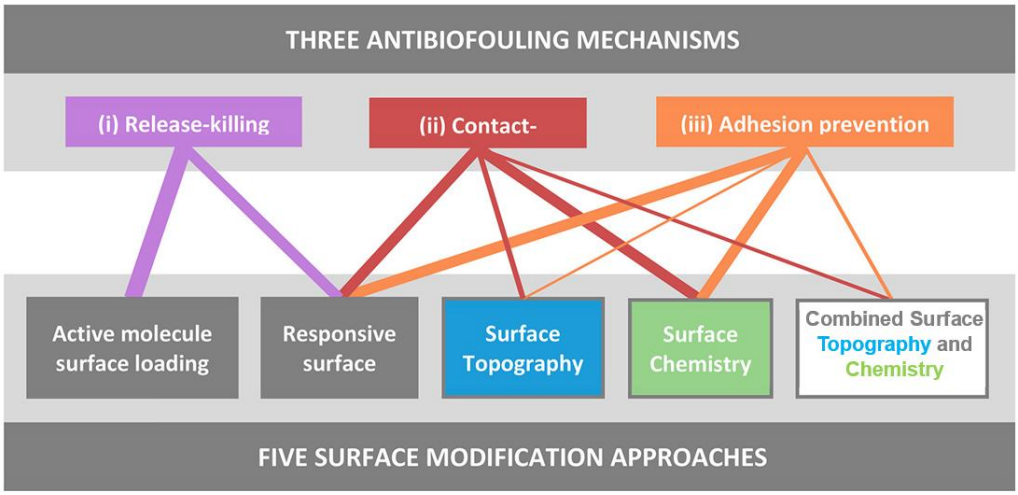


Figure 1.20: Three mechanisms by which antibiofouling surfaces work and the surface modification completed to create such surfaces adapted from Durand et al.[97] The thickness of the links are estimations of the amount of research articles on the topics.

Release killing involves addition of additives or chemicals to a surface which will in turn be released by a trigger, for example upon pH change, temperature change or enzymatic activity. Antibiotics are commonly deposited onto or incorporated into these surfaces.[96] Rai et al. reported an example of this by loading a PCL film with the antibiotic, vancomycin. The loaded PCL material demonstrated higher efficacy against methicillin-resistant *S. aureus* compared to the drug alone. The slow release of the drug from the PCL film, resulted in sustained release of drugs to fight the infection in rabbits over a longer period of time dissimilarly to the drug only study, which saw initial improvement followed by emergence of the infection after some time.[98] This study highlights the advantages of biodegradable polymers like PCL for slow, controlled and targeted drug release at the point of infection. This technique,

however, may still face the limitations of antibiotic resistance. The World Health Organization (WHO) recorded a rise of almost 40% in antibiotic resistance of the pathogen-antibiotic interactions analysed. South-East Asia is the area of the highest prevalence of antibiotic resistant infections with one in three reported to be resistant.[99]

Contact killing and adhesion prevention do not face the problem of antibiotic resistance in the same way. Both mechanisms aim to have similar outcomes while relying on opposing modes of action. Contact killing prioritises the killing of any bacteria that adhere to the surface while anti-adhesive surfaces strive to prevent adhesion altogether. These mechanisms of action can work via topographical or chemical methods; some utilise both simultaneously.[96] There are various approaches taken in literature to create such surfaces but this research focussed on two specific techniques namely, altering the surface charges and surface topography.

1.3.3 Influence of Surface Charge

Altering the surface charge of materials is one approach that has been taken to create antibacterial and antibiofouling surfaces. Many studies have been completed with cationic – positively charged – or zwitterionic – both negatively and positively charged – materials to give charged surfaces. These studies mainly focus on bactericidal activity of these surfaces. It has been found that overall, the large majority of bacteria have a net negative surface charge.[100] Cationic surfaces have demonstrated improved antibacterial properties through various methods, including improved adsorption by microbial membranes to destroy bacteria from within their membranes or the electrostatic attraction leading to the leakage of bacterial intracellular components from within the cell leading to cell death.[101,102]

There have been reports of problems with biocompatibility, haemolytic properties and cytotoxicity with densely cationic materials.[103] Zwitterionic surfaces have been demonstrated to be more biocompatible. At neutral pH, of approximately 7.4, the neutral surface charge enables repulsion of proteins that are inherently charged at the same pH, such as cationic lysozyme and anionic pepsin.[104] Research has also been conducted into the benefit of using zwitterionic materials due to their ability to undergo zwitterionic-to-cationic conversion under acidic conditions, as illustrated in **Figure 1.21**. This enables the materials to be biocompatible at physiological pH

while bactericidal activity is demonstrated by the cationic surface at acidic conditions mimicking the pH generally found at the site of bacterial infections.[105]

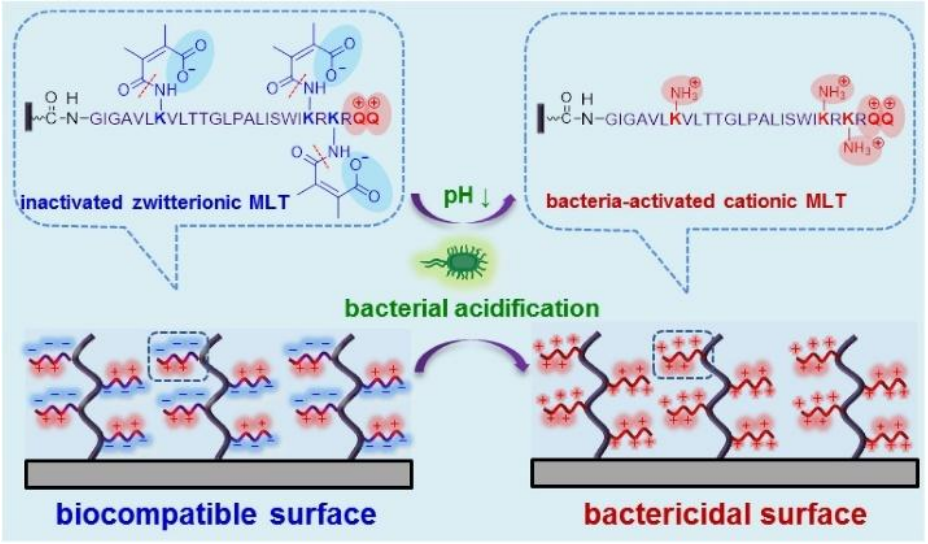


Figure 1.21: Illustration of conversion of zwitterionic surface to cationic surface due to bacteria induced acidic environment.[105]

For antibiofouling purposes, a lot of promise has also been shown with anionic surfaces. As mentioned, the surfaces of bacterial cells have a negative electrostatic charge. This is largely due to the ionized phosphoryl and carboxylate groups present.[100,106] There is evidence of electrostatic repulsion between negatively charged surfaces and bacteria, thus improving the antibiofouling properties.[107] Rzhepishevska et al. have reported the presence of anionic charge not only resulted in a reduction in biofilm formation, but also saw the shape of the biofilm that did form, differ due to the negative surface charge. They noted that there was also an increase in regulatory cyclic diguanylate (c-di-GMP), a signalling molecule that impacted bacterial activities relating biofilm formation, virulence and motility. It was suggested that the increase in di-GMP demonstrated the adaptive capabilities of bacteria. Despite the surface charge resulting in lower biofilm formation, researchers suggest that bacteria could physiologically adapt to the charged surface. They compared cationic, anionic and zwitterionic surfaces with other materials to assess differences in biofilm formation and found the zwitterionic and anionic surfaces to present the highest antibiofouling capabilities, as in **Figure 1.22**. Interestingly, they noted that a biofilm formed on the cationic layer, and additionally, that although the bacteria in direct contact with the surface were dead, the bacteria on top of this layer were still viable. It was thus theorised that although cationic surfaces demonstrated

bactericidal capabilities, constant cleaning of the surface would be required to ensure direct contact of bacteria with the surface.[108]

Research completed by Montag et al. observed that bacterial accumulation on the surface decreased linearly with increasingly negative zeta potential.[109] The fabrication of charged polymer materials has been achieved through the use of polymers with functional groups like amines in their repeating unit, such as ε-poly-l-lysine, or through post-polymerisation functionalisation.[110] These post-polymerisation additions of charged functionalities can be performed in many ways, including through quaternisation reactions or click reactions using, for example, thiol-ene or alkyne-azide approaches, as illustrated in **Figure 1.22**.[111,112]

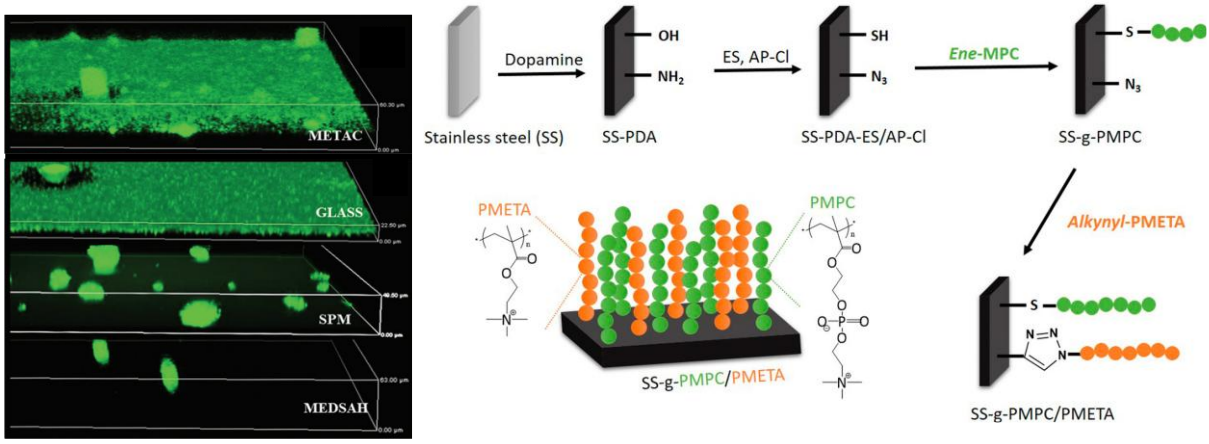


Figure 1.22: Confocal microscopy images of different biofilms formed on various surfaces using Pseudomonas aeruginosa*, adapted from Rzhepishevska et al. The samples named SPM and MEDSAH are the anionic and zwitterionic samples, respectively. METAC is the cationic sample (left)[108] and illustration for click-reactions used for post-polymerisation functionalisation (right).[112]*

Another technique that has been utilised to alter biofouling properties of a surface is changing the surface topography.

1.3.4 Influence of Surface Topography

Surface topography alteration has shown great promise in the area of antibiofouling surfaces. The research into the influence of microtopography on antibacterial and antibiofouling properties of a surface was originally inspired by surfaces found in nature, such as the wings of insects like cicadae, damselflies and dragonflies or the skin of animals like sharks.[113–118] The field of research into biomimetic surfaces has since grown. Micro- and nanoscale topographies of varying shapes, sizes and organisations have demonstrated antibacterial and antibiofouling capabilities.[119]

There are numerous theories for how nano- and microstructures perpetuate their antibiofouling and bactericidal properties. The presence of nanopillars on cicada wings has been reported to preferentially kill gram-negative bacteria and the mechanism of action was therefore believed to be mechanical disruption of gram-negative cells, while the thicker peptidoglycan layers on gram-positive cells made the structures less problematic.[115,116] More recent research by Jenkins et al. has suggested that the presence of nanostructures my not cause direct lysis of bacterial cells, but instead create an environment that induces oxidative stress, cell deformation and prevent successful cell division.[120]

The introduction of a new surface topography has also been demonstrated to alter surface wettability often resulting in superhydrophobic surfaces. These “self-cleaning” surfaces have thus been found to repel or prevent bacterial adhesion.[121,122] For example, Ibrahim et al. found that by simply changing the shape of the topography from rectangles to circles or spikes, the contact angle and therefore the hydrophobicity of the surfaces could be tailored, as in **Figure 1.23**.[123] A variety of different types of surface topographies can result in different surface properties and thus vary the antibiofouling and antibacterial abilities of such surfaces. The shape, size and height, width and spacing parameters can also have effects on the physical and chemical properties of materials.

Topographies and patterns that are close in size or smaller than that of the bacteria have been observed to better inhibit biofilm formation.[124] The inter-structure gapping is also a key factor to consider to minimise the attachment of bacteria between structures. Cuello et al. demonstrated that on surfaces with structural spacing of 1 or 2 μm, lower bacterial adhesion was seen when compared to a surface with 10 μm spacing between the structures. It was also noted that the samples with 1 and 2 μm gapping had higher water contact angles, and were therefore more hydrophobic, than those with 10 μm gapping which was found to be hydrophilic. This was also theorised to contribute to the antibiofouling properties displayed by the more narrowly spaced surfaces.[125] Francone et al. completed studies comparing the influence of nanoscale and microscale structures. As in **Figure 1.23**, samples with microstructures, nanostructures and a blend of both in a hierarchical manner were made and analysed. The complexity of the bacterial cell interaction with the sample surface was delved into, and it was theorised that due to the complexity of said

interaction, a myriad of overlapping properties could affect the antibiofouling capabilities of a surface. The research noted that the gram-positive *S. aureus* was more influenced by the hydrophobicity of the sample while gram-negative *E. coli* was more affected by the topography itself.[126]

Surface Pattern		Roll-Off Angle [°]	Apparent Contact Angle [°]
	Rectangle	>90	128
	Rounded rectangle	>90	133
	Circles	>90	130
	Spikes	10	167
	Rounded spikes	35	166

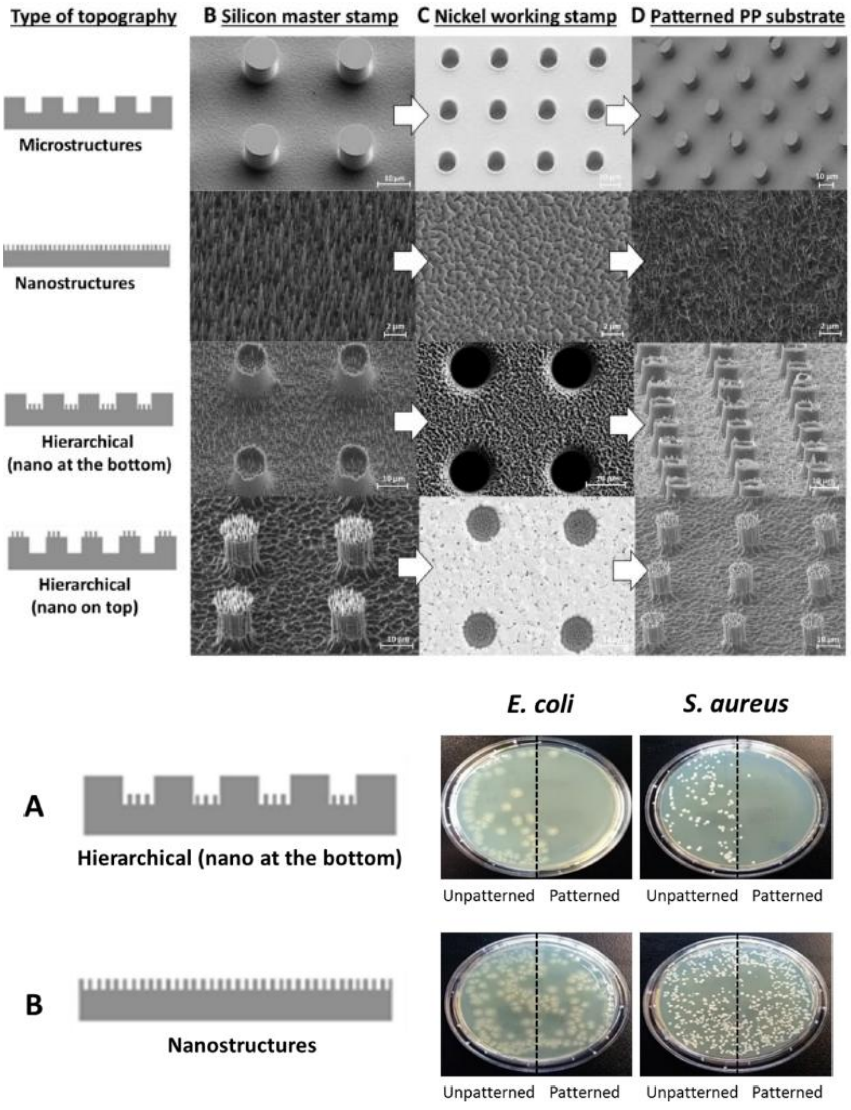


Figure 1.23: Water contact angles and roll off angles of different topographical shapes (top)[123]; SEM images of different nano- and microstructures including hierarchical templates (middle); photos taken of E. coli*, a gram-negative strain, and S. aureus, a gram-positive strain and their respective responses to nanostructures and hierarchical templates with nanostructures at the base of the micropillars.[126]*

There are a myriad of methods available and being developed to design materials with topographical features. These techniques include dry and wet etching, 3D-printing and various soft and hard lithographic techniques.[127] For the purpose of this research, replica moulding was selected as a technique for introducing structural changes. Replica moulding is a technique that uses a mask or template with the desired structures on as a master template. From this, a primary mould is made by introducing a liquid polymer to the master. The polymer is cured, normally via thermal or UV-initiated routes, to form the primary mould, which is, in turn, used as a template for a second liquid polymer to create an exact replica of the master.[128] This process is discussed in more detail in **Chapter 4**. Early work by Xia et al. demonstrated the ability to reproduce structures as small as 30 nm.[129] There are several reasons why replica moulding was selected for use in this research, some of which are; that it is cost-effective, it is efficient, the technique is easily adaptable, meaning the size and shape of the structures as well as the material desired to be structured are all easily interchangeable, and the technique can fabricate structures on a sub-micron and nanoscale.[128,130]

Literature reports on the successes and challenges faced by topographically altered materials as well as materials with various surface charges. As described in **Sections 1.3.2. and 1.3.3**, details on fabrication approaches and bacterial cell analysis have been researched and reviewed. As of yet, there has been little focus on the influence these two parameters have on antibiofouling properties when combined with or compared to each other directly.

1.4 Project Aims

This research aimed to demonstrate a versatile approach to creating crosslinked materials with controllably adaptable surface properties. It sought to design an adaptable platform for the creation of materials with interchangeable surface properties whilst maintaining the same backbone. Such a platform was planned to allow for the assessment of various surface properties independently or in combination and their influence on biofouling. The growing challenges faced due to antibiotic resistance require us to reinvent and reimagine the way that we approach bacterial infections. In the case of biomaterials and their implantation in the body, biofilm formation is a key issue. One of the primary goals of this research was,

therefore, to understand the influence of sub-micron surface topography and surface charge on antibiofouling. By expanding our fundamental understanding of what surface properties enhance antibiofouling properties through direct comparison, these studies aimed to lay the foundation for future fabrication of more effective and informed medical devices with antibiofouling surfaces.

In this research, PCL and PAOMEC were the two oligomers selected due to their biocompatibility, degradability and capacity to be adapted structurally and chemically. In this way, novel research was planned to elucidate the influence of sub-micron structures and surface charge on bacterial and mammalian cell interactions with these materials.

By using a single backbone material—PAOMEC—rather than the varied materials used in previous approaches, true like-for-like comparisons between samples was intended to be made possible. Furthermore, we could assess the individual and combined effects of surface topography and surface charge.

The introduction of sub-micron surface topography to PCL-based materials, and studies to investigate the effect of the same structures on endothelial cells were also planned. This looked to enable a better understanding of how the introduction of topographical features interact with mammalian cells, and how this differs from bacterial cells.

Chapter 2 Materials and Methods

2.1 Materials

Polycaprolactone diol (PCL diol, M_n 1250 g/mol), methacryloyl chloride, anhydrous magnesium sulfate, potassium hydroxide,1,6-hexanediol diacrylate (HDDA), 2-hydroxy-4'-(2-hydroxyethoxy)-2-methylpropiophenone (Irgacure-2959), phenylbis(2,4,6-trimethylbenzoyl) phosphine oxide (PBPO), trimethylolpropane allyl ether diol, ethyl chloroformate, trimethylolpropane allyl ether diol, triethylamine, polyethylene glycol diacrylate (PEGDA) (M_w 575 g/mol), polypropylene glycol diacrylate (PPGDA); (M_w 800 g/mol) (contains 100 ppm butylhydroxytoluene and monomethyl ether hydroquinone as inhibitors), atomic force microscopy (AFM) probes Tap300G (BudgetSensors®) with force constants of 40 Nm^{-1}, acetone (99% anhydrous), crystal violet (1% aqueous solution), LB Broth (Lennox), isopropanol (IPA, 99% anhydrous), hydrochloric acid (HCl, 37%, analytical grade), ethanol (EtOH, 99% anhydrous) dichloromethane (DCM,99% anhydrous), hexane (99% anhydrous), chloroform-d^3, molecular sieves 3Å and silica gel with a pore size of 60 Å, fetal bovine serum (FBS), penicillin-streptomycin (Pen Strep), lactate dehydrogenase (LDH) assay medium, industrial methylated spirits (IMS) and hydrogen peroxide solution (H1009) were purchased from Sigma Aldrich/Merck Life Sciences, Wicklow, Ireland. Polycaprolactone diol (PCL diol, M_n 530 g/mol) was purchased from Polysciences Inc., Heddesheim, Germany. Dichloromethane (99.9%, extra dry, stabilized, AcroSeal™), tetrahydrofuran (99.5%, extra dry over molecular sieve, stabilized, AcroSeal™), agar powder, yeast extract, Oxoid™ tryptone, 1,8-diazabicyclo[5.4.0]undec-7-ene (DBU), *Escherichia coli* DH5α (*E. coli*) and Oxoid™ antimicrobial susceptibility discs that were blank or loaded with 10 µg of Ampicillin or Gentamicin were purchased from Thermo Fisher Scientific, Dublin, Ireland. Cyclohexylamine and 3,5-bis(trifluoromethyl)phenyl isothiocyanate were sourced from TCI, Zwijndrecht, Belgium. SYLGARD™ 184 silicone elastomer base and curing agent were purchased from Farnell, Dublin, Ireland. DOWSIL silicone sealant (732 clear) was purchased from Dow, Cardiff, UK. 1,4-butane diol was purchased from TCI, Eschborn Germany. Ultimaker transparent poly(lactic acid) (PLA) was used as the material for 3D printing purchased from Inspire 3D, Wicklow, Ireland.

Staphylococcus epidermidis ATCC1228 (*S. epidermidis*) and *Pseudomonas fluorescens WCS365 (P. fluorescens)* were provided by Prof. Eoin Casey, University College Dublin. Rely+On Virkon Virucidal Disinfectant Tablets used to neutralise bacterial waste were purchased from Scientific Laboratory Supplies, Dublin, Ireland. The CellTiter 96® AQueous One Solution Cell Proliferation Assay, MTS Assay, was purchased from Promega, Hampshire, UK. Primary Human Aortic Endothelial Cells (HAECs) (C-12271) and Endothelial Cell Growth Medium MV (C-22020) were obtained from Brennan and Co., Dublin, Ireland. Vascular endothelial growth factor, 293-VE-050/CF, was purchased from Bio Techne, Minneapolis, USA.

2.2 Instrumentation

The precision balance, Quintix65-1S analytical balance was used (Sartorius Stedim, Ireland). Rotary evaporations were completed using the Rotavapor R-100 (Mason Technology, Dublin, Ireland). Polymer products were dried in Fistreem vacuum oven (Scientific Laboratory Supplies, Dublin, Ireland) and crosslinked samples as well as dried, purified polymers were stored in Pyrex® vacuum desiccators (Sigma Aldrich, Wicklow, Ireland). Ultraviolet (UV) radical polymerisations were performed with UVP Crosslinker 1000 L (Fisher Scientific, Dublin, Ireland) at an intensity of 200 kJ. The Fisherbrand™ mini vortex mixer was used to mix contents of centrifuge tubes (Fisher Scientific, Dublin, Ireland). VWR mini orbital shaker 980125 was used to shake inoculated buffers in cell studies in the oven, while the VWR incubating mini shaker was used to shake inoculated media at specific temperatures (Avantor Sciences, Dublin, Ireland). The Genlab classic incubator mini was used as an oven for cell studies (Genlab Ltd., Cheshire, UK). Bacterial cell studies were performed in the MSC-Advantage™ 0.9 class II biological safety cabinet (BSC), and UV analysis completed to find the OD_{600} was performed with the SPECTRONIC™ 200 Spectrophotometer (Thermo Fischer Scientific, Dublin, Ireland). Sterilisation of equipment was performed using the Prestige Medical 9 litre class N fixed cycle table autoclave (Prestige Medical, Blackburn, UK). Nuclear Magnetic Resonance (NMR) measurements were performed on Bruker Avance III 600 MHz ultrashield nuclear magnetic resonance spectrometer (Bruker, Enschede, Netherlands). Fourier Transform Infrared (FTIR) analyses were completed using a Nicolet Summit with Everest ATR (Thermo Fischer Scientific, Dublin, Ireland) and Perkin Elmer Spectrum Two FT-IR (Perkin Elmer, Buckinghamshire, United Kingdom). The viscosities of

different liquid polymers and reagents were analysed using a CAP 2000+ viscometer (Brookfield, Massachusetts, USA). Gel permeation chromatography (GPC) analysis was completed on polymers using the 1260 Infinity II GPC/SEC System (Agilent Technologies, Cork, Ireland). Differential scanning calorimetry (DSC) was performed on the Perkin Elmer DSC 400 (Perkin Elemer, Buckinghamshire, United Kingdom). Water contact angle (WCA) analysis was performed using the OCA35 (DataPhysics Instruments GmbH, Filderstadt, Germany). The ultimaker S3 (Inspire 3D, Wicklow, Ireland) with a nozzle 0.25 mm in width was used for 3D printing. OnShape (available online) and Cura (ultimaker Cura) were used for design and 3D printing. SurPASS 3 was used to measure surface charge by technicians in Anton Paar (Luton, England). Scanning electron microscopy was performed using the Hitachi S5500 field emission scanning electron microscope (Hitachi, Dublin, Ireland) in the Nano Research Facility in DCU, the Zeiss ulTRA plus (ZMCC, Cambridge, UK) in the Advanced Microscopy Lab in the CRANN Institute in Trinity College Dublin and the Hitachi S-3400 (Hitachi, Dublin, Ireland). Samples were prepared with gold using the Agar B7340 sputter coater (Agar Scientific, Rotherham, UK). Atomic force microscopy (AFM) analysis was completed with Bruker Icon AFM (Bruker, Dublin, Ireland). Nanoindentation was performed by Dr Barry O'Connell using Bruker Hysitron TI Premier Nanoindenter (Bruker, Dublin, Ireland). OriginPro8.5 (OriginLab, Massachusetts, USA, version 85E) was used for spectral design. Microsoft Excel and R were used for data analysis, statistical analysis and spectral design. ImageJ was used for image analysis with the Trainable Weka Segmentation plugin being used for quantitative analysis of bacterial surface coverage based on SEM images. BioRender was used for illustration design and ChemDraw was used to create reaction schemes and for chemical structure design. Gwyddion analysis software was used for AFM analysis. For the mammalian cell testing, the Biochrom WPA Biowave UV-Vis absorption (Scientific Laboratory Supplies, Dublin, Ireland) spectrometer was used for absorbance and transmittance readings. A validated HERASafe^{TM} laminar flow class II biological safety cabinet (Thermo Fischer Scientific, Dublin, Ireland) was used for cell culturing. Absorbance measurements from the assays were measured with a Tecan Infinite M200 plate reader (Tecan Trading AG, Switzerland).

2.3 Methods

2.3.1 Synthesis, Fabrication and Crosslinking

2.3.1.1 PCL Diol Methacrylation (M_n 1250 g/mol)

This procedure was modified based on a reaction completed by Tian et al.[131] Tetrahydrofuran, (THF, 99.5%, Extra Dry over Molecular Sieve) was dried over a 3Å molecular sieve overnight. Polycaprolactone diol (PCL diol, M_n 1250 g/mol) was dissolved in the dry THF (10% w/v) in an oven-dried 2-neck 500 mL round bottom flask. Triethylamine (Et_3N), (2.0 eq.) and methacryloyl chloride (2.2 eq.) were then added dropwise to the round bottomed flask and the reaction was left to stir at room temperature, covered with aluminium foil, for five days. The resulting mixture was gravity filtered to remove salts and precipitated using hexane as eluent. THF and hexane were removed by rotary evaporation, and the isolated product was further purified by a washing and extraction step. The methacrylated polymer was dissolved in a minimal amount of dichloromethane (DCM) and then washed with 1.0 M hydrochloric acid (HCl) three times. The isolated DCM layer was evaporated by rotary evaporation, and the product was dried under vacuum at 40°C for 2 days. ^{1}H NMR of a white, waxy solid was recorded and used to determine the degree of methacrylation of 84-99%, as seen in **Figure A.2** in **Appendix A**. A percentage yield of 81-89% was calculated. The degree of acrylate capping was calculated as per the method described in the procedure outlined by Tian et al.[131]

^{1}H NMR (600 MHz, $CDCl_3$), δ 6.09 (s, 2H, CH), 5.55 (s, 2H, CH), 4.26-4.20 (m, 5H, CH_2), 4.14 (t, 4H, *J* = 6.6 Hz, CH_2), 4.06 (t, 30H, *J* = 6.8 Hz, CH_2), 3.72-3.67 (m, 5H, CH_2), 2.41-2.25 (m, 37H, CH_2), 1.93 (s, 6H, CH_3), 1.72-1.57 (m, 72H, CH_2, CH_2), 1.47-1.31 (m, 42H, CH_2).

FTIR-ATR (cm^{-1}): 2946 (C-H), 2864 (CH), 1721 (C=O), 1637 (C=C), 1161 (C-O), 816 (C=C).

2.3.1.2 PCL Diol Methacrylation (M_n 530 g/mol)

The methacrylation reaction and purification was the same as above with the reaction time modified to 24 hours. ^{1}H NMR of the isolated yellow oil was completed and a methacrylation of 91-95% was determined with a yield of 72% calculated, as seen in **Figure A.4** in **Appendix A**.

^{1}H NMR (600 MHz, $CDCl_3$), δ 6.02 (s, 2H, CH), 5.48 (s, 2H, CH), 4.24-4.17 (m, 6H, CH_2), 4.07 (t, 4H, *J* = 6.5 Hz, CH_2), 3.99 (t, 9H, *J* = 6.7 Hz, CH_2), 3.68-3.66 (m, 1H, CH_2), 3.66-3.61 (m, 6H, CH_2), 3.61-3.58 (m, 1H, CH_2), 2.32-2.20 (m, 15H, CH_2), 1.87 (s, 6H, CH_3), 1.66-1.54 (m, 31H, CH_2, CH_2), 1.39-1.27 (m, 18H, CH_2).

FTIR-ATR (cm^{-1}): 2943 (C-H), 2864 (C-H), 1730 (C=O), 1639 (C=C), 1159 (C-O), 817 (C=C).

2.3.1.3 Polydimethylsiloxane (PDMS) Curing

PDMS is an elastomer commonly used to make moulds or spacers which, in this research, were used as spacers in between glass and Topas slides to create sealed crosslinking chambers, as discussed below in **Section 2.3.1.4**. PDMS solution was made by mixing SYLGARD™ 184 Silicone Elastomer Base and Curing Agent in a 10:1 ratio, respectively. The mixture was prepared in a centrifuge tube and stirred with a disposable stirrer to ensure homogenous solution. The mixture was then placed in a desiccator for 30 minutes to remove air bubbles. To cure the PDMS, it was poured into moulds and baked in the oven for two hours at 40 °C or left at room temperature overnight.

2.3.1.4 PCLDMA Crosslinking and Moulding

PCLDMA was mixed at different ratios with a chemical crosslinker and photoinitiator (PI) based on previous work completed in the group.[130,132] PCLDMA was mixed with 1,6-hexanediol diacrylate (HDDA) at two different ratios, 10% PCLDMA, 90% HDDA and 20% PCLDMA, 80% HDDA w/w. Phenylbis(2,4,6-trimethylbenzoyl) phosphine oxide (PBPO), the PI, was dissolved in the minimal amount of acetone and added to the different blends (1% w/w). The vials were covered in aluminium foil to prevent unwanted crosslinking in white light and UV light and were vortexed for 30 minutes, followed by sonication for 30 minutes, to ensure homogenous mixtures and no bubbles were present. A moulding chamber was created by placing PDMS spacers between a glass and Topas slide and clipping them together using grip clips. The different polymer blends were introduced to the chamber by micropipette and filled the space via capillary action. The solution was cured in the UV crosslinker for 90 minutes. The cured mould was removed from the moulding chamber using a scalpel and tweezers.

2.3.1.5 2-allyloxymethyl-2-ethyltrimethylene carbonate (AOMEC) Synthesis

The synthesis of AOMEC was adapted based on work completed by Thomas et al.[39] Trimethylolpropane allyl ether diol (20 mL, 94.2 mmol) was dissolved in 250 mL of THF. The solution was brought to 0 °C by stirring in an ice bath. Ethyl chloroformate (27 mL, 282 mmol) was then dissolved in 80 mL of THF – to give a total volume of 330 mL. The dissolved ethyl chloroformate was added to the mixture and left to stir for 20 mins. Et_3N (39 mL, 282 mmol) was then added dropwise over a 30-minute period. The reaction was then warmed to room temperature and left to react overnight under a nitrogen blanket. The following day, the mixture was vacuum filtered to remove the TEA salts. A pink oil was isolated after evaporation of THF on the rotary evaporator. Purified product was isolated by wash and extraction steps performed in triplicate. The oil was dissolved in minimal DCM and washed with 1.0 M HCl followed by deionised water. The isolated organic layer was dried with anhydrous magnesium sulfate and gravity filtered. The DCM was removed by rotary evaporation, and the isolated yellow oil was further purified by vacuum distillation using a Schlenk line. Distillation was performed at 0.13 mbar and 150 ºC and resulted in a colourless, viscous liquid being isolated. The purified AOMEC was isolated in yields of 70-75%. AOMEC was analysed by ^{1}H NMR and 13C NMR spectroscopy, as in the **Figures 3.10** in **Chapter 3** and **7.5** in the **Appendix**, respectively.

^{1}H NMR (600 MHz, $CDCl_3$): δ 5.85-8.77 (m, 1H, CH), 5.26 (dd, 1H, *J* = 32.3, 17.2, CH), 5.21 (dd, 1H, *J* = 32.3, CH), 4.34 (d, 2H, *J* = 10.4 Hz, CH_2), 4.13 (d, 2H, *J* = 10.8 Hz,CH_2), 3.98 (d, 2H, *J* = 6 Hz, CH_2), 3.40 (s, 2H, CH_2), 1.54 (q, 2H, *J* = 7.5 Hz, CH_2), 0.92 (t, 3H, *J* = 7.7 Hz, CH_3).

^{13}C NMR (150 MHz, $CDCl_3$): δ 148.6 (O-*C*=O), 134.1 (CH=*C*H_2), 117.5 (*C*H=CH_2), 72.9 (2, *C*H_2-O-C), 72.5 (CH-*C*H_2-O), 68.3 (C-*C*H_2-O), 35.5 (*C*-$(CH_2)_4$), 23.4 (*C*H_2-CH_3), 7.43 (CH_2-*C*H_3).

FTIR-ATR (cm^{-1}): 2911 (C-H), 1756 (C=O), 1647 (C=C), 1175 (C-O-C), 991 (CH=CH_2), 928 (CH=CH_2).

2.3.1.6 1-(3,5-bis(trifluoromethyl)phenyl)-3-cyclohexylthiourea (TU) Cocatalyst Synthesis

All glassware and utensils were dried overnight at 120 ºC. 3,5-bis(fluoromethyl) isothiocyanate (5.0 g, 18.5 mmol) was added to a 50 mL round bottom flask under N_2

gas. Still-dried THF (20 mL) was added to the round bottom flask followed by dropwise addition of cyclohexylamine (1.85 g, 18.5 mmol), which had been dried over activated 3 Å molecular sieves. The reaction was left to stir under a blanket of N_2 for 4 hours. The THF was removed by rotary evaporation. The isolated white solid with a yellow hue was dissolved in a minimal amount of chloroform. The mixture was heated to just below the boiling point of chloroform to dissolve the solid. The chloroform was allowed to cool to room temperature and left in the freezer at 0 ºC overnight. The recrystallised white powder was vacuum filtered and dried in a desiccator overnight. The purified TU catalyst was isolated in 72% yields. Analysis was completed using ^{1}H and ^{13}C NMR spectra in **Figures 3.11** and **7.6**, respectively.

^{1}H NMR (600 MHz, $CDCl_3$): δ 7.89 (br s, 1H, NH), 7.80-7.67 (m, 3H, Ar-H), 5.98 (br s, 1H, NH), 4.20 (br s, 1H, CH), 2.15-2.02 (m, 2H, CH_2), 1.79-1.55 (m, 3H, CH_2), 1.48-1.36 (m, 2H, CH_2), 1.32-1.09 (m, 3H, CH_2).

^{13}C NMR (150 MHz, $CDCl_3$): δ 180.1 (C=S), 139.7 (CH=*C*=NH), 134.0 (q, ^{2}J = 33 Hz, C=*C*-CF_3), 124.7 (br s, *C*H-C-NH), 123.5 (q, ^{1}J = 272 Hz, CF_3), 120.2 (p, ^{3}J = 15 Hz, *C*(=C-CF_3)$_2$), 54.9 ((CH_2)$_2$-*C*H-NH), 33.2 (CH-*C*H_2-CH_2), 26.1 (CH_2-*C*H_2-CH_2), 25.4 (CH_2-*C*H_2-CH_2).

FTIR-ATR (cm^{-1}): 3230 (N-H), 3081 (C-C=C-H), 2941 (C-H), 2865 (C-H), 1552 (Ar-C=C), 1472 (Ar-C=C), 1270 (C-F), 1128 (C-N).

2.3.1.7 AOMEC Polymerisation

AOMEC was polymerised by adapting the method published by Thomas et al.[39] DCM was dried over 3 Å molecular sieves overnight. AOMEC (3.01 g, 15.1 mmol) was dissolved in the dried DCM (5.0 mL). In a separate glass vial the initiator 1,4-butane diol (66.48 µL, 0.75 mmol), and co-catalysts 1,8-Diazabicyclo[5.4.0]undec-7-ene (DBU) (112.3 µL, 0.75 mmol) and TU (0.279 g, 0.75 mmol) were mixed and also dissolved in dry DCM (2.5 mL) – the total DCM volume was calculated to give a 2.0 M AOMEC solution concentration. The reaction was left to stir at room temperature over three days. The reaction was then quenched using acidic Amberlyst 15 ion exchange resin (10 mg per 1 mg DBU) which was washed repeatedly with methanol and air-dried prior to use. The sample was gravity filtered to remove any insoluble by-products and concentrated by rotary evaporation. Column chromatography was then performed. A slurry was made up with silica mixed in a solvent blend of 1:4 ethyl

acetate and hexane, respectively. A separating funnel was packed with cotton wool at the bottom and a layer of sand. The silica slurry was added and once settled, the unpurified PAOMEC blend was redissolved in ethyl acetate and loaded onto the column using a glass pipette. Once loaded onto the silica, a layer of sand was added, and the column was run. The 1:4 ethyl acetate and hexane solvent mixture was run through the column first to isolate the TU catalyst. This was confirmed by running silica thin layer chromatography (TLC) plates. The TU catalyst was observed under UV light and the PAOMEC could only be observed via potassium permanganate staining of the plate. Once all TU was removed, 100% ethyl acetate was run through the column to isolate PAOMEC which was condensed by rotary evaporation. The purified yellow/colourless oil was isolated in yields of 80-89% with a purity of 85% and was stored in a desiccator until use. Analysis of the polymer was completed with ^{1}H NMR and FTIR analysis to determine purity, as in **Figure A.7** in **Appendix A**.

^{1}H NMR (600 MHz, $CDCl_3$): δ 5.91-5.80 (m, 10H, CH), 5.31-5.08 (m, 20H, CH_2), 4.24-4.03 (m, 40H, CH_2, CH_2), 3.99-3.91 (m, 20H, CH_2), 3.78 (d, 2H, J = 8.4 Hz, CH_2), 3.59-3.51(m, 6H, CH_2), 3.46-3.36 (m, 7H, CH_2), 3.33 (s, 15H, CH_2), 2.71-2.57 (m, 3H, CH_2), 1.79-1.74 (m, 2H, CH_2), 1.58 (s, residual water), 1.56-1.45 (m, 16H, CH_2), 1.43-1.34 (m, 7H, CH_2), 1.34-1.28 (m, 2H, CH_2), 0.94-0.83 (m, 34H, CH_3), 0.07 (s, grease).

FTIR-ATR (cm^{-1}): 3527 (O-H), 2932 (C-H), 1739 (C=O), 1647 (C=C), 1229 (C-O-C-C=C), 1094 (C-O-C).

2.3.1.8 Crosslinking and Structuring of PAO_X and PAO_COOH

A 1:1 molar ratio of alkene in the repeating unit of PAOMEC to thiols present on pentaerythritol tetrakis(3-mercaptopropionate) (SHX) was estimated based on the molecular weight of PAOMEC to maximise crosslinking efficiency and minimise free alkene and thiol functionalities present post-crosslinking. For example, PAOMEC (0.25 g, 1.25 mmol) and SHX (38.1 mg, 0.31 mmol) were added to a glass vial. 2-Hydroxy-4'-(2-hydroxyethoxy)-2-methylpropiophenone (Irgacure-2959) (1% w/w) was dissolved in acetone (15% w/w) and sonicated for three minutes. It was then added to the same vial as the PAOMEC/SHX mixture and the vial was mixed in a vortex stirrer for 3 minutes at 1000 rpm and sonicated for a further 3 minutes. The mixture was left to settle for 1 minute and then added to the moulding chamber using a

micropipette. The crosslinking process was performed by exposing the sample in the crosslinking chamber to UV light at 365 nm for 60 minutes. The same process was repeated with 3-mercaptoproprionic acid (COOH) included in the mixture at a 3:7:10 molar ratio of COOH:SHX:PAOMEC this time also considering the moles of thiol present in COOH. To introduce structures to the crosslinked material, a silicon template that was structured by the Italian company Thundernil using nanoimprint lithography was included in the crosslinking chamber, as discussed in further detail in **Chapter 4**.

2.3.1.9 Amine Desalting

The desalting of cystamine dihydrochloride was performed based on a previously reported procedure by Bayraktutan et al.[133] Cystamine dihydrochloride (8.0 g, 35.8 mmol) was dissolved in deionised water (20 mL) in a 50 mL round-bottomed flask. The solution was mixed with aqueous sodium hydroxide (NaOH) (10% w/w) and left to stir at room temperature for 15 minutes. Washing and extraction was performed in triplicate using DCM as the organic phase. The organic phase was then dried with magnesium sulfate and the cystamine oil was condensed by rotary evaporation. An isolated yield of 75% was achieved.

2.3.1.10 3D-printed Moulding Chamber Fabrication

The moulding chamber was designed using computer aided design (CAD) on OnShape by a member of the research group, Dylan Doherty. The files were then sliced for the 3D printer with Cura (ultimaker Cura). The design was then 3D printed using the ultimaker S3 (Inspire 3D, Wicklow, Ireland) with a nozzle 0.25 mm in width and ultimaker transparent poly(lactic acid) (PLA) was used as the material for 3D printing.

2.3.2 Cell Testing

2.3.2.1 Making Agar Plates

Agar plates were made by mixing sodium chloride (5 g), tryptone (5 g), yeast extract (2.5 g) and agar powder (7.5 g) in a 1 L dewar and mixing the reagents with deionised water (200 mL). The funnel was washed with more deionised water to make the final volume of 500 mL of water. Once combined, a sterile stir bar was added and the lid of the dewar was closed. The reagents were stirred on a hot plate at 95 ºC to dissolve all reagents, specifically necessary for agar powder dissolution.

Once dissolution was completed, the lid on the dewar was loosened and the solution was sterilised by autoclave. The liquid agar solution was then poured into sterile petri dishes in the biological safety cabinet (BSC) until the bottom surface of the dish had been completely covered. The agar plates were left to cool with the lid half covering each plate in the back of the BSC. They were then covered and stored upside down in the fridge at 4 ºC until use.

2.3.2.2 LB Preparation

Luria Broth (LB) was made by adding Lennox LB powder (10 g) to a 1 L dewar that contained deionised water (200 mL). The funnel was washed with more deionised water to make the final volume of 500 mL of water. Once dissolved, the lid on the dewar was placed on loosely and the solution was sterilised by autoclave. The LB was stored at room temperature in a sealed dewar to keep sterile until use.

2.3.2.3 Plating of bacteria

The plating of bacteria was completed using cryostocks of bacteria. These cryostocks were prepared from a mixture of an overnight culture of the bacteria (600 µL) and glycerol solution (50% v/v) (400 µL) put into sterile Eppendorf vials. The vials were then shaken to mix the contents thoroughly and covered in aluminium foil. The vials were then stored in the freezer at either -20 ºC or -80 ºC until use. A sterile loop was used to take cells from the cryostock and streak them onto an agar plate. Prior to streaking the cells, the agar plate was heated in the oven at 37 ºC to warm from the fridge. The loop was then streaked back and forth in a downward zig zag motion towards the centre of the plate, in one quadrant of the plate. The plate was then rotated 90 º and the same motion was completed. This was repeated twice more to fill each quadrant of the plate. The plate was then placed upside down in the oven, set to the desired temperatures of 37 ºC for *E. coli* and *S. Epidermidis* or 30 ºC for *P. fluorescens* . The plates were left overnight to allow for growth and then stored in the fridge at 4 ºC until use. They could be stored in the fridge for up to two weeks.

2.3.2.4 Kirby-Bauer Disc Diffusion Method

The crosslinked samples were stored in a desiccator until use. All equipment was sterilised. Agar plates were prepared, as was LB medium. The bacteria to be tested, namely *E. coli*, *S. Epidermidis* and *P. fluorescens* were grown on agar plates. A sterile loop was used to collect a small number of colonies. LB medium (10 mL) was

then inoculated by stirring with the loop and then left to shake at 200 revolutions per minute (rpm) at the desired temperature - 37 ºC for *E. coli* and *S. Epidermidis* and 30 ºC for *P. fluorescens* – until the exponential growth phase was reached. This was measured spectrophotometrically and was achieved when an optical density at 600 nm (OD_{600}) ≥ 0.5 was observed. The inoculated LB (100 µL) was introduced to a sterile agar plate using a micropipette and a lawn of bacteria was then spread using a sterile spreader, until increased resistance was met. The PAOMEC samples, blank discs (kept in the fridge), 10 µg ampicillin or gentamicin discs – depending on the bacteria – were gently placed in separate quadrants of the petri dish using sterilised tweezers. The dishes were placed upside down in the oven, set to the same desired temperature mentioned above and left to grow for 24 hours. The dishes were then photographed on a dark background, next to a ruler for scale and ImageJ was used to measure the zone of inhibition. This was completed by drawing a line from one edge of the zone – the point where the bacteria were clearly no longer growing – to the other edge directly through the centre of the sample or disc to measure the diameter. Ten measurements were taken from each sample and the plates were prepared in triplicate.

2.3.2.5 MTS Assay

Direct and indirect assays were performed by Dr Graham Reid to investigate the suitability of this assay type for testing cell growth on PAOMEC crosslinked samples. For indirect testing, the PAOMEC samples, PAO_X, were left to soak in sterile LB medium at three timepoints, 24, 48 and 120 hours. Samples were placed in a 48-well plate and sterile 0.85% NaCl solution was added to each well that contained no sample to reduce evaporation overnight. The well plate was left in an oven for 24 hours at 37 ºC. After 24 hours, the samples were transferred to a new plate and the LB was also transferred to a separate new plate for analysis. The samples were immersed in fresh LB (200 µL) and again were left in an oven at 37 ºC. After 24 hours, the samples were again removed to a new plate as was the LB which was to be measured as the 48 hour timepoint. The above process was repeated once more to give the aforementioned 3 timepoints. Each test was performed with samples in triplicate. Inoculated LB with an OD_{600} of 0.9 (200 µL) was used as the positive control and sterile LB was used as the negative control. MTS (40 µL) was added into each well containing LB and the TECAN plate reader was used to measure the

absorbance at 490 nm every ten minutes over a 400-minute time period. The direct assay was performed using the same positive and negative controls. Fixatives, such as grease and sealant, were added fresh to the 48-well plate, and post-soaking in LB media for 20 hours were also measured alongside an inoculated LB medium with *E. coli* (OD_{600} 0.2) (250 µL) . The PAO_X samples were left to soak for three hours and 20 hours in sterile LB. MTS (40 µL) was added to each well and absorbances were measured as before.

2.3.2.6 Crystal Violet Assay

The crystal violet assay was performed under the guidance of Dr Graham Reid. A number of *E. coli* colonies were taken from a streaked plate using a sterile loop and mixed with LB (5 mL) in a sterile 25 mL centrifuge tube. Culture was left to grow in LB at 37 °C with shaking at 200 rpm. The inoculated LB (250 µL) was then used to make a subculture in fresh LB (25 mL). The subculture was left to stir at 250 rpm at 37 ºC for four hours until an $OD_{600} \geq 0.5$ and the exponential growth phase was reached. A bacteria pellet was made by centrifugation of the subculture at 5000 rpm for ten minutes. The pellet was resuspended in fresh LB (3 mL) and the OD_{600} was measured. The concentrated culture was diluted to give an OD_{600} of 0.2. The 48-well plate was prepared by adding two technical replicates of PAO_X, PAO_COOH and Topas planar samples. Aliquots of the diluted culture (500 µL) were added to appropriate wells of a 48-well plate. The 48-well plate was left in the oven over 48 hours at 37 °C shaking at 30 rpm. The LB was removed after 48 hours of incubation, and the appropriate wells were lightly rinsed with 0.85% sodium chloride solution to remove any planktonic cells. Crystal violet (CV) solution (0.1%) (250 µL) was added to each well and left to incubate at room temperature for 15 minutes. The CV solution was then removed from the wells, and each well was washed with sterile water in triplicate. Acetic acid (250 µL) was then added to each well to solubilise the CV that stained the cells, and the well plate was shaken at 250 rpm at room temperature for five minutes. The acetic acid was then mixed with a micropipette and was then transferred (200 µL) to a sterile 96-well plate. Absorbance measurements were taken at 590 nm wavelength with the TECAN plate reader.

2.3.2.7 Growth Curve

Growth curve analysis was performed with *P. fluorescens*. A number of *P. fluorescens* colonies were taken from a streaked plate using a sterile loop and mixed

with LB (5 mL) in a sterile 25 mL centrifuge tube. Culture was left to grow in LB at 37 °C with shaking at 200 rpm. The inoculated LB (250 µL) was then used to make a subculture in fresh LB (25 mL). This was completed in triplicate using sterile 50 mL conical flasks that had been autoclaved in advance of this experiment. The subcultures were left to stir at 250 rpm at 30 ºC. Over an 8-hour time period, samples were taken from the subcultures and analysed via spectrophotometry to give the OD_{600}. Post-experimental analysis was completed using Excel to create the growth curve and elucidate the log phase of growth. Once an OD_{600} of 0.2 was measured, inoculated LB (100 µL) was taken from the conical flask and diluted by mixing with sterile LB (900 µL). This process was repeated seven more times and the samples (100 µL) prepared from this serial dilution process were plated. They were left in the oven at 30 ºC overnight and colony counting was completed the next day to quantify the number of bacteria present in the concentrations planned for static cell testing.

2.3.2.8 Static Antibiofouling Testing Protocol

An overnight culture of *P. fluorescens* was grown by taking colonies from a streaked plate using a sterile loop and mixing it with LB (5 mL) in a sterile 25 mL centrifuge tube. The inoculated LB was left to shake at 200 rpm overnight at 30 °C. A subculture was prepared the next morning using a 1 in 100 dilution. The overnight culture (250 µL) was mixed with sterile LB (25 mL) in a sterile 50 mL conical flask that had been autoclaved in advance of this experiment. The samples were left to shake until an OD_{600} of approximately 0.5 was reached. Two technical replicates of each sample type, PAO_X and PAO_COOH, planar and structured were inserted into wells within a 48-well plate. A 1 mL syringe was used to add a small amount of grease in advance to secure the samples to the well. Any excess grease that surrounded the edges of the sample was removed using sterile tweezers. The samples were soaked with ethanol (70% v/v) for 20 minutes and then washed, in triplicate, with sterile LB. The LB was left in each well for approximately two minutes for each wash to ensure all ethanol was removed. Once the desired OD_{600} was reached, the inoculated LB was transferred to a 25 mL centrifuge tube and made into a pellet by centrifugation at 5000 rpm for ten minutes. The pellet was resuspended in sterile LB (3 mL) and the OD_{600} was measured. This inoculated LB was then diluted to give an OD_{600} of 0.2. This diluted suspension (500 µL) was added to each well with a sample present. The surrounding wells were then filled with deionised water (1.0

mL) to limit evaporation of the LB overnight. The well plate was transferred to the oven and stored there overnight, at 30 ºC, shaking at 50 rpm for 24 hours. After 24 hours, the liquid media was poured out of the well plate and the samples were gently washed with PBS, in triplicate, to remove planktonic cells. A 2.5% glutaraldehyde solution was prepared, and aliquots (300 µL) were added slowly, down the side of each, appropriate well. The well plate was left in the fridge at 4 ºC overnight to allow for cell fixation. The following day, the liquid media was again removed, and the wells were washed with PBS in triplicate. A serial dehydration process was performed with ethanol starting at 50% v/v ethanol and increasing by 5% v/v until 100% ethanol solution was used. Each concentration of ethanol (500 µL) was added to the wells and left to soak for five minutes. Once 100% concentration was reached, the samples were soaked for ten minutes, twice. The samples were left to dry for two hours and were then prepared for SEM analysis. Using sterilised tweezers, the samples were removed from the wells by clearing any grease from the side of the samples and carefully lifting them from the well. They were placed on SEM stubs on a carbon tab. Silicone sealant was used to hold the samples in place and the samples were then gold-coated with a gold sputter coater for 30 seconds. Silver paint was also added to the sides of the samples to connect them to the stub to improve conductivity. Five images were taken per sample, in the centre of the sample and in each of the four quadrants. Each image was taken at 1000X magnification, at a working distance of 6 mm. Low accelerating voltage was needed, between 1 and 5 kV, and a probe current of 50 µA was used. The post-imaging processing was completed with ImageJ software which is opensource software that can be accessed at this link. The analysis was completed using a plugin called Fiji Trainable Weka Segmentation, which is discussed in more detail at a later stage. Briefly, the scale was set by using the line tool to measure along the scale bar and set the measurement. The images were duplicated to remove the scale bar by using the rectangle select tool and the background was darkened if necessary. The image was set to an 8-bit image for processing, and the Weka Segmentation could then be performed. The bacteria were drawn around using the free hand tool and labelled class one, while the background was marked and labelled class two. The classifier could be trained and then improved upon by increasing the samples given to each class to ensure accurate processing. Then the result was created, which gave the percentage area of the image covered by class one, in this case bacteria.

2.3.2.9 Cell Culture

All lab work relating to mammalian cell studies were conducted by Dr Keith Rochfort in the Endothelium Biology Group in DCU. The HERASafeTM laminar flow Class II BSC was used for all cell culture work and aseptic technique was employed throughout all experimentation. Sanitisation of all equipment was completed with 70% industrial methylated spirits (IMS), and all relevant equipment was sterilised or autoclaved, as per the requirements.

2.3.2.10 Growth and Maintenance of Cells

Primary Human Aortic Endothelial Cells (HAECs) obtained from healthy donors were used for this work. Cells were cultured in sterile petri dishes in Endothelial Cell Growth Medium MV, 5% v/v fetal bovine serum (FBS) and penicillin (100 U/mL) and streptomycin (100 µg/mL) antibiotic. They were incubated at 37 °C, 5% CO_2 and 95% humidity. Cells were checked daily with a light microscope at 10X magnification to evaluate confluency. Fresh culture media was added every one to two days, and existing media was removed. Cells were passaged at 80-90% confluency.

2.3.2.11 Sterilisation of Polymers and Preparation of HAECs for Assays

PCLDMA:HDDA samples were left to soak in ethanol (70% v/v) for 20 minutes and then washed, in triplicate, with sterile PBS to remove residual ethanol. They were then transferred to relevant, sterile 96-well plates. HAECs were then seeded at the assay-specific seeding density per well, and assays were performed at the 24-, 48- and 72-hour time-points, at 37 °C incubation, post-seeding. For each assay, controls were employed and added to a sterile well containing cells with no sample present. All experiments were performed to n=3. All statistical analysis relating to these cell studies was performed using R and a p-value ≤ 0.05 was considered significant.

2.3.2.12 MTT Assay for Cell Viability

3-(4, 5-dimethylthiazolyl-2)-2, 5-diphenyltetrazolium bromide (MTT) assay was performed on planar and structured 1:4 PCL:HDDA sterilised samples, with a positive control of H_2O_2 treatment present in each well plate. For each experimental condition, 25,000 HAECs were seeded per well, and left to incubate for 24, 48 and 72 hours at 37 °C. CellTiter 96 AQ_{ueous} Assay (20 µL) was added to each well and incubated for four hours at 37 °C. Absorbance reading from each well was then taken at 590 nm with the Tecan Infinite M200 Pro Microplate Reader. The readings

were compared against the cells seeded directly on the 96-well plate for analysis of the respective fold change.

2.3.2.13 LDH Assay for Cytotoxicity

The lactate dehydrogenase (LDH) assay was used to assess cytotoxicity because it acts as a stress-related biomarker. The LDH assay was also performed with planar and structured 1:4 PCL:HDDA sterilised samples, with a positive control of H_2O_2 treatment, as discussed above (**Section 2.3.2.12**), present in each well plate. Additionally, a 'low' and 'high' standard were used in each well plate. The 'low' standard was cell culture media not containing cells, and the 'high' standard was the same amount of cell culture media, as in the wells containing the samples, but lysed with the provided buffer to maximise the amount of LDH present. 25,000 HAECs were then seeded per well in cell culture media (100 µL), and left to incubate for 24, 48 and 72 hours at 37 °C, as before. At the end of each time-point, the reaction mixture (100 µL) was added to each well and left to incubate for 30 minutes at 37 °C. Again, the absorbance readings were taken with the Tecan Infinite M200 Pro Microplate Reader. Measurements were taken at 490 nm and readings were compared against the cells seeded directly on the 96-well plate for analysis of the respective fold change, with additional analysis examining the percentage LDH release as calculated from the standard curve derived from the 'low and 'high' standard.

2.3.2.14 MTT Assay for Cell Proliferation

The MTT assay for cell proliferation was performed as before (**Section 2.3.2.12**), with the exception that measurements were taken at four time points, 0, 24, 48 and 72 hours. For analysis purposes, following cell seeding and subsequent adhesion, all experimental values were compared to the cells seeded directly on the 96-well plate at 0 hours in order to generate proliferation curves for each condition. Additionally, instead of a negative control, in this assay each well plated included a control of cells that were treated with Vascular Endothelial Growth Factor (VEGF) (50 ng/mL) and added to a sterile well with no sample present.

2.3.3 Analysis Techniques

2.3.3.1 Gel Permeation Chromatography (GPC)

The molecular weight of the polymers was analysed using GPC. For GPC analysis, samples with minimum concentrations of approximately 5 mg/mL were prepared. The purified polymer sample was dissolved in the required amount of chloroform, as measured by mass balance and the vial was sealed with aluminium foil and a lid. It was vortexed for five minutes to ensure complete dissolution, and filtration was performed if any solids remained. Once dissolved, the sample was added to a glass vial (1.5 mL) and sealed with aluminium foil. Each sample was run at a flow rate of 1.0 mL/minute for a run time of 55 minutes. The sample was run through 2 PLgel 5 µm MIXED-D, 300 x 7.5 mm columns, at 30 ºC, using chloroform as eluent. Processing and analysis of the data was completed using Agilent software and completed with a calibration curve that was created using polystyrene medium Agilent EasiVial standards, which range in weight average molecular weight (M_w) from 162 g/mol to 364,000 g/mol.

2.3.3.2 Fourier Transform Infrared Spectroscopy (FTIR) Analysis

Samples were analysed by FTIR to better understand the crosslinking process of different polymer blends. A background scan of air was taken prior to any sample analysis. The samples were placed on the diamond and secured in place using the arm of the FTIR to ensure maximal contact with the diamond. Each sample was scanned between the range 500 cm^{-1} and 4000 cm^{-1} with an average 16 scans. The stage and arm were washed with isopropyl alcohol (IPA) between each sample. Post-processing analysis was completed using OriginPro 8.5.

2.3.3.3 Viscometry

Using the Brookfield CAP 2000+ Viscometer, the viscometer was calibrated with a Brookfield certified viscosity standard. Following this, each polymer blend was deposited onto the viscometer stage beneath the spindle. The spindle used was spindle 001, which has a pre-calibration for the instrument. The spindle was lowered into contact with the solution, and a solvent sheath was then put over the spindle to prevent any evaporation during analysis. The hold time was set to 30 seconds to ensure thermal equilibrium had been reached before the measurement took place. The temperature was set to 25 °C. The run time was set to 12 seconds, and the spin

speed was 900 rpm – to ensure torque over 10% was achieved. Averages of three measurements of each polymer sample were taken.

2.3.3.4 Differential scanning calorimetry (DSC)

The sample was prepared by placing it in a DSC pan, measuring the mass and using the crimping tool to seal a cap onto the pan. Using the Perkin Elmer DSC 400, samples were analysed by heating them from low temperatures ranging between -80 and -90 °C to between 60 and 100 °C at a rate of 20 °C per minute and holding them for one minute at the highest temperature. The sample was then cooled at the same rate to the original low temperature and then held at this low temperature for 30 minutes to ensure the sample reached said temperature point. The sample was then heated to the same high temperature again. The first heat step was to remove any solvent and water from the sample, also known as removing the thermal history, and the second heating step was used for analysis of the sample. Analysis was performed using the Perkin Elmer software.

2.3.3.5 Scanning Electron Microscopy (SEM)

Prior to analysis, samples were prepared for SEM analysis using the gold-coat sputterer to add a layer of gold to the surface of the sample. This was done by exposure to gold sputtering for 30 seconds, performed in an inert atmosphere created by argon. The samples were also painted around the edges with silver paint to further increase conductivity. The analysis was performed at low accelerating voltage and high probe current, normally 1-5 kV and 50 µA, respectively, to reduce charging of the samples and increase image brightness. This analysis technique was used for samples from the static antibiofouling tests, specifically to assess bacterial cell coverage on the surface of samples.

2.3.3.6 Field Emission Scanning Electron Microscopy (FESEM)

For FESEM analysis, gold coating was not always needed as charging was not as much of a problem. If required, it was performed as in **Section 2.3.16** above. Structured samples were analysed by measuring structure period and width. The post-imaging processing was also completed with ImageJ software. The same steps were used as above to set the scale. The line measuring tool was then used to measure from one side of a structure, in this case lines, to the other. For structure pitch or period, the line tool was used to measure the distance between the

structures by measuring from the edge of one structure to the same edge of the next and pressing “Ctrl + t” to measure. At least 30 data points were taken from each sample image, and three images were processed. The mean and standard deviation for structure width and pitch were calculated using Microsoft Excel.

2.3.3.7 Atomic Force Microscopy (AFM)

AFM analysis was completed to find the height of the structured samples. To do this, no sample preparation was required. The analysis was completed with Tap300G AFM tips. The ScanAsyst or Tapping modes of the AFM were used. A 10 μm area was analysed at a scan rate of approximately 0.3 Hz, although this was increased, when possible to maintain accurate measurements at higher rates. A total of 512 samples per line were measured and the peak force amplitude was set to 150 nm to ensure the gap between the lines was accurately reached. Post analysis processing was completed using Gwyddion software (version 2.54) which can be downloaded at this link. The file from the AFM was processed by levelling the plane and facets, aligning the rows, correcting horizontal scars and shifting the minimum to zeros – all of which are available in the data processing section of the software. The heights were measured by using the extract profiles options followed by drawing a line across the structures, covering at least two structures. Multiple lines were drawn on each file, from there, the peaks could be found and heights measured. This process was repeated at least twice more. The mean and standard deviation of the heights were calculated in Microsoft Excel.

2.3.3.8 Water Contact Angle (WCA)

Samples were stored in a desiccator overnight prior to analysis. Deionised water was dispensed (5 μL) onto each sample from the needle at a rate of 5 μL/second. Once dispensed, the needle was moved upwards, away from the sample and an image was taken with the camera. Care was taken to keep consistent timing when imaging droplets across all samples. The baseline, the point at which the droplet and sample meet was identified with the software SCA20. The contact angle was then measured. Five samples were measured and the mean and standard deviation of the contact angles measured were calculated using Microsoft Excel.

2.3.3.9 Nanoindentation

Nanoindentation analysis was completed by Dr Barry O'Connell (NanoResearch Facility, Core Technologies, DCU). Two planar samples of each type, namely PAO_X and PAO_COOH, were measured by nanoindentation. Samples were 1 mm in depth and 4 mm in diameter. Each sample was indented 16 times in a 4 x 4 matrix to test a maximum load of 125 μN using a Berkovich tip. The reduced modulus and hardness of the samples were directly measured, and the Young's modulus could be calculated based on the results.

Chapter 3 Synthesis and Modification of Oligomers

3.1 PCLDMA

3.1.1 Introduction

The focus of work completed for this thesis was to create biocompatible, degradable crosslinked, polymer materials. As such, the choice of polymers was made based on the aforementioned criteria. PCL was the first polymer that was selected, as it is an extensively researched polymer. Information about its mechanical and physical properties are abundant in literature and as such, it has found use in many industries, specifically in healthcare.[21,134,135] There has been research completed utilising PCL in various medical devices such as in tissue engineering scaffolds and as a carrier for drugs that can be released controllably.[136–140] It has also been widely used due to its improved viscoelastic properties in comparison to other aliphatic polyesters, resulting in easier manufacturing and manipulation of the material.[135,141] For the purpose of this research, its malleability as well as its slow biodegradability made it ideal.

3.1.2 Methacrylation of PCL Diol (M_n 1250 g/mol)

PCL Diol (M_n 1250 g/mol) was reacted with methacryloyl chloride (MAC) to introduce methacrylate functional groups at the termini of the PCL chain. This is necessary for the replica moulding steps that proceed via free radical polymerization. In the presence of UV-activated initiators, acrylate functional groups can be activated to form covalent bonds. This will be discussed in more depth in **Chapter 4**. Originally based on a procedure published by Tian et al, a methacrylate functionality, in the form of methacryloyl chloride, was reacted with PCL Diol. The reaction was performed with THF as a solvent, which was dried over molecular sieves prior to commencement of the methacrylation.[131] The reaction involves nucleophilic addition of the terminal alcohol functionality to the electrophilic acyl chloride group on MAC, as in **Figure 3.1**.

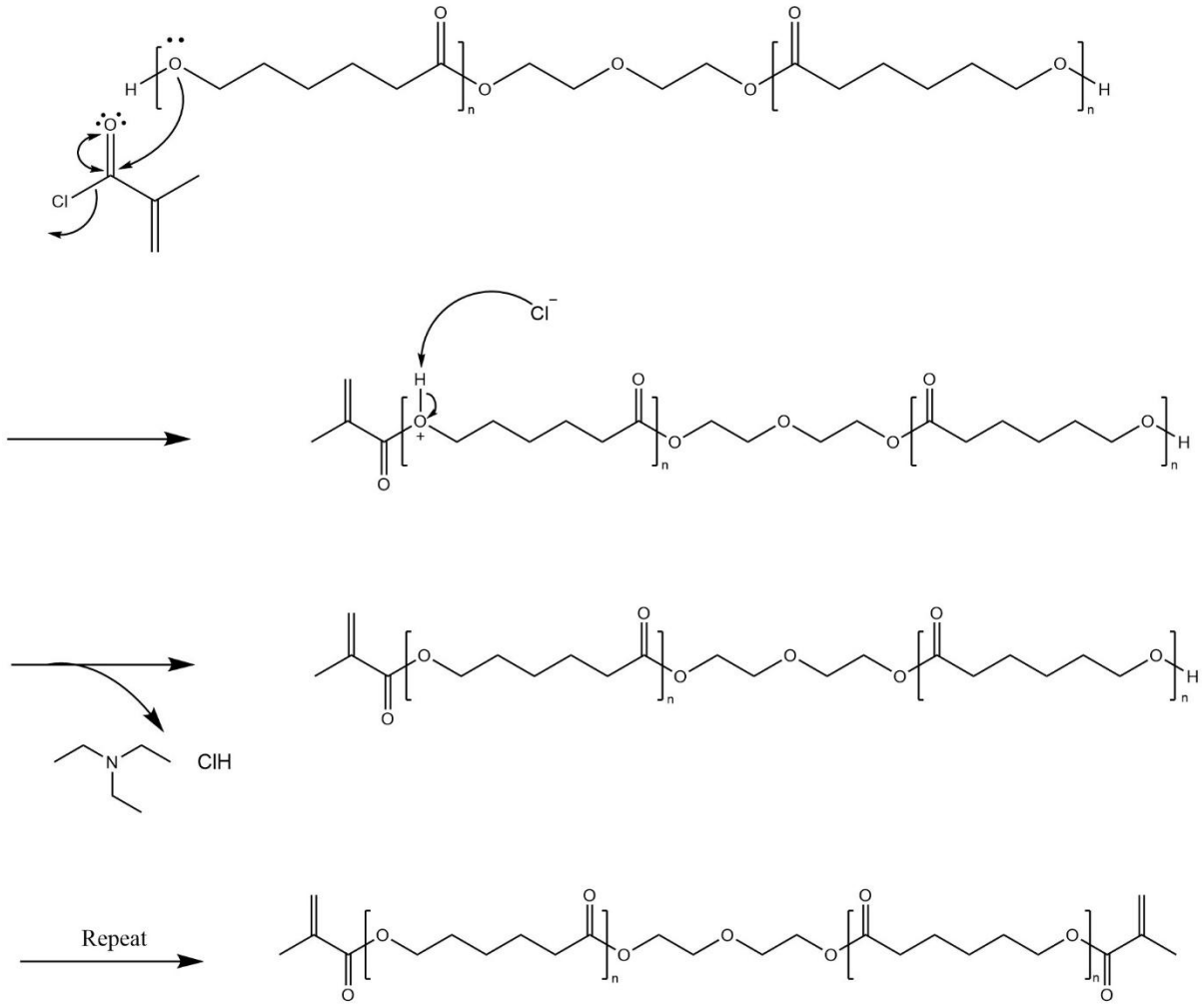


Figure 3.1: Curly arrow reaction mechanism for methacrylation of PCL Diol.

Et_3N has a pKa of 12.56 in THF, which is an increase when compared to its pKa in other solvents like water or DMSO. As such, Et_3N creates a basic environment thereby aiding the nucleophilic addition and elimination reaction.[142] The first stage of this project involved refining the reaction parameters to improve upon yields previously achieved in the group.[130] Methacrylation reactions were performed at varying molar ratios of reactants and over an array of timescales, to find the optimal parameters to synthesise PCLDMA (M_n 1350 g/mol), hereafter PCLDMA-1350. Percentage yield and percentage methacrylation values were used to evaluate the success of the various reactions.

Based on the ^{1}H NMR spectral analysis, the methacrylate peaks corresponding to the vinyl protons on the MAC at ~6.0 and 6.5 ppm, as highlighted in red box on **Figure 3.2**, were not observed in the PCLDMA ^{1}H NMR spectrum. Additionally, PCL diol starting material was compared with the isolated PCLDMA-1350 to ensure the

complete capping of the terminal alcohol groups. The peak at ~1.6 ppm, as highlighted in blue and outlined with a dashed blue line in **Figure 3.2**, corresponded to the proton on the alcohol group. This peak was not present in the purified PCLDMA-1350.

The percentage methacrylation was calculated based on the integration of peaks using ^{1}H NMR spectra, measured from samples taken from the crude reaction mixture at the end timepoint of the reaction. The methacrylation of PCL diol resulted in the peak corresponding to the CH_2 group adjacent to the terminal alcohol disappearing and a new peak, representing the CH_2 group on the chain end repeating unit, that was adjacent to the methacrylate functionality. Both of these peaks are highlighted with a purple dotted outline in **Figure 3.2**. The integration of the new triplet peak, observed at ~4.1 ppm, was compared to the singlet peak at ~5.5 ppm, which was representative of one of the protons on the methacrylate functionality.

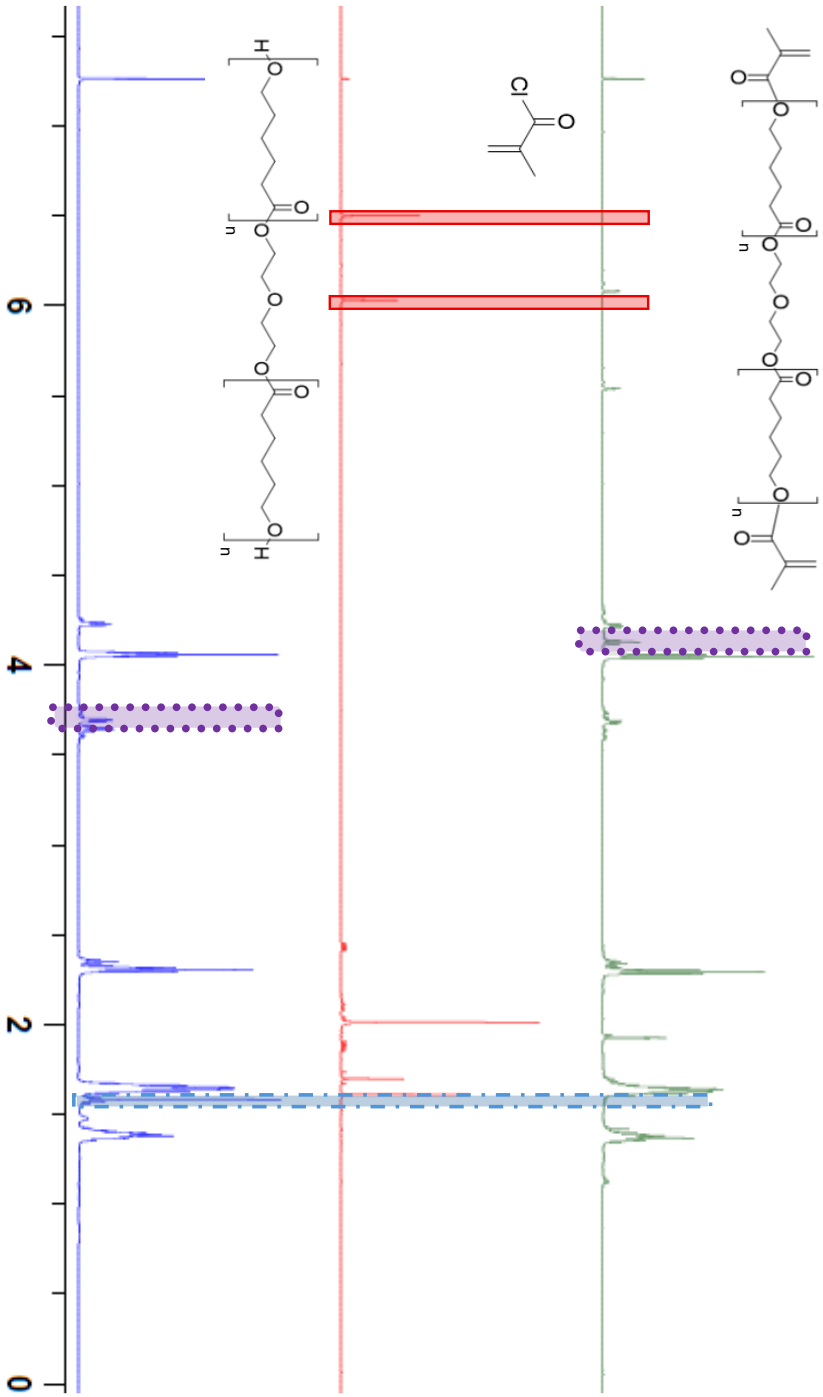


Figure 3.2: ^{1}H NMR spectra of starting materials including (left to right); PCL diol (blue), methacryloyl chloride (red) and PCLDMA-1350 (green). The peaks highlighted and outlined represent the acrylate protons of MAC and the alcohol proton of PCL Diol (top to bottom). The dotted purple outlines represent the CH_2 group of the repeating unit in both PCL diol and PCLDMA.

The first reactions were performed as per the methods used by previous members of the Kelleher research group, based on work completed by Tian et al.[130,131] This involved reacting the PCL Diol, Et_3N and MAC in a molar ratio of 2:1.6:1 over a three day period. This resulted in low yields and as a result, multiple tests were then carried out with single day durations and increased ratios of MAC to improve

percentage methacrylations and isolated yields, as displayed in **Table 1**. It was decided a minimum of a 1:2 molar ratio of PCL diol to MAC was required to give acceptable percentage methacrylation results but optimal results were calculated when MAC was in excess. From there, the duration of the methacrylation reaction was increased from one day to three, five and seven days. The optimal duration was originally decided to be three days as after five days the percentage yield and methacrylation did not appear to notably benefit from the increased duration. The molar ratio of Et_3N was also increased from 1.6 to 2.0.

Table 1: Methacrylation of PCLDMA using different ratios of reactants and reaction durations. Percentage methacrylation of PCLDMA was calculated by integration using H^1 NMR spectra of samples from the crude reaction mixture at the end of the reaction time. The percentage yield and percentage methacrylation were used to ascertain the success of each reaction.

PCL diol:	*2.0:*	*1.0:*	*1.0:*	*1.0:*	*1.0:*	*1.0:*	*1.0:*	*1.0:*
Et_3N:	*1.6:*	*1.6:*	*1.6:*	*2.0:*	*2.0:*	*2.0:*	*2.0:*	*2.0:*
MAC	*1.0*	*1.5*	*2.0*	*2.2*	*1.8*	*2.2*	*2.0*	*2.2*
Duration (days)	3	1	1	1	3	5	7	7
Methacrylation (%)	90.7	96.1	83.6	99.0	98.5	98.2	96.1	92.5
Isolated yield (%)	14.8	59.1	83.5	81.4	86.2	83.7	76.2	89.1

Other research has been published reporting the reaction of PCL diols, of differing molecular weights, being reacted with acrylates over a 12 to 24 hour period.[131,143,144] Additionally, it was observed that throughout the research, the percentage methacrylation achieved was lower when compared to earlier reactions with the same molar ratio of reactants used. As such, it was decided to complete a synthesis using the aforementioned optimised molar ratios of 1.0:2.0:2.2 of PCL diol, Et_3N and MAC, respectively, to investigate why the reaction duration required to achieve similar isolated yields and percentage methacrylations reported was longer than those in the literature. The reaction was carried out as before, in dried THF, and sampled at hourly intervals for the first six hours and at regular daily intervals after that. At 24 hours a percentage methacrylation was calculated to be 67% and from 96

hours onwards the percentage methacrylation fluctuated between 69 and 70%, as illustrated by the graph in **Figure 3.3**. Upon further investigation of the starting materials, the MAC being utilised was found to have started to form impurities.

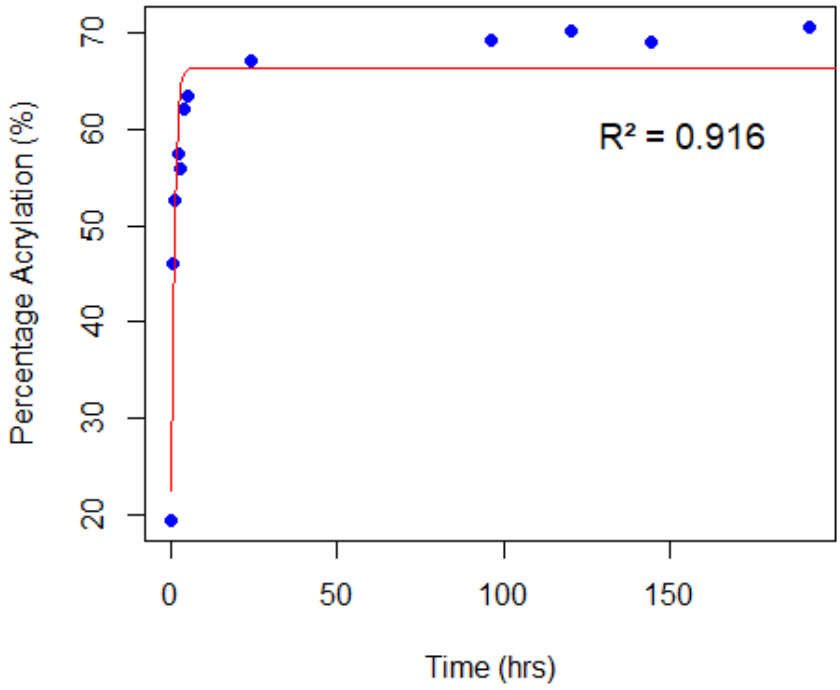


Figure 3.3: Percentage methacrylation versus time in hours calculated by ^{1}H NMR integration, graphed using R.

Exposure to moisture had resulted in the degradation of the MAC and the formation of different dimers, as previously reported by Warneke et al.[145] The most common of which forms as a result of Diels-Alder reaction due to exposure to air, as in **Figure A.1** in **Appendix A**. This dimer has been shown to be removed via vacuum distillation but for the purpose of this research this step was deemed unnecessary as neither the degradation products nor any unreacted MAC were observed in the isolated PCLDMA-1350, post-purification. This does, however, explain why higher percentage methacrylation results were not attainable and why the reaction required longer than others reported to cap the PCL diol chain with methacrylate groups.

When comparing integration of peaks attributed to protons within MAC and the impurity it was calculated that 21% of the available MAC had reacted to form the main impurity mentioned above. Even if it was assumed there were no other side reactions that had occurred forming other less common impurities, which is not likely, the highest percentage methacrylation that could be achieved with the material was

calculated to be 79%. Considering the amount of available MAC, approximately 69% methacrylation after 24 hours was achieved, which was deemed satisfactory.

Using ^{1}H NMR spectroscopy, a more in-depth analysis of the PCLDMA-1350 was completed. The reactants PCL diol and MAC were analysed alongside PCLDMA-1350, as in **Figure 3.2**, to ensure the successful removal of starting materials. MAC is reported to be toxic orally and via inhalation. Furthermore, if exposed to water, toxic gas can be produced.[146] The plan for these materials was eventual cell testing, so ensuring the completed removal MAC was important.

The purification process was evaluated and adapted from literature. The reaction mixture was gravity filtered and precipitated in cold n-hexane as done by Tian et al.[131] Subsequently, the isolated PCLDMA-1350 was redissolved in DCM and washed with 1.0 M HCl in triplicate to remove the Et_3N•HCl salts. The organic layer was dried with anhydrous magnesium sulfate, which was gravity filtered, and the DCM was removed using rotary evaporation. The white, waxy solid was dried in a vacuum oven at 40 °C for over 48 hours to remove any residual solvent. The isolated PCLDMA-1350 was then deemed to be sufficiently pure for further analysis, prior to crosslinking of the material, as in the ^{1}H NMR spectrum in **Figure A.2** in **Appendix A**.

Once the purified PCLDMA-1350 was isolated, FTIR analysis was utilised to evaluate the introduction of the methacrylate groups onto the PCL qualitatively. The key differences observed upon analysis of the FTIR spectra post-methacrylation, as in **Figure 3.4**, was the reduction of the peak at 3483 cm^{-1} representing the alcohol group and the appearance of two peaks at 1635 cm^{-1} and 817 cm^{-1} which are associated with vibrations of the stretching and bending of double carbon bonds in acrylate functionalities.

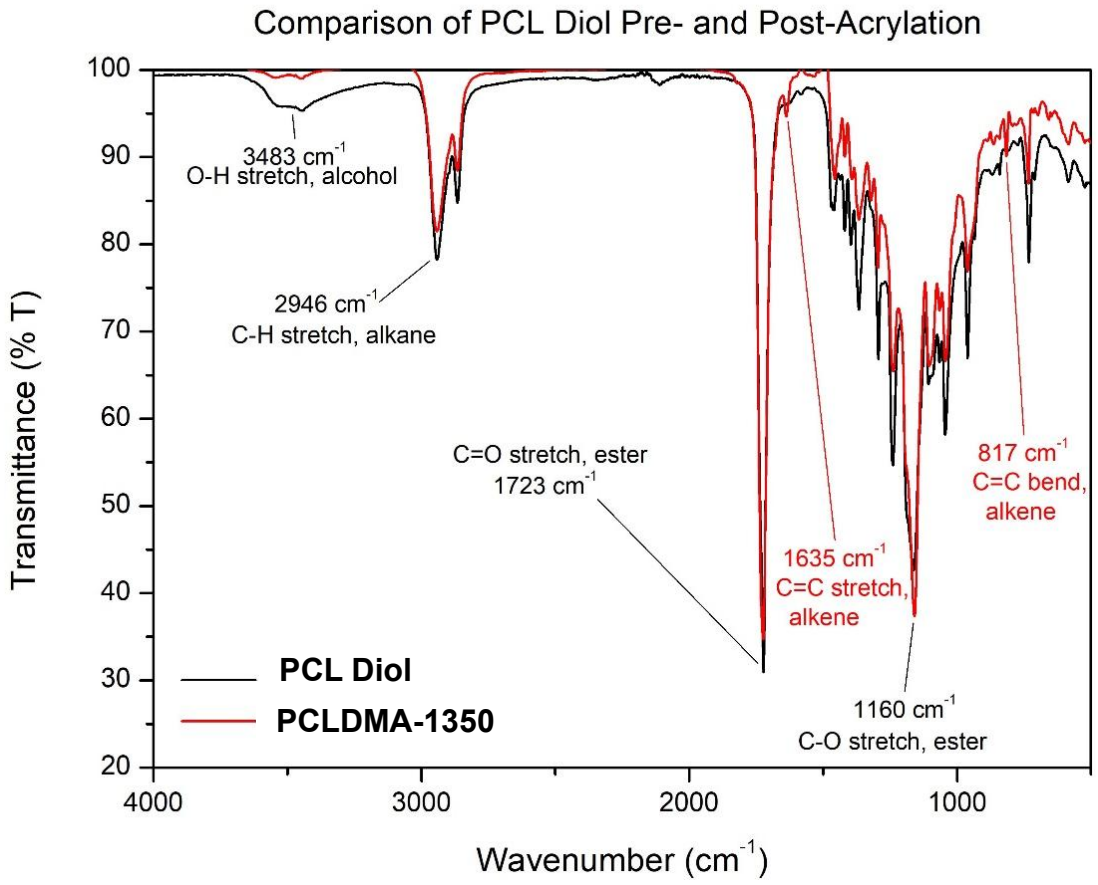


Figure 3.4: FTIR spectra of PCL Diol (black) and PCLDMA-1350 (red).

The PCLDMA-1350 was analysed further, using GPC to estimate the molecular weight of the methacrylated polymer. The GPC analysis of the PCLDMA-1350 approximated the M_w and peak molecular weight (M_p) to be 1008 g/mol and 878 g/mol, respectively, as in **Figure 3.5**. The dispersity (Đ), a measure of how uniform the sample is, was measured to be 1.37. A monodisperse polymer, where all chain lengths are the same, has a Đ of 1. The observed Đ value of 1.37 was therefore deemed acceptable, demonstrating the narrow distribution of molecular weights of PCLDMA-1350. The degree of polymerisation (DP) was also calculated by dividing the molecular weight of the polymer by that of the monomer. The M_w of 1008 g/mol was used in the equation and the DP was found to be 8.84. This firmly places the PCLDMA-1350 within the definition of an oligomer as oligomers are generally accepted to be species with 2 to 40 repeating units.[147,148] According to IUPAC nomenclature there is no specific molecular weight or DP used to define oligomers versus polymers rather the molecule must be of “intermediate relative molecular mass”, whereby its properties are affected “significantly” by the addition or removal of one or a few units.[149] It should also be noted that due to the low molecular weight

nature of oligomers and the calibration of the GPC used for analysis, the GPC results achieved can only be interpreted as approximations. Only three different standards were used to calibrate molar masses less than 1350 g/mol and as a result, the calibration in the low molar mass region was not very well defined. That being said, comparison between the GPC spectra of PCL diol and PCLDMA-1350 demonstrated consistent molecular weight ranges and as such, the preciseness of the data was confirmed.

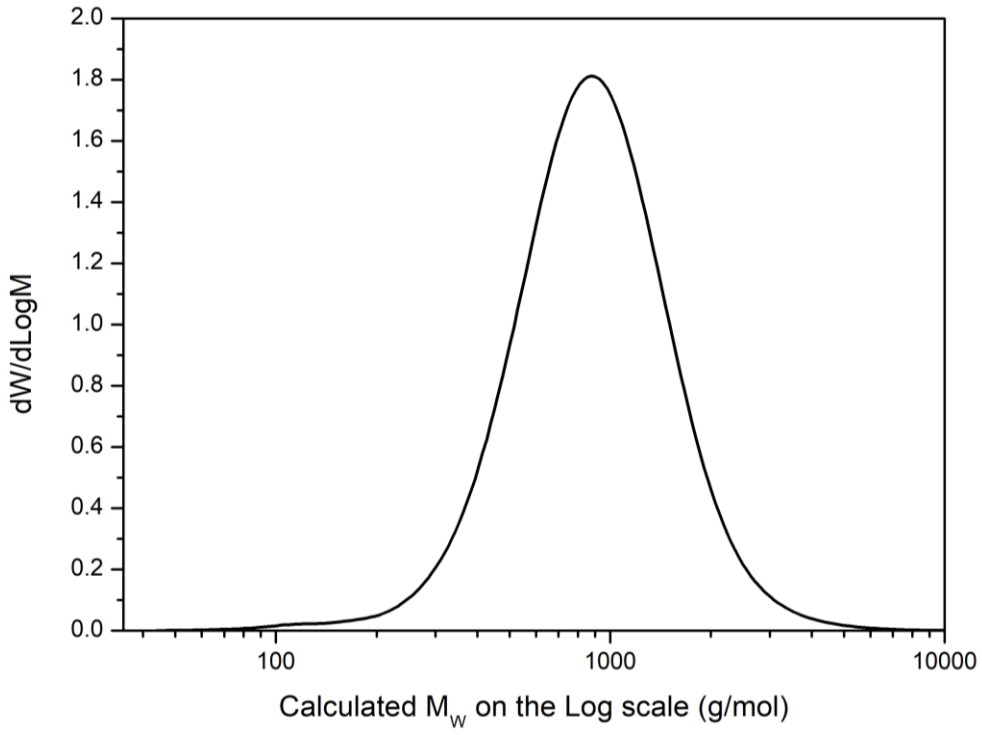


Figure 3.5: GPC spectrum of dW/dLogM versus the calculated M_w on the Log scale of PCLDMA-1350

The sample was also analysed by differential scanning calorimetry (DSC) to investigate its thermal properties. The sample was heated from -90 °C to 100 °C, cooled from 100 °C to -90 °C at 20 °C/min, held for a minimum of 30 minutes at -90 °C to ensure the sample reaches the low temperature and finally heated from -90 °C to 100 °C at 5.00°C/min. The first heating step was to remove the thermal history or process induced thermal properties, as is common practice.[150] The second heating step is used for analysis of the sample, as shown in the graph in **Figure 3.6**. The glass transition (T_g) was measured at –68.5 °C. PCL is a semi-crystalline polymer and as such a melting peak was also expected. Two melting peaks were measured at 34.0 °C and 41.6 °C, namely T_{m1} and T_{m2}. Similar results have previously been explained in literature, wherein Wang et al. reported that crystallisation of PCL at

lower temperatures, as was the case here, gave rise to two melting peaks. The lower crystallisation temperature (T_c) of the PCL during the cooling process may result in once-folded lamellae, therefore giving thin lamellae. These thin crystal structures can melt at lower temperatures, recrystallise into "chain-like" crystals, which in turn melt at higher temperatures.[151] This process likely gave rise to the double melting observed.

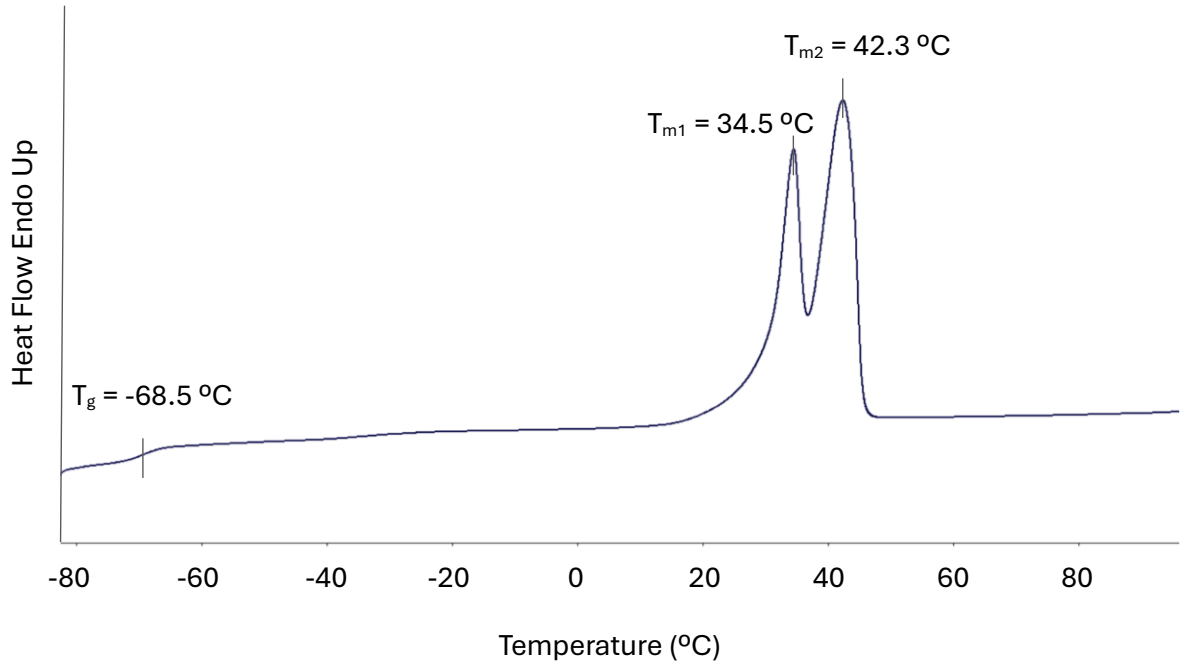


Figure 3.6: DSC of PCLDMA-1350 elucidating the T_g, T_{m1} and T_{m2}.

Once analysis was completed on the purified PCLDMA-1350, the next stage of the project involved using it to create crosslinked materials, which is discussed in more detail in **Chapter 4.** The crosslinked samples were also provided for mammalian cell testing to investigate biocompatibility of the PCLDMA-based materials. This research was published alongside studies on the tuneable degradation of PCLDMA based materials. The difference between degradation of the bulk material and material with microscale surface topography was also investigated.[132]

Based on the learnings from this research and the challenges faced by previous members of the group to create structures on the sub-micron scale with PCLDMA-1350, a shorter chain PCL diol was decided to be of interest.[130] PCL Diol (M_n 530 g/mol) was selected for further investigation.

3.1.3 Methacrylation of PCL Diol (M_n 530 g/mol)

When commencing work with the lower molecular weight PCL diol, the previously optimised conditions used to synthesise PCLDMA-1350 were used. The reactants were left to stir under a nitrogen blanket for five days but upon completion some of the PCLDMA appeared to be beginning to crosslink and was precipitating out of the solution. In response to this, a 7-day methacrylation reaction was completed, using a 1.0:2.0:2.2 molar ratio of PCL Diol:Et_3N:MAC, as before. The reaction was sampled at hourly intervals over the first seven hours and daily at regular intervals over a 7-day period. The percentage methacrylation was then calculated, using the same method as with PCLDMA-1350, and the results can be seen in **Figure 3.7**. Within the first 30 minutes of the introduction of methacryloyl chloride to the reaction mixture, an 81% methacrylation was calculated. A 91% methacrylation was observed after six hours of the reaction with this only increasing to 92% at 24 hours. The percentage methacrylation peaked at day six at 95% methacrylation, but it was decided, based on the above results, that a reaction time of six hours minimum would yield sufficient results in the methacrylation of PCL Diol (M_n 530 g/mol), hereafter PCLDMA-630.

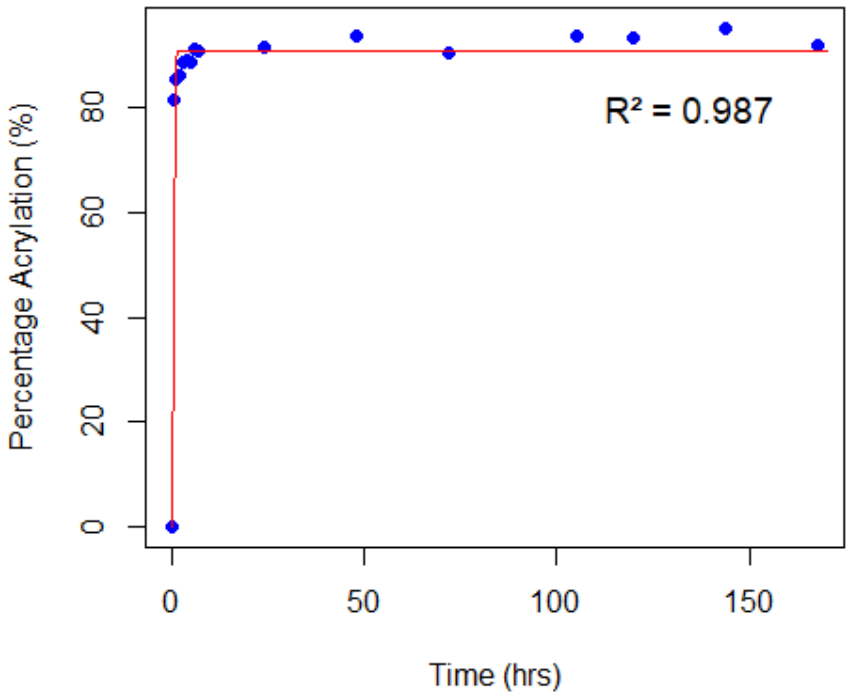


Figure 3.7: Methacrylation of PCLDMA-630 measured over 7 days, analysis was completed using R.

The same purification process was performed as before, and analysis of the ^{1}H NMR spectra was used to confirm the same purification steps were required. It was confirmed that the same process could be applied to PCLDMA-630, as seen in **Appendix A** in **Figure A.3**.

The gravity filtration step removed the majority of insoluble salts. The remaining PCLDMA-630 in THF was then precipitated in an excess of hexane and the remaining solvent was removed by rotary evaporation. A washing and extraction step using 1.0 M HCl followed by drying with anhydrous magnesium sulfate removed the remaining Et_3N•HCl salts, and any remaining hexane was removed by evaporation. Any residual solvents, primarily DCM, were then eliminated using the vacuum oven, set at 40 °C and left over three nights. The ^{1}H NMR spectrum of the isolated PCLDMA-630, as in **Figure A.4** in **Appendix A**, confirmed the purity of the final product.

Once purified, the oligomer was analysed using GPC as before and the results obtained can be seen in **Figure 3.8**. An average of M_w 352 g/mol and M_p 301 g/mol was measured. The Đ was calculated to average 1.55 and the DP was calculated to be 2.51. A slightly larger M_w was expected but the sensitivity of GPC analysis technique can result in inaccurate measurements of the molecular weights of oligomers such as PCLDMA-630, as previously discussed.

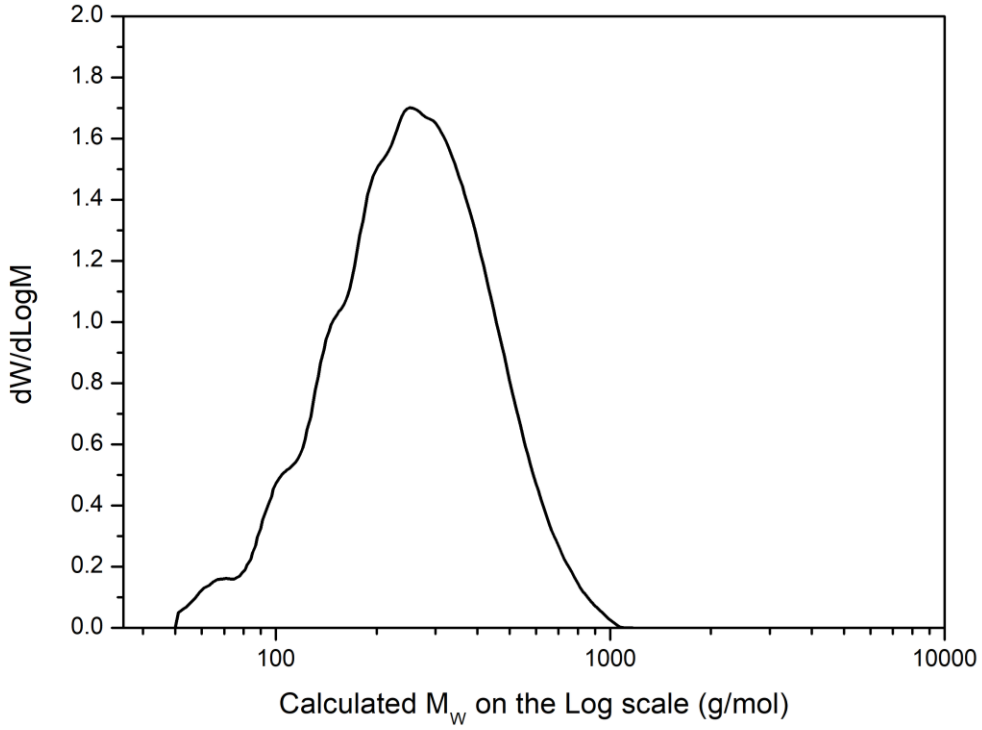


Figure 3.8: GPC spectrum of dW/dLogM versus the calculated M_w on the Log scale of PCLDMA-630.

The oligomer's thermal properties were analysed, as before, by DSC. Again, the second heating step, which was performed over a temperature range from -80 °C to 100 °C at a rate of 5 °C/min was used for analysis of the sample, as is displayed in **Figure 3.9**. The behaviour typical of a semicrystalline polymer or oligomer was observed due to the presence of a T_g, cold crystallisation and T_m.[152] When compared to the DSC analysis of PCLDMA-1350, which saw a T_g of -68.5 °C and two melting peaks at 34.0 °C and 41.6 °C measured, a similar T_g was observed during the analysis of PCLDMA-630. The crystallisation behaviour, however, saw slight differences arise. A T_g of -73.3 ºC was measured and a broad melting peak, within which, two peaks could be observed at -22.5 ºC and 8.76 ºC, T_{m1} and T_{m2} respectively. The two peaks, as explained previously, are likely due to the crystallisation of PCLDMA-630 at a lower temperature resulting in its partial melting and recrystallisation or reorganisation before the final melting at 8.76 ºC.[19,151] Due to the smaller chain length, the melting temperatures would be expected to be lower for PCLDMA-630 than for PCLDMA-1350, as was observed. This observation has been reported, specifically relating to lower molecular weight polymers and plateaus have been observed in higher molecular weight ranges.[19] An additional peak was also measured during the DSC run which was found to be a cold crystallisation peak.

Cold crystallisation can occur when polymers are heated above their T_g but below their T_m. It has been reported that cooling rates can influence the existence and area of a cold crystallisation peak, as slow cooling rates can result in no cold crystallisation, while speeding up the cooling rate can see cold crystallisation peaks appear and grow due to less crystallisation occurring during the cooling period.[153] The same cooling rate was used for both PCLDMA-630 and PCLDMA-1350; however, no cold crystallisation was observed in the DSC analysis of PCLDMA-1350. The cold crystallisation peak, T_{cc}, measured at -35.4 ºC, suggests that complete crystallisation of the oligomer did not occur during the cooling. During cooling, nucleation of the oligomer occurs. Fernández-Tena et al. reported that in oligomers with M_ns below 2000 g/mol crystallisation rates increase as M_n increase. As such, the lower molecular weight PCLDMA-630, may have faced a higher nucleation barrier during the cooling scan thus resulting in a reduced crystallisation rate which in turn could result in cold crystallisation.[19]

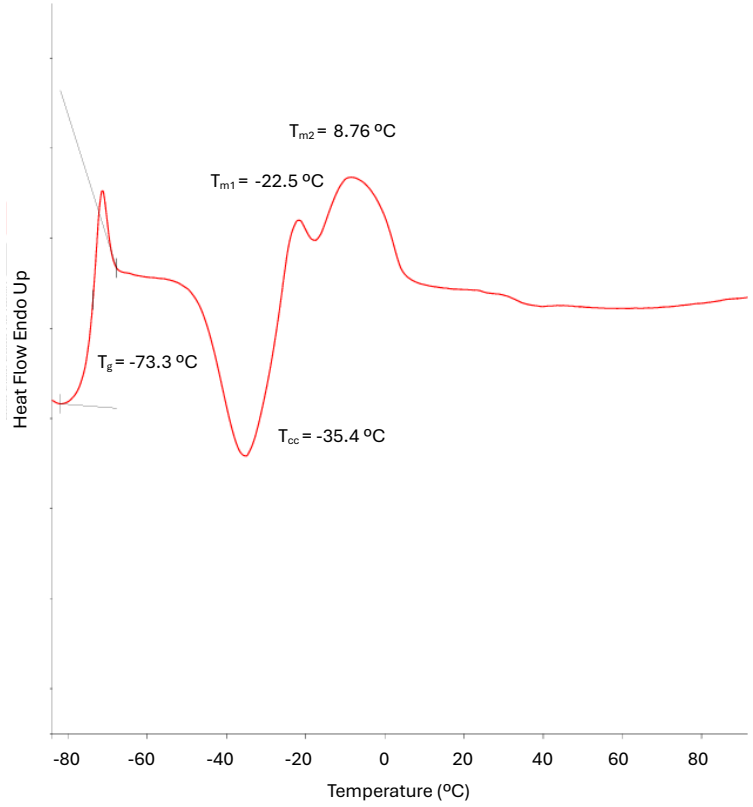


Figure 3.9: DSC of PCLDMA-630 elucidating the T_g, T_{cc}, T_{m1} and T_{m2}

Once PCLDMA-630 had been fully analysed, crosslinking studies and the introduction of sub-micron surface topography were carried out, as with PCLDMA-1350, which are discussed further in **Chapter 4**.

3.2 PAOMEC

3.2.1 Introduction

PAOMEC is an example of an aliphatic polycarbonate. Polycarbonates have commonly found use throughout a variety of industries due to their heat resistant, low water absorption and biocompatibility. As such, they have found popularity in the biomedical field.[154,155] PAOMEC was selected for the next stage of this research due to its liquid state at room temperature, which is advantageous for the crosslinking and structuring processes, discussed in **Chapter 4**. Additionally, the presence of the pendent alkene group on the repeating unit of the PAOMEC chain was advantageous. This alkene group could be crosslinked with small chains that have different functional groups, thereby enabling the alteration of functionalities on the backbone of the material and resulting in altered chemical properties.

3.2.2 Synthesis of Reagents for Polymerisation

The monomer 2-allyloxymethyl-2-ethyltrimethylene carbonate (AOMEC), a cyclic carbonate, was synthesised in a single step ring closing reaction between trimethylolpropane allyl ether diol (TMAD), which is commercially available, and ethyl chloroformate, as reported in the literature.[39] The reaction was commenced at 0 °C and warmed to room temperature to continue for 24 hours.

The ethyl chloroformate acts an electrophile to the nucleophilic primary alcohol present on TMAD. The Et_3N was added dropwise over a 30-minute period. As previously noted, in the solvent THF, Et_3N has a pKa of 12.5.[156] It acted as a base to form Et_3N•HCl and promote the nucleophilic attack of the carbonate group. The white, cloudy mixture that was left stirring overnight was filtered and removal of the THF was completed by rotary evaporation to give a yellow, viscous liquid. The liquid was dissolved in ethyl acetate, washed with 1.0 M HCl to remove any remaining Et_3N, followed by water to remove any salts and dried over magnesium sulfate. Further purification was completed by vacuum distillation, at a temperature of 150 ºC and pressure of 0.015 mbar, to remove the any unreacted diol, from the starting material, and any alcohol side products produced during the reaction. These can hinder the synthesis of PAOMEC by acting as unintentional initiators in the polymerisation reaction. The isolated monomer was achieved in yields of 70-75%

after purification and analysed using ^{1}H NMR and ^{13}C NMR spectroscopy, as in **Figure 3.10** below and **Figure A.5** in **Appendix A**.

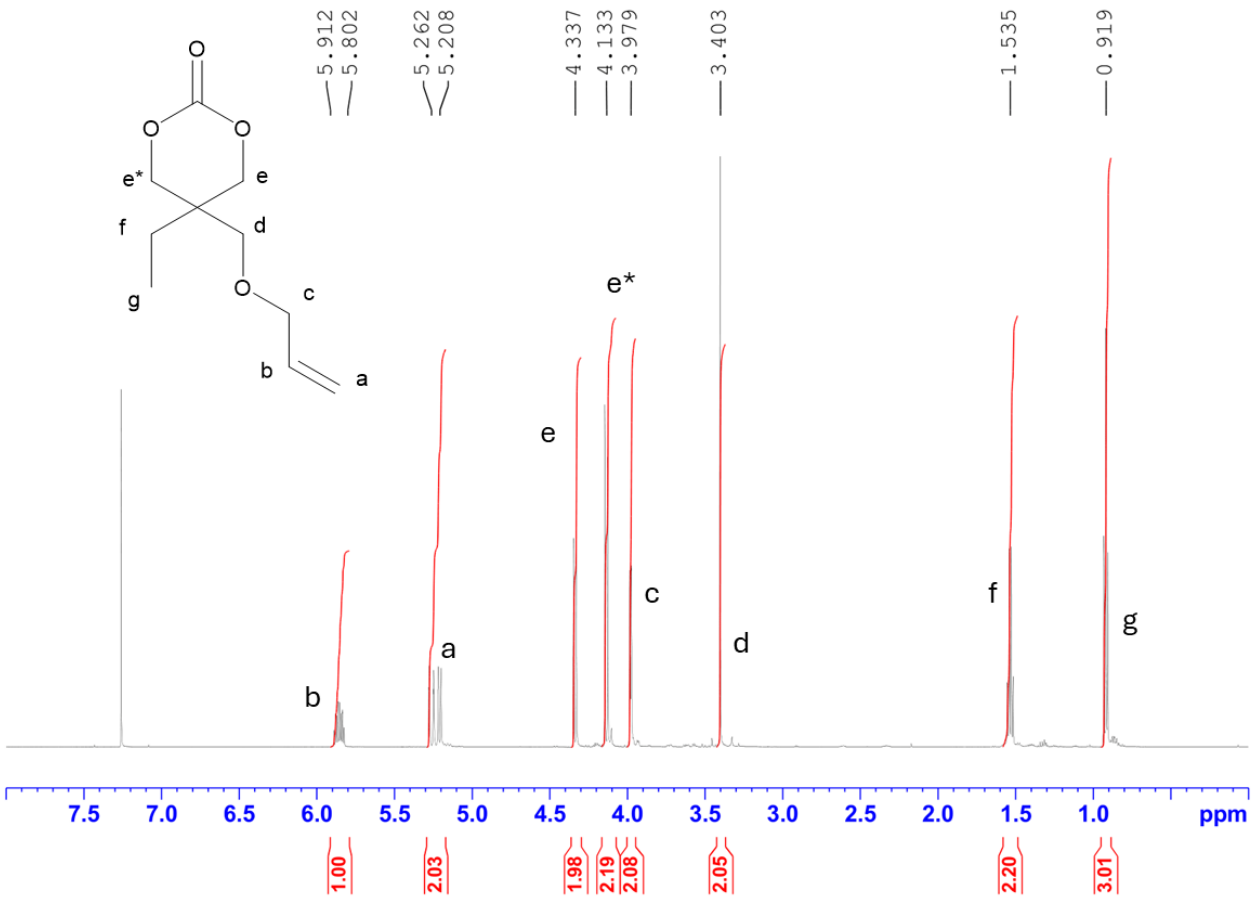


Figure 3.10: ^{1}H NMR (600 MHz, $CDCl_3$) spectrum of purified AOMEC.

Prior to synthesis of PAOMEC, 1-(3,5-bis(trifluoromethyl)phenyl)-3-cyclohexylthiourea (TU), a co-catalyst required for the polymerisation reaction, was synthesised based on work originally completed by Pratt et al.[157] The catalyst was synthesised in the lab due mainly to the low availability and high costs associated with buying it directly from suppliers. For example, 250 mg of the catalyst costs €305.[158] In the lab, it could be synthesised on the gram scale for a fraction of the price. This and other variations of organic, thiourea-amine based catalysts have been used in an array of ring opening polymerisations to improve reaction times and conversion rates.[159,160,160] The TU cocatalyst was synthesised under dry conditions, using oven-dried glassware, THF dried over sodium/benzophenone and cyclohexylamine and 3,5-bis(fluoromethyl) isothiocyanate dried over molecular sieves. The reaction was left stir under a blanket of N_2. The isolated white solid was

recrystallised from chloroform and left in the freezer overnight. The white solid formed was vacuum filtered, dried overnight in a desiccator and isolated yields of 72% were achieved. The purity of the TU cocatalyst was assessed via ^{1}H NMR spectrum analysis, as in **Figure 3.11**, and additionally a ^{13}C NMR was performed, as in **Figure A.6** in **Appendix A**.

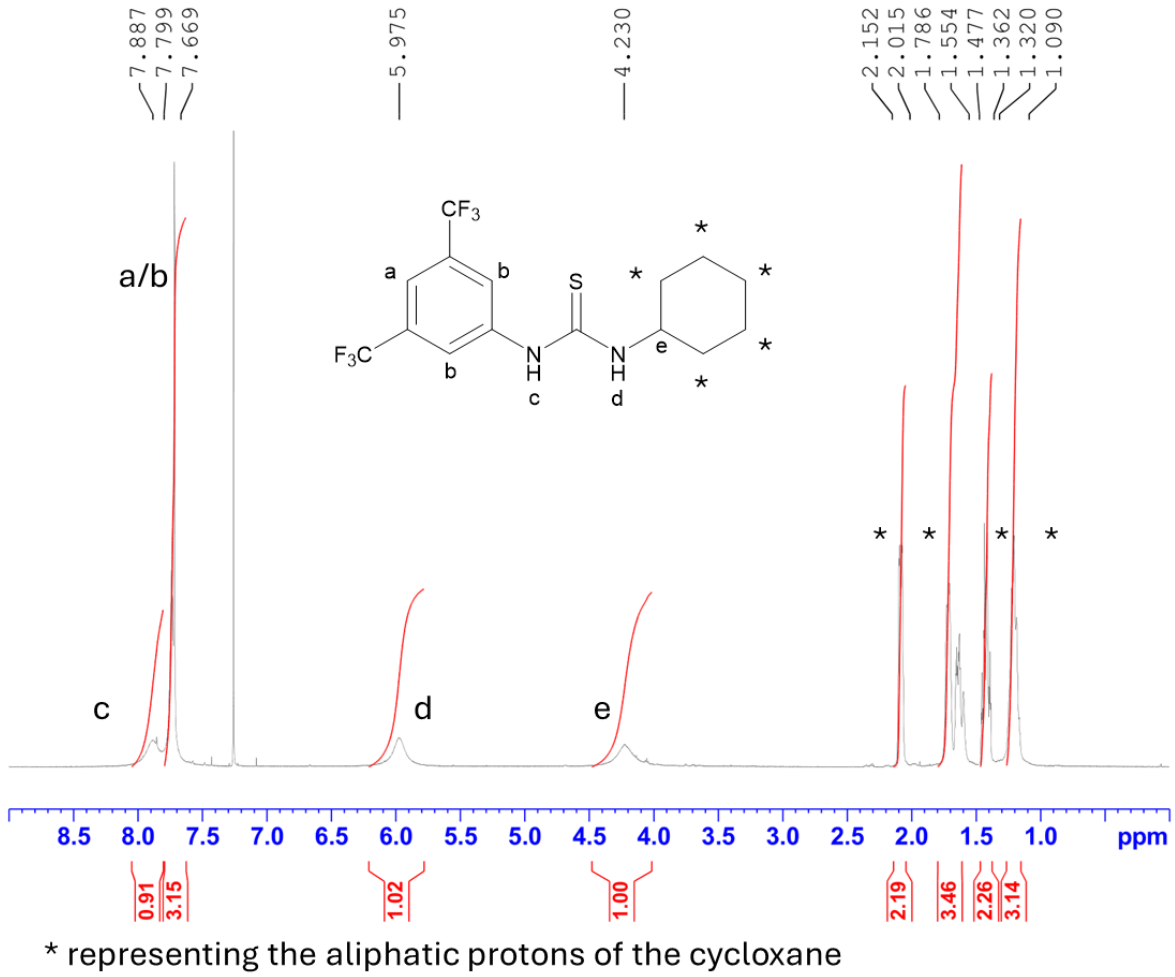


Figure 3.11: ^{1}H NMR (600 MHz, $CDCl_3$) spectrum of purified TU co-catalyst.

Once the reagents for the polymerisation were synthesised to a satisfactory quantity and quality, the synthesis of PAOMEC could commence.

3.2.3 Polymerisation of AOMEC

The polymerisation reaction itself was adapted from previously published work by Thomas et al.[161] As per the reaction scheme in **Figure 3.12**, AOMEC, 1,8-

diazabicyclo[5.4.0]undec-7-ene (DBU), 1,4-butane diol and TU, were reacted in dried DCM over 72 hours to give PAOMEC in isolated yields of 89%.

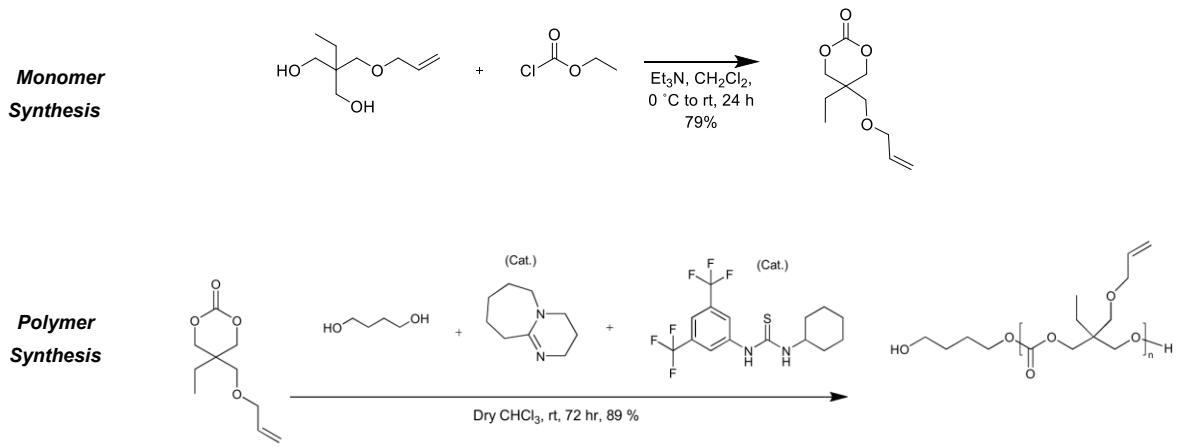


Figure 3.12: Reaction Scheme for both monomer and polymer synthesis.

In more detail, 1,4-butane diol (5 mol% to monomer), the alcohol initiator of the ROP reaction, alongside DBU (5 mol% to monomer), a bicyclic amidine base, used as a catalyst in this reaction, were dissolved in dried DCM along with the organic co-catalyst TU.

Separately, AOMEC was added to dried DCM and subsequently combined with the dissolved TU and DBU in a round bottomed flask. The reactants were stirred together at a final concentration of 2.0 M AOMEC. The polymerisation proceeds as an ROP, whereby the TU catalyst acts as a hydrogen bonding donor to the monomer and the 1,4-butane diol initiator is simultaneously activated by the hydrogen bond accepting amidine base, DBU, as seen in **Figure 3.13**.[162]

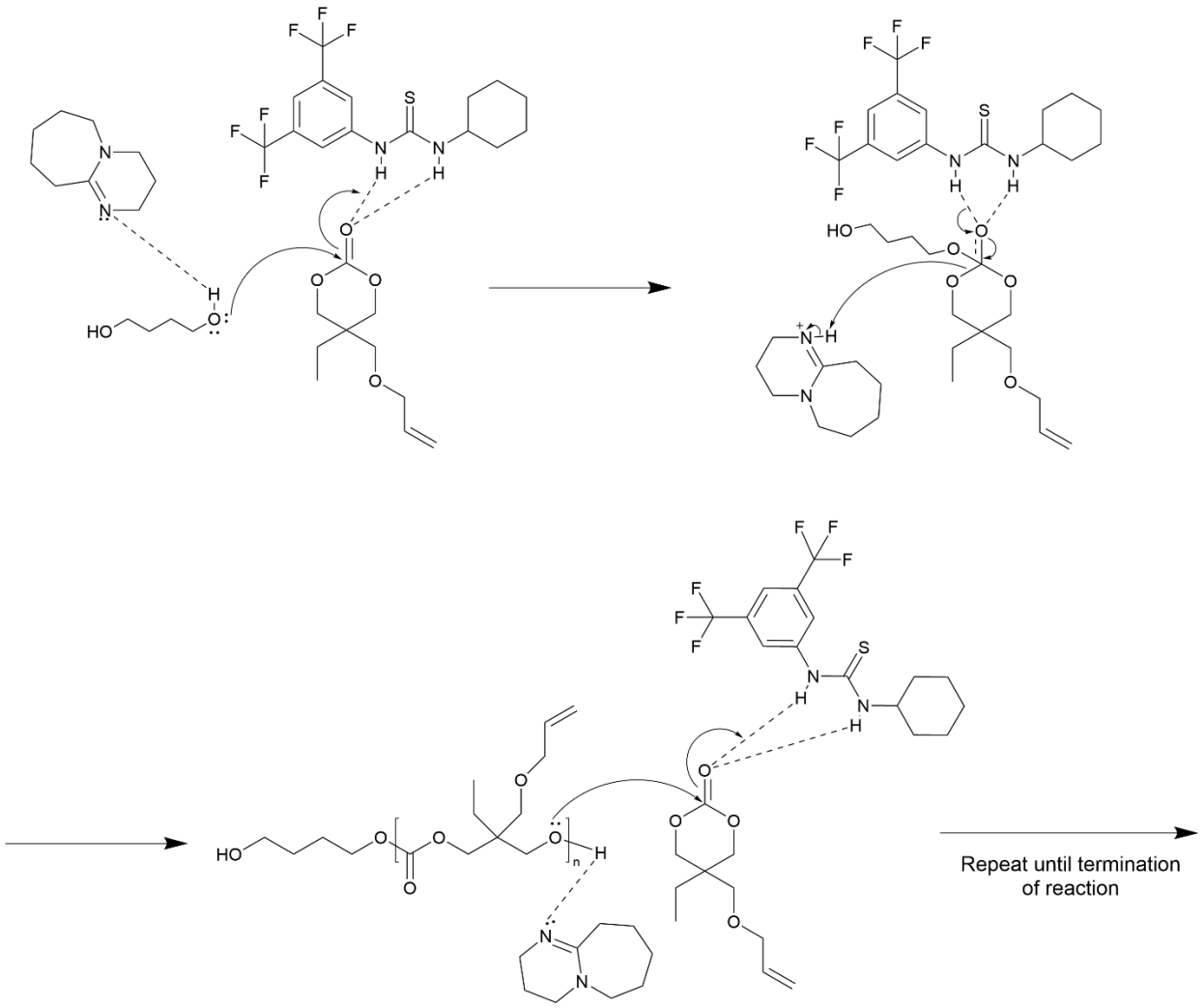
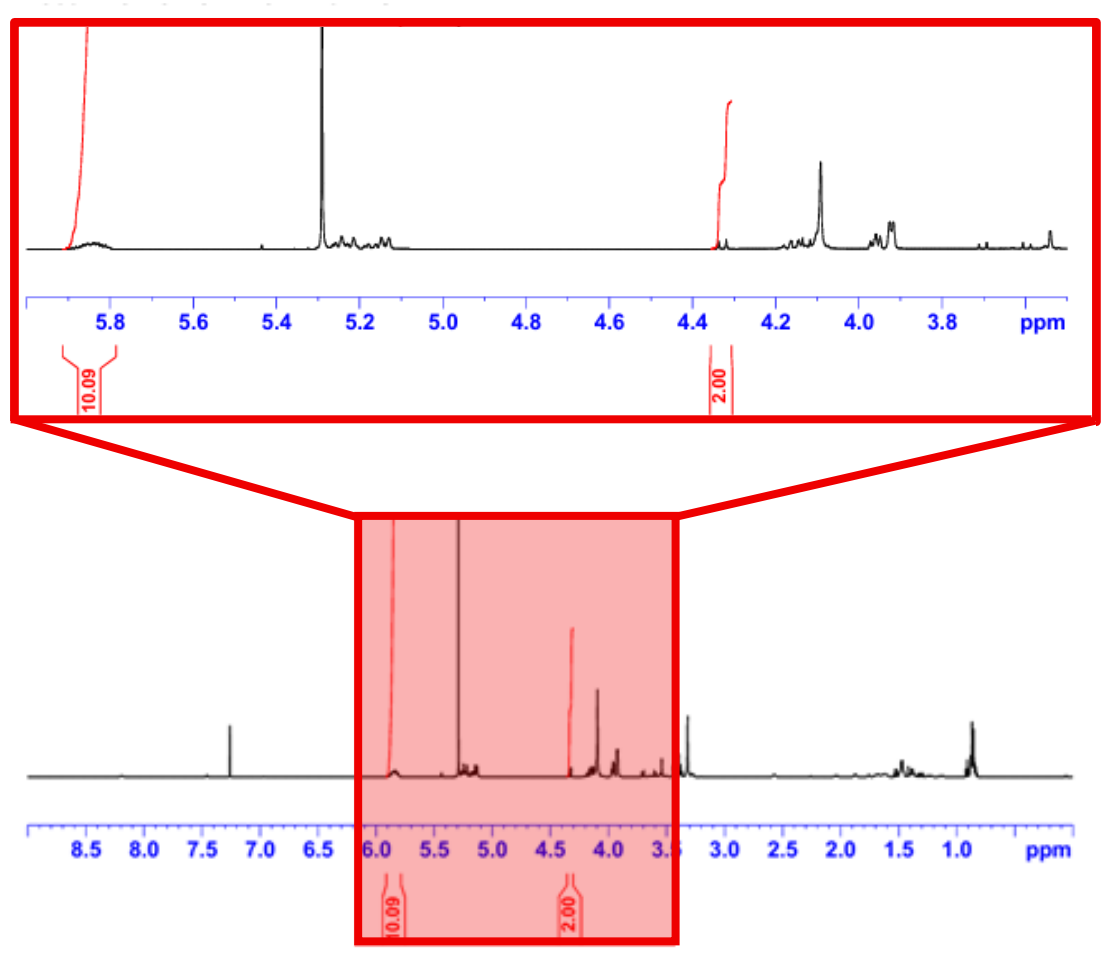


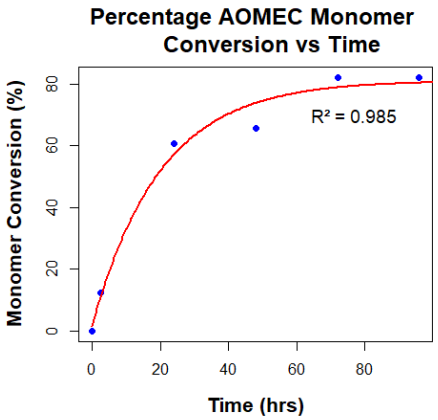
Figure 3.13: Proposed reaction scheme for ROP of AOMEC with TU catalyst and DBU.

The reaction was allowed to proceed with daily sampling and analysis using ^{1}H NMR spectra was completed to determine the percentage monomer conversion, as in **Figure 3.14**. Integration of the peaks corresponding to the C-H vinylic proton found in the repeating unit of PAOMEC were compared to the CH_2 methylene protons on the AOMEC ring. Based on the daily sampling over a 96-hour period, 72 hours was determined to be sufficient time for polymerisation as no increase in percentage monomer conversion was measured after this time point.

For the monomer conversion percentage calculations, the doublet at 4.33 ppm which corresponded to the CH_2 of the cyclic carbonate in the AOMEC monomer was selected and integrated for two. When choosing the polymer peak it was important to ensure the chosen peak was isolated and not overlapping with any other protons of the rest of the polymer chain. The multiplet between 5.92-5.78 ppm, the C=C-H of

the vinyl group, was selected for this reason. The multiplet was integrated and then doubled to account for the fact it was representative of one proton while the monomer integral was representing two. One was subtracted from said integral to account for the vinyl present on the monomer.





$$\%\ monomer\ conversion = \frac{(integration\ of\ polymer\ peak \times 2) - 1}{integration\ of\ monomer\ peak + ((integration\ of\ polymer\ peak \times 2) - 1)} \times 100$$

$$= \frac{(10.09 \times 2) - 1}{2 + (10.09 \times 2) - 1)} \times 100 = \frac{19.18}{21.18} \times 100 = 90.6\,\%$$

Figure 3.14: ^{1}H NMR spectrum of polymerisation reaction after 3 days, red outlined ^{1}H NMR spectrum is the zoomed in area (top) of the section of the full spectrum (middle) outlined and highlighted in red. Graph of percentage monomer conversion after daily sampling over a 96-hour period (bottom left) and equation used to calculate monomer conversion (%) (bottom right) from integration of ^{1}H NMR spectrum.

Once a percentage monomer conversion greater than 80% was achieved the reaction was quenched using Amberlyst A15 ion exchange (10 mg per 1 mg of DBU) which neutralised the basic DBU. The purification process was originally completed based on work completed by Thomas et al. and had to be adapted to refine purity and isolated yields.[161] The mixture was gravity filtered to remove any salts, insoluble impurities and the Amberlyst. The sample was condensed by rotary evaporation and redissolved in minimal amount of DCM and then precipitated in ice cold hexane. The collected mixture was condensed, by rotary evaporation, to isolate a colourless or pale, yellow oil. Isolation of the oligomer using hexane was proving difficult due to the oligomer, unreacted monomer and any remaining TU catalyst all being insoluble in hexane.

An ice-cold methanol precipitation step was investigated as a way to improve purity. This method resulted in the oligomer precipitating more readily than the monomer and any other impurities. The analysis of ^{1}H NMR spectra elucidated that this method worked as expected giving isolated PAOMEC of improved purity as in **Figure 3.15**. Yield optimisation remained a challenge as prior to this precipitation in ice-cold solvent, yields of up to 90% had been achieved. This step, however, resulted in a large loss of product with yields of purified PAOMEC between 7 to 38% achieved. As such a silica plug step was included in the purification process.

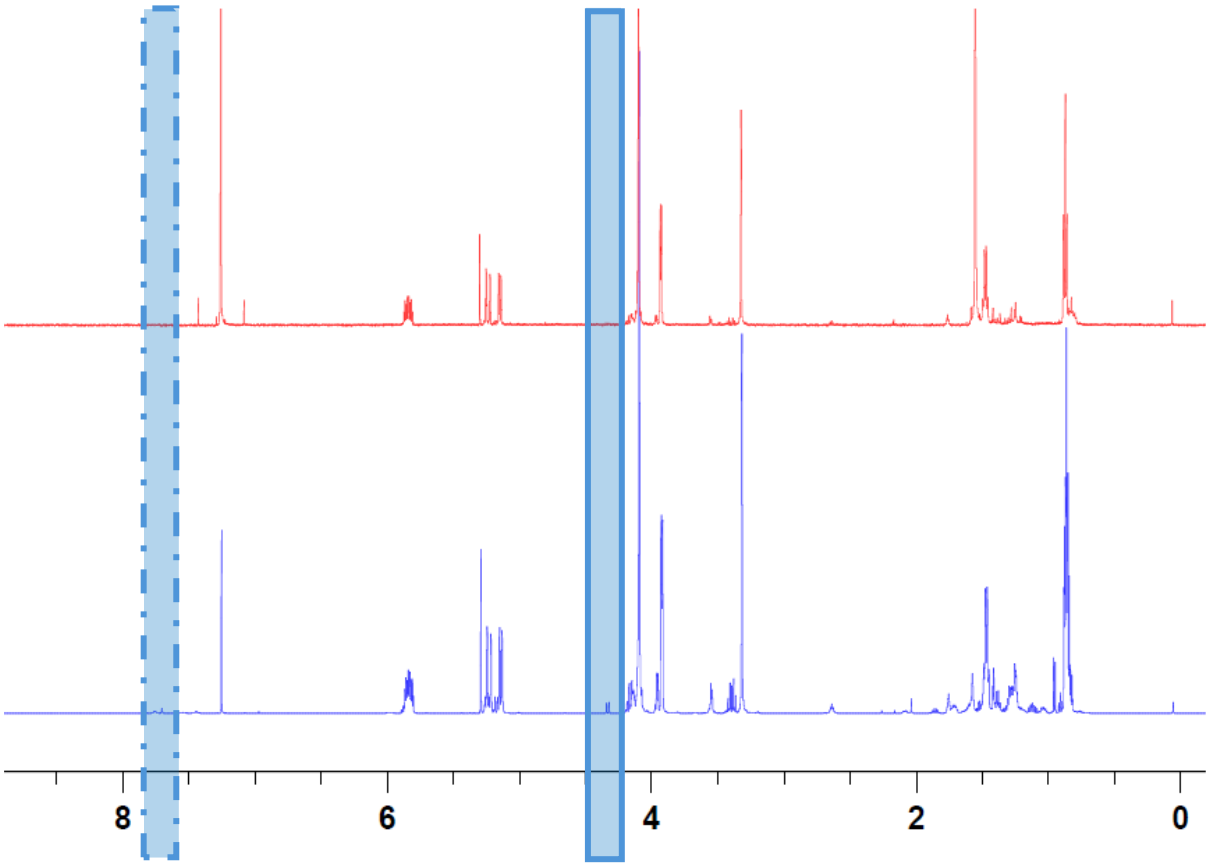


Figure 3.15: ^{1}H NMR spectra of purified PAOMEC using hexane (bottom, blue spectrum) and methanol (top, red spectrum). The blue highlighted and outlined at peaks at 7.76 ppm and 4.33 ppm highlight the presence of the TU catalyst (dashed outline) and AOMEC monomer (full outline), respectively, when hexane was used in the purification process.

After the gravity filtration, separation was attempted with a silica plug to remove the TU catalyst. The solute was first loaded onto the plug and after collection in fractions, ethyl acetate was introduced to the plug to minimise PAOMEC left behind. The collected mixture was again condensed by rotary evaporation to isolate a colourless or pale, yellow oil. This resulted in similar ^{1}H NMR spectra as before, wherein starting materials were still present.

Column chromatography was planned, as a result, with the aim of removing the starting materials, in particular the TU catalyst and monomer. A longer silica column was expected to improve the separation that could not be achieved with the silica plug. Thin layer chromatography (TLC) was performed to using different ratios of hexane and ethyl acetate including 0:1, 1:1, 2:1, 3:1, 4:1, 5:1 and 10:1. With pure ethyl acetate, as had been the problem with the silica plug, the polymer and catalyst run at the same rate making separation difficult. Based on TLC results, a 4:1 hexane ethyl acetate ratio was selected as separation of the PAOMEC and TU catalyst was shown to be sufficient. The column was packed and the impure PAOMEC, that was

condensed by rotary evaporation and redissolved in the minimal amount of ethyl acetate, was loaded onto the column. Once loaded, the separation process commenced, and samples were collected in fractions and tested via TLC. The TU was visible under short-wave UV light and once identified with a pencil, the TLC plate was dipped in permanganate stain. This stain is commonly used to identify organic compounds, by oxidising functional groups such as alkenes which are present in PAOMEC, as illustrated in **Figure 3.16**.[163] The fractions, once no longer shown to be UV active, demonstrating the removal of all TU catalyst, were collected and isolated.

Ethyl acetate was then used to wash any remaining PAOMEC through the column. The samples were checked and the successful removal of TU cocatalyst was confirmed by ^{1}H NMR spectroscopy. However, monomer was found in the isolated fractions. As such, TLC analysis was completed with different ratios of ethyl acetate and hexane, as in **Figure 3.16**, to investigate if separation of the PAOMEC and monomer was possible. It was decided that 1:2 ethyl acetate and hexane gave the most promising results.

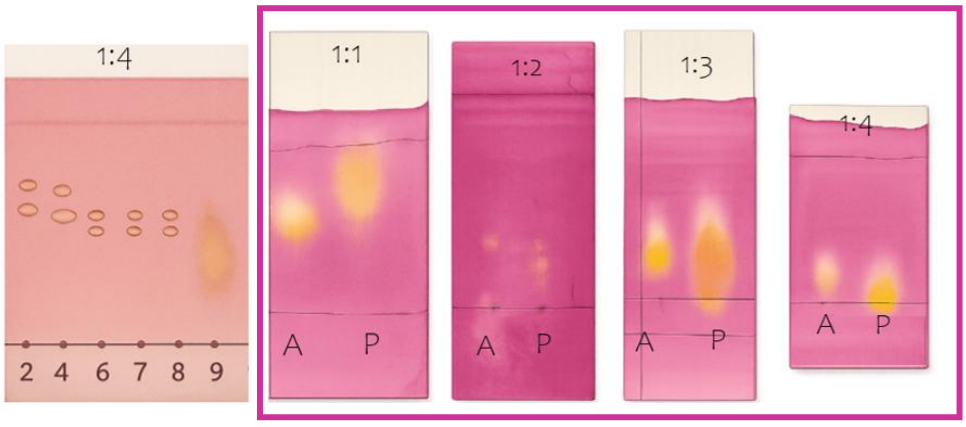


Figure 3.16: TLC plate of different fractions from the column separation of an impure PAOMEC sample. Fractions 2 to 8 were UV active as demonstrated by the pencil marks circling the UV active spots while fraction 9 only showed activity in the permanganate stain (left); TLC plates post staining with different solvent ratios of ethyl acetate and hexane, respectively (outlined, right). Rendering of TLC plates was completed using AI Illustrae.co.

An impure PAOMEC sample was run through the column, firstly with a 1:4 ratio to remove the TU catalyst, then a 1:2 ratio to isolate the monomer. Similar to the use of methanol, this method successfully isolated the some PAOMEC but complete separation of the lower molecular weight oligomer chains from the monomer was not possible. This resulted in a lower yield. As such, it was decided that the presence of

minimal monomer, for the purpose of this research, would not impede upon the future use of the PAOMEC. The purification process was hence decided to only involve the use of the column to remove the TU catalyst, which was completed with the 1:4 solvent ratio. PAOMEC after column separation, condensation by rotary evaporation and drying in a desiccator overnight was isolated as a yellow or colourless oil in yields of 80-89% with a purity of 85%. This was confirmed by ^{1}H NMR spectroscopic analysis of the PAOMEC sample, as shown in the spectrum in **Appendix A** in **Figure A.7**.

FTIR spectroscopy was also used to confirm the successful synthesis by comparison between purified AOMEC and PAOMEC samples, as in **Figure 3.17**. Similar peaks in both spectra were noted corresponding to alkyl stretching at approximately 2936 cm^{-1} and the carbon carbon double bond stretching of the alkene functionality at approximately 1647 cm^{-1}. Peaks corresponding to various carbon oxygen stretches of the carbonate and vinyl ether groups were observed between 1228 cm^{-1} and 1093 cm^{-1}. The major differences between the two samples were noted with the peak corresponding to the hydroxyl stretch of the alcohol present in PAOMEC due to the use of 1,4-butane diol as an initiator. Additionally, the ring strain present in the AOMEC monomer resulted in the increased wavenumber of the carbonate carbonyl stretch which was observed at 1756 cm^{-1} in the AOMEC spectrum and 1739 cm^{-1} in the PAOMEC spectrum.[164,165]

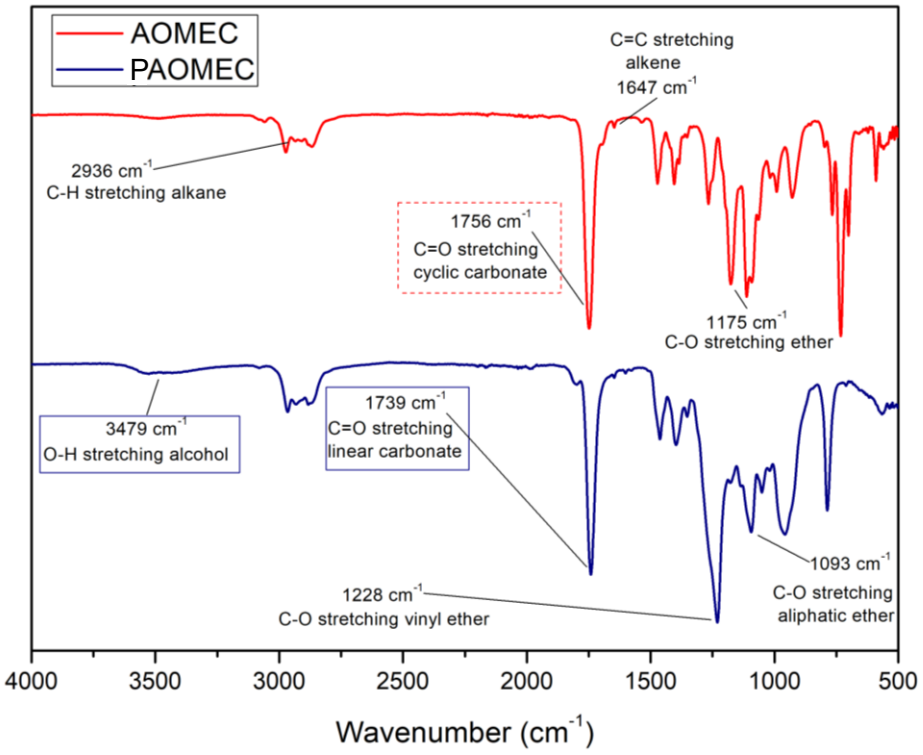


Figure 3.17: FTIR spectra of AOMEC (red, top) and PAOMEC (navy, bottom) with key peak differences outlined with boxes.

Once PAOMEC was identified and purified, each PAOMEC sample was analysed by GPC. The M_w of the isolated PAOMEC samples ranged between approximately 810 g/mol and 1200 g/mol with Đ ranging between 1.6 and 2.8. An example of a spectrum produced by said GPC analysis, as in **Figure 3.18**, approximated a M_w of 1257 g/mol and M_p of 1159 g/mol. The Đ was measured as 2.7 and the DP was calculated to be 6.23. The Đ was increased due to the presence of the monomer, as can be observed in the separate, narrow peak in **Figure 3.18**. When column chromatography was performed and the PAOMEC oligomer was isolated from the monomer, despite the low yields, an increased M_w of 1568 g/mol and decreased Đ of 1.6 was measured. Again, due to the calibration of the GPC used and the low molecular weight of the PAOMEC oligomers, the results are an approximation but the consistency of the results across all PAOMEC syntheses confirmed the reproducibility of the reaction.

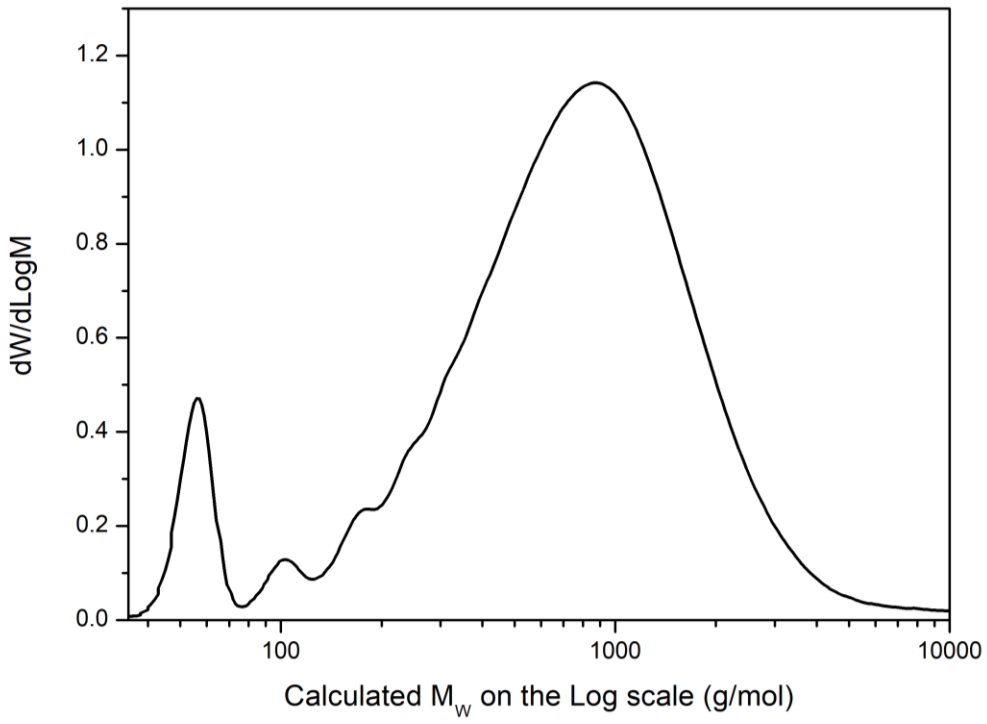


Figure 3.18: GPC spectrum of dW/dLogM versus calculated M_w on the Log scale of PAOMEC.

Based on the 20:1 monomer to initiator [M]:[I] ratio that was employed for this ROP, the molecular weight of the synthesised PAOMEC and DP were expected to be higher. The low DP of 6.23 calculated was theorised to be likely due to the performance of the polymerisation under conditions that were not sufficiently dry.

This theory was first investigated by increasing the [M]:[I] from 20:1 to 40:1 This alteration would be expected to increase the ratio of repeating units to initiator per chain. Instead, no increase was measured as a M_w of 957 g/mol and Đ of 3.3 was measured. This supported the theory that premature quenching of the reaction was occurring.

The presence of moisture in the reaction vessel further investigated by removing the 1,4-butane diol initiator and allowing the reaction to proceed using water as the sole initiator. The polymerisation reactions were otherwise performed identically to the previous reactions and were repeated twice to assess the reproducibility of the process excluding the initiator. The M_w of the resulting PAOMEC was estimated, by GPC as in **Figure 3.19**, to range between approximately 1350 and 1850 g/mol. These molecular weights were observed to be slightly higher than those previously achieved but were still very much oligomeric. This supported the theory that water was affecting the polymerisation process. It was briefly considered that the

polymerisation could be performed without 1,4-butane diol present to reduce the environment impact of the synthesis but the Đ ranged between 2.6 and 3.8. To ensure better uniformity and control over the polymerisation, it was thus decided to continue with 1,4-butane diol as the initiator. Future work would focus on drying the chemicals and reaction vessels more thoroughly as well as performing the reaction under an inert atmosphere using argon. For the purpose of this research, the PAOMEC samples, in reactions initiated by 1,4-butane diol, were of a satisfactory molecular weight for crosslinking purposes, as is discussed in **Chapter 4**, and were of a low Đ thus demonstrating good reproducibly.

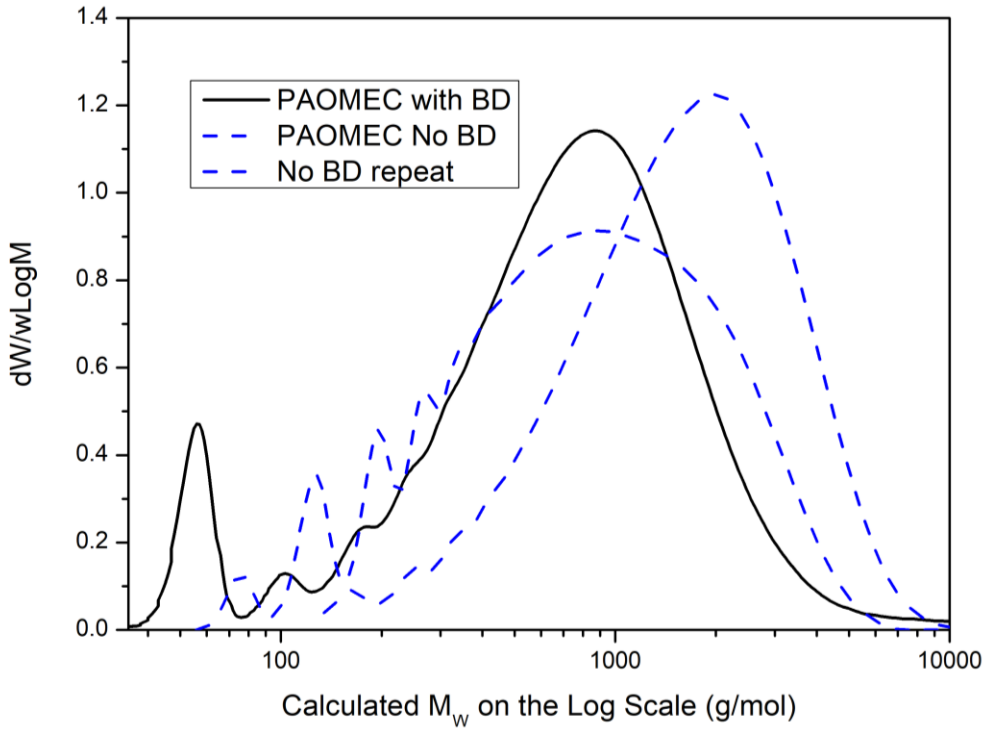


Figure 3.19: GPC of PAOMEC samples from syntheses with (black, line spectrum) and without (blue, dashed spectrum) 1,4-butane diol used as the initiator.

DSC was then carried out to complete thermal analysis of PAOMEC. The sample was heated from -80 °C to 60 °C, cooled from 60 °C to -80 °C, held for 30 min at -80 °C to ensure the sample reaches the low temperature and finally heated again from -80 °C to 60 °C, all completed at a 20 °C/min rate. Again, the second heating step was used for analysis and can be seen in **Figure 3.20**. PAOMEC demonstrated behaviours typical of an amorphous polycarbonate as only a glass transition was observed.

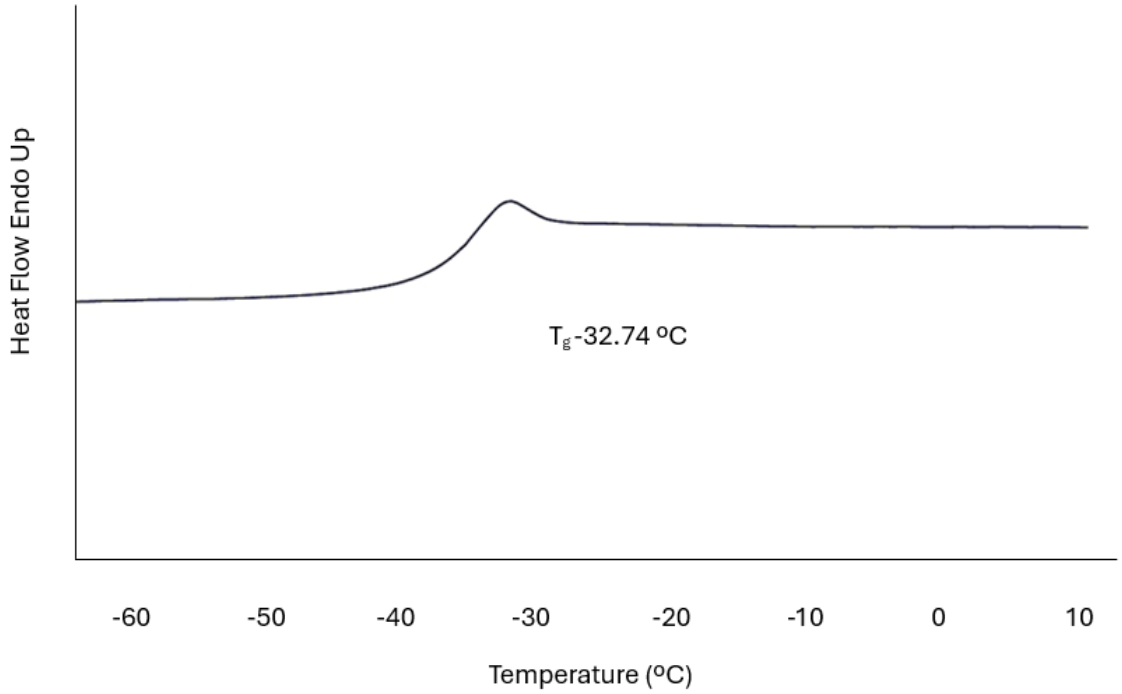


Figure 3.20: DSC analysis of amorphous PAOMEC.

The T_g peak observed at -32.74 °C corresponded well to the liquid state of PAOMEC at room temperature, which was deemed one of the key, advantageous properties of PAOMEC for this research. On completion of synthesis, purification and analysis of PAOMEC, crosslinking studies, as discussed in **Chapter 4**, were to be the next stage of the research.

3.3 Conclusions

The methacrylation of PCL diol (M_n 1250) and PCL diol (M_n 530) was completed in order to introduce UV-active alkene functionalities at the termini of the oligomer chains for photoinitiated crosslinking, as discussed in **Chapter 4**.

The reaction to form PCLDMA-1350 was performed originally over a number of time periods with varying ratios of the reactants, PCL diol, Et_3N and MAC. In early stages of the research, it was found that the optimal conditions were a reaction time of three days and reactant molar ratio of 1.0:2.0:2.2 of PCL diol, Et_3N and MAC. This gave isolated yields of 91% with percentage methacrylation, measured via integration of peaks measured on ^1H NMR spectra of 86%. Over time it was observed that the percentage methacrylation of PCLDMA-1350 was lower than expected when the reaction time was not altered. Analysis of the reactants resulted in impurities being

found in the MAC. The degradation products present in the MAC prompted re-examination of the time required for the methacrylation reaction with the molar ratio of 1.0:2.0:2.2 of PCL diol, Et_3N and MAC. It was found that any reaction time over 24 hours did not result in significantly increased percentage methacrylation and as a result, the methacrylation reaction was performed for approximately 24 hours. This gave isolated yields of 81-89% with 84-99% methacrylation measured.

The methacrylation of PCLDMA-630 was analysed in the same way and was found to give an isolated yield 72% with a percentage methacrylation of 91-95% after 24 hours with the same molar ratio of reactants mentioned above. This process involved the use of MAC prior to the degradation that was observed in the later stages of PCLDMA-1350 methacrylation. Both methacrylated samples were analysed by ^1H NMR spectroscopy as well as FTIR spectroscopy. GPC analysis was used to measure the molecular weight of the samples which confirmed both PCLDMA-1350 and PCLDMA-630 to be oligomers with estimated M_w of 1008 g/mol and 286 g/mol, respectively. DSC was performed to investigate the thermal properties of the PCL samples and confirmed the semi-crystallinity of both samples.

PAOMEC synthesis then became the central focus of the next stage of the research. This involved the synthesis of the monomer AOMEC via a ring closing reaction between TMAD and ethyl chloroformate to give isolated yields of 70-75%. The polymerisation reaction involved the use of the catalyst DBU, which was purchased and the co-catalyst TU. TU was synthesised by reacting cyclohexylamine and 3,5-bis(fluoromethyl) isothiocyanate together, in still-dried THF, under an N_2 blanket. The catalyst was purified by recrystallisation from chloroform to give an isolated yield of 72%.

Upon successful synthesis of the reactants, the polymerisation of AOMEC was performed. It was found that the optimal reaction time was three days. After this purification of the PAOMEC was performed with gravity filtration, condensation via rotary evaporation and redissolution in ethyl acetate. Column chromatography was performed with the redissolved sample loaded onto a silica column that was run with a 4:1 ratio of hexane and ethyl acetate to remove the TU catalyst. The PAOMEC was recovered by washing the column with ethyl acetate to achieve isolated yields of 80-89% and purity of 85%. Attempts were made to remove the unreacted monomer

from the PAOMEC sample, but due to the low molecular weight nature of the oligomer, it was difficult to achieve satisfactory yields whilst improving the percentage purity. It was decided that for the purpose of this research, the presence of the monomer in the final sample, in small quantities was acceptable.

Chemical analysis of AOMEC, TU catalyst and PAOMEC was performed with ^{1}H NMR and ^{13}C NMR spectroscopy and FTIR spectroscopy. The PAOMEC samples when analysed by GPC had an estimated M_w range between 810 and 1200 g/mol while the Đ of the samples synthesised ranged between 1.6 and 2.8. In the case of this research, working with oligomers was desirable for the next steps involving crosslinking and structuring, discussed in **Chapter 4**. Furthermore, the GPC analysis confirmed the reaction to be reproducible with consistent M_w and Đ measured. Thermal analysis was performed via DSC confirming the amorphous state of the PAOMEC, as was expected for this polycarbonate. Upon completion of analysis of PAOMEC and the aforementioned PCLDMA-1350 and PCLDMA-630, the next stage of the research involving crosslinking, structuring and functionalisation was commenced.

Chapter 4 Crosslinking, Structuring and Functionalisation

4.1 Introduction to Crosslinking and Patterning

Chemical crosslinking involves the covalent linking of two or more molecules by intermolecular or intramolecular bonds.[166] Crosslinking can proceed through many mechanisms, including, thermally, enzymatically or via photo-activation. Photopolymerisation is traditionally categorised into free-radical chain polymerization, thiol-ene photo-crosslinking, and photomediated redox cross-linking.

Free radical initiated photopolymerisation was the type of crosslinking reaction utilised in this research. The main benefits of photopolymerisation is that it can proceed in an energy and time efficient manner, and in low solvent or solvent free conditions, thereby minimising the production of volatile organic compounds.[167] Another advantage of photopolymerisation was the versatility offered by the approach. Chemicals with different functionalities could be used interchangeably. The photopolymerisation process could also be performed using different templates. This versatility enabled control over surface chemistry and topography which was key for this research. In general, photopolymerisation involves the mixing of a material, such as a polymer with active functional groups like alkenes and thiols, with short chain chemical crosslinkers, and photoinitiators (PIs). The liquid mixture can then be exposed to a light source, and the result is the formation of a chemically crosslinked, solidified material, as illustrated in **Figure 4.1**.

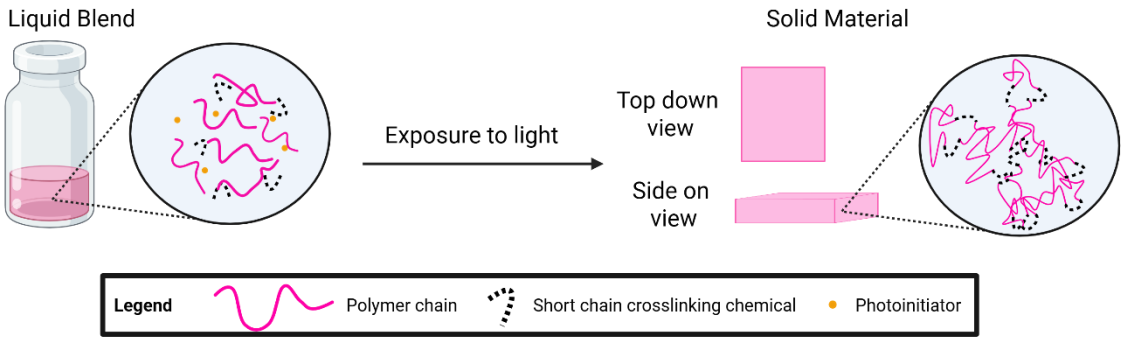


Figure 4.1: General photopolymerisation crosslinking scheme, illustrated using Biorender.com

This type of photoinitiated free radical crosslinking proceeds by initiation, propagation and termination. A PI is activated by light releasing free radical species

upon photolysis. Specifically, upon light exposure, the PI is excited to the triplet state and undergoes α-cleavage forming free radicals. This is often denoted as the initiation stage of the photo-crosslinking process and is illustrated in **Figure 4.2**. The radicals can react with different functional groups such as thiols, or acrylate groups. The presence of the terminal alkene functionality in both PCLDMA and PAOMEC oligomers made them ideal for this type of crosslinking process, as exemplified with the scheme of PCLDMA and activated PI Irgacure-2959 in **Figure 4.3**.[168]

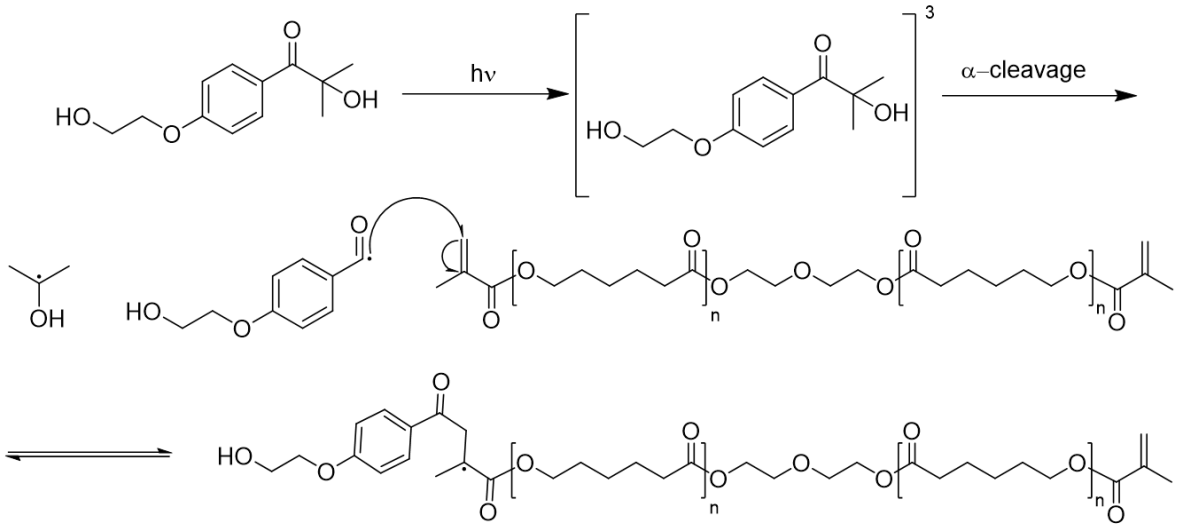


Figure 4.2: Reaction scheme of excitation of Irgacure-2959 to triplet excited state by UV light followed by α-cleavage. Example of how the radicals formed from this cleavage can interact with the acrylate terminal group of PCLDMA forming activated radical centres to enable photopolymerisation to continue between PCLDMA and HDDA, alike.

In relation to the crosslinking of PCLDMA with 1,6-hexanediol diacrylate (HDDA), a short chain acrylate capped monomer, the free radical polymerisation results in the formation of activated centres at the acrylate termini that are present in both HDDA and PCLDMA. This evokes polymerisation at this point. The radical centres can then interact with each other forming covalent bonds between the aforementioned acrylate terminal groups resulting in a solid, crosslinked network, as discussed further in **Section 4.2.1**.

PAOMEC, on the other hand, proceeds via thiol-ene photopolymerisation. This type of click chemistry that proceeds via a free radical mediated process, similarly to the previously discussed UV free radical polymerisation. The thiol functionality can be activated in a similar manner to the acrylate to form a thiyl radical. The propagation stage of this process sees a thiyl radical added to the carbon of the “ene” functionality. The hydrogen present is then abstracted from a different thiol group by

the radical at the activated carbon. This results in the formation of another thiyl radical. This continues until the termination of the process, as in **Figure 4.3**.[169] The reaction ceases in the termination step upon the radical quenching.[170] Thiols are different to the more conventional functionalities used in photopolymerisation like dimethacrylates, in that they are not sensitive to ambient conditions. As a result, more uniform crosslinked networks are expected to form in a more efficient manner.[171]

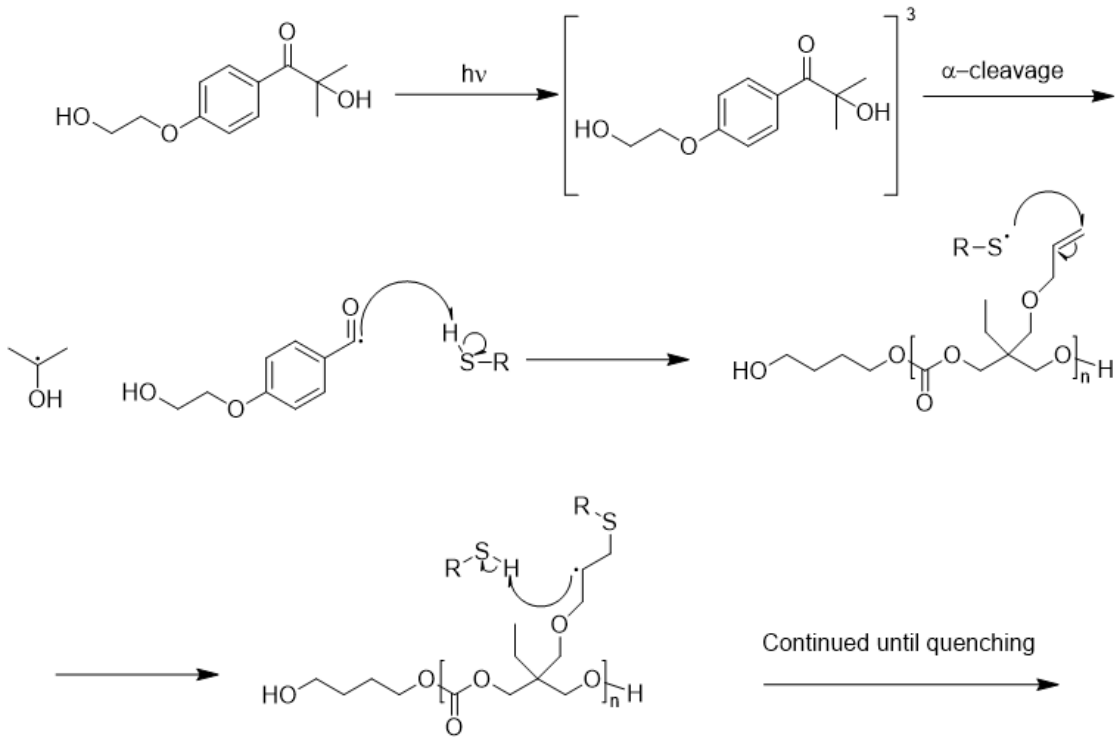


Figure 4.3: Free radical crosslinking example involving Irgacure-2959 as the PI, a thiol functionality and PAOMEC.

4.2 Crosslinking and Patterning of PCLDMA

4.2.1 Crosslinking of PCLDMA

Based on previous work completed by Dr Mark O'Loughlin in the Kelleher research group, the purified PCLDMA-1350 was mixed with HDDA and a PI, phenylbis(2,4,6-trimethylbenzoyl) phosphine oxide (PBPO), as in **Figure 4.4**. HDDA that was utilised in the photopolymerisation reaction, is a hydrophobic monomer that is liquid at room temperature, which made it a desirable material. It acted as a type of co-solvent for the waxy, white solid, PCLDMA, and was needed to increase the crosslinking density

of the materials. Adaptions were made to the original procedure reported; namely changing the preparation of the pre-crosslinking blend steps and use of a different PI. Irgacure-2959, as in **Figure 4.4**, was selected for use in the place of PBPO.[130]

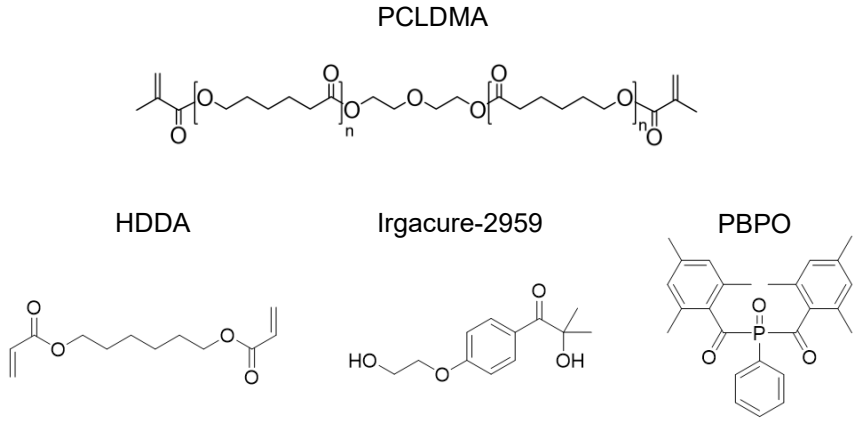


Figure 4.4: Reactants used for the fabrication of PCLDMA-based crosslinked materials, including short chain monomer HDDA and photoinitiators Irgacure-2959 and PBPO.

PBPO, also denoted BAPO in the literature, has a reported wavelength absorption band of 350 - 450 nm. As a result, radical generation in the photo-crosslinking process previously had been completed by the group using white light, which ranges in wavelength between 400 nm and 700 nm.[130,132] This required two hours of exposure, and it was hoped that by using UV light, the crosslinking process could be expedited. Irgacure-2959, despite having a reported absorption peak of approximately 260 nm, has still been shown to function in crosslinking processes when exposed to UV light at wavelengths of 365 nm.[172]

Secondly, biocompatibility of the PI was considered. PBPO has been demonstrated to be cytotoxic to mammalian cells. A study of seven PIs including PBPO, performed by Zeng et al., demonstrated the cytotoxicity of PBPO to a variety of cell lines to be the highest. An IC_{50}, a measure of concentration of chemical required to cause cell death of 33.58 μM with irradiation and 26.68 μM without irradiation was found for PBPO.[173] Another study by Kim et al. found that PBPO was cytotoxic to L929 cells, a fibroblast cell line, at concentrations of 25 μM and 50 μM.[174] Irgacure-2959 has been shown to be more biocompatible and has been used in various studies relating to biomedical applications.[175,176] One study demonstrated that a concentration of 22 mM of Irgacure-2959 was required to give cell viability less than 90% when exposed to Normal Human Dermal Fibroblasts cells.[177] Although no direct comparison between PBPO or Irgacure-2959 could be found in the literature, this value, when

compared to studies reported above, elucidated a 400-fold increase in the concentration of Irgacure-2959 required to cause cell death when compared with PBPO.

Despite the expectation that these PIs would completely decompose post exposure to the light source, as well as the low concentration present in the pre-crosslinking blend, it was decided to work with a more biocompatible PI like Irgacure-2959. This was desirable as it was planned to introduce different surface topography to these materials and perform cell testing with mammalian cell lines. As such, ensuring that the samples where chemically biocompatible was imperative to enable us to study the behaviour of the cells in response to the surface topography alone.

The liquid pre-crosslinking blend consisted of PCLDMA and HDDA at two different ratios; 1:4 and 1:9 PCLDMA:HDDA, specifically 20% PCLDMA and 80% HDDA or 10% PCLDMA and 90% HDDA w/w, respectively. These ratios were again selected to build on work completed by the group previously. The PI was dissolved in minimal acetone and was added to the PCLDMA:HDDA blend at a 1% w/w. Once activated, as previously discussed, the acrylate terminated PCLDMA and HDDA can form covalent bonds, as in the reaction scheme in **Figure 4.5**.

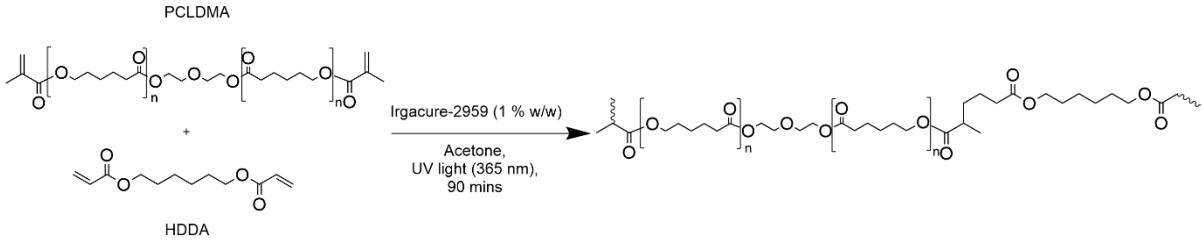


Figure 4.5: Reaction scheme for the crosslinking of PCLDMA with HDDA.

Once the crosslinking blend was created, the sample was mixed with a vortex mixer for 30 minutes followed by sonication for 30 minutes to remove air bubbles and ensure full dissolution of PCLDMA and PI. Once the pre-crosslinking blend was thoroughly mixed, a chamber for the crosslinking was set up, as illustrated in **Figure 4.6**. This chamber was made up of a glass slide or coverslip laid atop another glass slide, and polydimethylsiloxane (PDMS) was used to separate the two. The crosslinking blend was then introduced to the chamber, using a micropipette, and the sample was exposed to UV light at 365 nm wavelengths for a period of time.

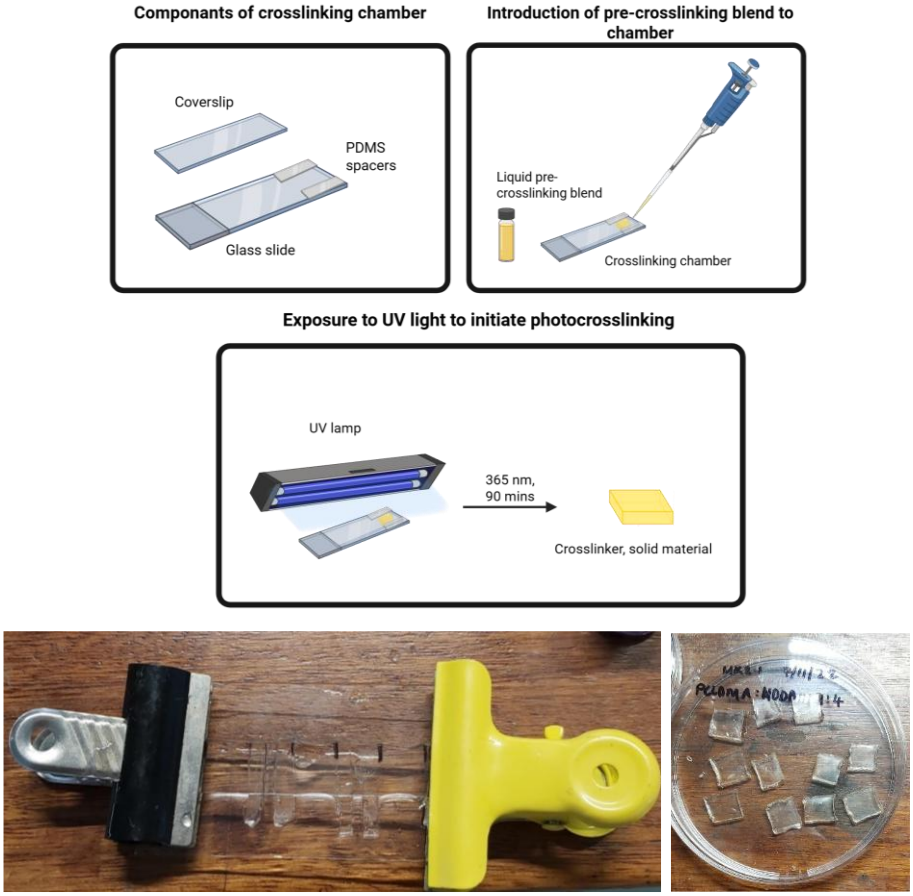


Figure 4.6: Illustration of components of the crosslinking chamber and crosslinking process (top) and images of the crosslinking chamber including grip clips used to secure the PDMS spacers between the glass slides as well as the resulting crosslinked samples.

PDMS is an elastomeric polymer which, when cured, remains stable when in contact with the PCLDMA:HDDA polymer blend. It was selected for use as a spacer in the crosslinking chamber as its curing process is both facile and controllable. Additionally, it's mechanical properties enabled a seal between the glass slide above and below the PDMS spacer. It is commonly used in research across many fields relating to engineering and biomedical applications.[178] The ratio of curing agent to base was kept constant at a 1:10 ratio but the elastic modulus of the material could be changed depending on the temperature and time selected for the curing process.[179] The thickness of the cured PDMS could also be adapted which, in turn, gave great control over the z-direction of the cured PCLDMA:HDDA. This enabled the tailoring of not only the x- and y-dimensions of the sample but also the z-dimensions which was important depending on the follow-on tests that were planned for the crosslinked samples. This control over the size and shape parameters of the

crosslinked materials is another example of the versatility provided by the replica moulding process.

The sealed nature of the chamber evoked capillary action - whereby the liquid, pre-crosslinking blend was pulled across the surface of the chamber due to the interaction between cohesive and adhesive forces. Capillarity has been used in the structuring and moulding of polymeric materials across a variety of soft lithography techniques including, “micro-moulding in capillaries (MIMIC)”, capillary force lithography and, as in this research, replica moulding.[180,180,181] It is a key consideration, especially when introducing new surface topography, as discussed later in this chapter.

Prior to introducing structures, the crosslinking reaction parameters required refinement. As such unstructured, hereafter denoted planar, samples of neat HDDA, 1:9 and 1:4 blends were crosslinked using the UVP Crosslinker 1000 L. The polymer blends were exposed to light at 365 nm for 120 minutes. Previous work, completed in the Kelleher group, found 120 minutes to be the optimal exposure time to ensure completion of crosslinking. Studies have demonstrated the acute toxicity of acylates. While HDDA is reported to cause significant long-term toxicity to aquatic life, methyl methacrylate has been shown to have a particularly high toxicity to humans, as it can be absorbed through the skin, causing death of animals.[182–184] For future cell testing, it was therefore imperative that the samples were fully crosslinked.

To confirm the success of the crosslinking reaction, FTIR analysis was performed. As observed in **Figure 4.7**, there were four main peaks of interest used to confirm successful crosslinking of the PCLDMA-1350:HDDA blends. Peaks at ~1635 cm^{-1} and 1620 cm^{-1} represented carbon-carbon double bond stretch of the terminal alkene groups, the peak at ~1407 cm^{-1} represented the carbon hydrogen terminal allyl alkane vibration and the peak at ~817 cm^{-1} represented the carbon-carbon double bond bend.

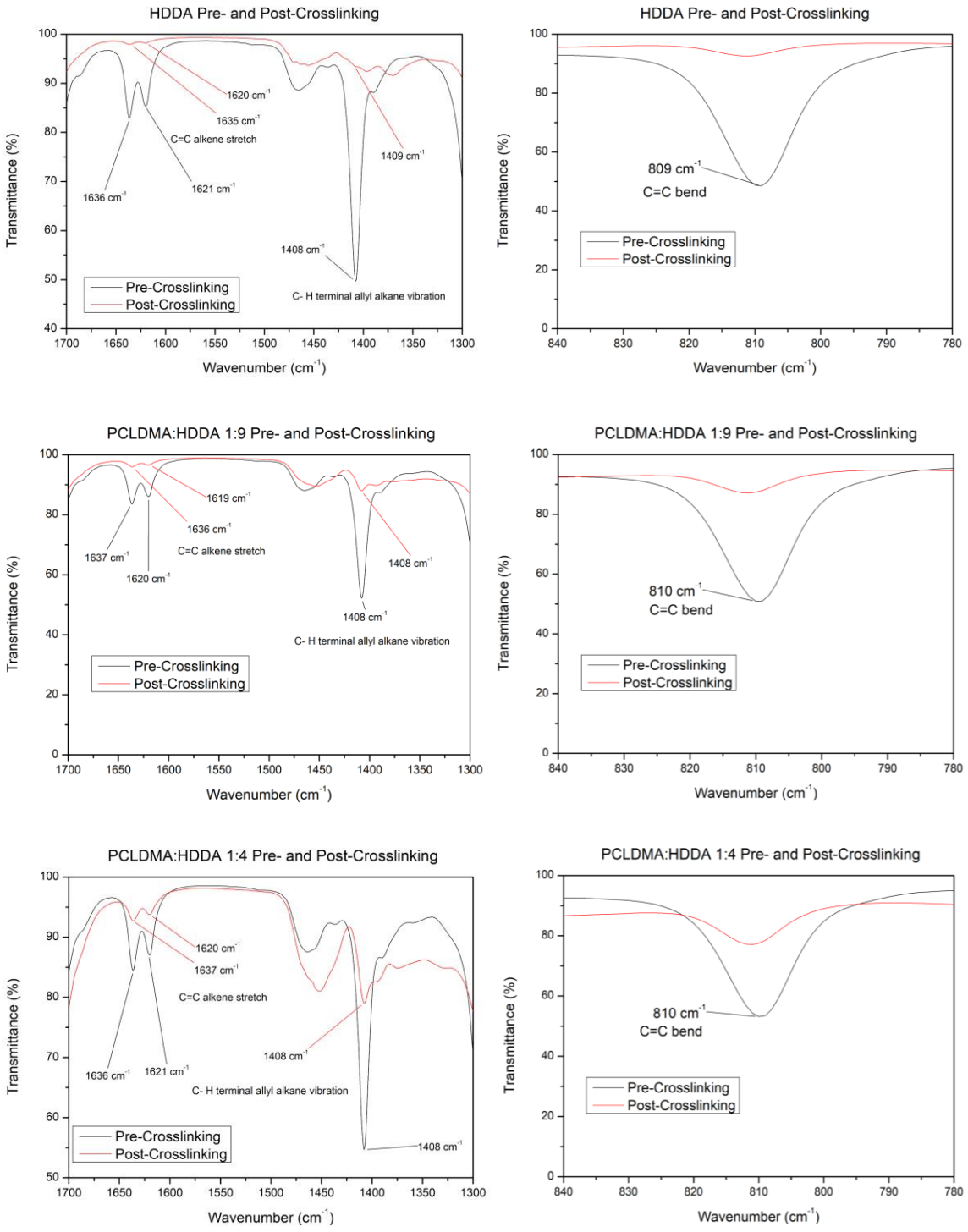


Figure 4.7: FTIR spectra of neat HDDA and PCLDMA-1350: HDDA 1:9 and 1:4 blends pre- and post-crosslinking for 120 minutes.

Once it was confirmed that the UV-initiated process was as successful as the crosslinking process completed using white light, attempts were made to shorten the time taken for the process. The cover slip or glass slide that was laid on top of the PDMS was replaced with Topas slides. Topas allows for high UV transmission

whereas glass slides have been observed to block some transmission. This is reported to be especially relevant at wavelengths below 300 nm but was found to still be of benefit at 365 nm.[185–187] The pre-crosslinking blends were then exposed to UV light for 60 minutes and 120 minutes. FTIR analysis was again performed to compare results, as can be seen in **Figure 4.8**. 60 minutes was shown to be sufficient for successful crosslinking to occur in relation to planar samples.

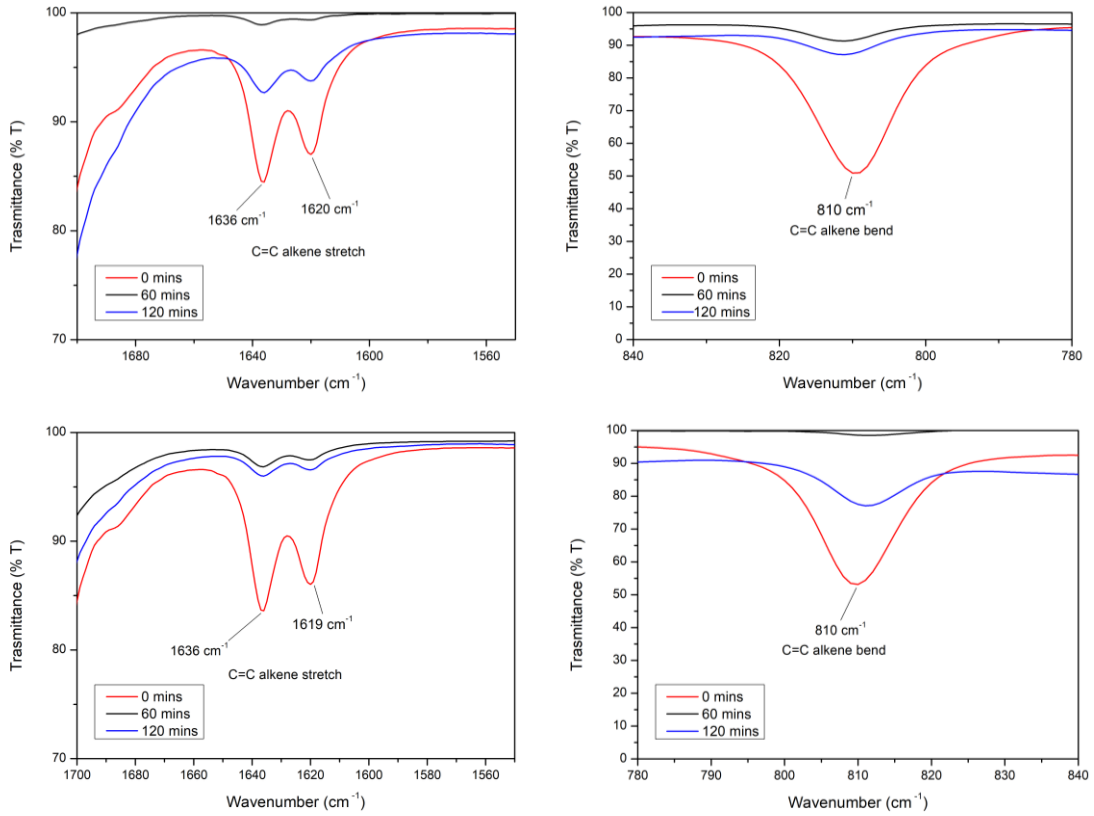


Figure 4.8: 1:9 (top) and 1:4 (bottom) FTIR spectra comparing exposure of samples to UV-light for 60 and 120 minutes.

The crosslinking of the shorter chain PCLDMA-630 was also analysed, as above. Crosslinking of planar samples was completed to ensure the procedure refined was still suitable for this shorter chain oligomer. Using FTIR analysis, successful methacrylation of the PCL Diol was confirmed. Comparison was also completed, as before, between pre- and post-crosslinking, as in **Figure B.1** in **Appendix B**. The disappearance of the O-H stretching peak of the primary alcohol group at 3436 cm^{-1} confirmed methacrylation of the PCL diol. Once methacrylated, non-crosslinked PCLDMA-630 was compared with non-crosslinked PCLDMA-630 mixed with HDDA

at a 1:4 ratio as well as a crosslinked sample of the same blend. As with PCLDMA-1350, the peaks corresponding to the two separate acrylate peaks were present prior to crosslinking and were not observed after exposure to UV light for 60 minutes.

The viscosity of both PCLDMA-1350 and PCLDMA-630 were analysed. The measure of a fluid's resistance to flow is defined as its viscosity. Liquids with a lower viscosity are observed to generally deform more easily when forces act upon them.[188] Previous research within the group has demonstrated that the PCLDMA (M_n 1250 g/mol) was unable to be replica moulded using nanostructures. As a result, pillars on the microscale were printed via similar replica moulding techniques.[130,132] It was possible to effectively replica mould on the sub-micron scale using HDDA, which was expected to have a lower viscosity than PCLDMA.[130] Low viscosity materials have a low cohesive energy between the molecules in the liquid as well as low frictional force between the blend and the walls of the cavity at the solid-liquid interface. These characteristics result in low shear stress which improves the extent to which a cavity is filled.[189] It was therefore thought that viscosity could be a consideration for improvement of structure uptake on the sub-micron size scale.

The viscosities of the PCLDMA samples with the two different molecular weights were measured, as displayed in **Figure 4.9**. Despite PCLDMA-630 being measured to be 15% less viscous, the addition of HDDA to both polymer samples was found to influence the viscosity in a way that made the measurements consistent across all ratios and both polymer samples.

WCA analysis was then completed with the crosslinked, planar samples. This technique was used to measure the hydrophilicity or hydrophobicity of the surface, by measuring the average angle of a water droplet on the surface of each sample. This was completed using PCLDMA-1350 and no difference was found between planar samples, made of pure HDDA when compared to 1:4 or 1:9 blends, as in **Figure 4.9**. Consistent results were observed upon completion of WCA analysis, with all samples being found to be hydrophilic, with WCAs below 50 º. This was in line with the conclusions drawn from the viscosity measurements, whereby the presence of HDDA is the predominant influence.

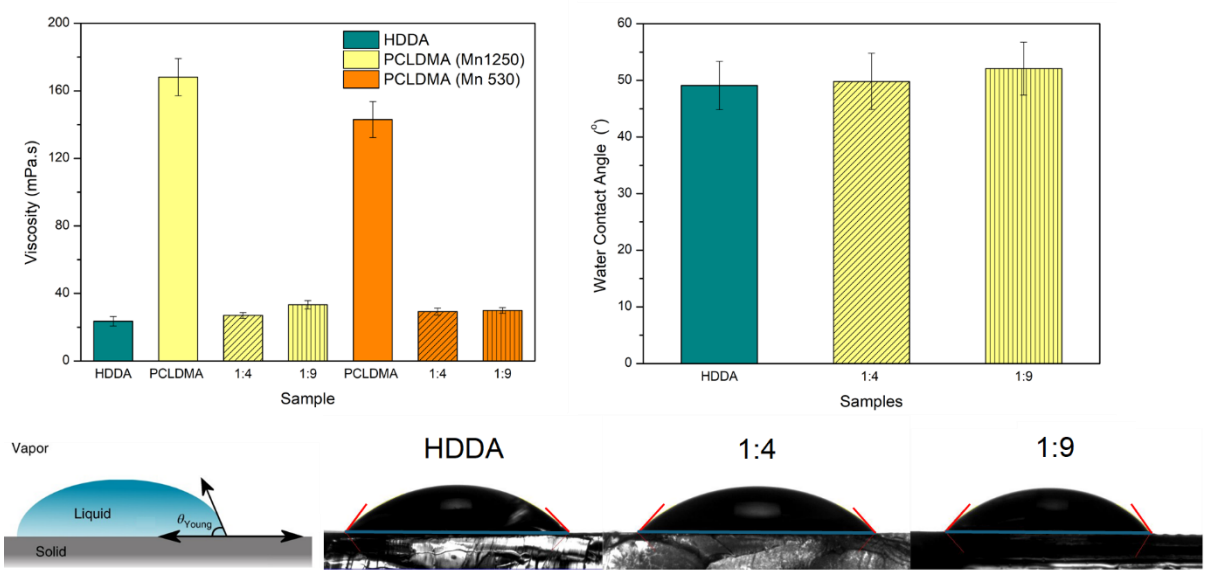


Figure 4.9: Viscosity (mPa.sec) measurements taken of both PCLDMA-630 and PCLDMA-1350 with different ratios of HDDA pre-crosslinking (top left); WCA measurements of planar, crosslinked samples using PCLDMA-1350 (top right); images taken from WCA measurements showing water droplets on each planar sample type demonstrating similarity across all three samples, with red lines illustrating the angles measured (bottom) and illustration of surface wetting characterisation between the vapour, liquid and solid interface giving the WCA, θ_{Young}, adapted from Huhtamäki et al. Error bars on both column charts represent the standard deviation.[190]

Planar samples of both PCLDMA-1350 and PCLDMA-630 were confirmed to be successfully crosslinked. After refining the crosslinking process, the next stage of the research was to introduce sub-micron structures to the crosslinked materials.

4.2.2 Crosslinking Structured Samples of PCLDMA

The introduction of surface topography to the crosslinked PCLDMA:HDDA blends could be completed by performing the replica moulding procedure as before, including a template in the crosslinking chamber from which a structure can be replicated. As in **Figure 4.10**, a liquid, pre-crosslinking blend was introduced to the template and exposed to UV-light. The resulting crosslinked material can then be used as a primary mould and the liquid, pre-crosslinking blend, in this case PCLDMA:HDDA, can be introduced to the primary mould and crosslinked as before. The secondary mould is thus an exact replica of the original template and is made from the desired material. The replica moulding method thus enables control over not only the final material but the various parameters of the surface topography including the pitch, width and height of the structures, as in **Figure 4.10**. The pitch of the structures is defined as the distance from the centre of one structure to the centre of the adjacent structure. For measurement and analysis purposes, discussed

later in this chapter, measurements of the pitch are taken from the edge of one structure to the same edge of the adjacent structure, as demonstrated by the arrow in **Figure 4.10**.

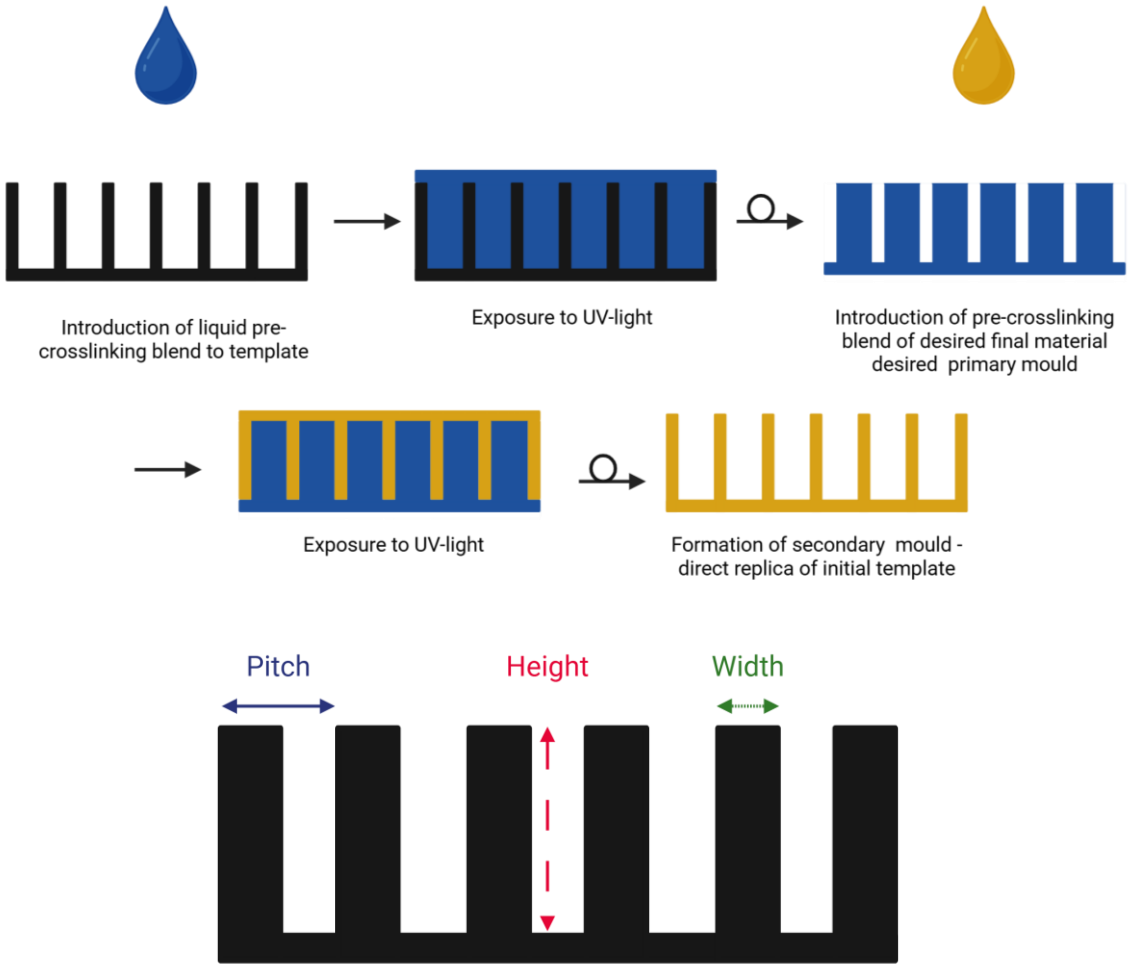


Figure 4.10: Illustration of side on view of the replica moulding process used to create structured, crosslinked materials (top); and the parameters of the structured materials that can be altered.

Initial training was completed using poly(propylene glycol) diacrylate (PPGDA) and poly(ethylene glycol) diacrylate (PEGDA) to learn the skills involved in the replica moulding process using structured templates. The process consisted of two stages, as depicted in **Figure 4.11**. The wings of a cicada, specifically the wings of the species *Tosena splendida blue*, were used as the primary template to improve replica moulding skills, as imaged in **Figure 4.11**. Replica moulding using this species and others, with PPGDA and PEGDA had been previously published by previous group members making it ideal for training purposes.[191–193] The wings were fixed to a base glass slide and a pre-crosslinking blend of PPGDA with PI Irgacure-

2959 (1% w/w) was used to make the primary mould while PEGDA with Irgacure-2959 (1% w/w) was introduced as the secondary mould.

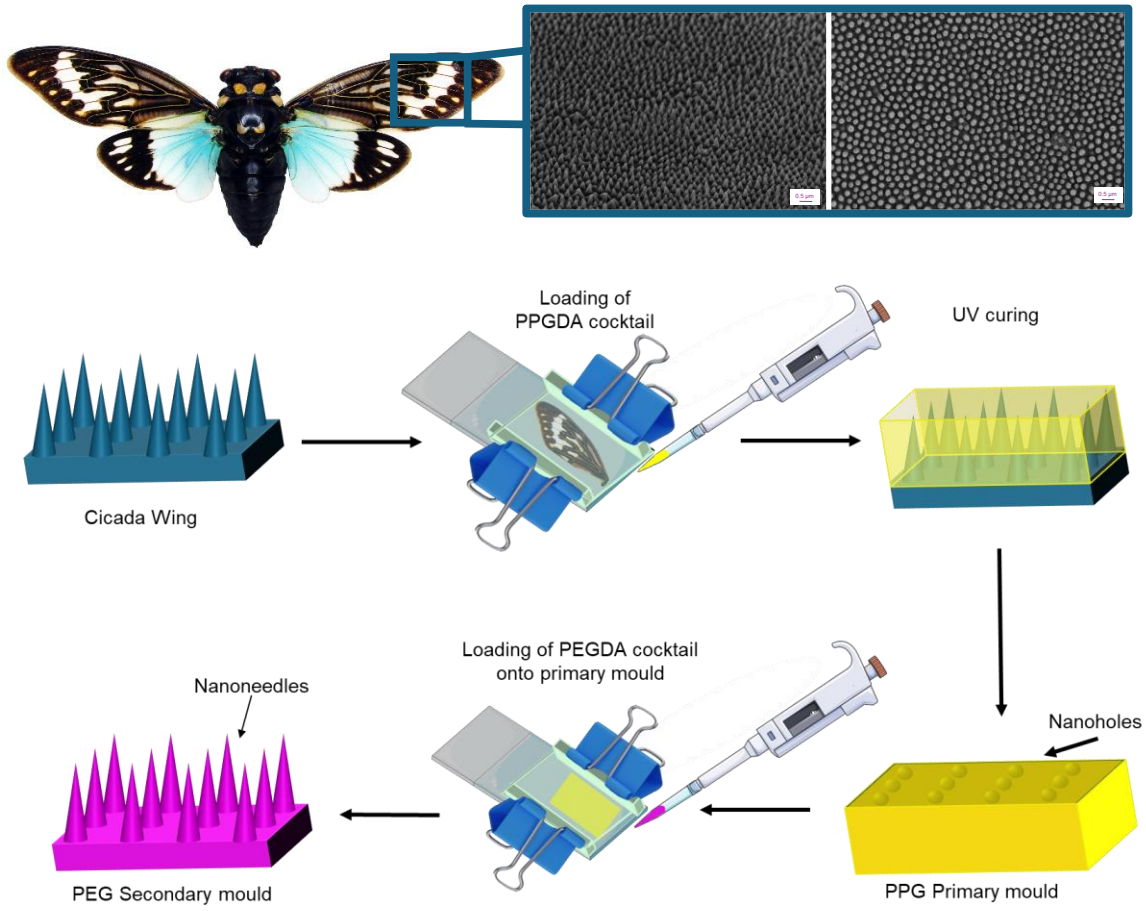


Figure 4.11: Image of Tosena splendida blue *cicada with zoomed in image of FESEM images taken from top-down and at a tilt (top); schematic of replica moulding process (bottom).*

Field Emission Scanning Electron Microscopy (FESEM) was performed to analyse the resulting primary and secondary moulds using Hitachi S5500 Field Emission Scanning Electron Microscope in the Nano Research Facility (NRF) in DCU. In general, scanning electron microscopy (SEM) is a form of analysis used to image the surface morphology of samples in a non-destructive manner. It functions through the detection of secondary electrons that originate from a focussed electron beam and are reflected by the sample. These secondary electrons, elucidate the surface morphology and can also be used to analyse surface topography and even composition with the use of energy-dispersive X-ray spectroscopy (EDS). Like SEM, FESEM functions by the same principles but gives higher resolution. This is due to

the higher intensity electron beam creating a smaller electron spot size on the sample.[194]

Samples were analysed in triplicate, with 50 data points taken from each image. Pitch was analysed by measuring the distance between three sub-micron structures, the gap between each microstructure was averaged from these measurements. The height measurements were made using a tilt feature on the Hitachi microscope. Comparison of the resulting height, pitch and diameter or width parameters of the structures was then be completed. Any significant differences between the original template and the replica would be indicative of poor fidelity. The samples, in this case, demonstrated issues with fidelity, as can be visualised in the column chart in **Figure 4.12.** The parameters measured showed significant differences when comparing the wing to the secondary mould. Attempts were made to perform the same process using the PCLDMA:HDDA blends.

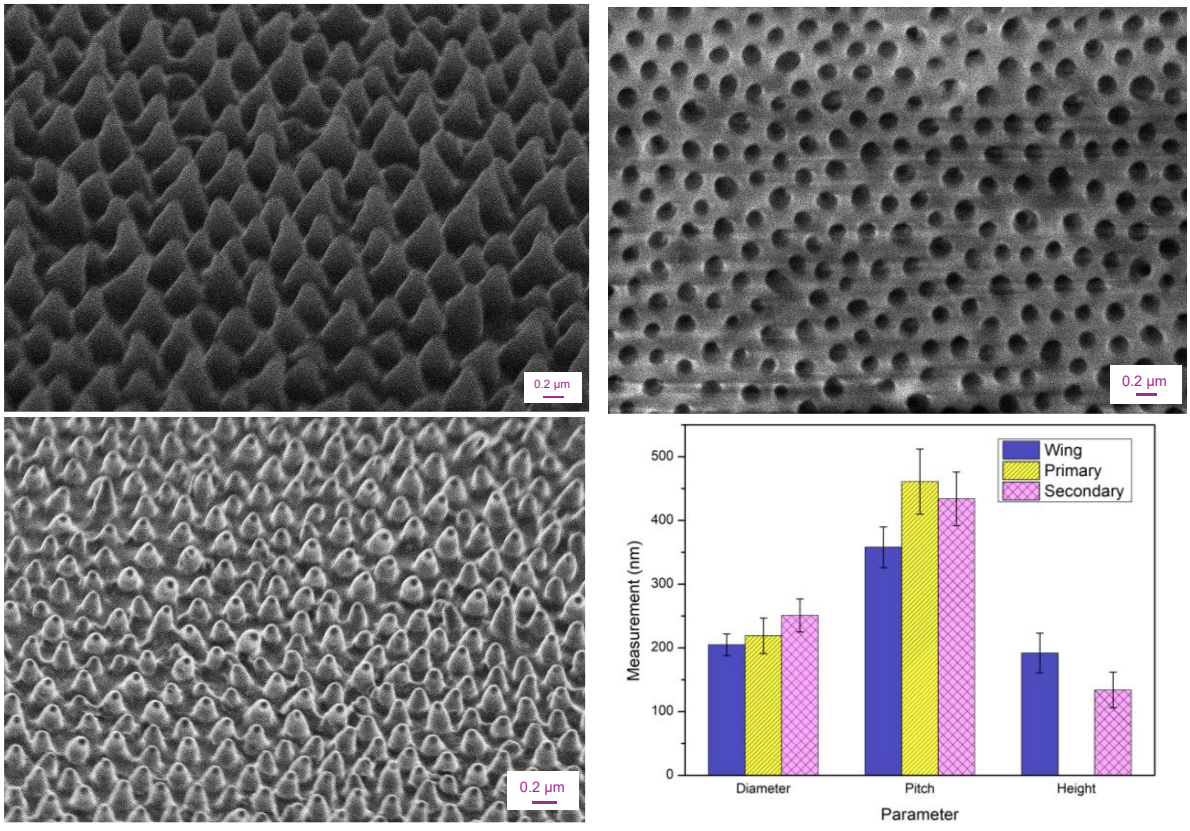


Figure 4.12: FESEM image of Tosena splendida blue *wing (top left), PPGDA primary mould with nanoholes (top right), PEGDA secondary mould with nanopillars (bottom left) and column chart of height, pitch and diameter measurements made. Error bars represent the standard deviation. All tilted FESEM images were taken at 40 ° tilts and scale bars are all 0.2 µm.*

The 1:4 and 1:9 PCLDMA:HDDA pre-crosslinking blends, using PCLDMA-630, were prepared as before, and the replica process and analysis was performed as above. In this case, PEGDA was used as the primary mould with the 1:4 and 1:9 blends used to make the secondary mould. The resulting secondary templates were compared to those achieved by PEGDA secondary moulds. The fidelity of the 1:9 blend was observed and measured, as can be seen in **Figure B.2** in **Appendix B**. The height differences of the nanostructures on both PEGDA and 1:9 PCLDMA:HDDA moulds, when compared, were shown to not be statistically significant. This demonstrated good consistency in relation to replica moulding secondary moulds with different materials. The measurements taken for the pitch varied most significantly from the *Tosena splendida blue* wing template.

Despite working at a low electron voltage of 1 to 2 kV and coating the wing sample in a thin layer of gold, which is a common practice used for creating a more conductive sample to minimise issues, charging of the wing samples was still observed. Charging is a common problem faced in electron microscopy, especially with non-conductive samples, which can result in charge build-up due to the interaction between the electron beam and sample.[195] These charging effects have been reported to impact the accuracy of measurements taken of structure shape and dimensions.[196] This loss in resolution may account for the smaller pitch lengths measured on the wing template. Further investigation was not carried out as both the PEGDA and 1:9 secondary templates had comparable pitches. As such, the 1:9 was concluded to have been moulded from PEGDA primary template to a satisfactory level, when compared to previous PEGDA secondary moulds. This was a promising result, but the same results were not found for 1:4 blends. As in **Figure B.2** in **Appendix B**, the nanopillars appeared to fall onto each other. This is likely due to the reduced HDDA , which resulted in reduced crosslinking density. This would correspond to less rigid samples thus leading to collapse.

A synthetic template was decided upon for use for future research and applications. Damage to the wing, either during the lifespan of the cicada or its drying and packaging, commonly causes areas of the wings to have little to no nanopillars present, as in **Figure B.2** in the **Appendix B**. To enable reproducibility and consistency at this stage of the process across all samples a structured silicon template, hereafter T1, was selected for use for further work with PCLDMA blends.

This silicon sample was structured by Thundernil, a company based in Italy using nanoimprint lithography, as illustrated in **Figure 4.13**.[197] This method involved spin coating a silicon template with a polymer photoresist. This polymer layer was as thick as the desired final height of the structures on the template. A stamp with the desired final structure was then pressed into the photo resist. The sample was then heated and after applying pressure the master stamp was removed. The photoresist acts as a mask for the silicon and is etched off using a gas mixture of sulfur hexafluoride and perfluorocyclobutane. This process was used to create a silicon template patterned with an array of lines, imaged and analysed using FESEM. The lined pattern of T1 had a pitch measuring 800 nm, structure width of 400 nm and structure height measuring 600 nm. These sub-micron structures had an aspect ratio of 1.5 and the pattern area measured 10 mm x 10 mm, as imaged in **Figure 4.13**.

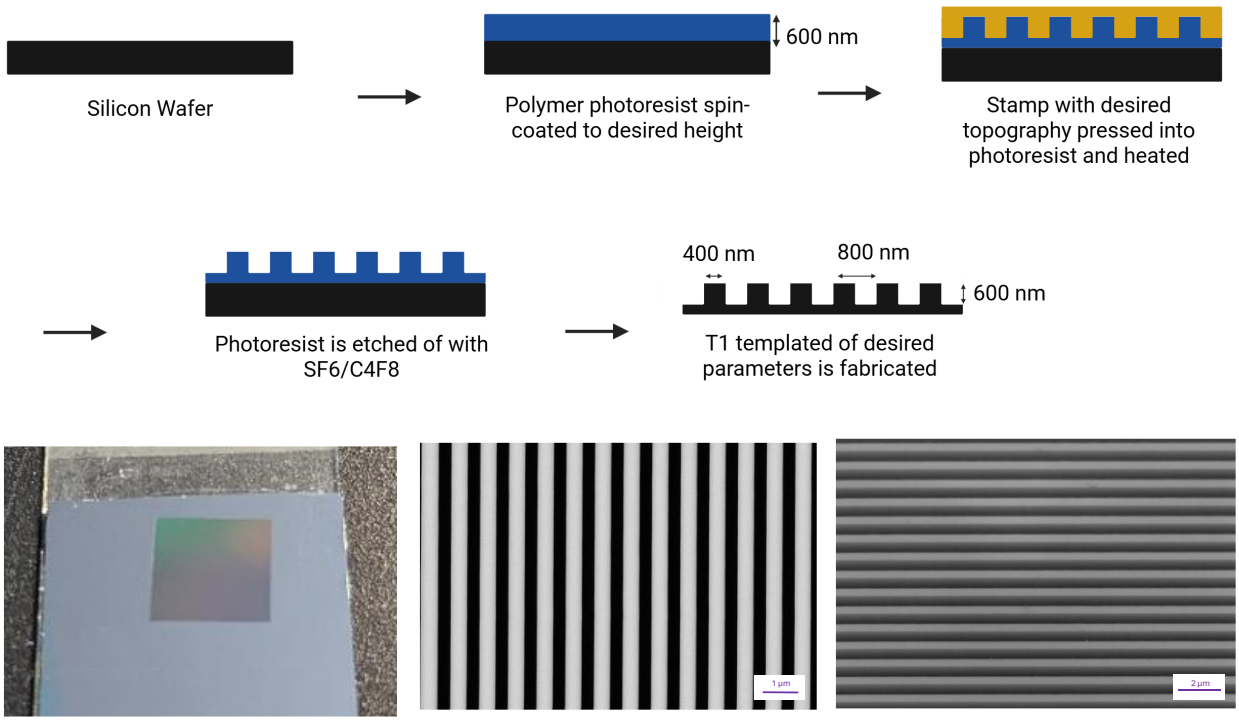


Figure 4.13: Illustration adapted from of NIL process to create T1 (top); image of iridescent, patterned 10 mm x 10 mm, T1 silicon template (bottom left); FESEM image of lined structure with 1 µm scale bar (bottom centre); FESEM image with 2 µm scale bar (bottom right).

As mentioned previously, the gap between structures on micro- and nano-structured surfaces has been observed to be as influential in the antibiofouling properties of a surface as the structure itself. This T1 template was selected due to its sub-micron features, specifically the 400 nm gap between the lines as well as the 400 nm width

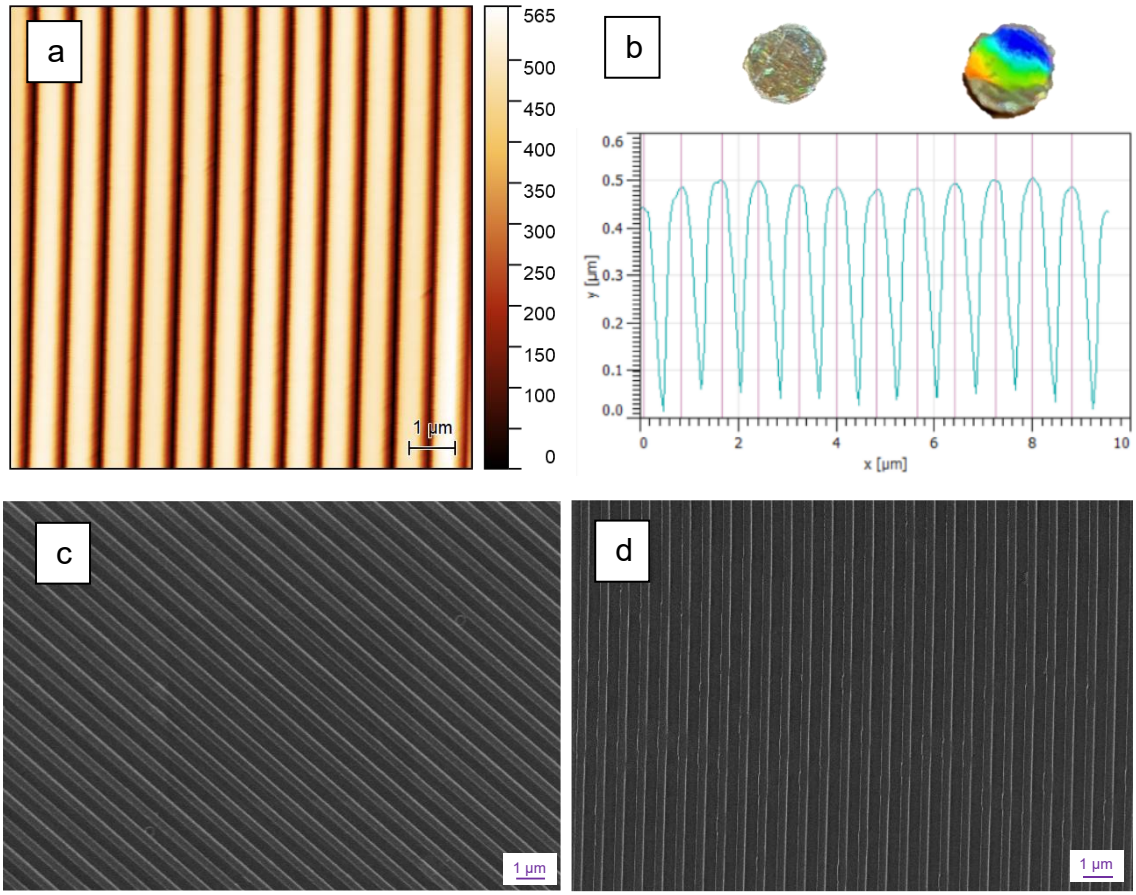
of the lines. Due to the width of most bacterial cells being between 0.2 μm and 1 μm, it was desirable to have a gap or channel with a width smaller than this. Gu et al. demonstrated that narrowing of the width of the line structures resulted in reduced cell attachment and cell alignment along these structures.[198] Furthermore, Hou et al. discussed the preference of *E. coli* to adhere to the gaps between structures rather than on the structures themselves regardless of structure size demonstrating the importance of narrow gaps. Cell-to-cell interaction was also theorised to be a key factor in the formation of a multi-layered biofilm. Creating patterned surfaces that prevent this by not allowing space for such interactions was, therefore, decided to be advantageous for antibiofouling purposes.[199] As a result, future work with all materials including the PCLDMA:HDDA blends was performed using this T1 template.

Despite the success of the 1:9 ratio that utilised the shorter chain PCLDMA-630 in replica moulding nanopillars, PCLDMA-1350 was elected for investigation and crosslinking with the T1 template first. This research hoped to build on previous work that was already completed using this longer chain oligomer. The stability and rigidity offered by the linear sub-micron surface topography in comparison to the nanopillars was also theorised to reduce the chances of structural collapse, as had been previously observed.

Originally, PEGDA was used as the primary template, as before, which was in turn moulded from using the PCLDMA blends. At times, difficulty was faced in separating the PEGDA primary mould from the PCLDMA secondary moulds. As such, it was decided that both the 1:4 and 1:9 blends would be crosslinked directly from the T1 template. The samples were set up in the crosslinking chamber, as before, and the exposure to UV light was extended to 90 minutes due to the presence of the impermeable silicon template. Preliminary observations of both blends post-crosslinking showed that structures were being taken up by both ratios. This was indicated through the iridescence, visible by eye, on the samples and the linear array was that was observed via digital microscope imaging at 40X magnification. It was decided to perform a more in-depth analysis of the 1:4 crosslinked samples from this point. The 1:4 samples were selected due to the increased ratio of PCLDMA present, improved consistency of this blend during the crosslinking process and its reported increased degradability. Previous alkaline degradation studies in the Kelleher

research group had demonstrated that ester hydrolysis was the most likely major degradation pathway for these crosslinked networks and increased degradation rates were observed for 1:4 blends.[130]

These samples were analysed using FESEM to measure structure width and pitch. Atomic force microscopy (AFM) was utilised to measure sample height. The basic principle of AFM involves using a scanning probe and a sharp tip at the end of a cantilever. The tip is scanned over the surface of a sample and as it moves over structures on the surface, there is a change in the position of the cantilever. This change is measured by a laser beam, thereby enabling the quantitative and qualitative analysis of surface features.[200,201] FESEM analysis of the 1:4 crosslinked samples, as in **Figure 4.14**, confirmed good fidelity of the crosslinked samples. The widths of the structures measured were found to have undergone 1% shrinkage when compared to the T1 template. The height and pitch of structures achieved during the replica moulding were slightly lower than the previously measured height of the T1 template. There was an approximate 14% difference when comparing the T1 template to the PCLDMA:HDDA 1:4 mould. However, this level of shrinkage has been reported in relation to acrylate crosslinking, so was considered to be within the margin of error for this type of crosslinking process.[202,203]



PARAMETER	SILICA MEASUREMENT (NM)	1:4 PCLDMA:HDDA MEASUREMENT (NM)
STRUCTURE WIDTH	440 (± 17)	378 (± 20.6)
PITCH	801 (± 25)	791 (± 35.8)
STRUCTURE HEIGHT	591 (± 22)	509 (±18.0)

Figure 4.14: Image of 1:4 mould from T1 taken by AFM (a); graph of the peaks measured by AFM below images of the crosslinked sample with light used to elucidate the iridescence (b); top down FESEM images taken of 1:4 samples (c and d); table of the averages and standard deviations of the measurements of T1 (provided by ThunderNil) and of PCLDMA:HDDA from the analysis completed. Scale bars for all images are 1 µm.

Outside of acrylate shrinkage, other factors can also influence the fidelity of replica moulds. As previously mentioned, capillary action is a force applied in the replica moulding process. Laplace pressure is the primary force influencing the capillary action that draws the liquid of the pre-crosslinking blend through the structures and therefore dictates the fidelity of the obtained mould. As such, the channel width, surface energy of the 1:4 blend and contact angle between the 1:4 blend and the silicon template all factor into the success of the replica moulding. In a case like this, where an impermeable mould was used, air can get trapped preventing capillary rise in a closed channel, thus limiting the height of the structure that can be achieved.[204]

The features measured using AFM can also be affected by many factors that influence the interaction between the tip and the sample surface. These can include the scan rate used to take measurements, the tip shape and side wall angles of the structures on the sample, to name a few. As can be observed in the sharp peaks measured in the graph in **Figure 4.14**, possible trench reduction was observed, whereby the gap between two structures differs at the base of the structures compared to the top of the structures. Due to the steep sidewall angle expected, based on the T1 structure, as well as the narrow structure width and inter-structure gapping, the resulting measurements of the height of the structures may also be affected due to the difficulty for the tip to reach the base of the structures.[205]

That being said, the low standard deviation of the measurements taken demonstrated preciseness of the data and the high reproducibility of the replica moulding process. There was also no observed structural collapse as had previously been reported with sub-micron structures made using the 1:4 PCLDMA:HDDA blend. The loss in structure height was also not anticipated to affect the planned cell testing as, at this scale, the influence of structure width and pitch were of more interest. The samples were thus satisfactory for future use in cell testing. The samples, once sufficiently analysed, were shaped using a 6 mm hole punch to create circular samples to fit the wells of a 96-well plate, as in **Figure 4.15.** This was required for the mammalian cell testing that is discussed in **Chapter 5**.

Prior to commencing crosslinking and structuring studies with the previously discussed silicon template, T1, a degradation study was commenced as per the International Organization for Standardization (ISO) and ASTM international. Specifically referenced for this study, was the biological evaluation of medical devices - Part 13: Identification and quantification of degradation products from polymeric medical devices (ISO 10993-13:2010) and Standard Test Method for in vitro Degradation Testing of Hydrolytically Degradable Polymer Resins and Fabricated Forms for Surgical Implants (F1635-24).[206,207] PCL is already a well-established biodegradable polymer and has found use in various biomaterials as a result.[208] Investigation into the degradation of the crosslinked materials was required to ensure the crosslinked samples were still degradable in biological conditions despite the presence of HDDA. The accelerated degradation test was performed at 70 ± 1 ºC in PBS with pH of 7.41. Samples were left in glass vials with a 1:100 w/v

ratio of sample to PBS buffer. The samples remained in an incubator for the duration of the experiment. For analysis, samples were only removed in triplicate, at three time points: 2, 30 and 60 days. The 1:9 ratio was selected to be studied as it had the highest percentage of HDDA, which was deduced to be the limiting factor in the degradation of said materials. Mass loss analysis was used to measure degradation, as in **Figure 4.15**.

The samples were concluded to slowly degrade over time. This conclusion was based on visual observations and through mass loss measurements. The samples were observed to yellow as they degraded. This is a common observation that has been reported across many polymer materials as they are degraded by UV light, heat or chemicals.[209–211] Specific to PCL, the cleavage of the ester bonds during the degradation process, resulted in the production of chromophore functional groups such as carboxyl and carbonyl groups.[212] Due to indications based on previous studies performed in 5 M sodium hydroxide (NaOH), it would be expected that increased degradation rates would be observed with the increased percentage of PCLDMA present in 1:4 blends, but future degradation studies with 1:4 blends are planned.[130,132]

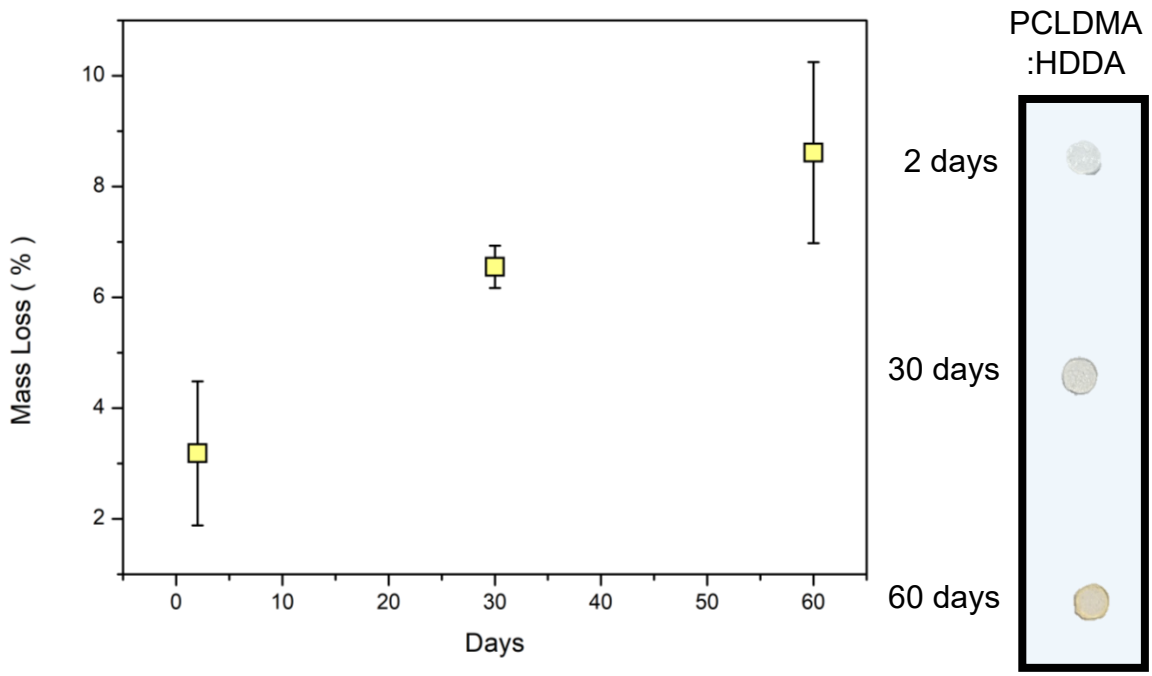


Figure 4.15: Scatter plot for percentage mass loss of 1:9 samples at three times points (left). The error bars are representative of the standard deviation. Image of one example of each sample at each time point showing yellowing as degradation continues (right).

FTIR and DSC analyses were completed on the degraded samples at each time point, as in the **Figure B.3** in **Appendix B**. No distinct differences between the samples were measured or observed but due to the low percentage mass loss from the samples, this was not unexpected.

PCLDMA-1350 and PCLDMA-630 were used to successfully crosslink planar and structured materials with a sub-micron surface topography. The replica moulding technique was refined and the use of silicon template T1 was studied. Successful replication of 1:4 PCLDMA-1350:HDDA moulds was completed and measured using FESEM and AFM techniques. Samples were then shaped and prepared for cell testing. Degradation studies were conducted in an accelerated approach confirming the PCLDMA:HDDA blend to be degradable under biological conditions.

4.3 Crosslinking, Functionalisation and Structuring of PAOMEC

4.3.1 Preliminary Crosslinking and Functionalisation of PAOMEC

Successfully polymerised and purified oligomer PAOMEC was utilised for crosslinking studies. The pendent alkene functionality in the repeating unit of the oligomer chain was ideal for UV-initiated photopolymerisation. Further to this, functionalisation of the crosslinked network was made possible via the addition of short chain functional groups through thiol-ene click chemistry, as previously discussed. Through this process, short chain functional groups with thiol caps could be introduced into the pre-crosslinking blend to functionalise the crosslinked material. Functionalities such as carboxylic acids and amines can be used to introduce anionic or cationic charges, respectively, to the surfaces of materials. The focus of this stage of the research was to create a crosslinked surface with the same backbone that could be tailored to have differing surface charges or topographies in a controllable manner. This would enable like with like comparison of the surfaces. These surfaces could then be utilised to investigate the influence of the altered properties, independently or combined, to understand their role in preventing biofilm formation.

The first step in this crosslinking process was to investigate whether this material could be crosslinked in a similar manner to the PCLDMA:HDDA blends. This was completed by mixing the PAOMEC with a tetra-thiol crosslinker, namely

pentaerythritol tetrakis(3-mercaptopropionate), hereafter SHX. Irgacure-2959 was used as the PI once again and was dissolved in minimal acetone.

Despite being liquid at room temperature, the PAOMEC was too viscous to be introduced to the crosslinking chamber using a micropipette. As such, a decision was made at early stages of refining the pre-crosslinking blend to add propylene carbonate (10% w/w) to the mix. Propylene carbonate is an organic co-solvent that was used to lower the viscosity of the pre-crosslinking blend. Based on previous work completed by Dr Anthony Thomas, it was successfully used to solubilise PAOMEC and sufficiently lower the viscosity for 3D printing purposes.[41] Preliminary crosslinking studies were conducted to investigate the effect of the crosslinker ratio present in the network. The amount of crosslinker required was calculated as per the equations in **Figure 4.16**. The moles of allyl groups present in the PAOMEC oligomer was measured based on the degree of polymerisation and molecular weight of the oligomer, as per GPC estimations. Once calculated a ratio could be calculated between the SHX and PAOMEC.

$$Moles\ of\ allyl\ groups\ present = \frac{weight\ of\ PAOMEC\ sample}{Molecular\ weight\ of\ PAOMEC}\ x\ degree\ of\ polymerisation$$

$$Moles\ of\ SHX\ required = \frac{moles\ of\ allyl\ group\ present}{4\ (due\ to\ the\ four\ thiol\ points\ of\ contact\ on\ SHX)}\ x\ desired\ ratio\ of\ SHX$$

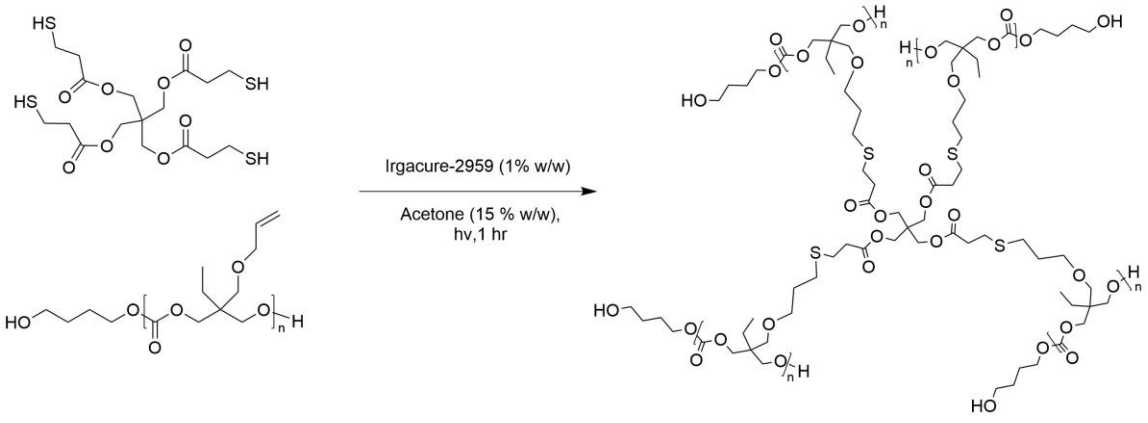


Figure 4.16: Equations used to calculate the moles of allyl groups present followed by moles of SHX required (top) and crosslinking reaction of PAOMEC and SHX (bottom).

The SHX was introduced to the pre-crosslinking blend at 1:10, 1:4, 1:2 and 1:1 molar ratio with respect to the allyl functional group. Successful crosslinking was observed for all four blends. At 10% SHX, the crosslinked material gave a stickier, gel-like consistency. With increasing SHX in the crosslinked network, the rigidity of the material increased. The 1:1 ratio was thus selected as it was required to minimise the presences of any unreacted alkene groups.

Once a 1:1 molar ratio of allyl groups on PAOMEC to free thiol groups on SHX was decided upon, selection of the UV exposure time was analysed. The ratio analysis was completed using a 90-minute exposure time. As previously mentioned however, thiol-ene chemistry is often more efficient than photo-crosslinking with dimethacrylate groups alone. As such, it was thought that 90-minute exposure may have been excessive. Exposure for 30 minutes left unreacted liquid pre-crosslinking blend visible, so as a result 60 minutes was attempted. There was no obvious sign that the crosslinking process had not been completed upon visual inspection. Follow-up analysis was completed using FTIR spectroscopy. It was confirmed, as in **Figure 4.17**, crosslinking had been completed in this timeframe, due to the disappearance of the peaks corresponding to the sulfur hydrogen stretch in a thiol bond at 2558 cm^{-1} in SHX, as well as the stretch of a carbon-carbon double bond of the free alkene in PAOMEC at 1636 cm^{-1} and 1580 cm^{-1}. This was the first time PAOMEC materials had been crosslinked in this manner.

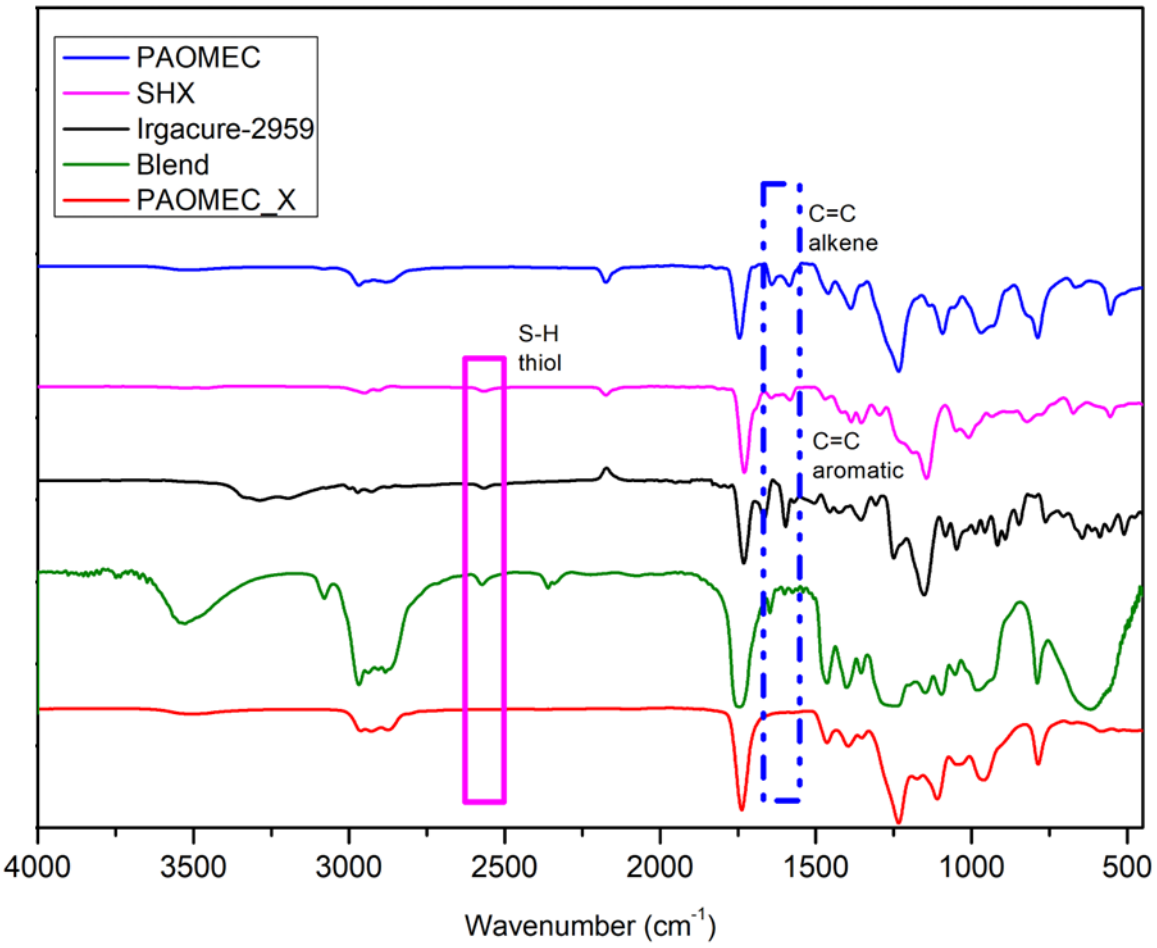


Figure 4.17: FTIR analysis of crosslinking process showing of reactants in the pre-crosslinking blend separately and combined and the post-crosslinking PAOMEC sample.

Functionalisation of the planar materials was then commenced upon successful refinement of the crosslinking process. The aim of this functionalisation was to introduce cationic and anionic surface charge to the crosslinked material. Two short chain chemicals, namely cystamine dihydrochloride and 3-mercaptoproprionic acid, were to be used to achieve this, as in **Figure 4.18**. 3-mercaptoproprionic acid, is a sulfur-capped, short chain chemical that was intended to add carboxylic acid functionality to the crosslinked PAOMEC sample. For antibiofouling purposes, a lot of promise has also been shown with anionic surfaces. The surfaces of bacterial cells have a negative electrostatic charge. This is due to the ionized phosphoryl and carboxylate groups present.[106] There is evidence of electrostatic repulsion between negatively charged surfaces and bacteria thereby improving the antibiofouling properties.[213] Rzhepishevska et al. have reported the presence of anionic charge not only resulted in a reduction in biofilm formation, but also saw the shape of the biofilm that did form differ due to the negative surface charge.[108]

Cystamine dihydrochloride was introduced as the source of a positive charge due to the presence of the amine groups. Studies have observed the bactericidal activity of cationic charges.[214,215] The electrostatic interaction between negatively charged bacteria and cationic surfaces was of interest to study, especially in comparison to a negatively charged sample surface which would be expected to repel bacteria via electrostatic interactions. The use of the same oligomeric backbone and thiol-ene bond process was thus believed to provide a suitable opportunity to compare the influence of both charges on the antibiofouling properties of a surface.

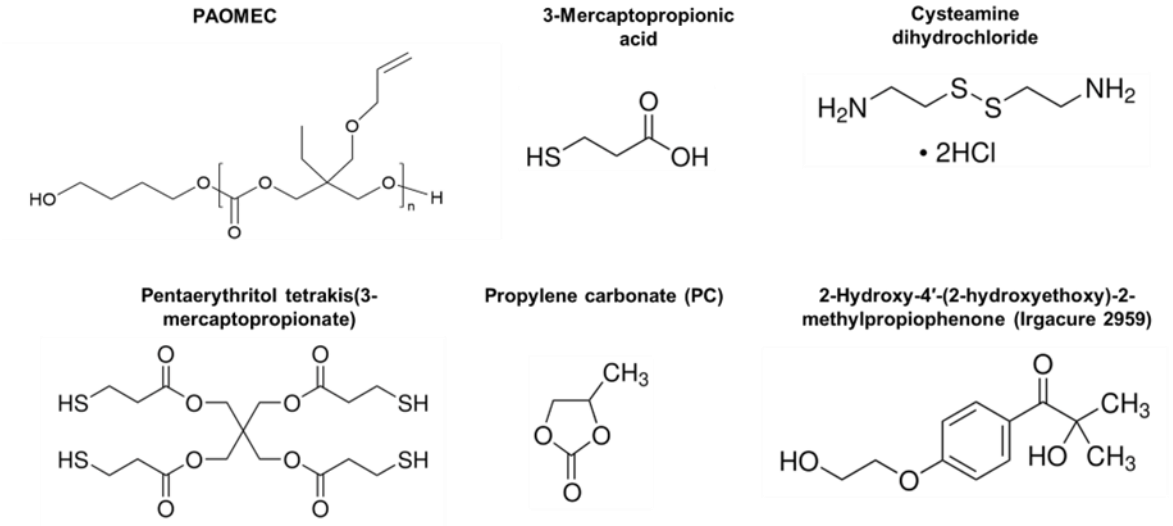


Figure 4.18: Reactants planned for use in crosslinking of PAOMEC and functionalisation of the crosslinked networks.

Based on the PAOMEC:SHX ratio analysis completed previously, it was decided to try to incorporate the amine salt, cystamine dihydrochloride, and the 3-mercaptopropionic acid utilising a 1:4 ratio of PAOMEC:SHX. The 10:1 ratio had too little crosslinker resulting in a malleable, gel-like sample while all other ratios investigated, namely 4:1, 2:1, 1:1, gave materials with satisfactory consistency. It was, thus, decided to commence initial functionalisation studies with the 4:1 ratio to maximise the surface charge density, as this suggested that 25% of available allyl functional groups would be reacted with the SHX, leaving 75% to interact with the amine salt. The introduction of 3-mercaptopropionic acid, clear, colourless liquid was straight forward, in that it was simply added into the pre-crosslinking blend, as before. However, there were more challenges faced with cystamine dihydrochloride.

The introduction of cystamine dihydrochloride to the pre-crosslinking blend and its subsequent exposure to UV light was expected to result in the degradation of the

disulfide bond. Similar reactions have been reported wherein disulfide bonds undergo radical cleavage, in response to carbon centre radicals that have been generated, in this case, by the presence of Irgacure-2959. Following this, thiyl radicals are predicted to enable bond rearrangement terminating in the formation of sulfur carbon bonds between the PAOMEC backbone of the crosslinked network and the cyteamine.[216]

Immediate solubility issues were faced with cystamine dihydrochloride as it was found to be insoluble in the pre-crosslinking blend. Further solubility tests were performed with acetone and propylene carbonate but were also unsuccessful. It was found that additions of 10% to 15% w/w of water to the pre-crosslinking blend enabled full dissolution of the cystamine salt. As before, to ensure a homogenous mixture, the pre-crosslinking blends were originally stirred using a vortex mixer and then sonicated for 15 minutes to aid dissolution of any remaining reagents. However, the reactivity of the cystamine dihydrochloride was observed to prematurely and uncontrollably crosslink during these steps. Based on the literature, it was thought that thiol-disulfide exchange maybe occurring, as in **Figure 4.19**. This reaction involves the breaking of the disulfide bond through attack of said bond, by the free thiol group, in this case present on SHX. Sulfur acts as the nucleophile, electrophile and leaving group in the displacement reaction.[217,218] Post-mixing and sonication, gelation was observed to have occurred, as in **Figure 4.19**.

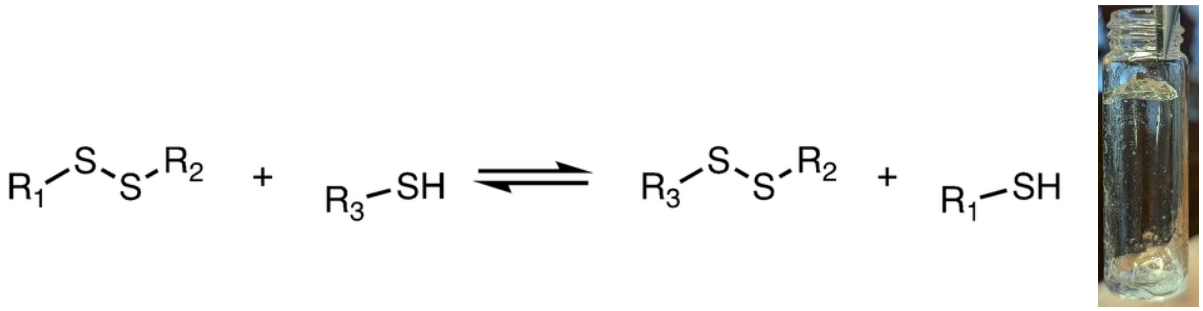


Figure 4.19: General reaction for reversible disulfide exchange adapted from Davis et al. and image of pre-crosslinking blend containing cystamine dihydrochloride that has undergone uncontrolled gelation.[219]

Both sonication and vortex mixing times were reduced to as low as three minutes each, to prevent this side reaction from occurring prematurely. Even at this, in the short time taken to pipette the solution into the crosslinking chamber, the pre-crosslinking blend began to react in the glass vial. It was decided, at this point, to

add all reactants to the glass vial prior to the SHX crosslinker. SHX was only added and manually stirred immediately prior to the pipetting process. This allowed more time to add the blend into the crosslinking chamber. The crosslinked samples were then utilised in a preliminary swelling test, as in **Figure 4.20**. The main aim of this test was to ensure the samples were not significantly affected by the deionised water they were submerged in.

Loss of mass was observed in the non-functionalised PAOMEC sample, PAO_X, and carboxylic acid functionalised sample, hereafter PAO_COOH. NMR analysis, as in **Appendix B** in **Figure B.4**, demonstrated that the propylene carbonate that was used in the crosslinking process but not covalently attached to the crosslinked network was present in the deionised water post-soaking. This was determined to be the most likely cause of the loss in mass measured.

The pre-crosslinking blend used to make PAO_X samples with the 1:1 PAOMEC:SHX molar ratio and Irgacure-2959 (1% w/w) dissolved in acetone (15% w/w) was found to be of a low enough viscosity to not require propylene carbonate. The same was found for the PAO_COOH pre-crosslinking blends. Due to the viscosity of the SHX being lower than that of PAOMEC, as illustrated by the column chart in **Figure 4.20**, and the presence of acetone which has 0.32 mPa.sec at 20 °C, the propylene carbonate co-solvent was removed from the pre-crosslinking blends.[220] This, in turn, removed any possibility of this solvent leaching from the samples during the planned cell testing which had previously been theorised as a possible issue and is discussed further in **Chapter 5**.

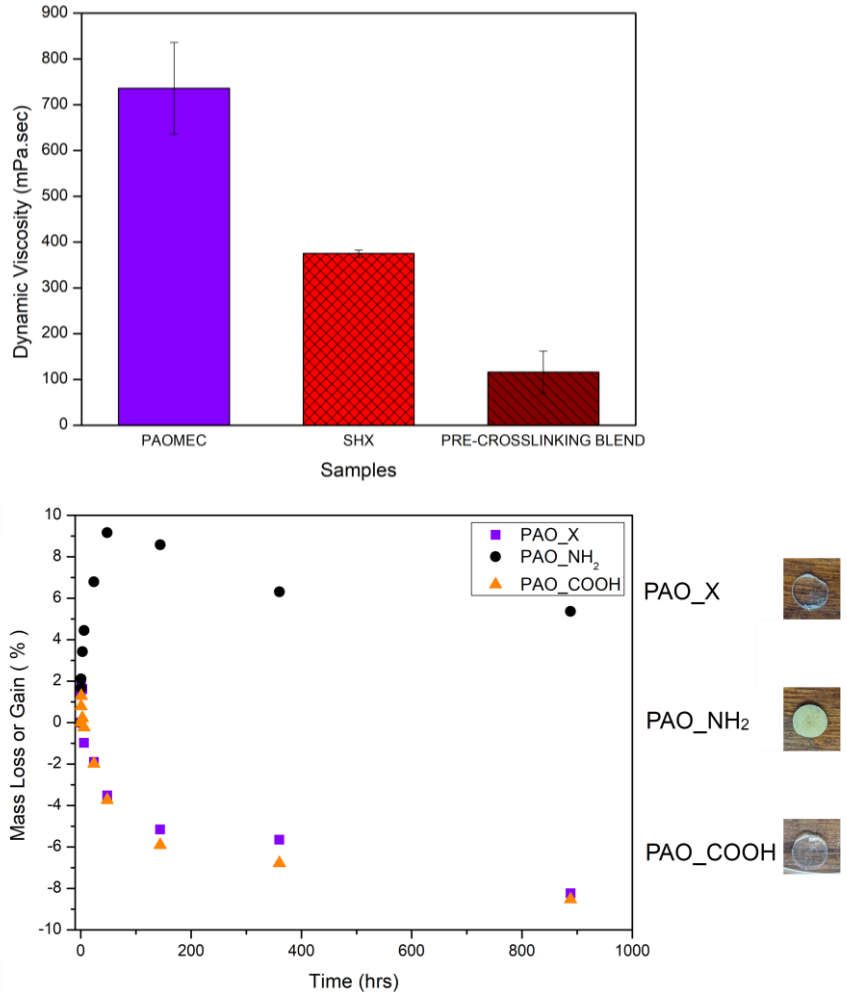


Figure 4.20: Viscosity analysis of PAOMEC, SHX and pre-crosslinking blend for PAO_X (top). Standard deviation is represented by error bars. Swelling studies and images of each sample type used in the studies (bottom).

Contrastingly, mass gain was observed in the amine functionalised samples, PAO_NH_2. Firstly, due to the presence of water in the pre-crosslinking blend, no propylene carbonate co-solvent was required, thus no loss of propylene carbonate would result in mass loss. The presence of water in the pre-crosslinking blend could, however, influence the overall hydrophilicity of the PAO_NH_2 sample, thereby increasing its swelling ratio. The swelling of a crosslinked network, according to the Flory-Rehner theory, can be measured as the equilibrium between the entropy of the polymer chains in the crosslinked network, also known as the elastic free energy, and the free energy of mixing.[221,222] More recently, this has been extended to include the ionic free energy. Generally, the ionic and mixing energy are summarised as what cause the crosslinked networks to swell, while the elastic free energy is what limits said swelling. The mixing free energy can be explained as the attractive forces between the solvent molecules, in this case deionised water, and the hydrophilic

polymer.[223] This is another possibility for the different behaviour of the PAO_NH_2 sample compared to PAO_X and PAO_COOH.

It was determined that the presence of water in the reaction vessel was thus not ideal as it changed the composition of the material. The aim was to fabricate the materials as similarly to each other as possible, to allow for fair comparison during the cell testing stages of the research. As such, minimising differences between the samples was a priority. Additionally, the mechanical properties of the material with water present may alter the capacity of the pre-crosslinking blend to take up and retain sub-micron structures. An unintended consequence of the different swelling behaviour could, therefore, be alteration of the surface topography of the structured samples. This theory was supported by previously published work from the Kelleher research group, by Flynn et al., which measured increased swelling of crosslinked PEG materials that contained higher ratios of water. The swelling resulted in 50% increase in heights of nanostructures on the surface.[193]

To remove the need for water in the pre-crosslinking blend, a desalting reaction was carried out based on a process reported by Bayraktutan et al.[133] This reaction involved the dissolution of cystamine dihydrochloride in water and its neutralisation with aqueous sodium hydroxide (10% w/w). The cystamine was extracted using DCM, dried with magnesium sulfate and condensed by rotary evaporation to give a colourless, viscous oil as in **Figure 4.21**. Once isolated, the sample was introduced to the pre-crosslinking blend, this time without the need for water, but again uncontrolled side reactions were problematic. In this case, precipitate formed almost instantaneously upon the mixing of the reactants, as in **Figure 4.21**. Based on the literature, it was theorised that two possible side reactions were occurring. Firstly, the same thiol-disulfide exchange, as spoken about previously. Secondly, it was theorised that nucleophilic attack of the propylene carbonate by the free amine functionalities could be occurring. The ring opening of cyclic carbonates has been reported under various conditions resulting in the formation of urethane groups.[224–226] Regardless, for the purposes of this research, it was agreed that cystamine was too reactive to utilise in the pre-crosslinking blend.

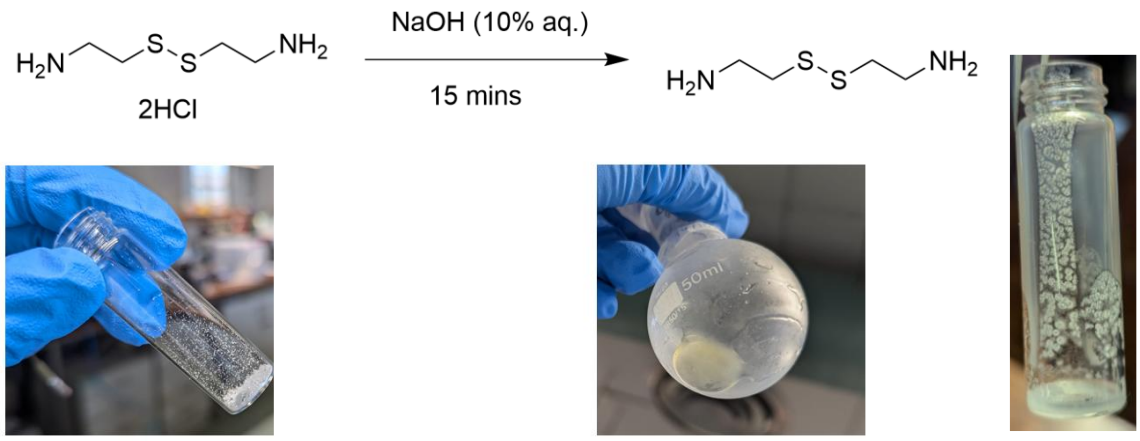


Figure 4.21: Reaction scheme for cystamine dihydrochloride desalting and images of the salt and resulting viscous, yellow liquid of cystamine. Image of glass vial containing pre-crosslinking blend after instantaneous precipitation of reactants.

Boc-protected cystamine (cystamine-Boc) was utilised to investigate its reactivity with the other reagents. It was successfully crosslinked without immediate uncontrolled gelation as had been observed with the non-protected cystamine. It was decided that the deprotection of the amine group would complicate the crosslinking of the samples too much due to the use of strong acids commonly required for this reaction.[227]

A new approach was taken to minimise the possibility of side reactions occurring in the pre-crosslinking blend. Instead of the “one-pot” approach, two separate two-step methods were devised. The first of these methods mixed the pre-crosslinking reactants, excluding the cystamine as before and exposed the sample to UV-light in the crosslinking chamber. Once crosslinked, the sample was soaked in a mixture of cystamine and Irgacure-2959 (1% w/w) that was dissolved in minimal acetone prior to mixing with cystamine. The soaked sample was then exposed to UV light for a second time, with the aim that any unreacted allyl groups would be reacted to form sulfur cardon bonds. The second approach involved a pre-crosslinking step whereby the steps in the first approach were reversed. Specifically, the PAOMEC was reacted with cystamine by mixing the two in a beaker alongside the PI (1% w/w), as before, followed by exposure to UV light for 30 minutes. The mixture was then solubilised in propylene carbonate and mixed with SHX and PI (1% w/w), then exposed again to UV for 60 minutes.

At this point, a specific way to analyse the samples, both quantitatively and qualitatively, for the presence of amine functional groups had not yet been decided upon. Preliminary analysis was completed using ninhydrin to simply observe whether the amine functionalisation had been successful, in a qualitative manner. Ninhydrin is commonly used as an assay to amines and amino acids as upon reaction with primary amines, a colour change from colourless to purple occurs due the formation of diketohydrindylidene-diketohydrindamine, also known as Ruhemann's purple.[228] A 1% ninhydrin solution was made in ethanol, due to its poor water solubility.[229] It was then added to a glass vial containing each of the samples submerged in water. The vials were heated to 90 ºC to accelerate the reaction and colour change was observed after approximately ten minutes. The reaction, as pictured in **Figure 4.22**, elucidated a positive response in both the pre- and post- crosslinking functionalisation processes, as reported above. Both PAO_X and PAO_COOH samples were also exposed under the same conditions and no colour change to purple was observed.

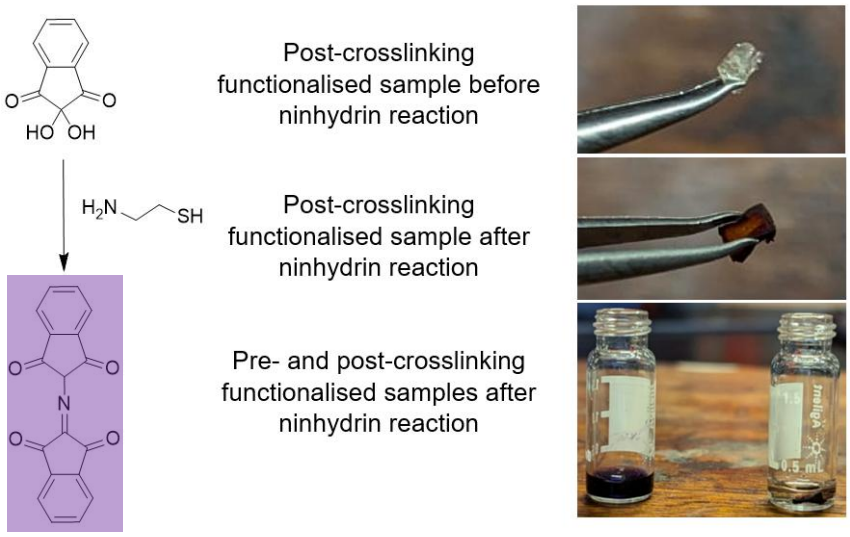


Figure 4.22: Reaction of ninhydrin with cystamine that results in purple colour (left); images of samples before and after ninhydrin exposure and the vials in which the qualitative analysis was carried out (right).

Both crosslinked samples changed colour from cloudy white to purple indicating the presence of primary amines within, or on the surface of the crosslinked samples. However, colour change was also observed in the water in each vial. This was suggestive of free cystamine present on the samples but not covalently attached to the surface. Control over the density of the positive charge, in this case, would therefore be difficult. Additionally, post-crosslinking functionalisation could cause

issues with samples that have different surface topography. As such, the process involving pre-crosslinking cystamine functionalisation was deemed to be the most promising. At this stage, investigations into the structuring of crosslinked samples with and without 3-mercaptopropionic acid were prioritised. Future work is planned for pre-crosslinking cystamine either through refinement of the briefly attempted UV-initiated approach or through thermal reactions adapted from present literature.[230,231]

It was decided to continue with PAO_X and PAO_COOH samples. Refining the molar ratio of PAOMEC:SHX:COOH was required to investigate the minimal amount of SHX needed to give defined, high-fidelity, sub-micron structures in the replica moulding process.

4.3.2 Structuring and Analysis of Crosslinked PAOMEC

Prior to the completion of any structural analysis using functionalised PAOMEC samples, understanding the basics of whether PAO_X could be structured was important. As such, 2-photon polymerisation was utilised, by my colleague Emma Nolan. 2-photon polymerisation is a form of 3D-printing utilising photopolymerisation processes to design structures of an array of shapes with microscale resolution.[232] In this case, a rough primary template was printed to the size 10 mm x 10 mm, with and array of lines that were of height, width and spacing of 50 μm. This was used as the microstructures are larger than the sub-micron structured silicon templates that were available in the lab. As in **Figure 4.23**, the printed sample was moulded using the elastomer PDMS by curing the PDMS at 50 ºC for one hour. The PDMS primary mould, as pictured, had air bubbles present but this was deemed unimportant due to this process simply being used as a proof of concept. A pre-crosslinking blend of PAOMEC and SHX at a 1:1 ratio, mixed with Irgacure-2959 (dissolved in acetone 15% w/w) was vortexed for three minutes and sonicated for five minutes. No propylene carbonate was required due to the pre-crosslinking blend being low enough viscosity without it. The sample was replica moulded as before, in a crosslinking chamber, exposed to UV light for 60 minutes. The PAO_X was examined using FESEM, which elucidated satisfactory uptake of the printed template. The PDMS primary mould, and the bubbles within, were observed, demonstrating the ability of the PAOMEC pre-crosslinking blend to uptake microstructures, of varying shapes. This result demonstrated the first time, to our

knowledge, that these PAO_X materials were structured on the microscale in this manner and showed great potential as a suitable material in replica moulding.

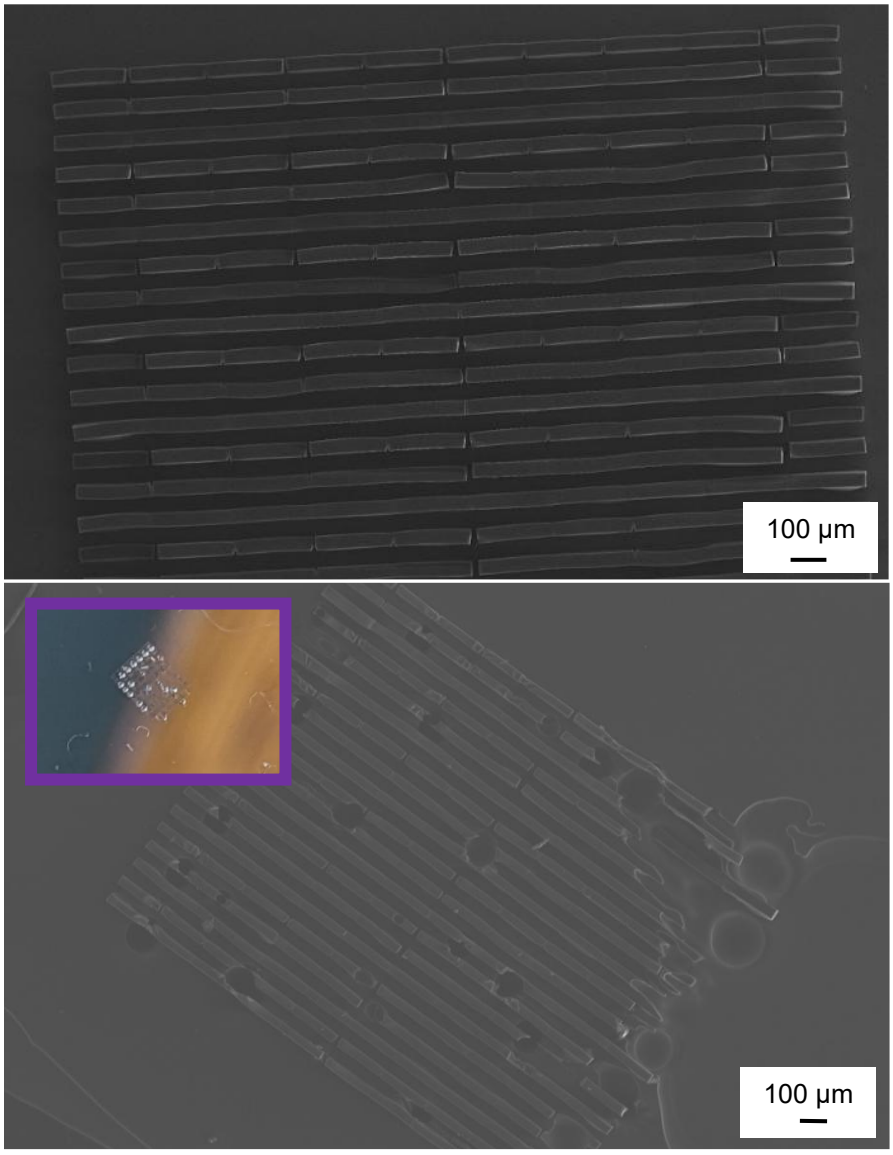


Figure 4.23: FESEM image of 2-photon polymerisation template (top) and SEM image of replica moulded PAO_X, inset picture of moulded PDMS where bubbles are visible, as outline in purple.

Once successful replica moulding on the microscale was demonstrated, work commenced on the submicron scale. The T1 template was again used for the same reasons previously mentioned. Early molar ratios of SHX:COOH were mixed with PAOMEC and the ability to structure them was tested. Visual observation of iridescence on the crosslinked PAO_COOH samples was used as an indicator of successful uptake of structures, as was previously discussed in **Section 4.1**. At a 1:1 SHX:COOH ratio, inconsistent iridescence was observed. As a result, SHX:COOH molar ratios of 3:2, 7:3 and 2:1 were analysed. On preliminary observation,

iridescence was seen on each sample, as such FESEM analysis was performed. The 3:2 ratio was concluded to not be rigid enough. As in **Figure 4.24**, the amount of crosslinker was deemed too low as the structures were observed to be inconsistent and some had collapsed. High fidelity was observed for both 7:3 and 2:1 samples. In order to maximise the anionic charge density while also ensuring successful uptake of the T1 structures, the 7:3 molar ratio was chosen to achieve both.

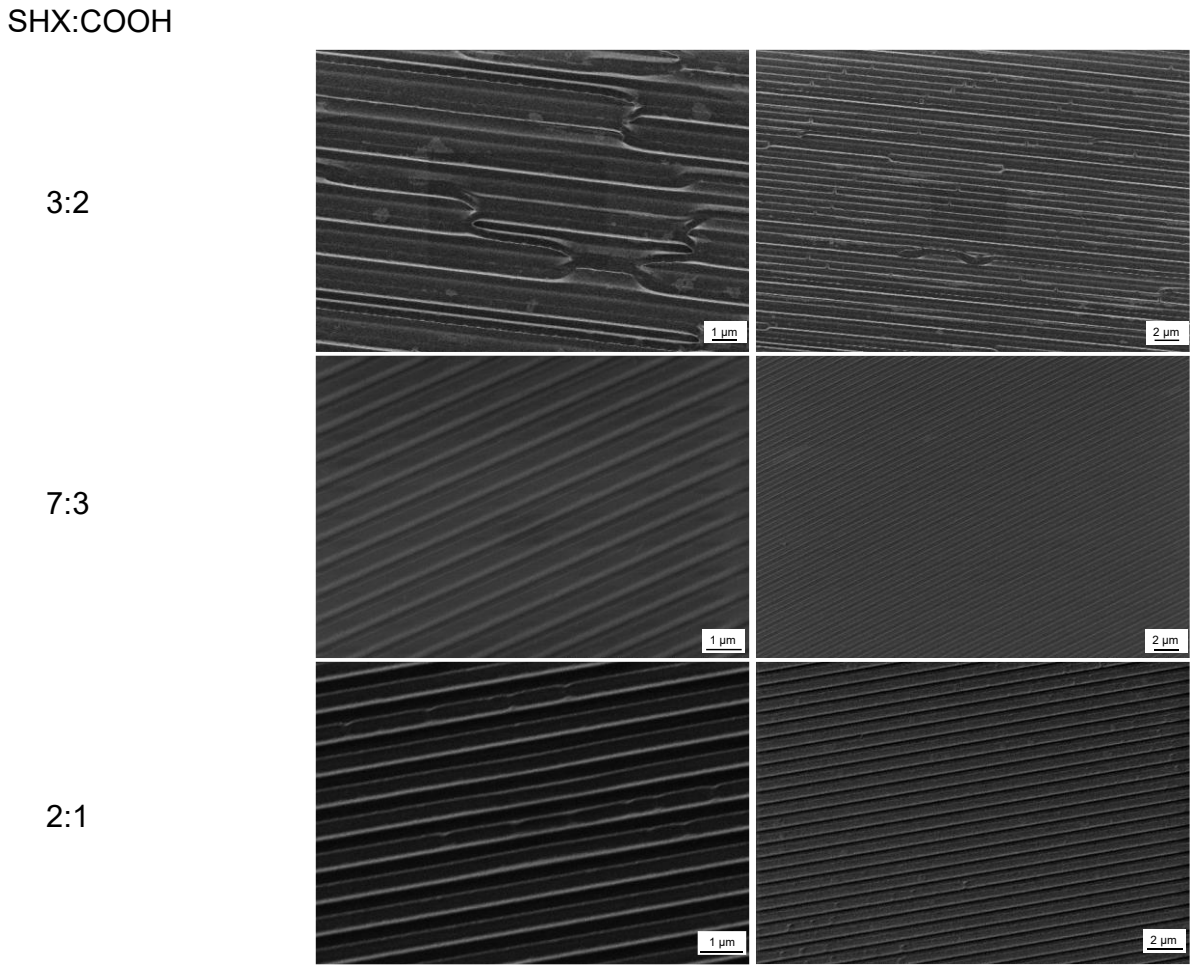


Figure 4.24: FESEM images of PAO_COOH samples of three different ratios of SHX:COOH, 3:2, 7:3 and 2:1 that were replica moulded from PEG primary mould from the T1 template.

After successfully refining the pre-crosslinking blends and reactant ratios required for the introduction of different functionality and sub-micron structures to the crosslinked samples, focus was turned to the crosslinking chamber. The chamber used to crosslink samples of PCLDMA mentioned previously has been effective but required some improvements to promote more consistency across samples. Bacterial cell testing was to be completed in 48-well plates, wherein each well has a 10 mm diameter. To overcome this challenge, a template was designed, and 3D printed

using poly(lactic acid) (PLA), from which a replica mould could be made using PDMS. This mould would have a cylindrical hole 10 mm in diameter and 0.75 mm in depth, as displayed in **Figure 4.25**. Control of the crosslinked sample size in the z-direction was also key as if the samples were not thick enough, curling or bending of the edges of the samples could occur. The depth of 0.75 mm was thus selected as it was the minimal sample depth that saw no sample deformation and also minimised waste of pre-crosslinking materials. The PDMS template removed the need for a hole punch, as used before with PCLDMA:HDDA samples, and enabled consistent crosslinking of any material which could then easily be transferred to 48-well plates for testing. With these moulding chambers, replica moulding was planned to be more efficient and consistent.

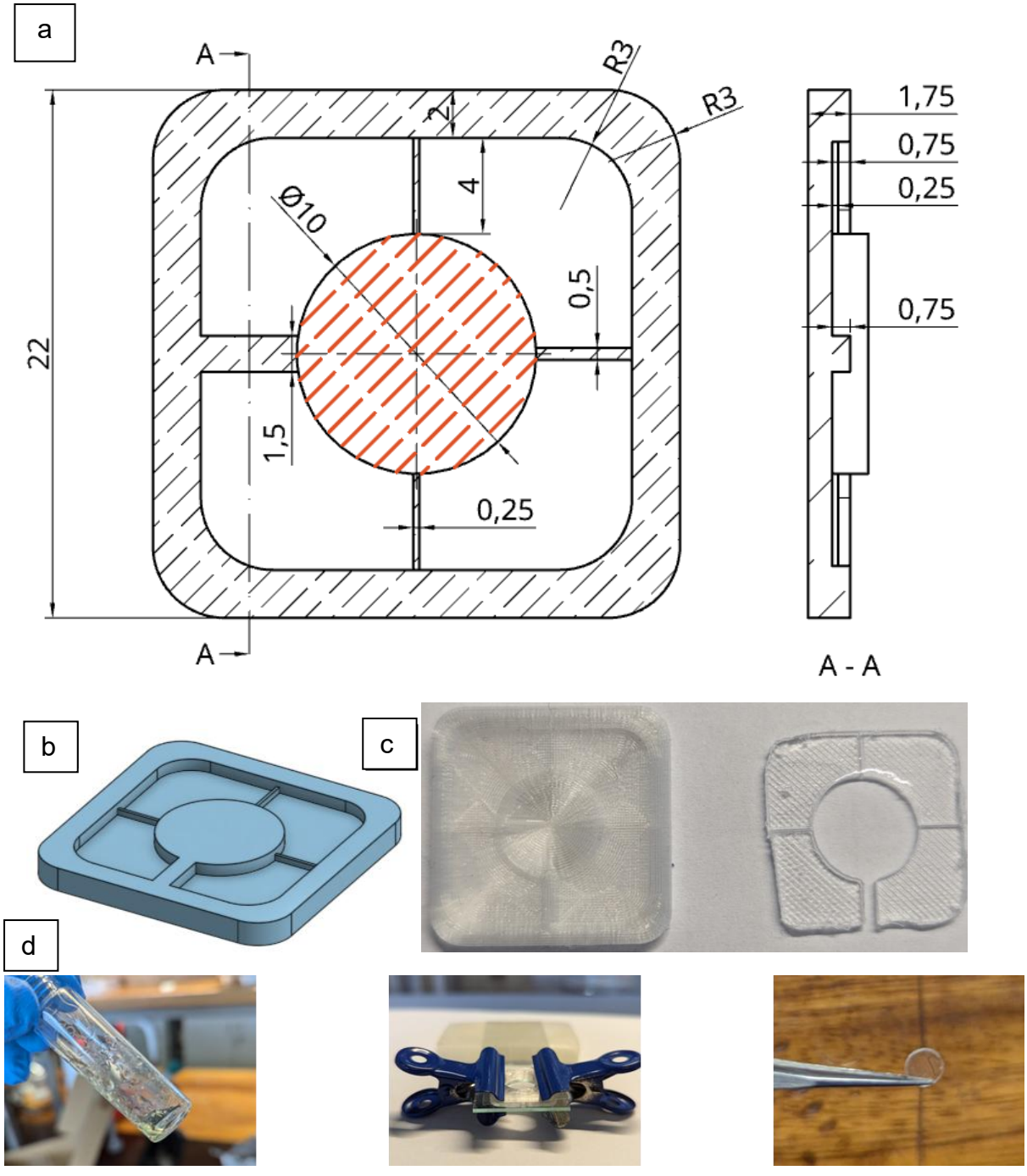
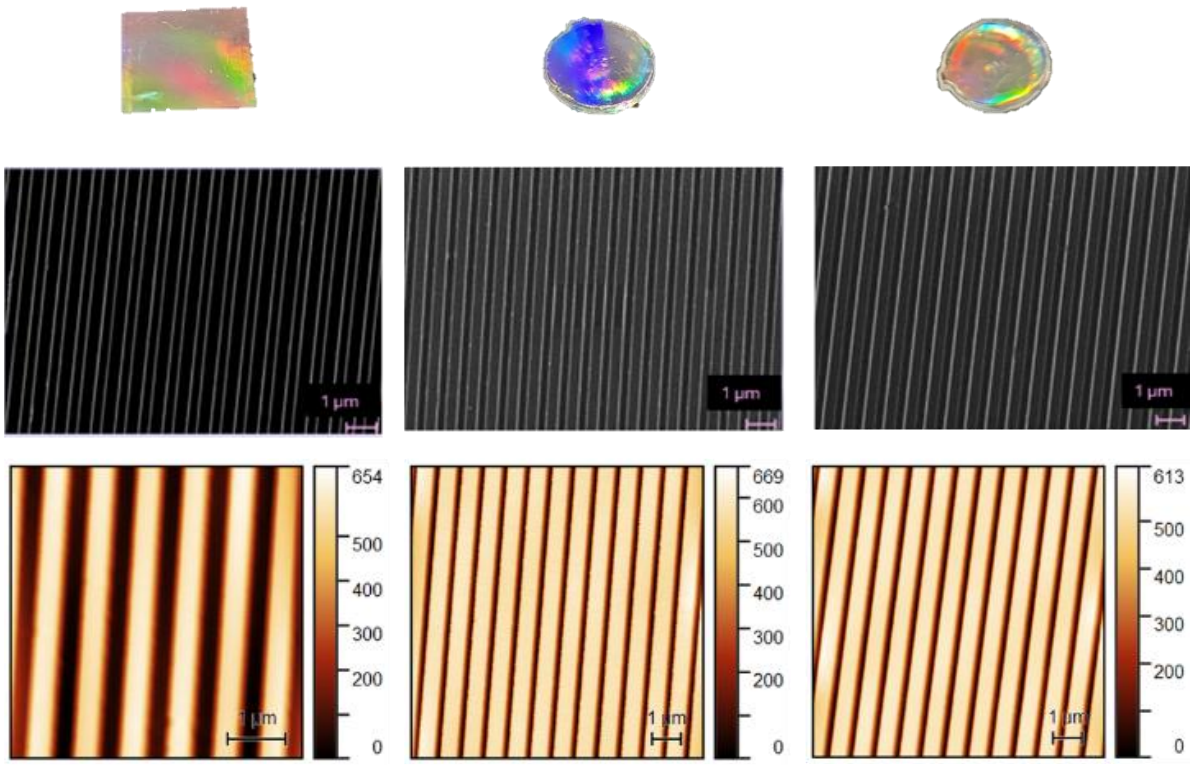


Figure 4.25: Schematic of 3D-printed PLA template with measurements (a); 3D digital replica of 3D-printed PLA mould (b); image of 3D-printed PLA mould and PDMS replica mould (c); images of pre-crosslinking blend, crosslinking chamber and 10 mm diameter PAO_X sample post-crosslinking (d).

Once the crosslinking chamber and process had been successfully designed and finalised, replica moulding using the T1 template began. The samples were structured by the same replica moulding process, as before. The PAOMEC, SHX and Irgacure-2959 (1% w/w) previously dissolved in acetone (15% w/w) were mixed in a glass vial using a vortex mixer for three minutes followed by sonication for five

minutes. In the case where carboxylic acid functionalised samples were to be made, the 3-mercaptopropionic acid was also added into the pre-crosslinking blend. The primary mould was made using PEGDA (with Irgacure-2959 1% w/w). From this primary mould, PAO_X and PAO_COOH secondary moulds were fabricated, as imaged in **Figure 4.26**. The structured samples were then analysed using AFM and FESEM. The analysis confirmed the successful introduction of sub-micron, surface topography on both PAO_X and PAO_COOH crosslinked samples, for the first time. The resulting widths, pitches and heights of the structures are displayed in the table in **Figure 4.26**. These samples were then utilised in bacterial cell testing as discussed in **Chapter 5**.



	SILICON TEMPLATE	PEG PRIMARY MOULD	PAOMEC_X SECONDARY MOULD	PAOMEC_COOH SECONDARY MOULD
STRUCTURE WIDTH (NM)	440 (± 17)	401 (± 32.2)	386 (± 14.3)	404 (± 17.9)
STRUCTURE PITCH (NM)	801 (± 25)	800 (± 13.9)	774 (± 10.7)	762 (± 36.8)
STRUCTURE HEIGHT (NM)	591 (± 22)	601 (± 20.0)	568 (± 10.6)	607 (± 21.8)

Figure 4.26: Images of structured PEGDA, PAO_X and PAO_COOH samples, examples of FESEM and AFM images and a table of the resulting measurements of the various structure parameters compared to the T1 silicon template.

These samples were measured to have high fidelity when compared to both the T1 template and the PEGDA primary mould. As with the crosslinking of methacrylates,

shrinkage has been reported for thiol-ene crosslinked materials. Chen et al. reported on the use of the thiol-ene crosslinking for direct laser printing purposes. A variety of thiol crosslinking chemicals were used including SHX, which was measured to have a shrinkage > 10%.[233] The research published by Dr Anthony Thomas, which discussed the use of PAOMEC and SHX for 3D-printing via microstereolithographic methods, as previously discussed, reported a 5% shrinkage of the bulk materials after crosslinking.[41] Based on the results in the table in **Figure 4.26**, all pitch and height measurements were calculated to have < 5% shrinkage when compared to T1. The widths of the sub-micron lines on the surface of PAO_COOH samples were measured to have < 9% shrinkage compared to the T1 template. 12% shrinkage was measured between the widths of the structures on PAO_X samples compared to T1. However, it must be noted that < 4% shrinkage was measured when comparing the width of the structures on PAO_X and those on the PEGDA primary mould. As such, it was deduced that the source of the shrinkage, in this case, may have been due to the acrylate crosslinking of PEGDA, when replica moulding from T1 to make the primary mould. When comparing all parameters of the structures on the surfaces of PAO_X and PAO_COOH samples to those on the PEGDA primary mould < 6% shrinkage was measured. As such, based on literature, these samples demonstrate good fidelity.

Mechanical and chemical analysis of the crosslinked samples was also completed. WCA analysis was performed on the planar samples to measure hydrophilicity, as imaged in **Figure 4.27**. PAO_X was measured to have a WCA of 72 ± 4 º and to be more hydrophilic than PAO_COOH which had a water contact angle of 91 ± 7 º. The additional carboxylic acid groups present resulted in the formation of a slightly hydrophobic surface. The packing of the carboxylic acid moieties has been reported to affect the WCA measurements of surface. Increased packing density has been linked with increased dimerization of carboxylic acid groups when protonated which will result in such functionalities being less readily available to interact with water resulting in more hydrophobic surfaces.[234] There have also been reports of correlations between increased WCA and decreased zeta potential. It has been reported that hydrophobic surfaces attract a larger number of hydroxide ions to the interface between the surface and water. The increase WCA of PAO_COOH could

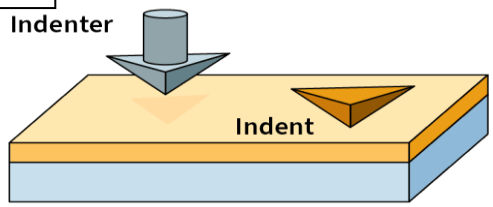
therefore be indicative of a more negative zeta potential for this surface compared to PAO_X.[235–239] Further studies would be required to quantify this surface charge.

Mechanical analysis of the samples was completed by nanoindentation and DSC. Nanoindentation, a type of analysis involving the use of a Berkovich diamond tip, in this case, to puncture a material, is utilised to understand various mechanical properties of said material.[240] The hardness and reduced moduli were measured directly and are displayed in **Figure 4.27**. The hardness of a material measures the resistance of a material to deformation under a load.[241] The modulus of a material, is, in essence, the stiffness of a material in relation to the strain it is being exposed to. The reduced modulus is a common measurement associated with nanoindentation and takes into account the modulus of the tip used in the measurement, the modulus of the sample and the Poisson's ratio of both the tip and sample.[242] Poisson's ratio is a unitless measure of a material's deformation perpendicular to the force being applied to said material.[243] Young's modulus, also known as the elastic modulus, of the sample can then be approximated using the Oliver-Pharr method and specifically the equation shown in **Figure 4.27**.[244] Poisson's ratio ranges, in theory, from values -1 to + 0.5. Soft materials, such as polymers and elastomers generally range between 0.36 and 0.5.[245–247] The Poisson's ratio of the Berkovich tip, v_i, is 0.07 and Young's modulus is 1.141 GPa.[248] The reduced elastic modulus, E_r, was measured, and the Poisson's ratio of the samples, v_s, were approximated to be 0.44.

(a)

	PAO_X	PAO_COOH
WCA (˚)	72 ± 4 	91 ± 7 

(b)



$$E_s = (1 - v_s^2)/(\frac{1}{E_r} - \frac{1 - v_i^2}{E_i})$$

(c)

	PAO_X	PAO_COOH
Hardness (GPa)	0.01 (±0.001)	0.005 (±0)
Reduced Modulus (GPa)	0.038 (±0.001)	0.018 (±0.001)
Youngs Modulus (GPa)	0.033	0.015

Figure 4.27: WCA measurements and images of each sample type with a water droplet (a); illustration of nanoindentation process,[249] and calculation used to find Young's modulus (b); hardness, reduced elastic and Young's moduli of each sample (c).

Both PAO_X and PAO_COOH samples measured low hardness closer to that of the behaviour of elastomers than many polymers.[247,250–252] The low molecular weight of the material and crosslinking density are two influential factors that could affect these elastic properties. The PAO_COOH, would be expected to be less densely crosslinked due to the lower molar ratio of SHX present and thus the lower hardness and reduced modulus were expected to be measured.

The hardness of the PCLDMA:HDDA 1:4 and 1:9 samples, were measured as 0.04±0.005 GPa and 0.105±0.001 GPa.[130] The hardness of the PAO_X was approximately 10 times less than that of the 1:9 PCLDMA:HDDA material and four times less than the 1:4 material. The crosslinking density of the material was also demonstrated to be influential in these crosslinked materials as the increased HDDA ratio resulted in more than a two-fold increase in resistance to deformation, or hardness values. This is consistent with the findings when comparing PAO_X and PAO_COOH.

DSC analysis was used to better understand the thermal properties of the PAOMEC material prior to, and post-crosslinking. The resulting analysis of the pre-crosslinking, purified PAOMEC demonstrated typical properties of an amorphous polymer. No T_m or T_c were observed, while a T_g was observed at -39 ˚C. DSC analysis was performed on the crosslinked samples between the temperatures of -80 ˚C and 320 ˚C to investigate the stability of the samples at high temperatures and no degradation was observed. The crosslinked samples were compared with the isolated PAOMEC oligomer over the temperature range of -60 ˚C and 80 ˚C. The characteristic T_g of the PAOMEC when in a crosslinked network was not observed. The T_g, as in **Figure 4.28**, increases slightly within the crosslinked networks from approximately -3 ˚C to -1 ˚C. This has been reported in other polymers with a variety of crosslinkers, including but not exclusive to SHX.[253–255] The increase in T_g has been widely reported and can be explained by the reduced chain mobility due to increased crosslinking density.[256,257]

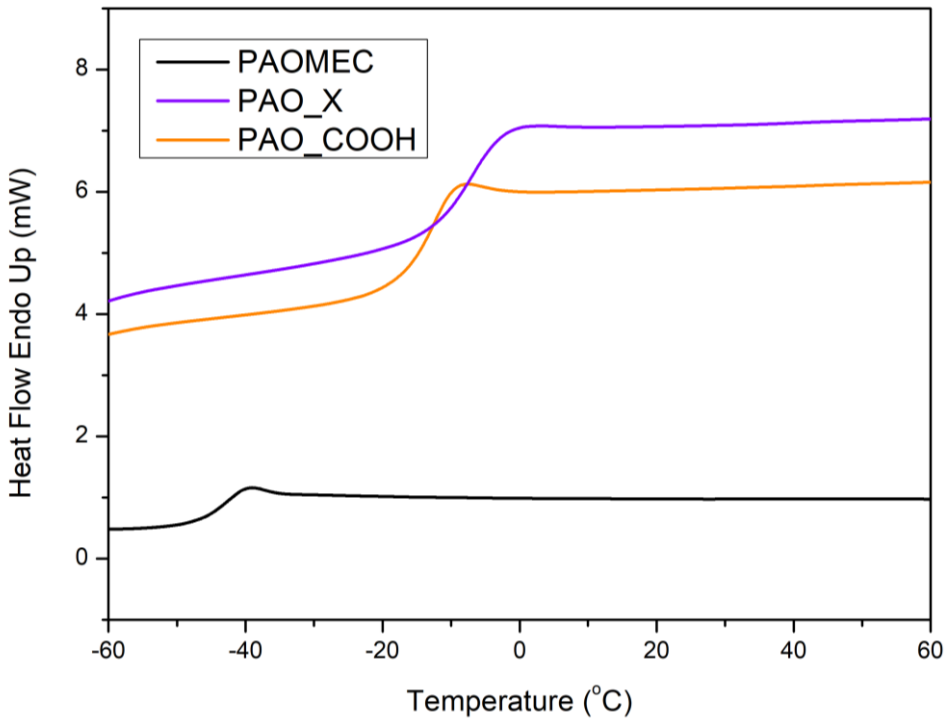


Figure 4.28: DSC analysis of purified PAOMEC and crosslinked samples PAO_X and PAO_COOH.

Degradation studies were conducted on both PAO_X and PAO_COOH. As before with PCLDMA:HDDA, ISO 10993-13:2010 and ASTM Standard F1635-24 were used as references for the accelerated study for biodegradable materials.[206,207] The samples were left in glass vials in an incubator set to 70 ˚C (±1 ˚C) for three

timepoints, 2, 30 and 60 days. Mass loss was used as a measure to demonstrate the extent of the degradation. Both samples degraded over time and at 60 days, approximately 46% and 75% mass loss were measured for PAO_X and PAO_COOH, respectively. Again, these results are not unusual due the lower crosslinking density of the PAO_COOH sample. As with the degraded 1:9 PCLDMA:HDDA, yellowing was also observed with both PAO_X and PAO_COOH. Specifically in the case of PAO_COOH, extreme yellowing was seen, and the material had less structural integrity and was a softer, more gel-like consistency, as imaged in **Figure 4.28**.[209,210] The samples were also analysed by DSC, FTIR and the PBS buffer in which the samples were soaked was analysed by ^{1}H NMR spectroscopy.

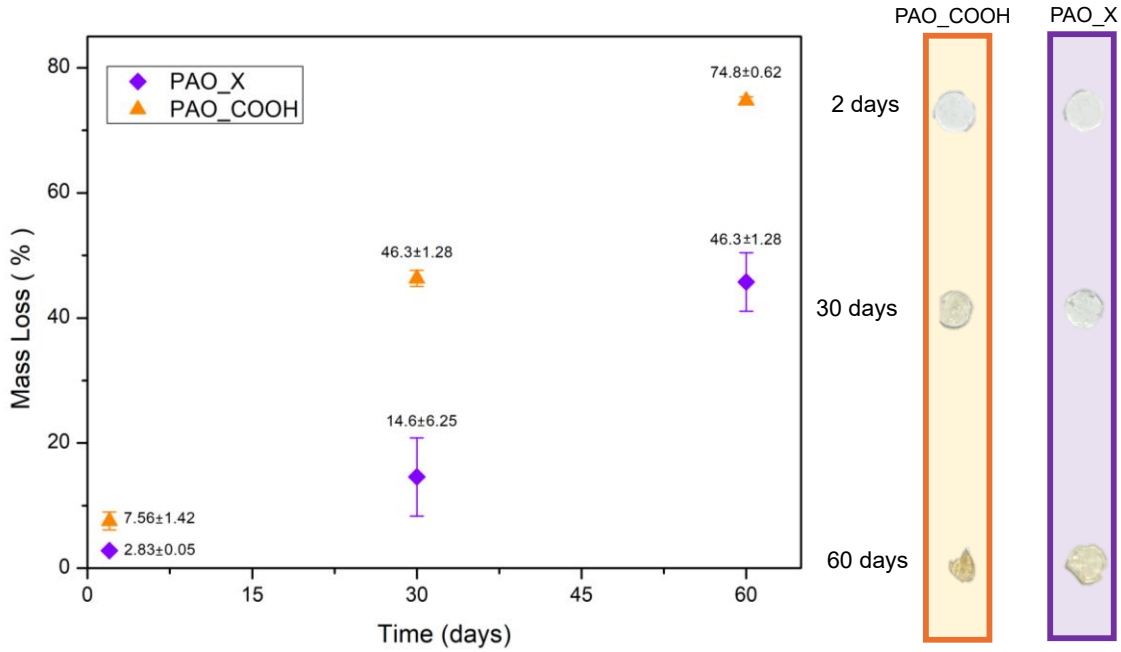
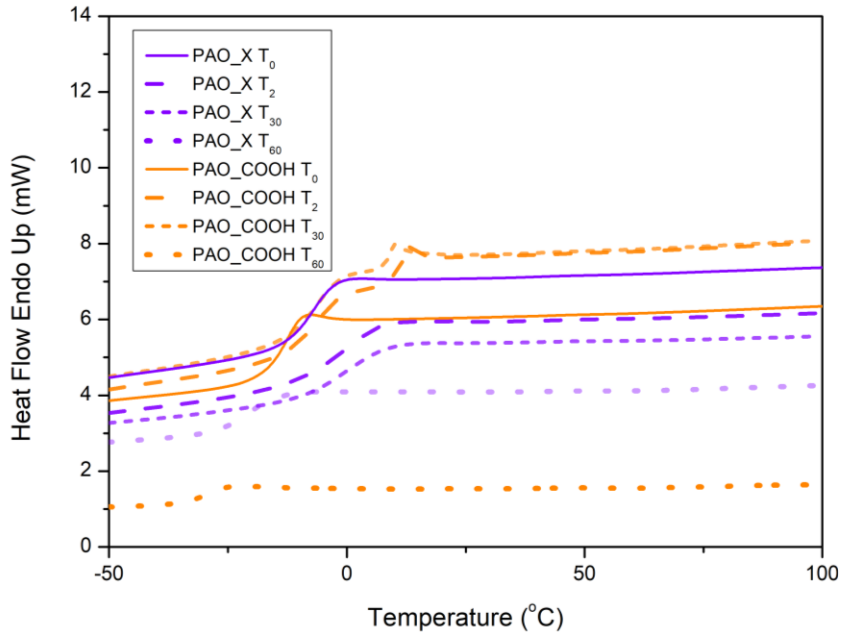


Figure 4.29: Mass loss analysis of degraded samples after 2, 30 and 60 days and images of these samples at said time points. The error bars represent the standard deviations.

DSC analysis gave indications of the degradation reaction process. The main observation of note was the drop in the T_g measured in both PAO_X and PAO_COOH samples after 60 days, at timepoint T_{60}, as in **Figure 4.30**. The T_g would be expected to decrease in networks post-degradation. This is likely due to a reduction in crosslinking density due to the hydrolytic degradation of the crosslinked network. This would result in more free movement within the network, therefore lowering the temperature required to reach the T_g.[258]

At T_2 and T_{30}, the T_g saw an increase in temperatures measured in both samples when compared to the samples at T_0. It was expected that the T_g would lower, as stated above, due to degradation but this was not the case until T_{60}. A possible explanation for this was the hydrogen bonding that could occur during the hydrolytic degradation process. Misha and Singh reported on two different types of interactions that water molecules can have with crosslinked networks. Type I was known to have a plasticising effect, that lowered the T_g due to increased mobility in the crosslinked network, and results in alteration of Van der Waals interactions. This can be removed through drying the sample; however, Type II does not have the same effect on the T_g. This type of hydrogen bonding of the water molecules, more commonly possible in hydrophilic networks, can result in a type of secondary crosslinking throughout the crosslinked network. This may therefore explain the increase in the T_g observed prior to T_{60} where the extent of the degradation removed any secondary crosslinking that had occurred throughout the hydrolysis of PAO_X and PAO_COOH.[259]



Samples	T_g (°C)	T_g 2 (°C)
X_0	-7.69	
X_2	-0.44	
X_{30}	0.70	
X_{60}	-19.01	
$COOH_0$	-13.91	
$COOH_2$	-7.96	11.56
$COOH_{30}$	-7.69	8.39
$COOH_{60}$	-30.07	

Figure 4.30: DSC analysis of PAO_X and PAO_COOH samples after degradation over 2, 30, 60 days and table of the corresponding T_gs.

Additionally, a second T_g peak was observed in the PAO_COOH samples at timepoints T_2 and T_{30}. This type of "secondary crosslinking" may also be the reason that two T_g peaks were observed in the PAO_COOH samples. The increased carboxylic acid groups in PAO_COOH samples compared to PAO_X could provide

more hydrogen bond sites to give two distinct phases within the sample. This was supported by the fact that these two peaks were not observed in samples that underwent the same conditions, namely exposure to 70 ˚C (±1 ˚C) in a glass vial for two days. When analysed by DSC, a single peak was observed therefore ruling out the possibility of a post-photopolymerisation curing step solely through exposure to the increased temperature. It also ruled out a theory that as the degradation process continued, the so-called loosening of the network resulted in phase separation giving two distinct T_g peaks rather than one, as has been reported in certain cases relating to heterogeneously crosslinked samples.[260]

The hydrogen bonding of the water was further supported by FTIR analysis of the samples, as displayed in the spectra in **Figure 4.31**. A peak corresponding to hydroxyl bond stretching of free water molecules has been reported to be found between 3600 cm^{-1} and 3700 cm^{-1}. Intermolecular hydrogen bonding interactions are expected to show peaks at the slightly lower wavenumber approximately between 3200 cm^{-1} and 3500 cm^{-1}. This corresponded to the peaks observed at around 3440 cm^{-1}, which was noted to increase in size over the course of the degradation process.[261] Additionally of note was the increase in the peaks observed at approximately 2930 cm^{-1}, corresponding to the stretch of alkyl groups. This may be due to the increase in free alkyl chains post hydrolysis of the ester bond, for example.

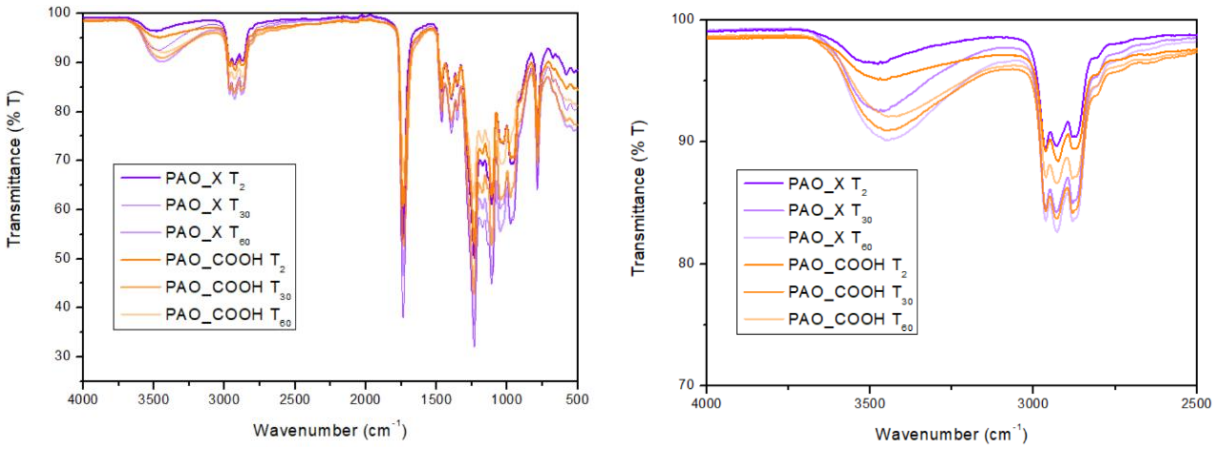


Figure 4.31: FTIR spectra of PAO_X and PAO_COOH samples at each time point of the degradation study; full spectrum (a) and zoomed in to between the wavenumbers of 2500 cm^{-1} and 4000 cm^{-1}.

Analysis of the PBS buffer via ^1H NMR spectroscopy was also completed and demonstrated the degradation products that were solubilised. As in **Figure B.5** in

Appendix B, there was an increase in the degradation products found in the PBS after 60 days.

Based on the analysis completed the samples were confirmed to be degradable in biological conditions by hydrolytic pathways. In future work, the non-accelerated biodegradation study will be completed, followed with further in-depth analysis of the degradation products to better understand their biocompatibility and ensure their safety for use in biomaterials.

4.4 Conclusions

The crosslinking process of PCLDMA:HDDA was refined based on previous work completed in the Kelleher group. Both PCLDMA-1350 and PCLDMA-630 were successfully crosslinked in a UV-initiated photopolymerisation reaction over 60 minutes to form planar crosslinked samples. The soft lithography technique of replica moulding was learned and used to structure PCLDMA:HDDA samples. The 1:9 ratio of PCLDMA-630:HDDA was successfully structured on the sub-micron scale using cicada wings as a template, for the first time. The 1:4 ratio showed collapse of the nanoneedle-like structures due to the lower crosslinking density. Once the silicon template, T1, was decided upon, replica moulding was performed using 1:4 and 1:9 PCLDMA-1350:HDDA blends. Successful structuring of the 1:4 blend on the sub-micron scale was concluded by FESEM and AFM analysis. An accelerated degradation study of the 1:9 blend was conducted and demonstrated the slow hydrolytic degradation of the material, in biological conditions, via mass loss analysis.

Crosslinking and functionalisation of PAOMEC was also discussed in this chapter. The replica moulding process was again utilised and its parameters refined for use with PAOMEC, as this material had not been crosslinked using this approach before. Different pre-crosslinking blends were trialled and various ratios of SHX were also tested with planar samples. The 1:1 molar ratio was concluded to be the best option for PAO_X samples. Functionalisation of the planar samples with 3-mercaptopropionic acid was successful whereas introduction of amine functionalities to the crosslinked material was found to be more difficult. The reactivity and solubility issues faced with cystamine dihydrochloride resulted in various adaptions to the preparation of the pre-crosslinking blend. The most promising of which involved a

two-step process whereby the PAOMEC was to be reacted with cystamine first and then the crosslinking process could be completed. Novel PAO_X and PAO_COOH samples were then structured successfully using the T1 template, after the 10:7:3 molar ratio of PAOMEC:SHX:COOH was found to be likely to give the highest charge density as well as good structural fidelity. The success of the structuring was again measured through FESEM and AFM while the planar samples were analysed by WCA and nanoindentation. The samples also underwent an accelerated biodegradation study which confirmed both samples to be degradable in biological conditions, based on mass loss, DSC, FTIR and ^{1}H NMR spectroscopy analysis.

Once both materials had been crosslinked, functionalised and structured to a satisfactory standard, both bacterial and mammalian cell testing protocols could commence.

Chapter 5 Cell Testing

Upon the successful fabrication of crosslinked, degradable materials, bacterial and mammalian cell testing was performed. PAO_X and PAO_COOH samples, with and without sub-micron structures were analysed for antibiofouling properties. The priority of this static, bacterial cell testing was to better understand the influence of sub-micron surface topography and anionic surface charge in collaboration with each other and independently. The PAOMEC backbone of the materials allowed for like-with-like comparison to enable the sole analysis of the antibiofouling effects of the surface properties. The planar and structured PCLDMA:HDDA were not analysed for antibiofouling properties due to time constraints but were prioritised for mammalian cell testing.

Due to the challenges faced with colorimetric assays and PAOMEC-based materials, as is discussed in more detail in **Section 5.2**, PCLDMA:HDDA samples were selected for mammalian cell studies. Earlier studies had demonstrated the PCLDMA:HDDA materials to be biocompatible with mammalian cells.[132] As such, it was decided that a more in-depth analysis of these materials, and the difference in interactions between endothelial cells (ECs) and the structured and planar surfaces was of interest, as discussed further in **Section 5.4**.

5.1 Introduction to Antibiofouling Surfaces of Biomaterials

There have been various approaches taken to test the antibiofouling properties of materials. In general, cell studies are performed under either static or flow conditions. Under static conditions the most common methods used to analyse antibiofouling surfaces, as reported in the literature, were found to be quantitative analysis via fluorescent imaging or microscopy followed by use of image processing software such as ImageJ or through counting of colony-forming units (CFUs).[262,263]

Various microscopy techniques are commonly used for different purposes in cell analysis. Crystal violet (CV) is an example of a purple stain commonly used for cell viability studies. It functions through binding to DNA and proteins in bacteria.[264] Cao et al. used the stain to quantify the presence of adhered bacteria to polyurethane films.[265] Fluorescence microscopy, specifically live/dead staining, is a technique that is regularly used to fundamentally assess antibacterial activity of surfaces.

"*Bac*Light™" bacterial viability kits are fluorescence imaging kits which use two different colour stains to quantify the amount of bacterial cell death.[266] SYTO-9 is a nucleic acid stain that gives a green colour to all bacterial cells present. It binds to the DNA and RNA of both viable and dead bacterial cells. Propidium iodide is a red stain that is used for quantification of dead or damaged cells as it can only penetrate cells that have compromised cell membranes.[267] Park et al. exemplified a dual approach to live/dead staining. Bacterial assays were performed with gram-positive and gram-negative bacteria, namely *Bacillus subtilis (B. subtilis)* and *E. coli*, respectively. The assays were performed at various time points and were then stained and analysed by confocal fluorescent microscopy. The resulting images were then analysed with ImageJ software, thereby quantifying the total presence of cells both dead and alive, as imaged in **Figure 5.1**. The percentage area coverage of bacteria on each surface was used as a measure of antibiofouling properties of each surface. The results were then supported by CFU counts.[268,269]

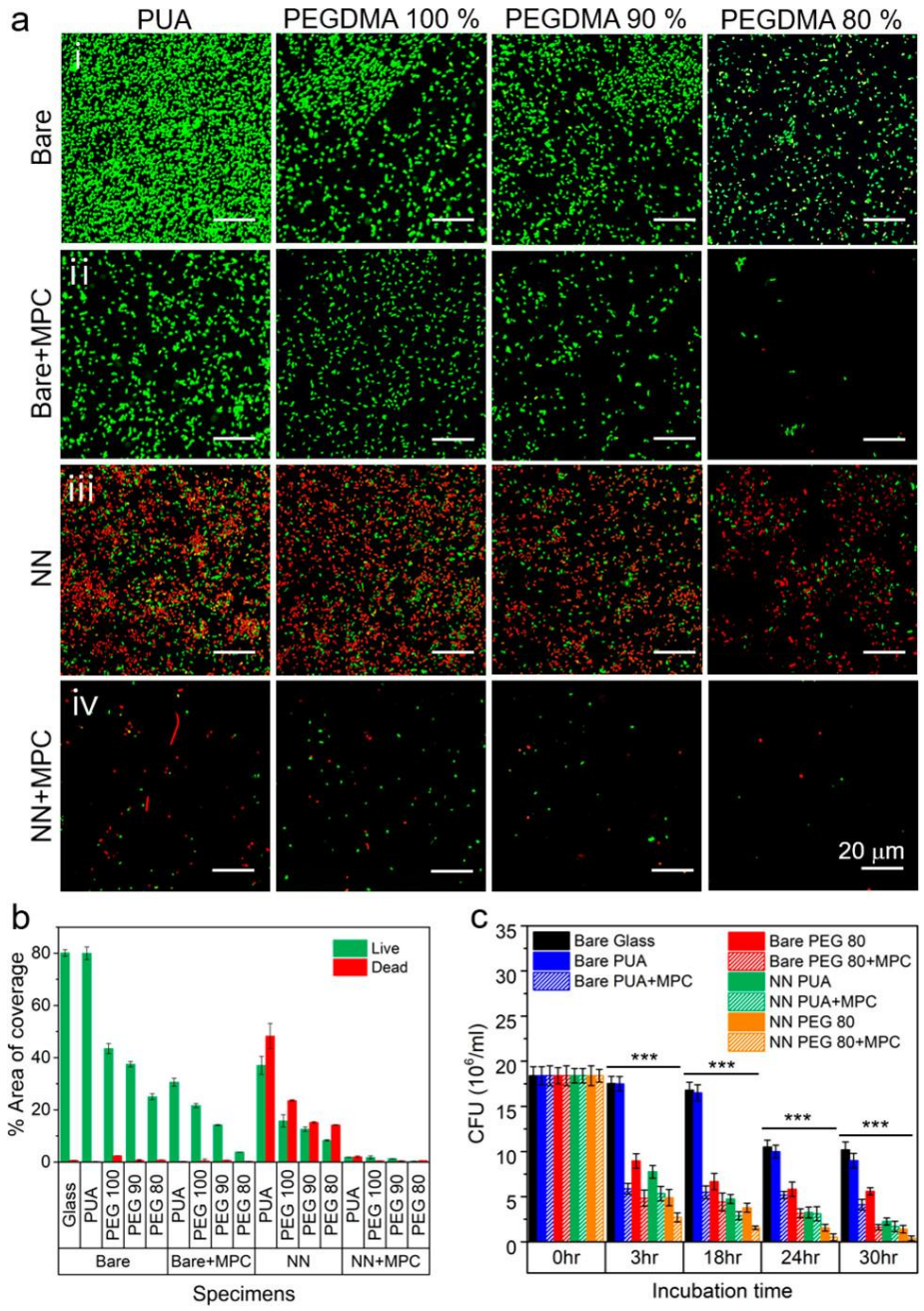


Figure 5.1: Confocal microscopy images of stained samples (a); post-microscopy image analysis with ImageJ (b); and CFU counting utilised to support the results obtained through staining studies.[268]

CFU counts have also been used as the sole method for antibiofouling analysis. Dolid et al. reported CFU counts by performing bacterial cell assays using gram-positive, *S. epidermidis* and gram-negative, *E. coli*. The bacteria were allowed grow for 22 hours on four different sample types and after removal of planktonic bacteria from the media through serial wash steps, the bacteria adhering to the surfaces were isolated. Sonication was used to remove said bacteria and CFUs were performed to quantify the amount of bacteria adhered to each surface.[270] A similar approach was taken by Song et al., utilising *S. aureus* and *E. coli,* and calculating the CFU per area

unit of the sample surface instead of percentage area coverage, as a means of quantitative antibiofouling analysis, as in **Figure 5.2**.[271] CFU counting is generally utilised as it is an efficient and facile process. It is performed by serial dilutions of a media containing bacteria which are spread on petri dishes, commonly containing nutrient agar. These plates are left under optimal conditions and the single colonies formed after overnight growth, are counted. For optimal counting conditions, colonies between 30 and 300 are allowed, any less is thought insufficient and can lead to larger standard deviations and any more may lead to overlapping colonies making it impossible to accurately count the amount of colonies present.[272]

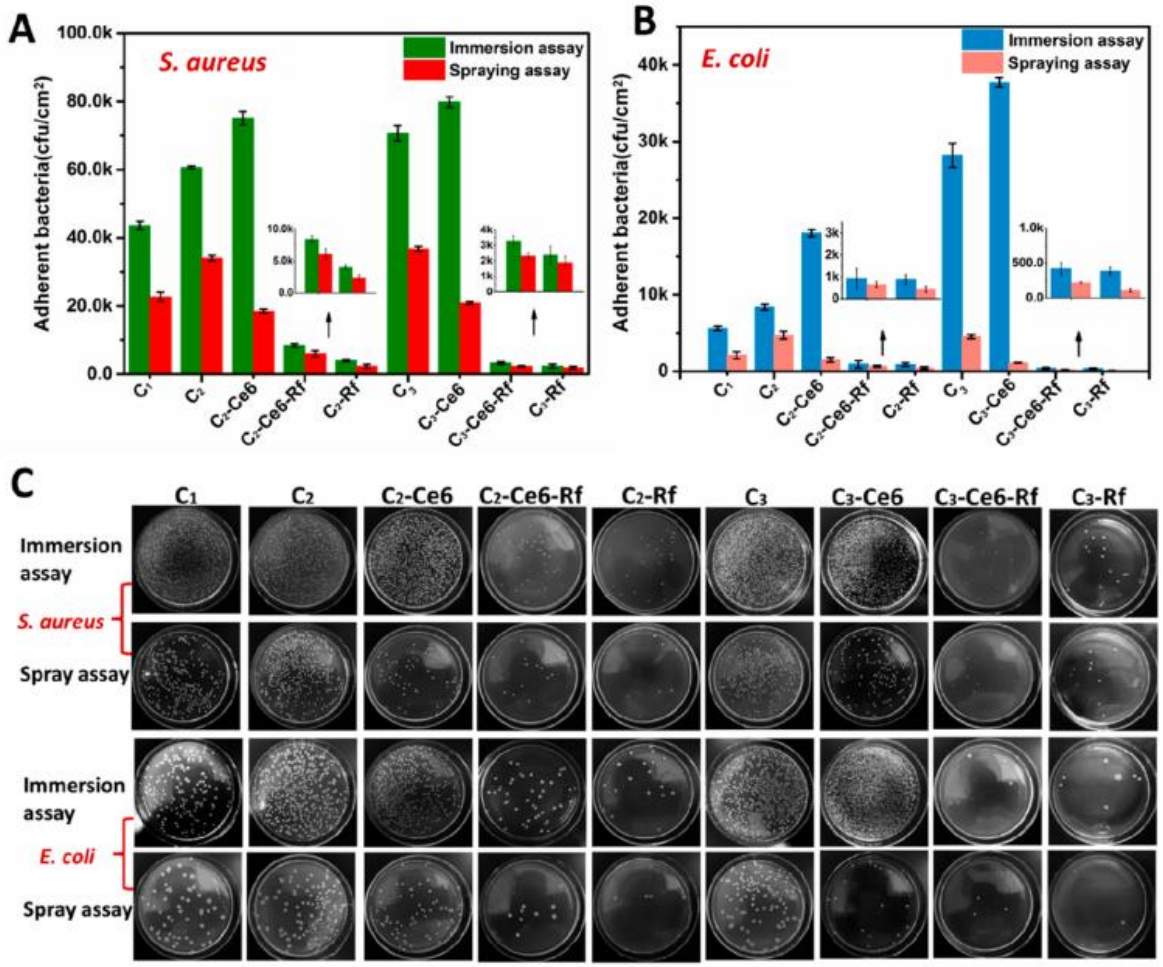


Figure 5.2: Quantitative analysis of adhesion of bacteria based on the CFU of the petri dishes imaged.[271]

As with many techniques, issues have been reported relating to different colorimetric analyses and CFU approaches. For example, Rosenburg et al. published research that found the significant under estimation of viable cells when analysing biofilm formation of *E. coli* and *S. epidermidis* with propidium iodide.[273] With respect to CFU

counting, it has been reported to likely favour rapid growing bacteria over slower growth, resulting in the under-estimation of bacteria cell numbers.[274] Specific to biofilm formation, CFU counts have been noted to have issues with reproducibility of quantification results, due to the aggregation of cells preventing accurate colony counting.[275]

Microscopic analysis is another technique that has been reported in literature. This technique avoids the use of stains altogether focussing instead on imaging techniques such as SEM to take images of the bacteria on sample surfaces. As before, ImageJ or other software for image processing can be used to calculate percentage coverage of the surface with bacteria. This analysis technique is thought to be advantageous as there is direct imaging from the sample. As a result, no loss of bacteria through the various steps required for CFU counting, such as the sonication and plating, nor use of stains are required. The samples once washed, undergo a cell fixation step followed by dehydration in preparation for use under vacuum conditions. The images collected from SEM analysis, like the other microscopy techniques mentioned above, can then be analysed with software to quantify the bacteria present. Wang et al. used this analytical technique to quantify the antibiofouling properties of a silicone surface under both static and flow conditions. Generally, static conditions involve the performance of bacterial assay on surfaces with a fixed volume culture media with minimal agitation or flow. Performance of cell testing under flow can be completed using a variety of methods but is generally completed with the aim of mimicking *in vivo* conditions. For example, in research produced by Wang et al., bacteria were exposed to the silicone sample, for four hours, to mimic exposure to a bacterial infection. This sample was then placed in a flow cell and fresh media was introduced to the sample at a set flow rate of 0.5 mL/min to mimic a bacterial infection in the body.[276] Contrastingly, Epstein et al. exposed samples to bacterial culture in a flow cell over three time points, 24 hours, 48 hours and 7 days, at a flow rate of 10 mL/min.[277]

5.2 Bacterial Cell Testing of PAOMEC

Once crosslinking and structuring of the samples was completed, cell testing was performed. PAOMEC was investigated for antibiofouling behaviour. Static cell testing was performed with the aim of better understanding of the antibiofouling behaviour of

materials due to the presence of sub-micron structures and anionic carboxylic acid functionalities on the surfaces.

5.2.1 Preparation of a Cell Testing Protocol

The PAOMEC samples PAO_X and PAO_COOH, both planar and structured, were to be investigated for antibiofouling properties. Static biofouling testing was originally planned to be completed as the first stage of cell testing with the samples. Prior to any cell assays being performed, the samples had to be prepared. This involved ensuring that no leachable chemicals that could kill bacteria were present in the sample. To do so, samples were soaked in ethanol overnight to kill any bacteria, if present, and to remove any residual solvents, such as ethyl acetate from the PAOMEC synthesis process or acetone from the crosslinking process. The samples were then soaked in deionised water overnight to remove any ethanol as it could kill bacteria during the cell testing process. Once this was complete, the Kirby-Bauer disc diffusion test, hereafter called the disc diffusion method (DDM), was performed.[278]

DDM is a qualitative test generally used to measure antimicrobial susceptibility and antimicrobial resistance of various aerobic and facultative anaerobic bacteria. This is a short test with visually obvious results. As such, it has found use in a variety of fields; as an educational tool for undergraduate students, as an aid to doctors looking at treatment options for infections and as a preliminary test in research prior to performing further, more complex cell assays.[279–283] As stated above, in the case of this research, the aim of the DDM was to ensure any residual solvents remaining in the crosslinked samples, did not have antimicrobial activity. It was also completed to rule out any inherent antibacterial properties of the bulk crosslinked materials themselves. This was a necessary step to be certain that any conclusions drawn from results achieved, related directly to the surface structures or charge and nothing else.

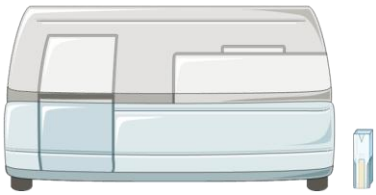
The DDM was carried out as illustrated in **Figure 5.3**. Overnight cultures were performed using a gram-negative and gram-positive strains of bacteria, namely *E. coli*, and *S. epidermidis*, respectively. A subculture was then isolated and grown for each of these samples. The newly inoculated Luria Broth (LB), a liquid medium that is nutrient rich for bacteria growth, was left stir for approximately four hours to ensure

mid-exponential phase of growth was reached, as had been confirmed based on growth curves performed, as well as data reported in literature,.[284,285] The inoculated LB suspension was spread on agar plates to create a lawn – a thin layer – of bacteria. As in **Figure 5.3**, the crosslinked samples, post soaking in ethanol and water, were placed on the agar after the lawn of bacteria was spread. A positive control, a disc containing ampicillin, and a negative control, a blank disc, were also placed on the plate. The plates were left in the oven overnight at 37 ºC and the next day analysis was completed.

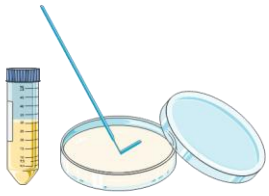
The zones of inhibition, the diameter of the space around the samples that showed no bacterial cell growth, were measured by ImageJ analysis. In this case, as observed in the images in **Figure 5.3**, zones of inhibition were only observed around the positive controls demonstrating the effect of ampicillin. There was no difference observed between the negative control and the PAOMEC samples. As such, it was concluded that any residual solvents or chemicals, if present, did not demonstrate bactericidal behaviour.



Inoculated LB shaken with bacteria



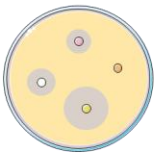
OD_{600} of 0.5 of inoculated LB measured



Lawn of inoculated LB spread on agar petri dish



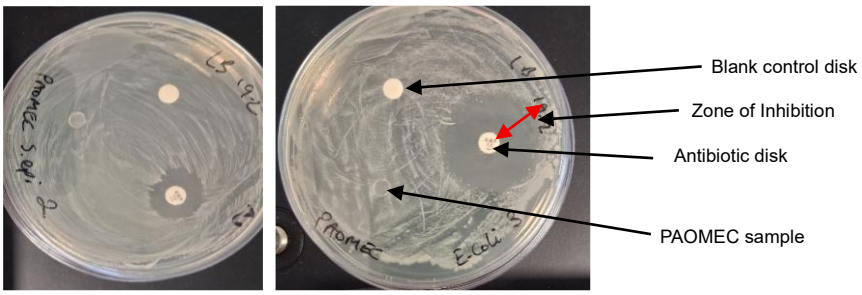
Samples were placed on dish and left in oven overnight



Samples were pictured



Images were analysed to measure zone of inhibition



Bacteria	Zone of Inhibition (mm)
E. coli	14.2 (± 1.7)
S. epidermidis	25.3 (± 2.3)

Figure 5.3: Illustration of DDM procedure (top); results of PAOMEC sample, blank disk (negative control) and ampicillin loaded disc (positive control) on agar plates with a lawn of bacteria, namely S. epidermidis *(left) and* E. coli *(right). Table of the zone of inhibition around the positive control (bottom).*

Once confirmed, preparation began for performance of a cell viability MTS assay. MTS assays involve the use of water-soluble tetrazolium salt, (3-(4,5-dimethylthiazol-2-yl)-5-(3-carboxymethoxyphenyl)-2-(4-sulfophenyl)-2H-tetrazolium) (MTS). MTS undergoes reduction to purple formazan, as illustrated in **Figure 5.4**, in the presence of electron carrier chemicals such as phenazine methosulfate. The reduction occurs only when viable cells undergo activity that result in the oxidation of nicotinamide adenine dinucleotide (NADH) to NAD+.[286] The colour change from yellow to purple

can then be quantified via spectrophotometric analysis between wavelengths of 490 and 500 nm.

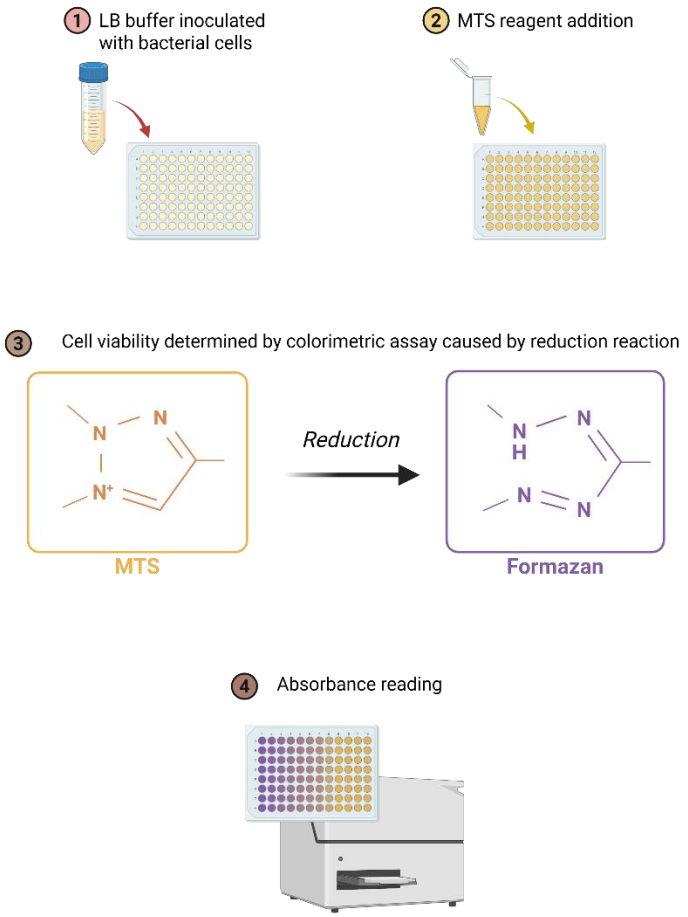


Figure 5.4: Illustration of MTS assay procedure, created with BioRender.com

Preliminary tests were done in advance of the cell assay to evaluate the suitability of this analysis method for the PAOMEC samples. These tests included measuring the absorbance of the PAOMEC samples at the wavelength of 490 nm, with measurements taken every 10 minutes, to measure baseline absorbency at this wavelength, as in **Figure 5.5**. Further tests were conducted on the absorbance of other chemicals that may have found use in the cell testing protocol, specifically fixatives like grease and sealant. This was assessed by soaking grease and sealant in LB for 20 hours, and then incubating the LB with MTS. This was carried out to ensure there would be no interference with the assay due to the presence of residual acetic acid in the sealant, for example. LB, as well as cells in the presence and absence of MTS were also analysed, as in **Figure 5.5**.[287] As was anticipated, minimal absorbance was measured for all samples excluding the MTS control. In the

presence of the *E. coli*, the conversion of yellow MTS to purple formazan saw almost a 10-fold increase in absorbance at 490 nm when compared to all other fixatives and controls analysed.

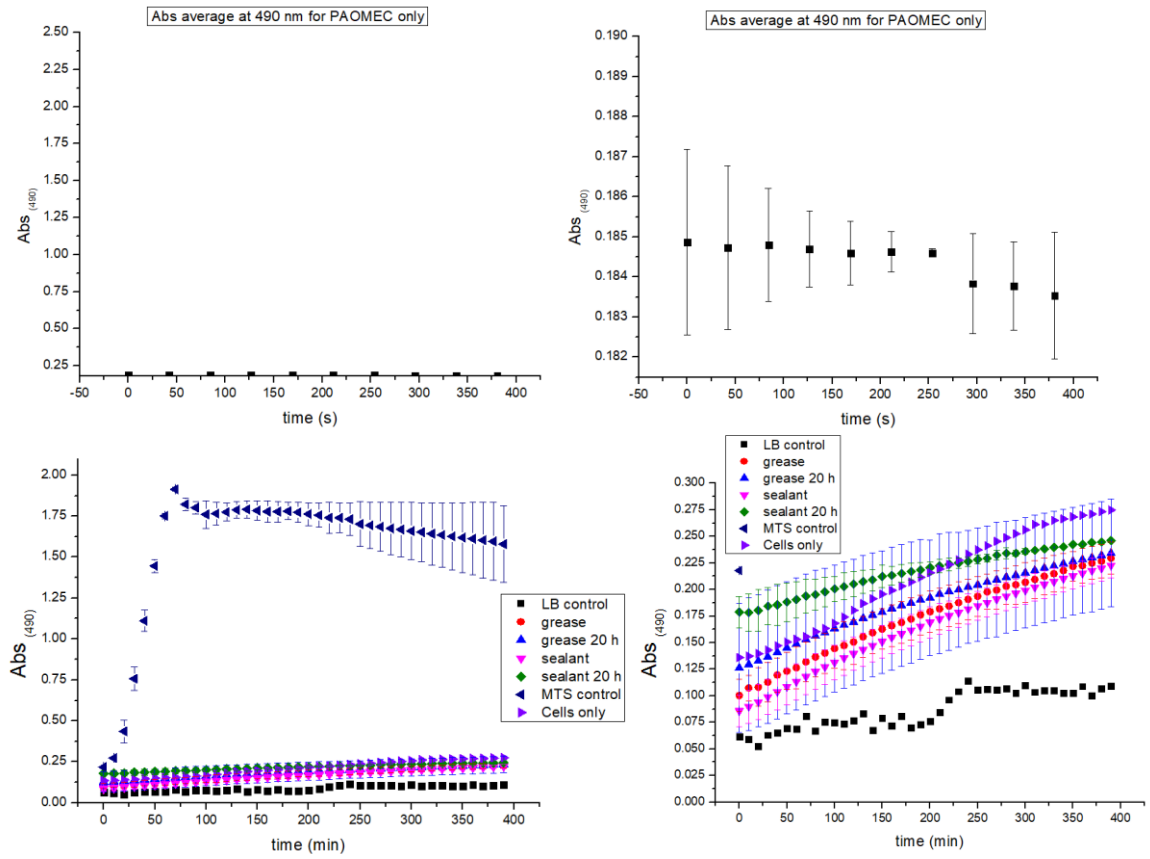


Figure 5.5: Absorbances measured for PAO_X samples not yet exposed to MTS solution, with no cells presence (top); and absorbances measured for fixatives planned for use in testing (bottom). Graphs made by Dr Graham Reid.

Following on, direct and indirect assays were performed. Direct assays were performed to assess any side reactions that may occur between the planar, crosslinked PAOMEC sample, PAO_X, and MTS salt. *E. coli* cells were cultured in LB until an OD_{600} of approximately 0.2, measured via spectrophotometry, was reached. The direct assay was completed using a 48-well plate, in which two technical replicates of the inoculated LB were added. Two PAO_X samples were also added as well as the controls, autoclaved LB with no cells present and MTS solution with cells present at an OD_{600} of 0.9. The assay was carried out at two separate timepoints, three hours and 20 hours. Absorbances were measured at 10-minute timepoints over a 400-minute time period revealing that side reactions between MTS

and planar PAOMEC samples were occurring. As can be observed at both three-hour and 20-hour timepoints, early measurements show overlapping absorbance with the absorbance measurements taken of MTS interacting with *E. coli*.

An absorbance of 1.73 was measured for the PAO_X samples while the negative control, LB with no cells present, measured an absorbance in the range of approximately 0.12. The LB control was then plated onto agar plates and left in an oven at 37 ºC, over 48 hours to demonstrate no contamination of the LB control had occurred. Non-enzymatic conversion of MTS has been reported in literature. For example, free thiol groups have been observed to reduce MTS salts.[288] The SHX crosslinker was therefore theorised to have some unreacted thiol groups present thereby reducing the MTS almost instantly upon interaction with the PAOMEC samples. This would explain the early colour change from yellow to purple, as circled in red in **Figure 5.6,** that resulted in high absorbance measured at t_0.

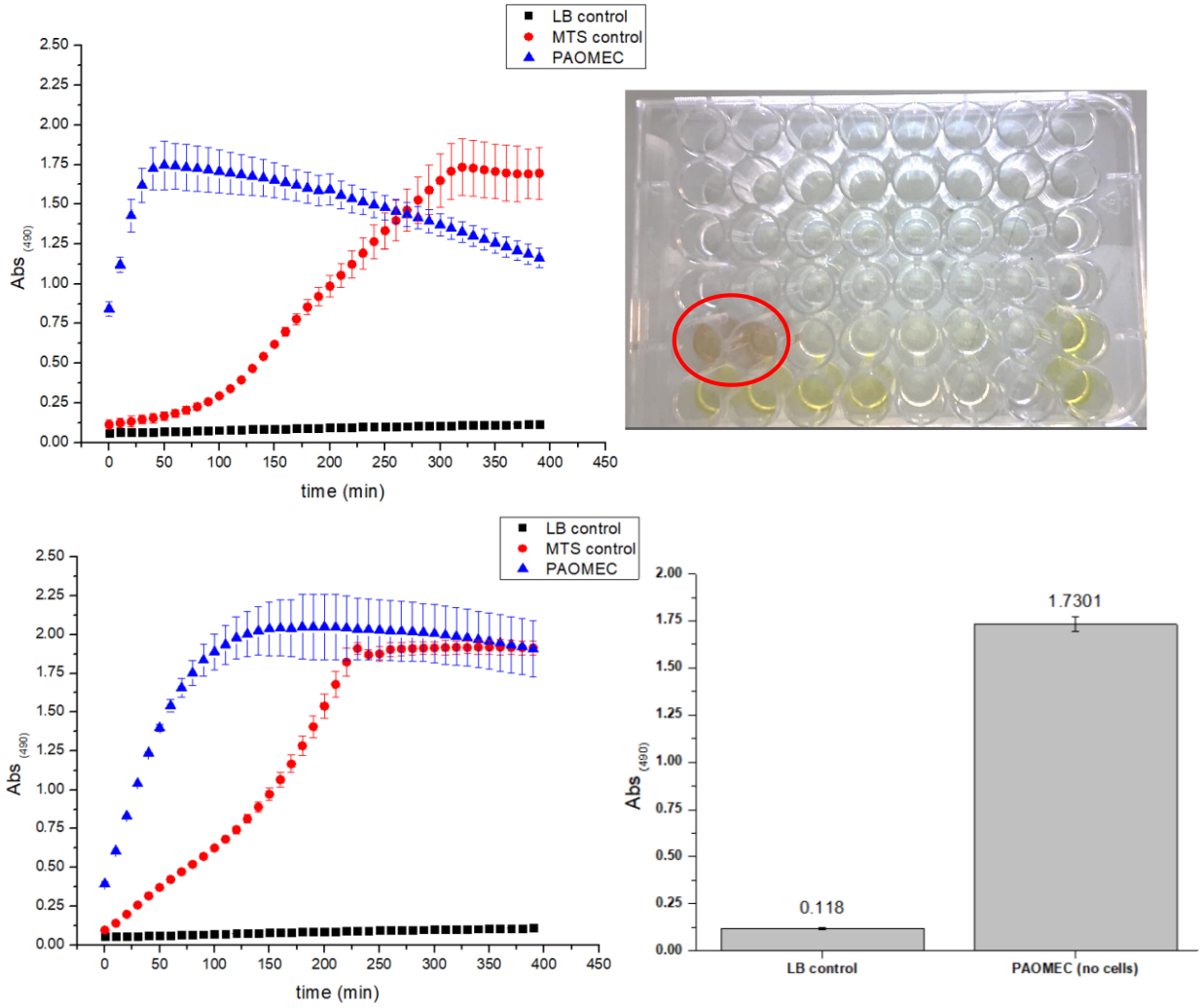


Figure 5.6: Direct assay absorbances measured after 3 hours (top left) and 20 hours (bottom left) soaking in LB with no cells present; photograph of 48-well plate with circle of the PAO_X samples soaked in LB for 3 hours and exposed to MTS solution; and column chart comparing absorbances measured from negative control (LB with no cells or sample present) and PAO_X sample at the 60-minute time point (t_{60}) (bottom right). Standard deviations are represented by the error bars. Graphs were made by Dr Graham Reid.

Indirect assays were also performed during this time to investigate the effect of any leachates, from the PAO_X samples, on the MTS, thereby resulting in false readings. Planar PAO_X samples were left to soak, in triplicate, in LB over three time points, 24, 48, and 120 hours, as in **Figure 5.7**. The LB was then removed from the samples and added into new wells. MTS was subsequently added to each well. LB left in wells, not containing samples, was used as a negative control while inoculated LB with and OD_{600} of 0.9 reacted with MTS was again used as a positive control. The LB at each time point was also plated and left in the oven over 48 hours, at 37 ºC, to confirm no cells were present.

These indirect assays confirmed that no leachates were going to interact with the MTS assays, and no cells were present in the LB control, as in **Figure 5.7**. This result supported the theory that the reaction observed in the direct assay was due to the interaction between the PAO_X sample and the MTS. This again corroborated the supposition that reduction of MTS was occurring due to the presence of free thiol groups.

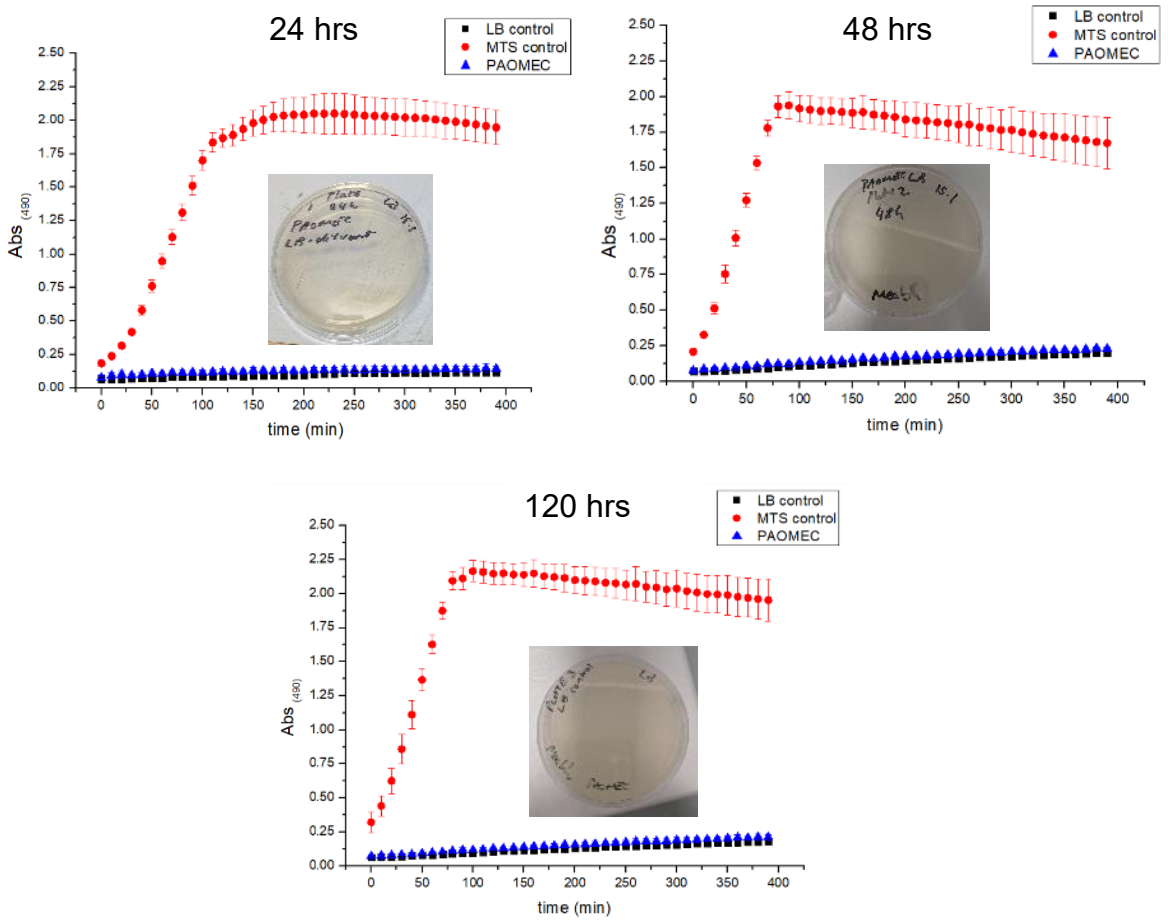


Figure 5.7: Absorbances measured from indirect MTS assay with inset images of petri dishes used to confirm no cells were present in the LB negative control, at three different timepoints. Graphs were made by Dr Graham Reid.

Based on the results it was determined that the MTS assay was not suitable for our required purpose. Following this, a CV assay was prepared. This assay has been used in quantitative analysis of biofilms for a variety of bacteria. The dye binds to peptidoglycan layer present in both gram-positive and negative bacteria.[264,289–291] The preliminary cell testing analysis was completed using *E. coli* and samples were prepared as before, by soaking in ethanol overnight. The samples were subsequently soaked in autoclaved, deionised water overnight, to remove any

ethanol. The LB, inoculated with *E. coli* with an OD_{600} of approximately 0.2, was pipetted into the appropriate wells of a 48-well plate. The samples were left for 48 hours at 37 ºC under mild shaking conditions at 30 rpm. The samples were then washed and stained with a CV stain (0.1%). Post incubation, the samples were rinsed to remove any unbound CV stain. The samples were left dry and acetic acid was then used to solubilise the CV that was bound to the cells on the surface of the samples. The absorbances of the solutions were measured at 590 nm.

The planar and structured PAOMEC samples PAO_X and PAO_COOH were analysed and LB, inoculated LB with an OD_{600} of approximately 0.2, and acetic acid were analysed as controls. It was decided this assay was also not suitable for the PAOMEC samples, despite data collected as in **Figure 5.8**. The negatively charged surface of the PAO_COOH, both planar and structured, resulted in non-specific binding. The CV bound to not only the cells present on the surface but also to the crosslinked materials themselves. This was observed once the CV stain had been introduced to the samples and washed in triplicate with sterile water to remove any unbound CV stain. The acetic acid was then used to release the bound CV, to enable absorbance measurements to be taken. As a result of the dye staining both the cells and the PAO_COOH samples, dye was released from both. Consequently, the solution measured was too concentrated to be read by the spectrophotometer. CV is a cationic molecule, as in **Figure 5.8.** As such, it binds to anionic groups present in the peptidoglycan layer such as amino acids but also to the carboxylic acid functionalities in the PAO_COOH samples.

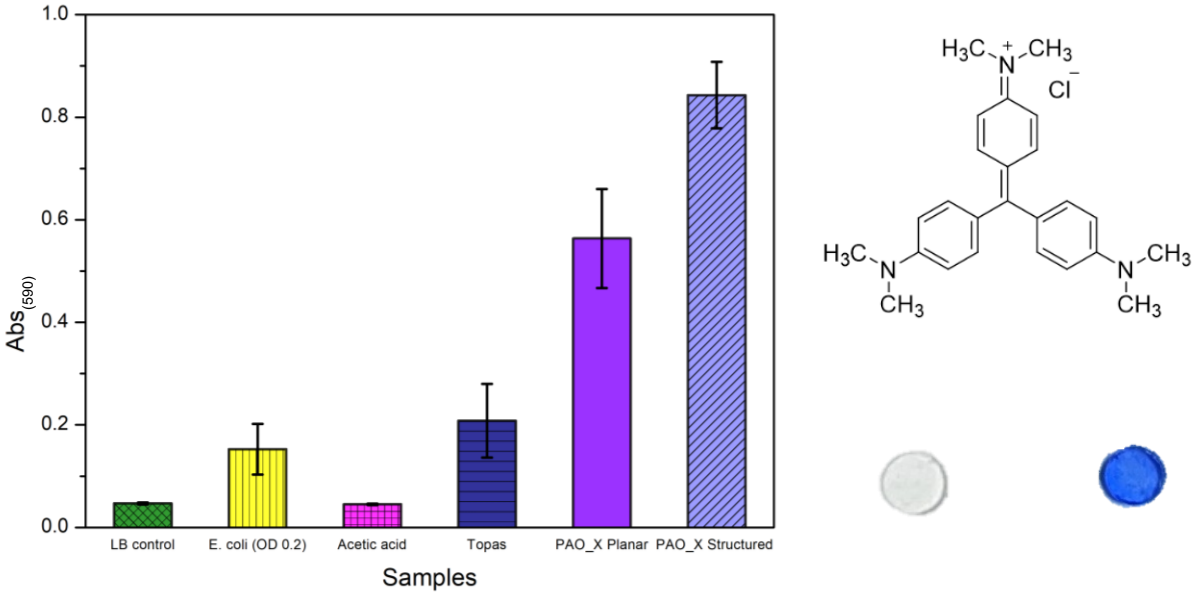


Figure 5.8: Column chart of absorbances measured from from crystal violet assay performed where the erro bars represent standard deviation (left); chemical structure of crystal violet showing positive charge (top right); colour change of PAO_COOH sample due to non-specific binding of the crystal violet stain to the crosslinked network.

It was therefore decided that this assay was also unsuitable for analysis of these samples due to the inaccuracy caused by non-specific binding. To avoid non-specific binding and minimise chemical side reactions that had caused challenges, a different approach was decided upon.

5.2.2 Cell Testing Protocol Refinement

Inspired by previous literature, quantification of the bacteria on the samples was planned to be completed via imaging of biofilm formation and bacterial adherence covering the surfaces of the PAOMEC samples. Instead of spectrophotometric analysis techniques, as previously described in **Section 5.2.1**, this method used SEM imaging to visualise bacteria which were then quantified via an AI-assisted approach.[292,293] Richards et al., reported on the use of the AI-assisted analysis of SEM images to quantify fouling of microscale structured surfaces by the diatom species, *Amphora coffeaeformis* and *Nitzschia ovalis*.[293] A similar analytical approach was used by Ding et al. to quantify the presence of *Porphyromonas gingivalis* and *Fusobacterium nucleatum* on dental zirconia surfaces.[292] SEM images, exemplified in **Figure 5.9**, were used, in this research, to image the cells on the surface of each sample, which could in turn be quantified.

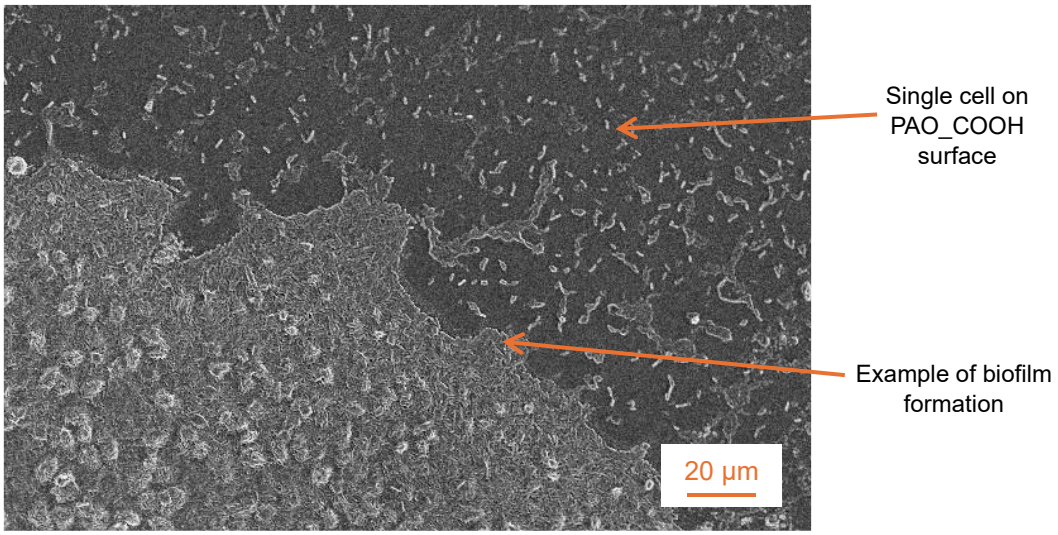


Figure 5.9: SEM image of PAO_COOH planar sample, with scale bar of 20 µm.

Fiji is an open source image analysis programme. Within the programme, is a plugin called Trainable Weka Segmentation which is trained by user input. It uses machine learning algorithms to complete a number of tasks, including but not exclusive to data clustering, classification, visualisation and feature selection.[294] In the case of this research, it was used to analyse images of the samples, after the cell testing and fixing of the cells to the samples had been performed, as in **Figure 5.10**.

SEM analysis was performed whereby five images were taken from the centre of the sample and each quadrant to ensure unbiased, representative data were collected. Once the images taken were imported into the Fiji software, they were prepared by setting a size scale and darkening the background. The plugin was then used to set two classes for the analysis, “bacteria” and “background”. Using the freehand selection tool in the software, multiple samples were taken of bacteria by drawing the outline of the bacterial cells or biofilm and adding these to class one. The same tool was used to isolate areas of the PAOMEC sample where no bacteria were present, and the areas were added to class two to be denoted as the background. The plugin then used these samples to train the classifiers and once completed it was possible to see what had been defined as bacteria versus background according to the programme. The classifiers could be retrained by the user via the supply of more samples to the programme. Once satisfied with the results, for example the boundaries drawn around the cells were correct, and the areas marked as background contained no cells, the result could be created. This result was used to calculate the percentage of the image that is taken up with class one compared to

class two. In this way, the percentage coverage of bacteria on the sample was determined.

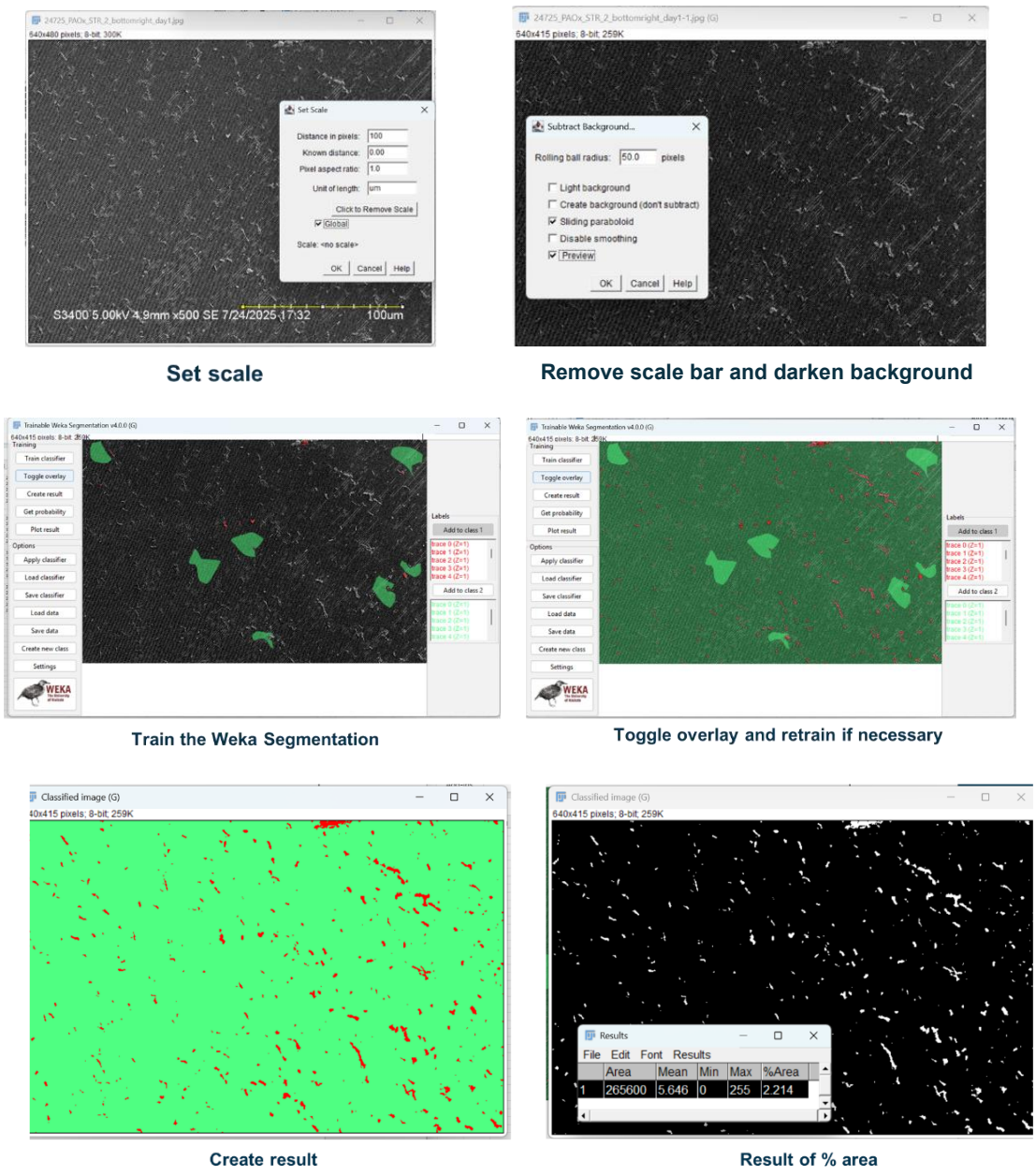


Figure 5.10: Process for percentage area coverage by bacteria on PAOMEC samples using Trainable Weka Segmentation plugin in Fiji ImageJ software.

Prior to performing the cell adhesion assays, the test organism was changed from using *E. coli* to *P. fluorescens*. *P. fluorescens* is a gram-negative, rod shaped bacteria that has been well-documented to have a capacity to form biofilms.[295,296] Although not a human pathogen, this soil-based bacteria was selected for this work due to its biofilm-forming properties. It was decided that this would sufficiently test the antibiofouling properties of the PAOMEC surfaces compared to the bacteria used

in earlier, preparatory work. The *E. coli* and *S. epidermidis* strains that had been used in preliminary studies, are both reported to be a low biofilm forming strains in their respective species.[297,298]

Once confirmed, cell testing was performed under similar conditions as before, as imaged in **Figure 5.11**. An overnight culture of *P. fluorescens* was prepared in LB and grown at 37 ºC. A subculture was made in fresh LB and left to shake at 250 rpm at 37 ºC. Once the log growth phase was reached, the mixture was centrifuged for ten minutes at 5000 rpm and the pellet that formed was resuspended in fresh LB to give a highly concentrated mixture. The sample was then diluted to give a suspension with an OD_{600} of 0.2. Samples were prepared as before by soaking in sterilised, deionised water overnight. The overnight ethanol soaking step was removed to shorten the preparation process. Instead, after samples were allowed to dry in sterile conditions and fixed into wells of a 48-well plate using grease, they were then rinsed with ethanol to ensure each well was sterile and no bacteria were present and then left to dry. There were two technical replicates of each sample type present and the surrounding empty wells were filled with sterile, deionised water to prevent evaporation of LB overnight. The suspension, with an OD_{600} of 0.2, was then added to each well containing a sample, and the well plate was placed in an oven overnight and shaken lightly at 50 rpm at 37 ºC. The following day, PBS washes were performed in triplicate to remove any planktonic cells. A glutaraldehyde solution (2.5%) was prepared using PBS and added slowly on top of each sample. They were left in the fridge overnight to fix the bacteria to the sample, and a series of dehydration steps were performed the following day, using ethanol, to allow for imaging of the samples by SEM which is performed under vacuum. The samples were allowed to dry, then prepared for SEM analysis by attaching them carbon tabs on SEM stubs and gold coating them. As mentioned in **Chapter 4**, gold coating is a common technique used to help reduce charging issues faced with non-conductive samples, like the PAOMEC crosslinked materials.

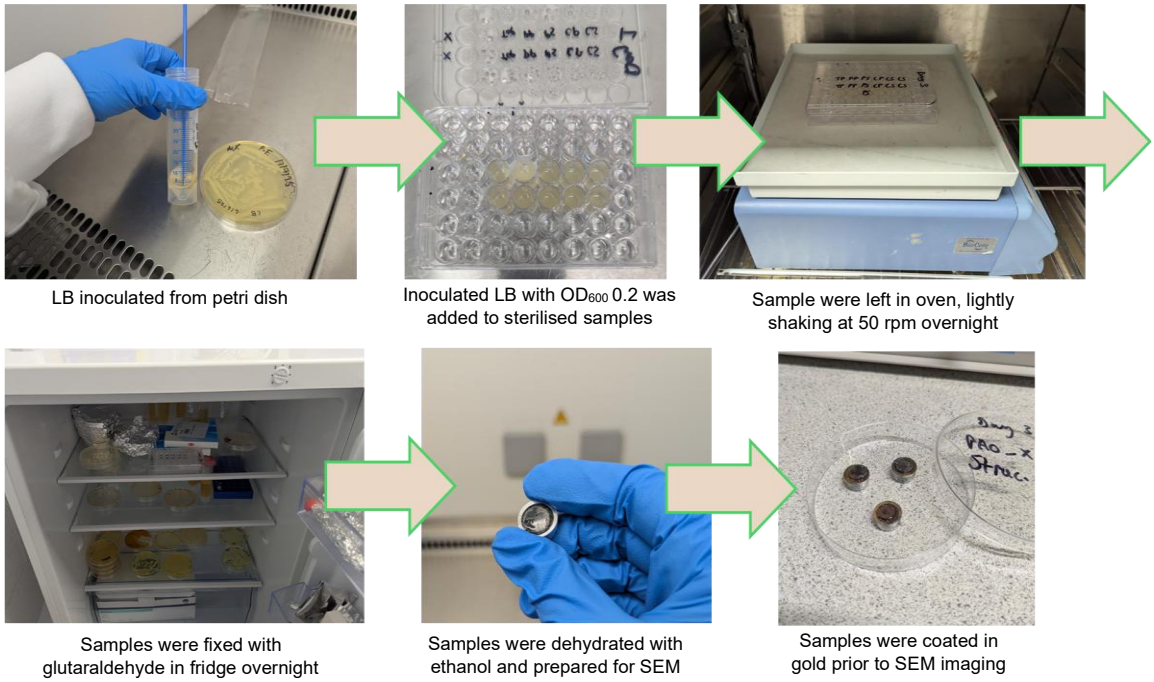


Figure 5.11: Cell testing protocol in preparation for SEM imaging for quantitative analysis of biofouling.

Analysis was completed via ImageJ and the Weka Segmentation plugin. The percentage area of the samples covered in bacteria ranged between approximately 2 and 10%. There was no definitive trend displayed in the data due to the impact of the standard deviation. The coefficient of variation was used to demonstrate the issue caused by the large standard deviation.[299] It is a statistical measure that is used to quantify the variability of data in relation to the mean value. In this analysis, values ranging from approximately 20 to 95% were measured demonstrating the high relative variability of this data, as calculated based on data and equation displayed in **Figure 5.13**. This was not unexpected as this experiment would need to be repeated twice more to have sufficient data for analysis, but a higher baseline for bacterial cell growth was desirable at this stage. It was theorised that increasing the concentration of cells introduced to the sample, could increase the overall amount of bacterial cell growth and therefore biofilm formation. The aim of this was to reduce the relative variability of the results thereby enabling easier comparison of results.

A second round of cell testing was conducted as before, this time using Topas and PDMS samples in order to preserve PAOMEC samples. Topas and PDMS were also selected as they have been reported to be used in cell testing in literature, and planar samples were readily accessible in the lab.[300,301] The same procedure was followed with one alteration made, two different cell suspensions were introduced to

each sample type, one with an OD_{600} of 0.2 and another with an OD_{600} of 1.0. The same sample cleaning, cell fixation and sample preparation steps were performed as before, and SEM analysis was completed. No obvious difference between cell coverage was observed based on the SEM images acquired. At this stage, it was decided that the growth of the *P. fluorescens* would be investigated.

It was originally selected that experimentation be completed at 37 ºC when working with *E. coli* and *S. epidermidis*. The eventual goal of these materials is to find use in healthcare and thus creating conditions mimicking the human body was prioritised. Additionally, future experiments were planned with other bacterial strains under flow conditions. As such, the aim was to reduce as many other variables as was possible, hence work was commenced at 37 ºC with *P. fluorescens* so that results from future testing were comparable. Due to the nature of *P. fluorescens* and it not being a human pathogen, it was thought that the lower cell growth could be due to the non-optimal conditions for cell growth. Some strains of *P. fluorescens* have been identified within the human body and as such can survive in conditions of 37 ºC.[302] That being said, it has been theorised that the ability of *P. fluorescens* to exist in such conditions is due to its ability to exist in viable-but-not-culturable conditions. This is the state in which bacteria can continue to survive and have metabolic activity but do not replicate.[303] Strains of *P. fluorescens* isolated from non-mammalian sources have been reported to have a permissive growth range between 4 and 32 ºC while those isolated from mammalian sources can reach 37 ºC.[303] As demonstrated in the earlier cell tests, the culturing of *P. fluorescens* was possible but the time taken for the sub cultures to reach the exponential stage of growth, with an OD_{600} of 0.32, was seven hours. It was therefore clear that these temperature conditions were likely suboptimal and to confirm this, growth curve analysis was completed.

The analysis was performed at three different temperatures, 25 ºC, 30 ºC and 37 ºC. At both 30 ºC and 37 ºC, the growth curve analysis was completed in conical flasks and centrifuge tubes. Colleagues had previously noted differences in growth rates of different bacteria when using each vessel type. It had been theorised that increased growth rates were due to better aeration in the conical flask during stirring of the media. Growth curves, as in **Figure 5.12**, confirmed slowest bacterial growth at 37 ºC in both vessels. Faster growth was observed at room temperature, approximately

25 ºC, but the growth curves at 30 ºC were elucidated as the optimal temperature. As a result, it was decided to proceed with cell testing using 30 ºC conditions. These temperature conditions were commonly reported in the literature surrounding analysis of biofilm formation using the same strain of *P. fluorescens WCS365.*[304,305]

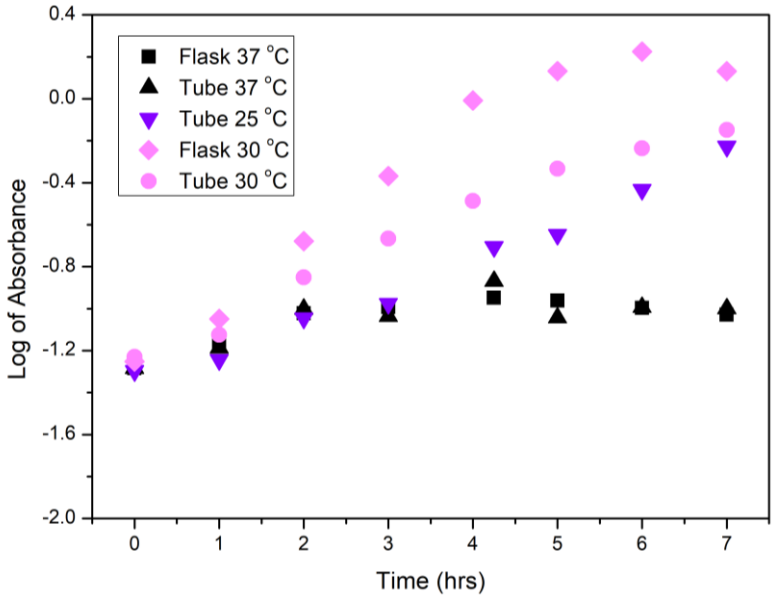
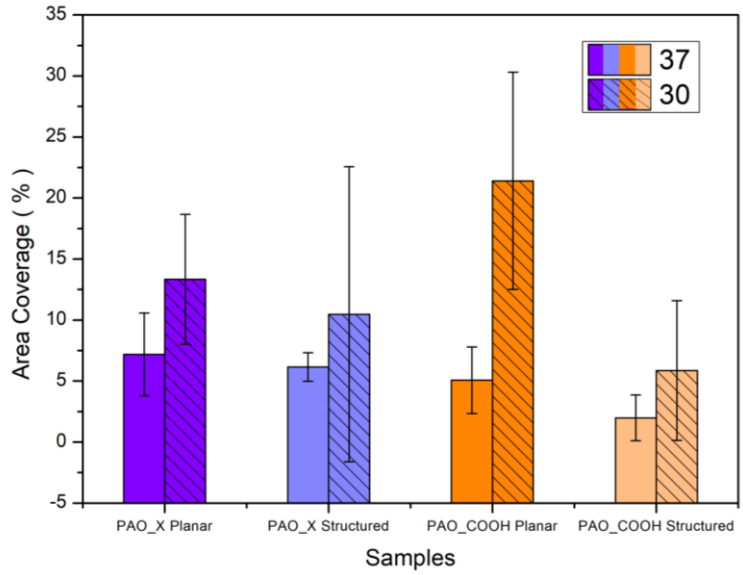


Figure 5.12: Growth curve of P. fluorescens *at three different temperatures 25 ºC, 30 ºC and 37 ºC.*

Cell testing was performed as before, with the exception that samples were left incubate with inoculated LB in an oven at 30 ºC and the samples were again analysed by SEM. It became evident, when under the microscope, that one of each of the structured samples had been placed into the wells upside down. The iridescence discussed and shown previously is a good indication of the structure on the sample. Due to the height of the samples prepared for cell testing being less than 1 mm thick; however, determining which side of the sample the structure is on was very difficult. As such, it was common practice to etch a mark on the planar side of the sample to aid identification by eye. The pre-soaking steps in sterile water added a further complication. Post soaking and before the samples had fully dried, the iridescence and etched marks were more difficult to see. This difficulty gave rise to more opportunity for human error, as had occurred in this round of cell testing. To solve this problem, removal of this pre-soaking step was suggested. To do this another DDM was performed to ensure no leachates from the materials would cause bacterial cell death if the samples were not soaked. This is discussed in further detail below.

The results, as in **Figure 5.13**, could not be used to make any conclusive statements due to the lack of a technical replicate. However, they did demonstrate that 30 ºC growth conditions increased the rate at which the exponential growth phase was reached by the inoculated LB thereby making this stage of the cell testing process more efficient. After four hours an OD_{600} of 0.5 was reached compared to the seven hours taken to reach OD_{600} of 0.37. Additionally, increased percentage area coverage was noted on planar sample surfaces in comparison to structured surfaces in the case of both PAO_X and PAO_COOH samples. Instead of bacteria covering, at most, approximately 10% of the planar samples, up to 20% coverage was noted. The difference in percentage area coverage between testing performed at 30 ºC and 37 ºC is displayed in **Figure 5.13**. It was decided that conditions had been sufficiently optimised, and the cell testing was to be repeated using these conditions.



$$\frac{\delta}{\mu} \times 100\,\% = coefficient\ of\ variation$$

$$where\ \ \delta = stardard\ deviation$$

$$and\ \mu = mean\ of\ data$$

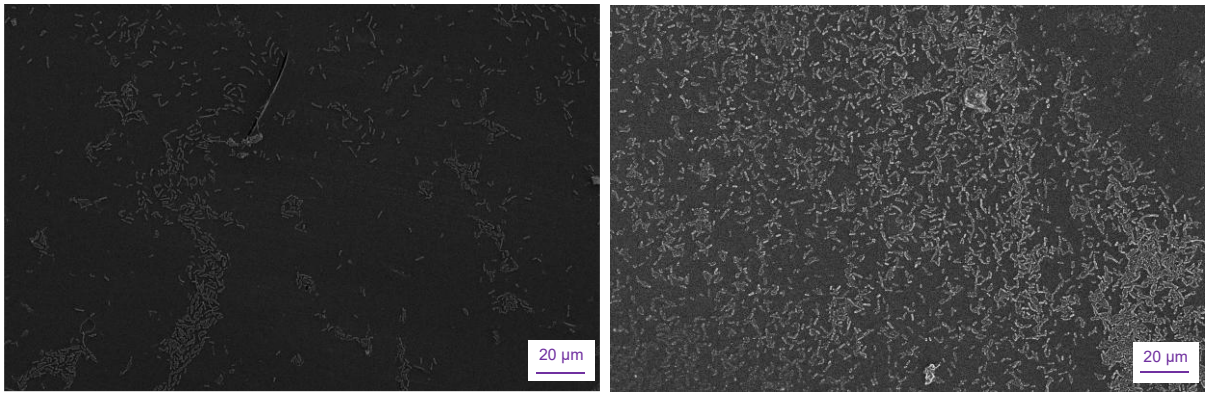


Figure 5.13: Comparative column chart showing percentage area coverage of each sample type by P. fluorescens *at 37 ºC and 30 ºC (top right) where error bar represent standard deviation; equation used to calculate coefficient of variation demonstrating the variability of data collected at 30 ºC (top right); and SEM*

images of PAO_X at 37 ºC (bottom left) and 30 ºC (bottom right) highlighting the difference observed in percentage coverage of samples by bacteria.

Prior to this, DDM was once again carried out. This was completed for two reasons; firstly, it had not yet been performed using *P. fluorescens*, and secondly, it was important to ensure any leachates present would not cause any damage to *P. fluorescens*. Each agar dish was introduced to a lawn of *P. fluorescens*, four samples were then introduced to each plate. PAO_X and PAO_COOH planar samples, one post-soaking in water and one from storage in a desiccator without soaking. As before, a positive and negative control were also placed in the petri dish, namely a disc containing gentamycin and a blank disc, respectively. Preliminary tests were run with ampicillin loaded discs, as had been previously used. No measurable zone of inhibition was observed with *P. fluorescens,* and thus gentamycin loaded discs were used instead. The plates were left in the oven overnight at 30 ºC and, as before, analysis was completed the following day. A diffusion diameter of 18 mm (±2.0 mm) was calculated from the gentamycin loaded discs. There were no measurable diffusion diameters observed around any of the crosslinked PAOMEC samples. As such, it was decided that the pre-soaking step could be skipped. This not only resulted in each round of cell testing being shortened by a day, but it also lowered the chance of a structured sample being placed in a well incorrectly.

The cell testing was then performed again under said conditions, and no soaking steps were incorporated. After fixation of the cells using glutaraldehyde and dehydration steps, the surfaces of some of the samples were noted to have a residual gel-like substance on them, as imaged in **Figure 5.14**. Upon performing SEM imaging, it became clear that a new problem had arisen. It was observed that clear images of bacteria could be seen on some samples but for many others this was not the case. As in **Figure 5.14**, there were samples where it looked as though a thick covering had formed preventing visualisation of bacterial cells. Additionally, in some cases with the structured samples, areas of the linear surface topography were also not visible. In literature, mention has been made of the polymerisation of glutaraldehyde in aqueous conditions. The polymerisation reaction is pH- and temperature-dependent.[306,307] The glutaraldehyde solution made up in PBS buffer that was used in the aforementioned cell testing round had been made up over a week prior to the cell testing. Although stored in the fridge at 4 ºC, it was possible

that the glutaraldehyde, having been taken in and out of the fridge to fix samples from the previous cell testing run, had partially polymerised.

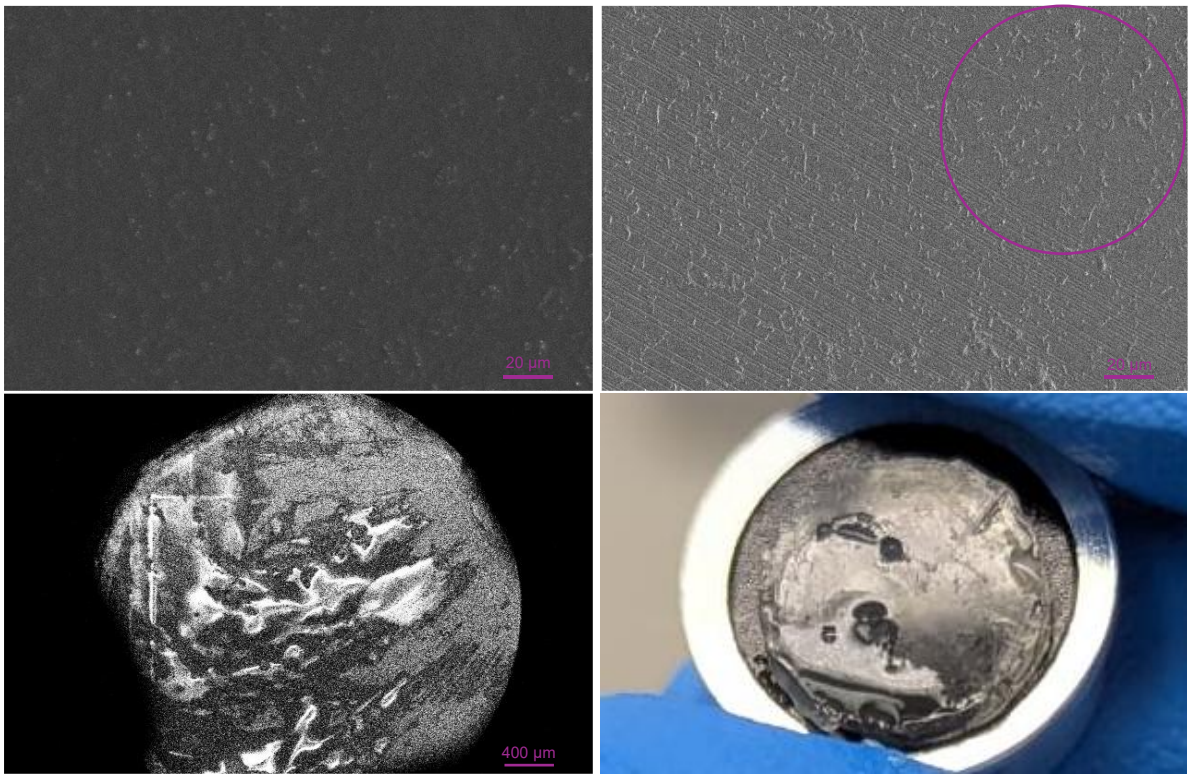


Figure 5.14: SEM images of planar and structured sample demonstrating less visible bacteria and structures - as circled, with 20 µm scale bar (top); SEM of full sample (bottom left) with 400 µm scale bar; and photograph of the same sample showing the polymerised, gel-like substance observed.

Based on these observations, no quantitative analysis could be performed, and it was decided to make fresh glutaraldehyde prior to each cell testing round as a precaution and preventative measure.

5.2.3 Static Antibiofouling Cell Testing – The Results

The cell testing was carried out as per the conditions that were defined in **Section 5.2.2**. Fresh samples were prepared and stored in a desiccator. Once the cell testing protocol was ready, two technical replicates of each sample type were introduced to the 48-well plate. The samples were washed three times with ethanol, with a final soak for 20 mins to remove any contaminants. They were rinsed with sterile LB and left to dry, and once dried cells were introduced. Cells were grown overnight, and a subculture was isolated and stirred at 200 rpm until an OD_{600} of 0.5 or greater. Once reached, the inoculated culture was shaken at 5000 rpm for ten minutes. The resulting pellet was resuspended in fresh LB, and the concentrated solution was

used to create a diluted inoculated LB sample. This was added to each well containing the fixed samples. The samples were allowed to shake at 50 rpm overnight in an oven set at 30 ºC. After 24 hours, the LB was removed, and the samples were rinsed thrice with PBS buffer to remove any planktonic cells. The freshly made glutaraldehyde solution (2.5%) was then added to each sample and left overnight at 4 ºC to fix the cells to the sample surfaces. A dehydration step was carried out by a series of ethanol washes with increasing concentrations. The samples were left to dry and then prepared for SEM analysis. As before, each sample was added to a SEM stub and fixed to the stub with sealant. They were gold coated, and five images were taken of each sample, in the four quadrants of each sample and in the centre. ImageJ Weka Segmentation analysis was completed and the results represented in a box plot, as in **Figure 5.15**.

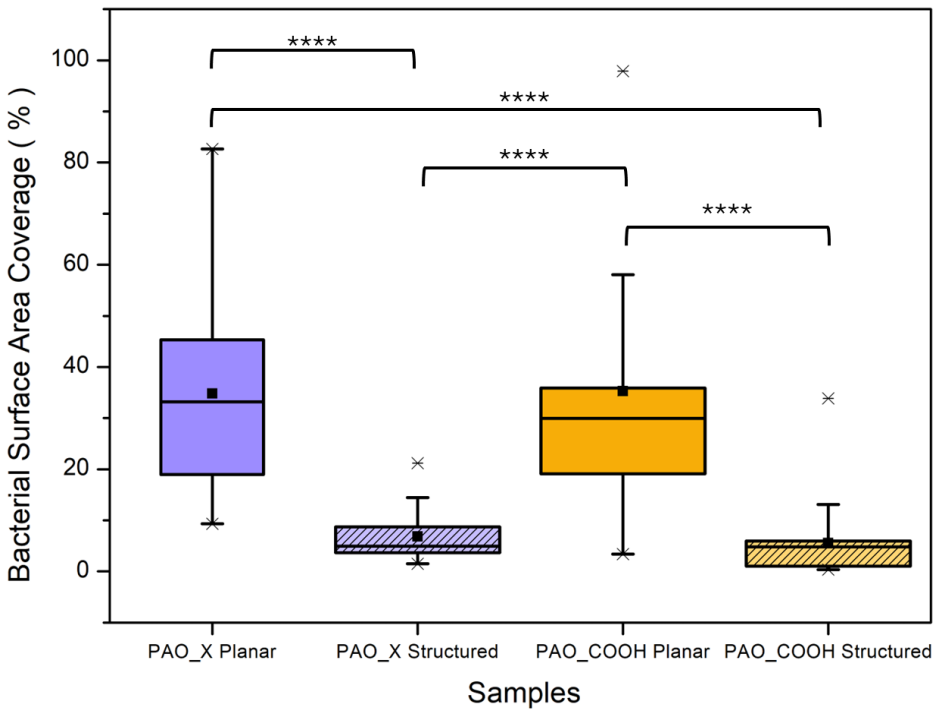


Figure 5.15: Box plot of the percentage area coverage of the crosslinked surfaces with P. fluorescens. *The maximal and minimal data point of each dataset were displayed with crosses with a dash; the mean of each dataset is represented by a black square. The statistical analysis, specifically Kruskal–Wallis H test, and a Dunn post-hoc test with a Bonferroni correction showed statistical significance between samples where **** is noted where p ≤ 0.0001.*

As in **Figure 5.15**, the results of the static antibiofouling testing elucidated the influence of structures and surface charge. Based on observations alone a clear pattern was observed. Higher percentages of bacterial cell coverage were measured on planar surfaces in comparison to structured surfaces. There were no differences

between charged and uncharged surfaces based on preliminary observations. Statistical analysis was then carried out using R.

Firstly, analysis of the normality of the data was completed. The Shapiro-Wilk test, a normality test used for sample sizes generally smaller than 50, was utilised.[308] It showed that only one of the four samples, the planar PAO_X, had a normal distribution. The skewness of the data was not unexpected. Due to the nature of the static cell testing and the way biofilm formation proceeds in *P. fluorescens*, outliers in the data were observed. Once attached to a surface, the bacteria begin to produce extracellular polysaccharides and form a sessile, highly-structured community of bacteria.[295] Biofilms form in a three dimensional manner and due to the complex aggregation of bacteria and EPS matrices, they can take many different shapes and sizes, as can be observed in **Figure 5.16**. For this reason, some areas of the sample have high concentrations of bacteria and biofilm formation while others have far less. The different colours in **Figure 5.16** are used to highlight the variance in coverage and biofilm shape and size and are for visualisation purposes only, no data analysis was completed with these FESEM images.

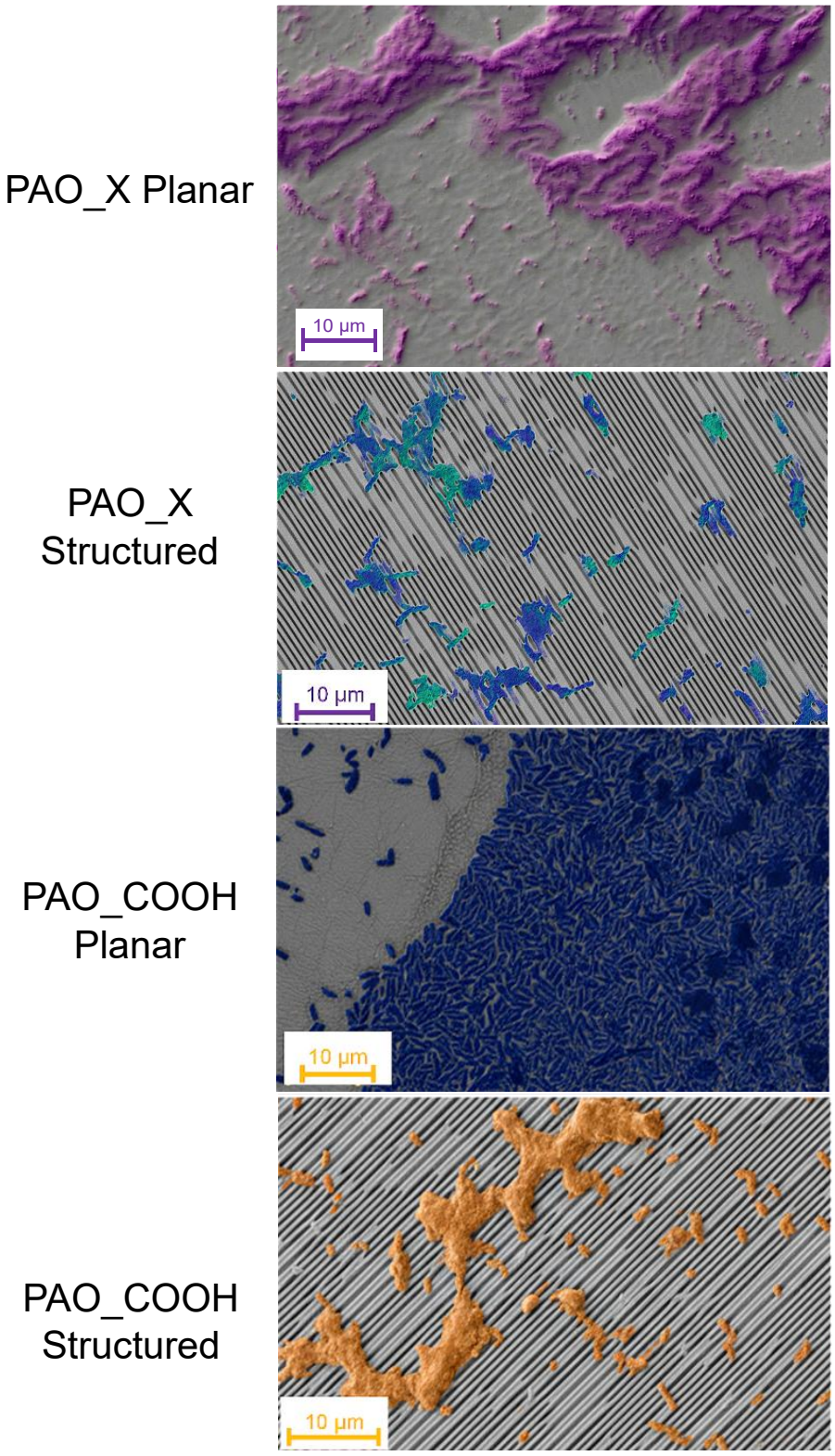


Figure 5.16: FESEM images of PAO_X and PAO_COOH structured and planar samples to highlight the difference in bacterial cell coverage of the surfaces as well as the different types of biofilms observed. Colour added using AI-assisted image editor.[309]

Due to the non-normal distribution and the factorial nature of the data, a variety of non-parametric tests were performed. The Scheirer–Ray–Hare test, a non-parametric version of a 2-way analysis of variance (ANOVA) test, was performed. This test was selected to compare the two independent variables, structure and charge. This showed structures on the surface had a statistically significant effect on the biofilm formation on the sample. P-values greater than 0.05 were calculated in relation to charge and the interaction between structure and charge, as in **Table C1** in **Appendix C**. This analysis confirmed that the antibiofouling capabilities of the samples, was not significantly affected by surface charge. Additionally, the surface charge had no effect on the antifouling properties of the structured surfaces.

As a follow-up, to support previous statistical analysis, the Kruskal–Wallis H test, was completed followed by a Dunn post-hoc test with a Bonferroni correction analysis. This was performed to confirm the findings of the Scheirer–Ray–Hare test. It is often denoted a non-parametric version of a one-way ANOVA. It was used to determine whether there were significant differences between two or more independent variables on a dependent variable. A p-value < 2.2e-16 was calculated demonstrating that there was a statistically significant difference between at least one of the four groups being analysed. A post-hoc test was then performed to further investigate the source of the significance. The Dunn post hoc test is a pairwise multiple comparison procedure that can be completed once the null hypothesis of the Kruskal–Wallis H test has been rejected, as is the case here. The Bonferroni adjustment was used to allow for multiway comparison, essentially allowing for comparison between each of the sample types.[310,311] This analysis gave results in agreement with the Scheirer–Ray–Hare test. Statistical significance was found between the planar and structured samples, but charge was found to have no significant effect on the antibiofouling properties of the samples, as displayed in the in **Table C.2** in **Appendix C**

It has been theorised that sub-micron and microstructured surfaces reduce the ability of the bacteria to form biofilm due to the uneven surface. As in **Figure 5.17**, based on FESEM analysis completed, bacterial cells can lie atop and at times fill in between the ridges and gaps. This uneven surface is believed to be impeding either the first or second stages of biofilm formation, namely: attachment of the cells to the surface and colony or microcolony formation, respectively.[74,75] There have been

previous reports that the overall reduction in the top surface area fraction, in this case due to the presents of the channels in between the lines, may inhibit interaction between the available surface and bacterial cells.[312]

The surface topography may also influence the maturation stages involved in biofilm formation. Based on literature sources, different strains of *P. fluorescens* vary in size but generally range in width between 0.3 μm and 1 μm and lengths between 1.0 μm and 2. 5 μm.[313–316] No values were observed in the literature specifically relating to *P. fluorescens* strain, *WCS365;* however, based on FESEM analysis completed on samples, the cells were measured to be approximately 0.8 ± 0.1 μm. This may remove the ease of bacterial cells fitting between the ridged lines into the channels, which are 0.4 μm wide, therefore preventing the clustering of bacteria that is required to form biofilms.

That being said, the elasticity of the surfaces may also play a role in the antibiofouling nature of the structures. Studies have been performed investigating the effect of elasticity on biofouling. For example, Tian et al. found that under flow surfaces with higher elasticity were less likely to be fouled by bacteria over rigid surfaces.[317] Although both planar and structured samples had low Youngs' Moduli due to the elastic nature of the crosslinked material, the bacterial cells, when landing on the structured surface, may cause ridges to move and partially collapse together, as in **Figure 5.17**. The unstable nature of the surface may also enable the bacteria to fit between the gaps despite the cells being generally larger than the gaps themselves. This partial collapse and instability again may result in lower bacterial adhesion to the surface or the prevention of clustering upon bacterial cell growth due to an unsatisfactory environment.

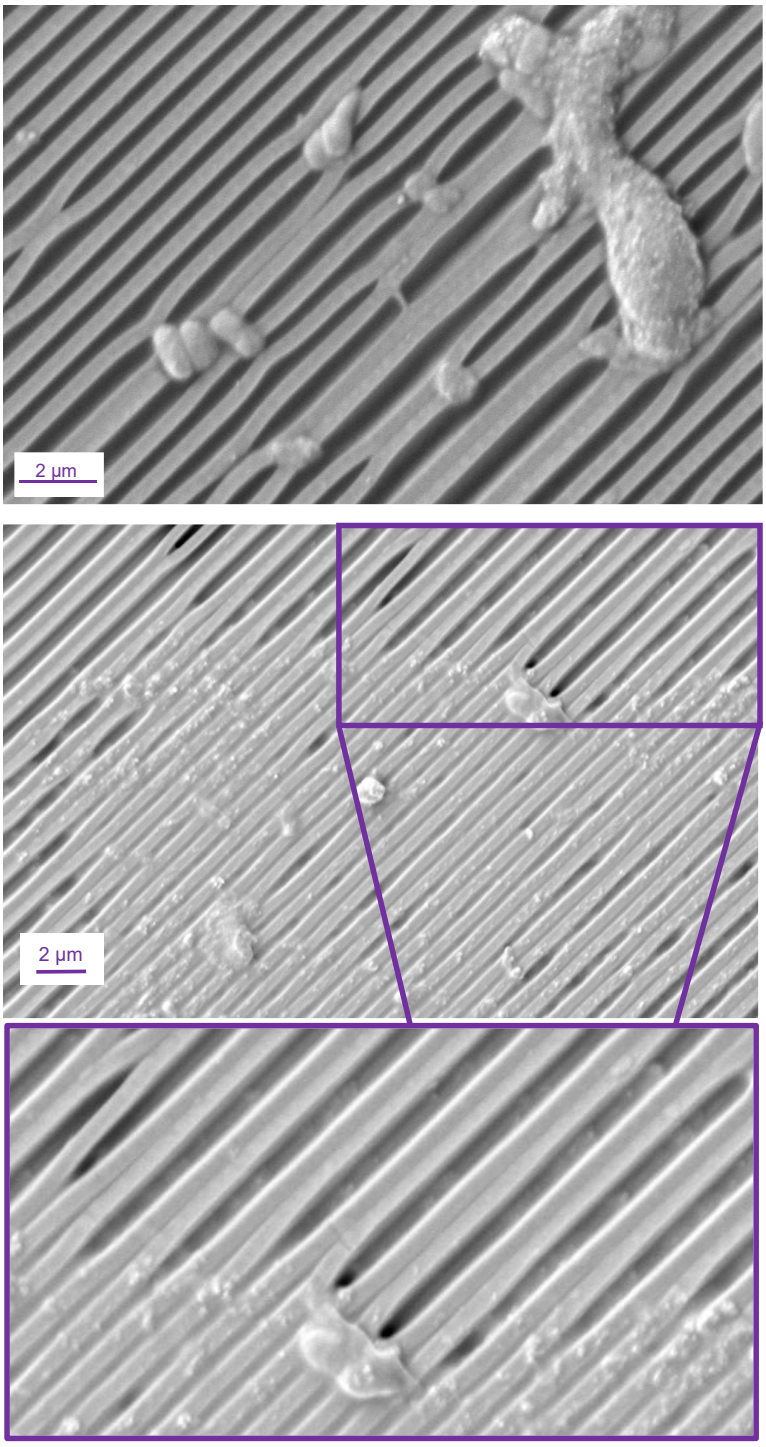


Figure 5.17: FESEM images which elucidate the bending of structures. The zoomed in area (bottom) of one of the FESEM images highlights the possibility of some bacteria cells falling between the lined ridges into the channels.

Chung et al. reported that microscale structured surfaces moulded from Sharlet AF, a biomimetic pattern that mimics shark skin, resulted in 47% reduction in biofilm formation when compared to planar surfaces. It was suggested that the *S. aureus* could not form biofilm as efficiently, due to the cells growing between the structures

while the structures behaved as obstacles preventing cell clustering.[318] Similar observations were made by Pingle et al. when different size surface topographies demonstrated reduction in *P. aeruginosa* biofilm formation.[319]

The results demonstrated that surface charge had no significant effect on the antibiofouling properties of the samples. *P. fluorescens,* like a majority of other bacteria is negatively charged. Zeta potential different strains of *P. fluorescens* has been reported as ranging from approximately -10 to -30 mV at pH 6 and approximately -50 mV at pH 7.[320,321] It was thus anticipated that cells could be repelled from the surface in the case of the surface being negatively charged. Preliminary tests were run by Anton Paar using the SurPASS, a piece of equipment that can measure the zeta potential of surfaces at various temperatures, pH values and in various solvents. Early results showed both PAO_X and PAO_COOH surfaces to have negatively charged surfaces in PBS buffer at pH values of approximately 7.5. More testing is required across a variety of conditions before any conclusions can be drawn about the surface charge of either sample. That being said, however, temperature, pH, and salt concentrations are just some conditions that can influence zeta potential measurements and, as a result, surface charge.[322–324] The antibiofouling properties of surfaces functionalised in this way would therefore likely be affected by the environment in which the surface is placed. This would need to be considered in future testing and analysis for this type of surface functionalisation.

Based on the cell testing and analysis completed, under the conditions used, the change in surface functionality had no significant effect on the antibiofouling properties of PAOMEC materials, but sub-micron surface topography demonstrated exciting potential as an antibiofouling surface. No bacterial cell analysis could be completed on PCLDMA-based samples due to time constraints. However, due to the antibiofouling properties observed relating to the structured PAOMEC, investigation into the effect of this structure on mammalian cells was completed with PCLDMA:HDDA samples.

5.3 Introduction to the Influence of Surface Topography on Endothelial Cells

When fabricating surfaces with different surface chemistry and topography for antibiofouling purposes, performance of bacterial cell studies is not the only cell

testing of interest. Mammalian cell studies are also imperative. Such studies are needed to understand the influence of such alterations to a surface on the behaviour of mammalian cells.

While the primary goal of this research was to further understand how changing surface properties can influence cellular response in relation to bacteria and biofouling. The long-term aim for the materials fabricated and analysed in this project is for eventual use in biomaterials. A key consideration must therefore be how such materials and surfaces affect mammalian cells.

Endothelial cells (ECs) are a cell line of interest when investigating the potential of biomaterials for medicine, like in implantable medical devices or in relation to wound healing. ECs form the monolayer that acts as a cellular interface between circulation system and the underlying tissues. Their role is to control the movement of circulatory materials into and out of the blood stream. During foetal development the entire circulatory system is originally made up of basal lamina, a support layer of extracellular matrix, and ECs. From the signalling of said ECs, development of connective tissue and muscle, for example, to line arteries and veins can occur. In this way, the endothelium, as a whole, has a critical signalling role. Its response to such stimuli can impact the health of vascular system and various other adjacent systems.

Blood supply is a fundamental consideration when discussing the wound healing process. The growth of new tissue at the site of the wound depends heavily on ECs. During the process, activation of ECs can lead to the formation of a network of microcapillaries. This is performed to restore blood supply, and the associated benefits, to areas that have been damaged. This can, in turn, promote further angiogenesis and eventual tissue growth to enable successful wound healing.[325] The introduction of antibiofouling surfaces on implantable devices and understanding the interaction and effects that biomaterials have on ECs is therefore vital to not only preventing the rejection of said materials, but also enables the promotion of faster healing upon use.

Surface topography has, as a result, been an area of interest for improving endothelialisation of many biomaterials, including stents. Poor endothelialisation of stents can lead to thrombosis or restenosis, the re-narrowing of arterial walls. It has

been reported by Mirhosseini et al., that after the introduction of microscale texturing to coronary stents via a laser ablation process proliferation of Human Aortic Endothelial Cells (HAECs) increased.[326] The size and design of the structures also influence the behaviour of ECs. Almonacid Suarez et al. found that structured linear arrays with heights of 0.176 μm and periods of 1.5 μm had no effect on the alignment of ECs, while the large sizes of 2.1 μm in height and 9.9 μm periods resulted in alignment of the ECs along the grooves between the structures. This, in turn, prevented vascularisation over a 48-hour period but not cell proliferation.[327] Formentín et al. demonstrated that the ordering of the microstructures can be influential. Micropillars of widths approximately 1.8 μm and periods of 3 μm were shown to affect the morphology of HAECs, as imaged in **Figure 5.18**, giving more rounded and compact cells. Disordered structures also resulted in lower cell growth than planar and ordered microstructured surfaces.[328] Lutter et al elucidated how the shape of the microstructures, as imaged in **Figure 5.18**, can affect cell functionality and response too. Endothelisation was found to be significantly higher on the “pillow” structures which were 1 μm in height and 5 μm wide and had 5 μm distance between each. Dissimilarly, the peak structures that were 2 μm high, 2 μm wide and 4 μm apart, were found to negatively affect cell migration and significantly increase platelet adhesion thereby demonstrating possible thrombotic effects. The researchers theorised the shape of the structures was influential in these results with the “smooth” surfaces aiding endothelisation but the sharp or so-called “spikey” surfaces of the peaks resulting in negative implications for the ECs.[329]

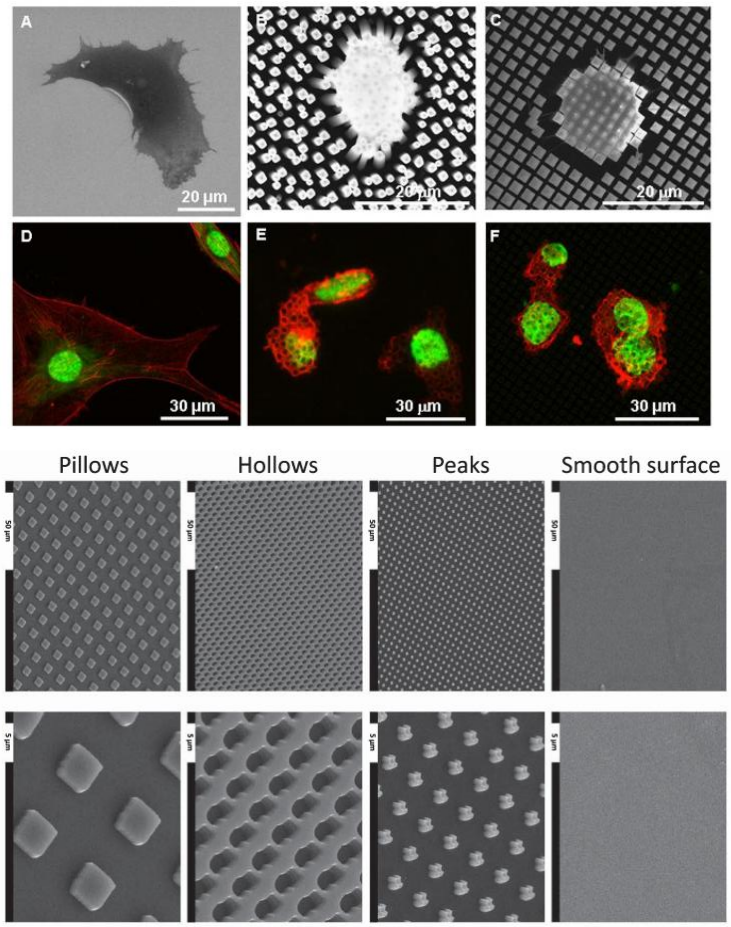


Figure 5.18: Influence of micropillars on cell morphology demonstrated with SEM and fluorescent confocal microscopy (top)[328]; and SEM images of different structured surfaces investigated for effects on ECs (bottom).[329]

This research, thus sought to investigate the possible influence of structures moulded from the T1 silicon template. Based on the exciting preliminary results that elucidated the antibiofouling properties of the sub-micron linear array, as discussed in **Section 5.2** of this chapter, further insight into cellular interactions between the sub-micron structures with the aforementioned parameters and HAECs was sought.

5.4 Cell Testing of Structured PCLDMA with HAECs

Based on the published work previously mentioned, planar crosslinked samples composed of neat HDDA, and PCLDMA:HDDA 1:4 and 1:9 blends were investigated for biocompatibility. A variety of assays that were performed demonstrated all three samples to be non-cytotoxic when tested with the epithelial cell line A549.[132] PCLDMA:HDDA crosslinked samples were given to a collaborator who examined the response of A549 cultures to the materials in question.

Building on insights gained from that research and the confirmed compatibility with A549 cells on planar surfaces, performing similar investigations on structured materials of the same crosslinked blend was of interest. Both A549 and ECs are adherent cell lines that form monolayer structures. This means that direct comparisons between the results could also be performed. Primary human cells were selected as the next model to use due to their sensitivity. As the cells are human-derived and primary in nature they are also extremely translational. ECs were chosen, as discussed above, due to the regular interface with biomedical devices. HAECs were specifically chosen for further studies as a model of vessels that commonly interact with medical devices such as catheters and stents. HAECs are cells obtained from the endothelium of the aorta.[330] This cell line is commonly used to model cardiac related diseases such as hypertension and arteriolosclerosis and are often used for coronary stent research.[331–333]

The primary focus of the cell testing was therefore to analyse primary cell viability on the planar and structured surfaces and add to the emerging literature surrounding the topic of the relationship between ECs and different surface topography. In addition to this, proliferation studies were to be performed to better our understanding of the behaviour of the HAECs and how they are affected, if at all, by the presence of the sub-micron structures.

5.4.1 Preliminary Cell Viability Analysis

Prior to commencement of HAEC experimentation, the crosslinked samples were prepared, as discussed in **Chapter 4**, by introducing sub-micron structures to the surface through replica moulding of the 1:4 PCLDMA:HDDA blend using the T1 silicon template, as in **Figure 5.19**. The samples were then shaped using a 6 mm hole punch to ensure secure placement, flush against the walls of the wells in a 96-well plate. The design of the cell studies discussed below, as well as the cell testing and analysis was completed alongside Dr Keith Rochfort, in the School of Biotechnology, DCU.

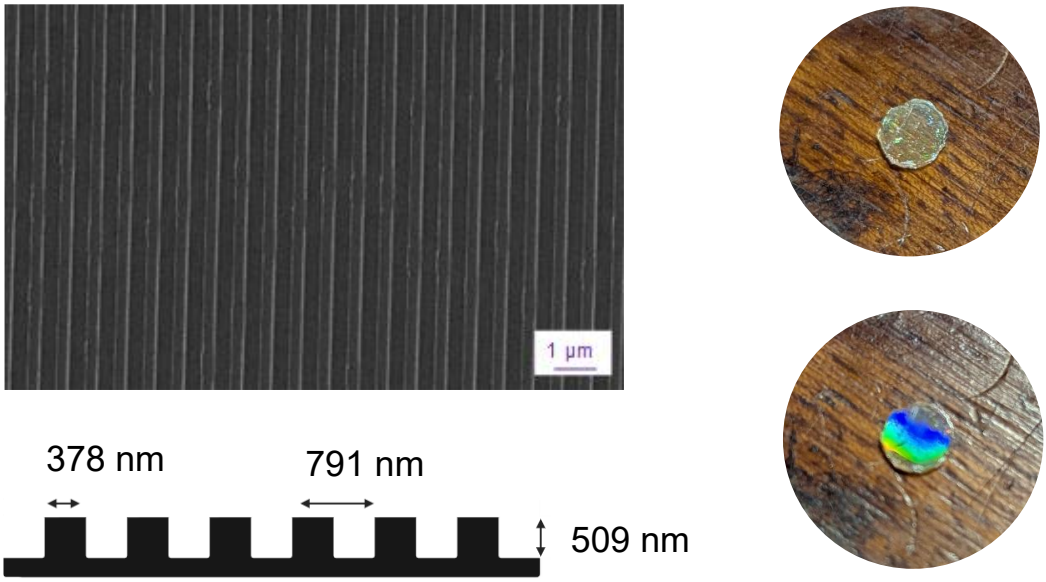


Figure 5.19: FESEM image of 1:4 PCLDMA:HDDA and side on illustration of the measured parameter of the structures; images of planar (top right) and structured (bottom right) PCLDMA:HDDA samples cut to 6 mm circles.

3-(4, 5-dimethylthiazolyl-2)-2, 5-diphenyltetrazolium bromide (MTT) assays were first performed to investigate the biocompatibility of the samples with the HAECs. Similar to the previously depicted MTS assay, as in **Figure 5.4**, MTT is a colorimetric assay, wherein the yellow MTT is converted to a purple formazan product through the reduction of the tetrazolium dye. The MTT can be taken up by the living cells as it is water soluble and can then undergo reduction by the reductase enzymes present in cells. The assay can therefore be used to assess cell viability and metabolic activity, as in **Figure 5.20**.[334]

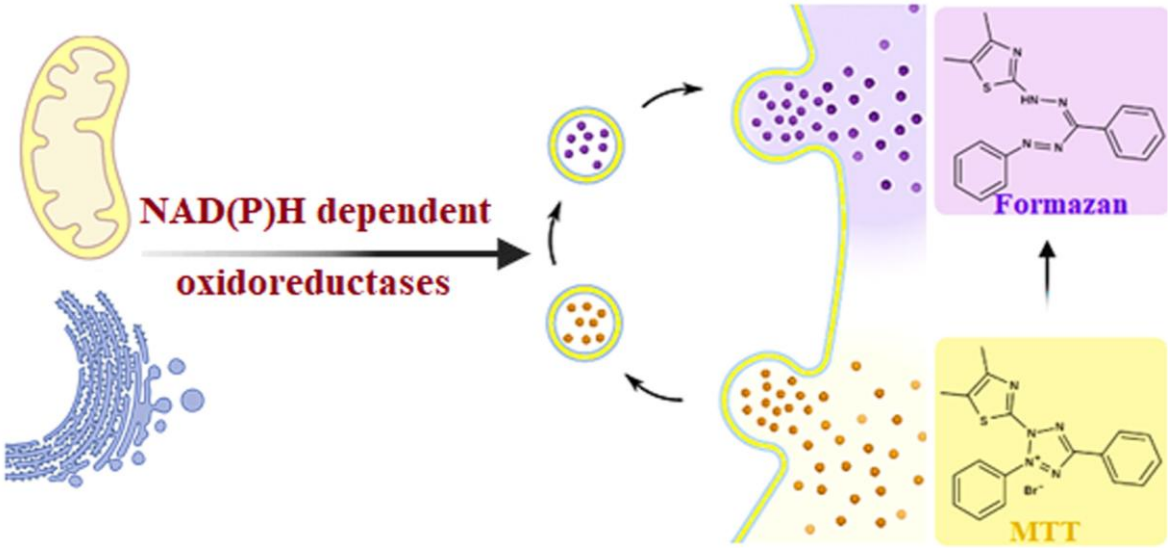


Figure 5.20: Reduction of MTT by enzymes to give purple formazan.[334]

The HAECs were exposed to the planar and structured crosslinked materials and left incubate at 37 ºC over three different time-points, 24, 48 and 72 hours. The MTT was then added to each well and left to incubate for four hours and absorbances were measured. The well, with no sample present and solely healthy HAECs was used as a negative control, and labelled control and hydrogen peroxide (H_2O_2) treated cells were utilised as a positive control. The results from the assay, as in **Figure 5.21**, were represented as a fold change when compared to the control. The absorbances measured were calculated to be relative to the control of each plate, by taking the negative control to be one. This technique was used for consistency purposes to account for unavoidable variables between plates. Based on the column chart, the negative control, planar and structured PCLDMA:HDDA crosslinked materials were all observed to show similar absorbance, while H_2O_2 treated cells had a lower absorbance.

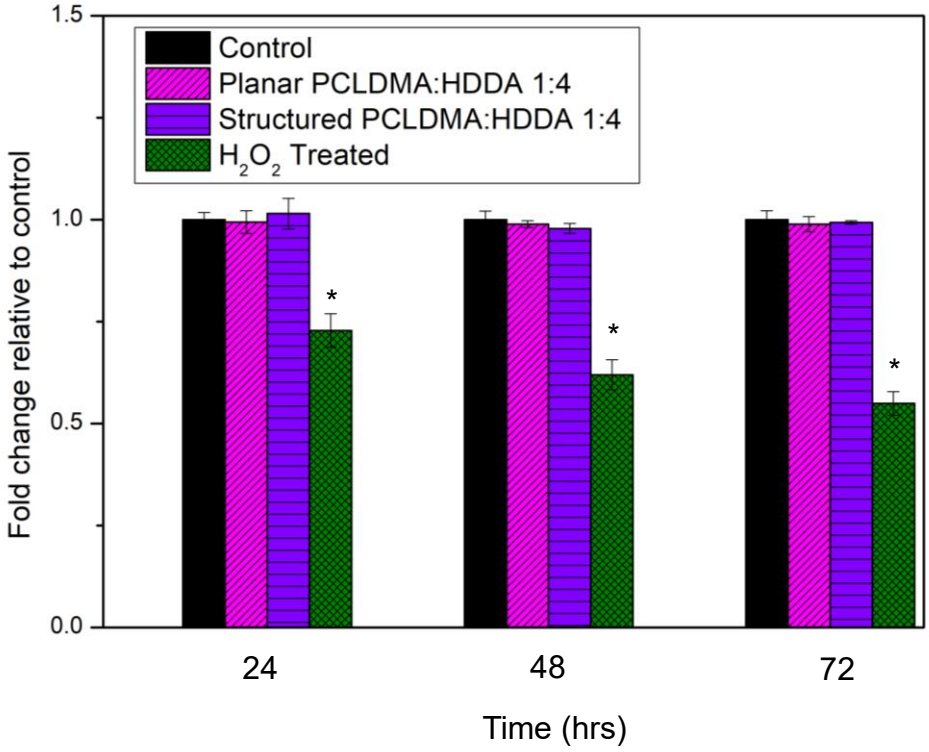


*Figure 5.21: Results from MTT assay of positive and negative controls and planar and structured PCLDMA:HDDA samples at three time-points. Error bars represent standard deviation. A p-value of < 0.05, signifying statistical significance, is represented using an *.*

Statistical analysis was carried out using R. A 2-way ANOVA followed by Tukey's honesty significant difference post-hoc tests were performed. 2-way ANOVA measures the relationship between two independent factors, in this study, time and sample type, and one dependent variable, in this case, absorbance measured.[335]

Once a significant difference was measured by this test, a Tukey post-hoc analysis was performed. This test was used to pairwise comparisons between the means of the data collected from each sample type. Through this type of analysis, the source of the significance reported by the 2-way ANOVA can be reported.[336]

As per the cell viability assay, significance was measured by the 2-way ANOVA and pairwise comparison found the source of this significance to be the cell viability of HAECs treated with H_2O_2 when compared with all other sample types. The analysis also confirmed that no statistically significant differences were measured between either of the PCLDMA:HDDA sample types and the control healthy cells. This result supported the previous studies reported with A549 cells, which demonstrated that planar PCLDMA:HDDA 1:4 crosslinked materials had no negative effect on cell viability. Further to this, the MTT assay confirmed that sub-micron structures had no effect on cell viability when compared to the planar surfaces. Due to the novelty of these structured samples, further analysis was needed to ensure that the samples were not cytotoxic to the HAECs.

While the MTT assay measured the presence of living cells, the lactase dehydrogenase (LDH) assay was used to investigate if cell death was being caused by the samples, and specifically by the presence of the structures. This assay was used to quantitatively measure the concentration of LDH that was released from lysed cells, with high sensitivity.[337] Measurements, as with the MTT assay, were taken spectrophotometrically. The samples were again incubated with HAECs for three time-points, 24, 48 and 72 hours. At the end of each timepoint, the LDH assay medium was added to the wells, and the samples were incubated to enable the two-step enzymatic process to commence. LDH catalyses the conversion of lactate to pyruvate and as a result, NAD^+ is converted to NADH by reduction. The diaphorase enzymes then reduces the present tetrazolium salt, using the previously generated NADH, which causes a measurable colour change; from yellow to formazan red, as illustrated in **Figure 5.22**.[334]

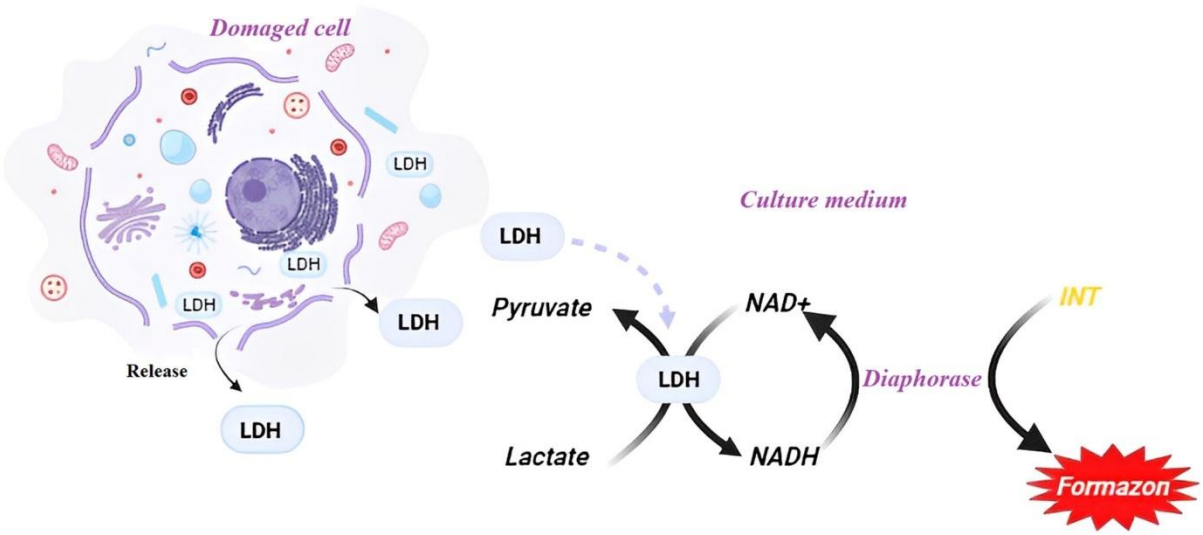


Figure 5.22: LDH assay mechanism of action via two-step enzymatic process, as illustrated by Khalef et al.[334]

The results of the LDH assay, as in **Figure 5.23**, were calculated based on the fold change relative to the control, as before with the MTT assay. Additionally, when performing this assay, in each well plate a top and bottom standard were measured, which represented the maximal and minimal amount of LDH that can be released by the volume of cells added to each well. The top standard consisted of a well of the same number cells, as were seeded in other wells, that were lysed controllably to give the maximum amount of LDH that can be produced. The second graph in **Figure 5.23** , represented the percentage of LDH produced compared to the maximal, top standard.

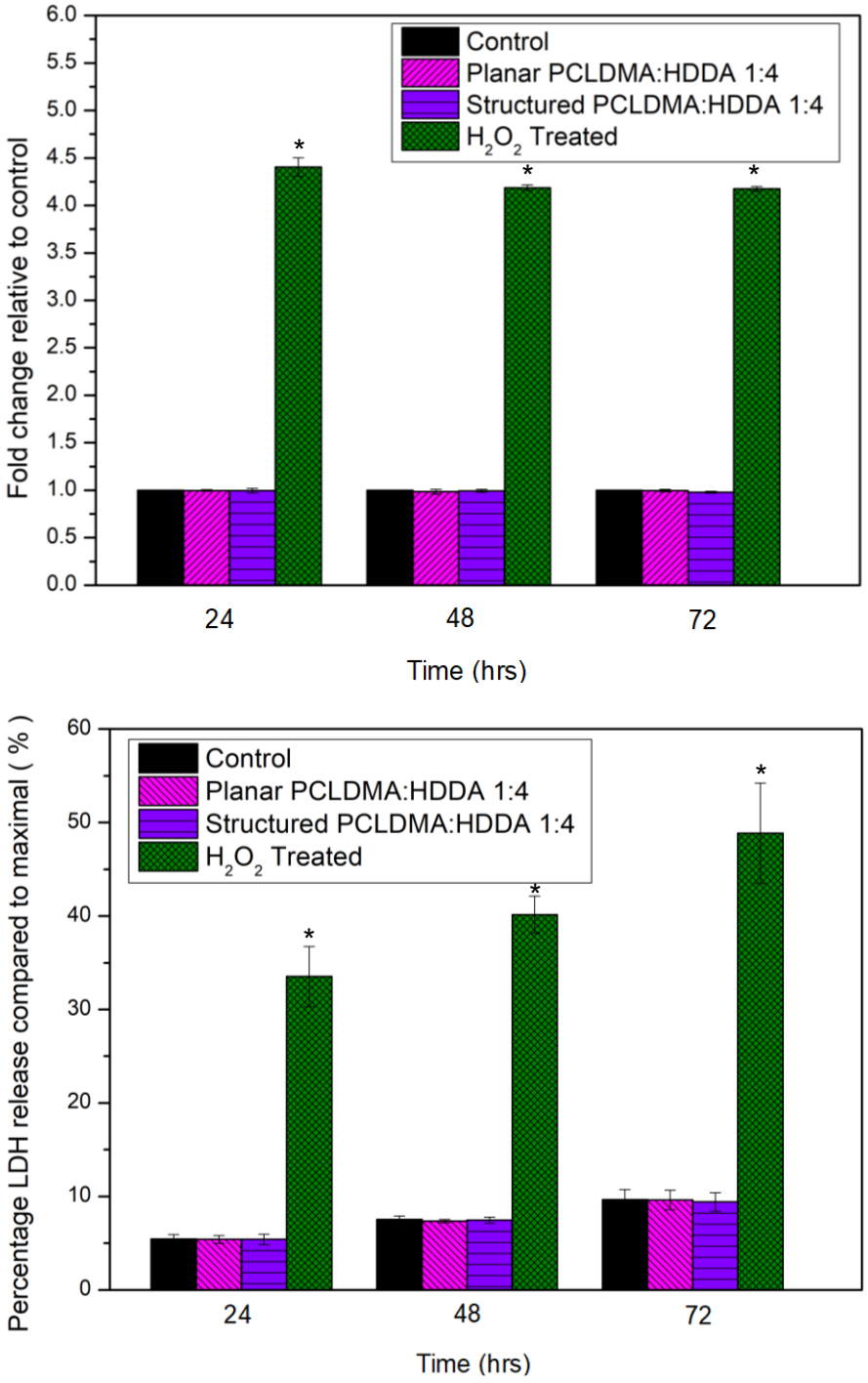


*Figure 5.23: LDH production represented by; fold change relative to the control (top); and percentage released relative to the top standard (bottom). Error bars represent standard deviation. A p-value of < 0.05, signifying statistical significance, is represented using an *.*

Both graphs, in **Figure 5.23**, illuminate the consistency of measurements taken at each time point when comparing the planar and structured surfaces with each other and the control. The H_2O_2 treated cells, as was expected, saw significantly higher percentages of LDH release. This was also confirmed by statistical analysis by 2-

way ANOVA and Tukey post-hoc tests. The percentage of LDH release was noted to increase for all samples across the three different time-points. This is a common observation measured in this type of cell testing due to natural cell turnover.

Based on the MTT and LDH assays, the structured and planar PCLDMA:HDDA samples were concluded to show no cytotoxic behaviour towards HAECs, and good cell viability was confirmed.

5.4.2 Preliminary Cell Proliferation Analysis

Once cell viability was confirmed, the influence of the PCLDMA:HDDA samples and specifically the structures on cell proliferation was investigated. Cell proliferation is an important consideration when designing materials for medical devices.[338,339] The MTT assay was used to assess cell proliferation with time points at 0, 24, 48 and 72 hours. Chemically, the assay functions in the same manner as previously discussed, but here cell metabolic activity serves as an indirect indicator of proliferation. The control was, again, healthy cells in a well plate with no samples present. Additionally, a positive control was used wherein Vascular Endothelial Growth Factor (VEGF) was introduced to the same volume of seeded cells to increase cell growth. This has been shown to increase cell growth for ECs.[340] Analysis, as in **Figure 5.24**, was completed where each measurement was compared to a fold change relative to the absorbance measured in the control, at 0 hours.

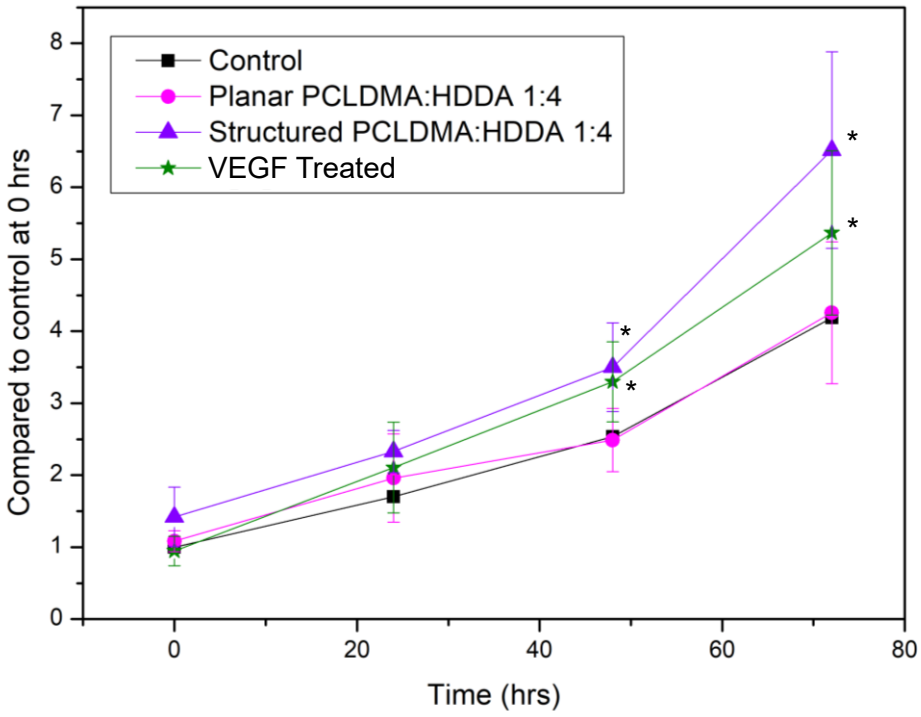


*Figure 5.24: Scatter plot of proliferation MTT assay performed over 4 timepoints, with measurements relative to T_0 of the control. Error bars represent standard deviation. A p-value of < 0.05, signifying statistical significance, is represented using an *.*

The results of this assay, as in **Figure 5.24**, and further supported by 2-way ANOVA followed by Tukey post-hoc tests demonstrated no difference in the proliferation of HAECs in the control and on planar PCLDMA:HDDA samples. This, again, confirmed the compatibility of the planar PCLDMA:HDDA with the HAECs. VEGF treated cells and cells on structured samples both showed significantly higher proliferation when compared to the control and planar cells. However, even more compelling results were ascertained from the assay of the structured PCLDMA:HDDA samples. The proliferation of HAECs on samples with sub-micron surface topography saw significantly more proliferation when measured against proliferation that was encouraged by the presence of VEGF.

It has been theorised in the literature that surface topography can result in increased cell proliferation for a variety of reasons. Mirhosseini et al., discussed how the surface topography resulted in increased hydrophilicity of the surfaces which has been observed to increase cell proliferation and cell adhesion. Additionally, due to the introduction of surface topography the surface area available to cells was also increased.[326] Similar conclusions were drawn in research that involved the

fabrication of nanoimprinted membranes using PCL. Increased cell proliferation of EA.hy926 cells was observed and it was theorised that increased surface area was a contributing factor. Additionally, the increased ability of the cells to adhere to and rearrange due to the presence of structures on the samples was suggested to influence cell morphology and proliferation.[341]

Further cell studies are required to better understand the reasoning behind the increased proliferation measured on the structured PCLDMA:HDDA samples, and the potential impact. Increased surface area and the increased ability for cells to attach to the structures, in favour of a flat surface, are possible reasons for the results discussed. Investigations of cell adhesion and inflammation behaviour are, for example, important to better understand. This would enable better understanding of the behaviour of HAECs on the surface. Furthermore, the inflammation assays would ensure the proliferation was not a result of dysregulation due to stress.

Further analysis including WCA of the structured surfaces and SEM of the samples, post incubation with cells, could be used to investigate the hydrophilicity of surfaces and cell morphology, respectively. Furthermore, bacterial cell testing with the structured PCLDMA:HDDA samples would need to be completed to confirm the influence of the structure on biofilm formation is consistent with different materials.

These results, act as early indicators of the potential of this novel sub-micron surface topography, not only as a means for creating antibiofouling surfaces but also as a support for cell proliferation.

5.5 Conclusions

The first section of this chapter reported on the bacterial cell testing used to assess the antibiofouling properties of crosslinked PAOMEC materials. Due to the novelty of the PAO_X and PAO_COOH samples, various assays including CV and MTS assays were tested for their suitability. Issues were faced with these assays due to the non-specific interactions between the samples and the chemicals in the assays. As such, a protocol for the testing of the samples that avoided the used of colorimetric assays was designed. The samples were exposed to *P. fluorescens* for 24 hours and after the removal of any planktonic bacteria in the media, the bacteria or biofilms attached

to the surfaces of the samples were fixed using glutaraldehyde. After cell fixation, the samples were prepared for SEM analysis.. Images were taken of each sample and analysis of the percentage coverage of the samples by bacteria was completed using image analysis software. This analysis, along with statistical analysis, confirmed the presence of the sub-micron structures on the PAO_X and PAO_COOH samples resulted in significantly lower biofilm formation over the 24-hour period. No significant differences in fouling were measured relative to the increased presence of carboxylic acid group surface functionality in the PAO_COOH samples.

Building on the potential demonstrated by the sub-micron structures, it was decided that cell testing using mammalian cells would be performed. Structured and planar PCLDMA:HDDA samples were selected for this analysis, and the cell testing was completed using HAECs. The biocompatibility of the samples was first tested using MTT assays to measure the cell viability and LDH assays to quantify cytotoxicity of the samples. Both crosslinked materials demonstrated high cell viability and low cytotoxicity comparative to the healthy HAECs used as a control. Analysis of cell proliferation was then performed via MTT assay. This assay confirmed comparable HAEC proliferation of the planar crosslinked PCLDMA:HDDA samples and the healthy control cells. More notably, significantly higher cell proliferation was measured on the structured PCLDMA:HDDA samples compared not only to planar samples of the same material and the control, but also to the VEGF treated cells.

These preliminary cell tests, both bacterial and mammalian, suggest the potential benefits of using this sub-micron surface topography in biomaterials. It not only has been shown to have potential antibiofouling properties but also demonstrated positive interactions with HAECs.

Chapter 6 Conclusions and Future Work

6.1 Chapter 3: Synthesis and Modification of Oligomers

PCL diol (M_n 1250) and PCL diol (M_n 530) underwent methacrylation reactions. The reaction parameters were refined to a molar ratio of 1:2:2.2.0 of PCL diol, Et_3N and MAC. The resulting PCLDMA-1350 and PCLDMA-630 were synthesised in isolated yields of 81-89% and 72%, respectively. To improve purity and yields in future experiments, new MAC would be purchased, and all reactants will be sufficiently dried prior to performing the percentage methacrylation.

The samples were chemically analysed by ^{1}H NMR and FTIR spectroscopy and the M_w and Đ of the samples were approximated using GPC analysis. PCLDMA-1350 was estimated to have the M_w 1008 g/mol and Đ of 1.37, while PCLDMA-630 was found to have the M_w 352 g/mol and Đ of 1.55. DSC was used to measure the thermal properties of PCLDMA materials and confirm the semi-crystallinity of the oligomers through observation of glass transitions and melting temperatures.

A second oligomer, PAOMEC was synthesised and analysed. The synthesis of the monomer AOMEC was performed and isolated yields of 70-75% were achieved. TU cocatalyst was synthesised and isolated in yields of 72%. Both reactants were analysed with ^{1}H NMR and ^{13}C NMR spectroscopy and upon confirmation of successful synthesis and purification, AOMEC was polymerised. PAOMEC was synthesised over three days and purified by column chromatography giving isolated yields of 80-89% and purity of 85%.

Chemical analysis of PAOMEC was also performed with ^{1}H NMR and FTIR spectroscopy. DSC analysis confirmed the PAOMEC to be amorphous, as is similar to other APCs. GPC analysis was used to estimate the M_w to range between 810 g/mol and 1200 g/mol with Đ ranging between 1.6 and 2.8. Future work would focus on further investigation of the quenching of this reaction, and optimisation of the conditions including working under dry conditions. Additionally, further refinement of the purification process would be performed to attempt to improve the percentage purity without sacrificing on percentage yield.

6.2 Chapter 4: Crosslinking, Structuring and Functionalisation

Crosslinking of planar surfaces was first performed with both PCLDMA-1350 and PCLDMA-630, to improve the process based on previous work completed in the Kelleher group. The replica moulding process was performed via UV-initiated photopolymerisation. PCLDMA, and the short chain monomer HDDA were blended as 1:4 and 1:9 mass ratios, respectively. FTIR analysis was completed to confirm successful crosslinking by removal of the peaks associated with the acrylate functionalities that are present on PCLDMA and HDDA. Structures on the sub-micron scale, of height 600 nm, width 400 nm and pitch 800 nm were introduced, for the first time, to the surface through the same replica moulding using the silica template, T1. Qualitative and quantitative analysis was carried out using FESEM and AFM techniques confirming the successful introduction of sub-micron surface topography.

Future work will involve improving the fidelity of the height of the structures moulded from this silicon template using PCLDMA-1350. Attempts to structure PCLDMA-630-based samples, with the same template, will also be made. WCA analysis of the planar crosslinked samples revealed consistent hydrophilic properties across all ratios of pre-crosslinking blends. Further WCA analysis will be completed on the structured samples to investigate the influence of the sub-micron structures on surface chemistry properties, such as the hydrophilicity and surface energy. An accelerated degradation study of the 1:9 blend was conducted, and the slow hydrolytic biodegradation of the material was demonstrated via mass loss analysis. Future studies on the degradation products will be performed, and a non-accelerated experiment will be designed.

Crosslinking and functionalisation of PAOMEC was also discussed in **Chapter 4.** This chapter discussed the first reported successful crosslinking of planar PAO_X and carboxylic acid functionalised PAO_COOH. Attempts were made to introduce amine functionalities to the crosslinked material with cystamine dihydrochloride, which were met with challenges. Future work will focus on the two-step process discussed in detail in the chapter, whereby the PAOMEC material will be crosslinked with the amine short chain functionality first, followed by the addition of SHX and formation of the crosslinked material. Qualitative FTIR analysis was undertaken to

demonstrate the addition of these functionalities but further is needed to provide quantitative results demonstrating the successful addition of carboxylic acid and amine functionalities.

This research also provided first evidence of the introduction of sub-micron surface topography to PAOMEC-based materials. PAO_X and PAO_COOH samples were structured successfully, again using the T1 template. FESEM and AFM confirmed successful moulding of the surface topography, as before. As with PCLDMA:HDDA samples, viscosity measurements were used to analyse the reactants. WCA analysis was performed on the planar crosslinked samples showing PAO_X to be more hydrophilic than PAO_COOH. Attempts were made to analyse the structured samples by WCA analysis, but no accurate results could be ascertained. This was due to the dispersion of the droplet within the microchannels that were created by the linear array of structures on the surface. Further investigation will be performed to determine the WCA of the structured surfaces.

Additionally, rheometric studies of the pre-crosslinking blends, to better optimise the viscosity of the materials for improved fidelity during the replica moulding process, as well as UV-rheometry to understand the crosslinking of the materials in more depth, would be of interest. Nanoindentation was utilised to measure the mechanical properties of the crosslinked networks as closer to that of elastomeric materials. An accelerated biodegradation study confirmed both samples to be degradable in biological conditions based on mass loss, DSC, FTIR and ^{1}H NMR analysis. Further analyses of the degradation products and the biocompatibility of said degraded materials are planned.

6.3 Chapter 5: Cell Testing

Bacterial cell testing was performed to assess the antibiofouling properties of PAO_X and PAO_COOH. In this way, because all crosslinked materials had a PAOMEC backbone, the influence of surface functionalisation and sub-micron surface topography could be investigated. Bacterial cell tests were thus conducted on the planar and structured, PAO_X and PAO_COOH samples. Due to the novelty of these materials, early tests were performed with MTS and CV assays to assess their suitability, but problems arose with both. It was thus decided that SEM analysis would be used to quantify the antibiofouling abilities of each surface type. *P.*

fluorescens was selected as the bacteria for this process due to its ability to form biofilms. Under optimal growth conditions, static antibiofouling tests were performed in triplicate and quantification of the biofouling was completed via SEM analysis with post-analysis image process completed with the Weka Trainable Segmentation plugin on ImageJ.

The presence of carboxylic acid functionalities, which were expected to introduce anionic surface charge, showed no statistically significant antibiofouling behaviour. Further analysis is required to quantify surface charge of PAO_X and PAO_COOH surfaces to better the bacterial cell interactions at the surface interface. Based on the statistical analysis performed, it could be concluded that the presence of sub-micron surface topography significantly reduced biofilm formation demonstrating exciting potential for this type of surface modification.

Further tests to assess cell viability of the bacteria on the samples would also aid in understanding if the structured samples were antibacterial or solely antibiofouling. Additionally, at this stage only static antibiofouling tests have been performed but future work is planned to be completed in a flow cell. This set up aims to mimic conditions in the body to give further insight into how the antibiofouling nature of these structured materials could behave in the body as biomaterials. Analysis with bacterial cell lines that are more commonly associated with infection at the site of medical device implantation such as *S. aureus* and *S. epidermidis* as well as comparison between these gram-positive bacteria and gram-negative bacteria such as *E. coli* are also planned. Due to the potential demonstrated by the sub-micron structures, future cell testing is also planned with planar and structured PCLDMA:HDDA samples to assess the universality of this antibiofouling surface topography across various materials.

Mammalian cell testing has been commenced with Dr Keith Rochfort to better our understanding of how ECs, specifically HAECs, interact with the structured surfaces. Structured and planar PCLDMA:HDDA samples were fabricated and tested with cell viability, cytotoxicity and cell proliferation assays. Due to time constraints, mammalian cell testing was performed on the PCL-based samples and not the PAOMEC-based samples. This was due to the issues faced with colorimetric assays with crosslinked PAOMEC materials, which would have required the design of new

cell testing protocols. Additionally, the cell testing with ECs was aiming to build on earlier work done within the group which analysed to biocompatibility of PCL-based materials with other ECs.

Both planar and structured samples demonstrated good biocompatibility and proliferation. The sub-micron structured surfaces were shown to have significantly higher cell proliferation than the control, planar samples of the same material, and cells that had been treated with a growth factor. Further tests are planned to better understand the interaction between the HAECs and the structured surface including adhesion and inflammation assays.

This work has demonstrated the use of PAOMEC-based materials to assess the antibiofouling effects of different surface properties, individually or in combination, enabling like-with-like comparison. In the future, this material platform could be used to assess and compare a variety of surface properties to further understand the influence of different properties on biofouling. The preliminary bacterial and mammalian cell tests completed in this thesis also demonstrated the promising potential of the sub-micron surface topography with the aforementioned structural parameters. The encouraging results of these structured, crosslinked materials could be great interest for use in medical devices, not only due to the antibiofouling properties of but also due to the low cytotoxicity and high cell proliferation of mammalian cells.

Bibliography

1 P. S. Stewart and T. Bjarnsholt, Risk factors for chronic biofilm-related infection associated with implanted medical devices, *Clin. Microbiol. Infect.*, 2020, **26**, 1034–1038.
2 Recent Strategies to Combat Infections from Biofilm-Forming Bacteria on Orthopaedic Implants, https://www.mdpi.com/1422-0067/22/19/10243, (accessed 22 October 2025).
3 L. Lunelli, C. Potrich, L. Pasquardini and C. Pederzolli, in *Encyclopedia of Nanotechnology*, Springer, Dordrecht, 2012, pp. 1760–1766.
4 A. Rudin and P. Choi, in *The Elements of Polymer Science & Engineering (Third Edition)*, eds A. Rudin and P. Choi, Academic Press, Boston, 2013, pp. 1–62.
5 B. van Genabeek, B. A. G. Lamers, C. J. Hawker, E. W. Meijer, W. R. Gutekunst and B. V. K. J. Schmidt, Properties and applications of precision oligomer materials; where organic and polymer chemistry join forces, *J. Polym. Sci.*, 2021, **59**, 373–403.
6 Crystalline or amorphous, https://www.unsw.edu.au/science/our-schools/materials/engage-with-us/high-school-students-and-teachers/online-tutorials/polymers/structure-and-form/crystalline-or-amorphous, (accessed 26 October 2025).
7 Polymer | Description, Examples, Types, Material, Uses, & Facts | Britannica, https://www.britannica.com/science/polymer, (accessed 22 October 2025).
8 R. B. Chavan, S. Rathi, V. G. S. S. Jyothi and N. R. Shastri, Cellulose based polymers in development of amorphous solid dispersions, *Asian J. Pharm. Sci.*, 2019, **14**, 248–264.
9 Polymerization | Definition, Classes, & Examples | Britannica, https://www.britannica.com/science/polymerization, (accessed 22 October 2025).
10 Condensation Polymers (examples, answers, activities, experiment, videos), https://www.onlinemathlearning.com/polymers-condensation.html, (accessed 22 October 2025).
11 A. Rudin and P. Choi, in *The Elements of Polymer Science & Engineering (Third Edition)*, eds A. Rudin and P. Choi, Academic Press, Boston, 2013, pp. 305–339.
12 G. Odian, in *Encyclopedia of Polymer Science and Technology*, John Wiley & Sons, Ltd, 2011.
13 X. Xie, Z. Huo, E. Jang and R. Tong, Recent advances in enantioselective ring-opening polymerization and copolymerization, *Commun. Chem.*, 2023, **6**, 202.
14 S. Penczek, J. Pretula and S. Slomkowski, Ring-opening polymerization, *Chem. Teach. Int.*, 2021, **3**, 33–57.
15 O. Nuyken and S. D. Pask, Ring-Opening Polymerization—An Introductory Review, *Polymers*, 2013, **5**, 361–403.
16 C. Jérôme and P. Lecomte, Recent advances in the synthesis of aliphatic polyesters by ring-opening polymerization, *Adv. Drug Deliv. Rev.*, 2008, **60**, 1056–1076.
17 Z. Abdel Baki, H. Dib and T. Sahin, Overview: Polycarbonates via Ring-Opening Polymerization, Differences between Six- and Five-Membered Cyclic Carbonates: Inspiration for Green Alternatives, *Polymers*, 2022, **14**, 2031.
18 M. A. Woodruff and D. W. Hutmacher, The return of a forgotten polymer—Polycaprolactone in the 21st century, *Prog. Polym. Sci.*, 2010, **35**, 1217–1256.

19 A. Fernández-Tena, R. A. Pérez-Camargo, O. Coulembier, L. Sangroniz, N. Aranburu, G. Guerrica-Echevarria, G. Liu, D. Wang, D. Cavallo and A. J. Müller, Effect of Molecular Weight on the Crystallization and Melt Memory of Poly(ε-caprolactone) (PCL), *Macromolecules*, 2023, **56**, 4602–4620.
20 M. A. Ntrivala, A. C. Pitsavas, K. Lazaridou, Z. Baziakou, D. Karavasili, M. Papadimitriou, C. Ntagkopoulou, E. Balla and D. N. Bikiaris, Polycaprolactone (PCL): the biodegradable polyester shaping the future of materials – a review on synthesis, properties, biodegradation, applications and future perspectives, *Eur. Polym. J.*, 2025, **234**, 114033.
21 M. Labet and W. Thielemans, Synthesis of polycaprolactone: a review, *Chem. Soc. Rev.*, 2009, **38**, 3484–3504.
22 C. D. Grande-Tovar, J. I. Castro, C. H. Valencia Llano, D. L. Tenorio, M. Saavedra, P. A. Zapata and M. N. Chaur, Polycaprolactone (PCL)-Polylactic Acid (PLA)-Glycerol (Gly) Composites Incorporated with Zinc Oxide Nanoparticles (ZnO-NPs) and Tea Tree Essential Oil (TTEO) for Tissue Engineering Applications, *Pharmaceutics*, 2022, **15**, 43.
23 M. Chountoulesi, D. Selianitis, S. Pispas and N. Pippa, Recent Advances on PEO-PCL Block and Graft Copolymers as Nanocarriers for Drug Delivery Applications, *Materials*, 2023, **16**, 2298.
24 K. Wu, L. Yu and J. Ding, Synthesis of PCL–PEG–PCL Triblock Copolymer via Organocatalytic Ring-Opening Polymerization and Its Application as an Injectable Hydrogel—An Interdisciplinary Learning Trial, *J. Chem. Educ.*, 2020, **97**, 4158–4165.
25 M. R. Dethe, P. A, H. Ahmed, M. Agrawal, U. Roy and A. Alexander, PCL-PEG copolymer based injectable thermosensitive hydrogels, *J. Controlled Release*, 2022, **343**, 217–236.
26 F. J. V. Natta, J. W. Hill and W. H. Carothers, Studies of Polymerization and Ring Formation. XXIII.[1] ε-Caprolactone and its Polymers, *J. Am. Chem. Soc.*, 1934, **56**, 455–457.
27 C. Braud, R. Devarieux, A. Atlan, C. Ducos, and Michel Vert, Capillary zone electrophoresis in normal or reverse polarity separation modes for the analysis of hydroxy acid oligomers in neutral phosphate buffer, *J. Chromatogr. B. Biomed. Sci. App.*, 1998, **706**, 73–82.
28 H. Chen, S.-Y. Lee and Y.-M. Lin, Synthesis and Formulation of PCL-Based Urethane Acrylates for DLP 3D Printers, *Polymers*, 2020, **12**, 1500.
29 S. C. Woodward, P. S. Brewer, F. Moatamed, A. Schindler and C. G. Pitt, The intracellular degradation of poly(ε-caprolactone), *J. Biomed. Mater. Res.*, 1985, **19**, 437–444.
30 R. Pawar, A. Pathan, S. Nagaraj, H. Kapare, P. Giram and R. Wavhale, Polycaprolactone and its derivatives for drug delivery, *Polym. Adv. Technol.*, 2023, **34**, 3296–3316.
31 G. Rokicki, Aliphatic cyclic carbonates and spiroorthocarbonates as monomers, *Prog. Polym. Sci.*, 2000, **25**, 259–342.
32 H. Tian, Z. Tang, X. Zhuang, X. Chen and X. Jing, Biodegradable synthetic polymers: Preparation, functionalization and biomedical application, *Prog. Polym. Sci.*, 2012, **37**, 237–280.
33 W. Yu, E. Maynard, V. Chiaradia, M. C. Arno and A. P. Dove, Aliphatic Polycarbonates from Cyclic Carbonate Monomers and Their Application as Biomaterials, *Chem. Rev.*, 2021, **121**, 10865–10907.

34 S. Kühling, H. Keul and H. Höcker, Polymers from 2-allyloxymethyl-2-ethyltrimethylene carbonate and copolymers with 2,2-dimethyltrimethylene carbonate obtained by anionic ring-opening polymerization, *Makromol. Chem.*, 1990, **191**, 1611–1622.
35 P. Olsén, K. Odelius and A.-C. Albertsson, Ring-Closing Depolymerization: A Powerful Tool for Synthesizing the Allyloxy-Functionalized Six-Membered Aliphatic Carbonate Monomer 2-Allyloxymethyl-2-ethyltrimethylene Carbonate, *Macromolecules*, 2014, **47**, 6189–6195.
36 A. Chuma, H. W. Horn, W. C. Swope, R. C. Pratt, L. Zhang, B. G. G. Lohmeijer, C. G. Wade, R. M. Waymouth, J. L. Hedrick and J. E. Rice, The Reaction Mechanism for the Organocatalytic Ring-Opening Polymerization of l-Lactide Using a Guanidine-Based Catalyst: Hydrogen-Bonded or Covalently Bound?, *J. Am. Chem. Soc.*, 2008, **130**, 6749–6754.
37 P. Olsén, J. Undin, K. Odelius, H. Keul and A.-C. Albertsson, Switching from Controlled Ring-Opening Polymerization (cROP) to Controlled Ring-Closing Depolymerization (cRCDP) by Adjusting the Reaction Parameters That Determine the Ceiling Temperature, *Biomacromolecules*, 2016, **17**, 3995–4002.
38 P. Olsén, J. Undin, K. Odelius, H. Keul and A.-C. Albertsson, Correction to “Switching from Controlled Ring-Opening Polymerization (cROP) to Controlled Ring-Closing Depolymerization (cRCDP) by Adjusting the Reaction Parameters That Determine the Ceiling Temperature”, *Biomacromolecules*, 2018, **19**, 4710–4710.
39 A. W. Thomas, P. K. Kuroishi, M. M. Pérez-Madrigal, A. K. Whittaker and A. P. Dove, Synthesis of aliphatic polycarbonates with a tuneable thermal response, *Polym. Chem.*, 2017, **8**, 5082–5090.
40 P. Olsén, K. Odelius, H. Keul and A.-C. Albertsson, Macromolecular Design via an Organocatalytic, Monomer-Specific and Temperature-Dependent “On/Off Switch”. High Precision Synthesis of Polyester/Polycarbonate Multiblock Copolymers, *Macromolecules*, 2015, **48**, 1703–1710.
41 A. W. Thomas, PhD Thesis, University of Warwick, 2016.
42 Bacterial isolates degrading aliphatic polycarbonates | FEMS Microbiology Letters | Oxford Academic, https://academic.oup.com/femsle/article/161/2/255/513613, (accessed 27 October 2025).
43 T. Artham and M. Doble, Biodegradation of Aliphatic and Aromatic Polycarbonates, *Macromol. Biosci.*, 2008, **8**, 14–24.
44 T. Șucu and M. P. Shaver, Inherently degradable cross-linked polyesters and polycarbonates: resins to be cheerful, *Polym. Chem.*, 2020, **11**, 6397–6412.
45 R. Chandra and R. Rustgi, Biodegradable polymers, *Prog. Polym. Sci.*, 1998, **23**, 1273–1335.
46 R. D. Saini, Biodegradable Polymers, *Int. J. Appl. Chem.*, 2017, **13**, 179–196.
47 N. Lucas, C. Bienaime, C. Belloy, M. Queneudec, F. Silvestre and J.-E. Nava-Saucedo, Polymer biodegradation: mechanisms and estimation techniques, *Chemosphere*, 2008, **73**, 429–442.
48 R. R. A. Silva, C. S. Marques, T. R. Arruda, S. C. Teixeira and T. V. de Oliveira, Biodegradation of Polymers: Stages, Measurement, Standards and Prospects, *Macromol*, 2023, **3**, 371–399.
49 A. Samir, F. H. Ashour, A. A. A. Hakim and M. Bassyouni, Recent advances in biodegradable polymers for sustainable applications, *Npj Mater. Degrad.*, 2022, **6**, 68.

50 G.-Z. Yin and X.-M. Yang, Biodegradable polymers: a cure for the planet, but a long way to go, *J. Polym. Res.*, 2020, **27**, 38.
51 Web of Science - Analyze Results, https://www-webofscience-com.dcu.idm.oclc.org/wos/alldb/analyze-results/81330af4-2521-4850-938f-2b157c10d245-01884b9b5a, (accessed 11 November 2025).
52 J. Kurowiak, T. Klekiel and R. Będziński, Biodegradable Polymers in Biomedical Applications: A Review-Developments, Perspectives and Future Challenges, *Int. J. Mol. Sci.*, 2023, **24**, 16952.
53 F. Zhao, J. Sun, W. Xue, F. Wang, M. W. King, C. Yu, Y. Jiao, K. Sun and L. Wang, Development of a polycaprolactone/poly(*p*-dioxanone) bioresorbable stent with mechanically self-reinforced structure for congenital heart disease treatment, *Bioact. Mater.*, 2021, **6**, 2969–2982.
54 A. A. Barros, C. Oliveira, A. J. Ribeiro, R. Autorino, R. L. Reis, A. R. C. Duarte and E. Lima, In vivo assessment of a novel biodegradable ureteral stent, *World J. Urol.*, 2018, **36**, 277–283.
55 M. B. Sordi, A. C. C. da Cruz, Á. Aragones, M. M. R. Cordeiro and R. de S. Magini, PLGA+HA/βTCP Scaffold Incorporating Simvastatin: A Promising Biomaterial for Bone Tissue Engineering, *J. Oral Implantol.*, 2021, **47**, 93–101.
56 S. Huang, H.-J. Chen, Y.-P. Deng, X. You, Q. Fang and M. Lin, Preparation of novel stable microbicidal hydrogel films as potential wound dressing, *Polym. Degrad. Stab.*, 2020, **181**, 109349.
57 S. Huang, H.-J. Chen, Y.-P. Deng, X. You, Q. Fang and M. Lin, Preparation of novel stable microbicidal hydrogel films as potential wound dressing, *Polym. Degrad. Stab.*, 2020, **181**, 109349.
58 Y. Zou, Y. Sun, W. Shi, B. Wan and H. Zhang, Dual-functional shikonin-loaded quaternized chitosan/polycaprolactone nanofibrous film with pH-sensing for active and intelligent food packaging, *Food Chem.*, 2023, **399**, 133962.
59 Y. Zhao, R. M. Templonuevo and J. Chun, Enhancement of polycaprolactone nanofiber film performance by hydrogen bonding interactions with chitosan for food packaging, *Int. J. Biol. Macromol.*, 2025, **300**, 139437.
60 T. M. El-Messery, E. Aly, R. López-Nicolas, T. Sánchez-Moya and G. Ros, Bioaccessibility and antioxidant activity of PCL-microencapsulated olive leaves polyphenols and its application in yogurt, *J. Food Sci.*, 2021, **86**, 4303–4315.
61 A. Cesari, M. V. Loureiro, M. Vale, E. I. Yslas, M. Dardanelli and A. C. Marques, Polycaprolactone microcapsules containing citric acid and naringin for plant growth and sustainable agriculture: physico-chemical properties and release behavior, *Sci. Total Environ.*, 2020, **703**, 135548.
62 S. Chen, X. Wu and X. Ding, One-step side-by-side electrospraying of Janus particles for durable multifunctional coatings on cotton textiles, *Colloids Surf. Physicochem. Eng. Asp.*, 2025, **710**, 136227.
63 S. J. Ory, C. B. Hammond, S. G. Yancy, R. Wayne Hendren and C. G. Pitt, The effect of a biodegradable contraceptive capsule (Capronor) containing levonorgestrel on gonadotropin, estrogen, and progesterone levels, *Am. J. Obstet. Gynecol.*, 1983, **145**, 600–605.
64 G. Ma, C. Song, H. Sun, J. Yang and X. Leng, A biodegradable levonorgestrel-releasing implant made of PCL/F68 compound as tested in rats and dogs, *Contraception*, 2006, **74**, 141–147.
65 R. Augustine, E. A. Dominic, I. Reju, B. Kaimal, N. Kalarikkal and S. Thomas, Electrospun polycaprolactone membranes incorporated with ZnO nanoparticles

as skin substitutes with enhanced fibroblast proliferation and wound healing, *RSC Adv.*, 2014, **4**, 24777–24785.
66 B. Lei, X. Gao, R. Zhang, X. Yi and Q. Zhou, *In situ* magnesium phosphate/polycaprolactone 3D-printed scaffold induce bone regeneration in rabbit maxillofacial bone defect model, *Mater. Des.*, 2022, **215**, 110477.
67 I. A. Barker, M. P. Ablett, H. T. J. Gilbert, S. J. Leigh, J. A. Covington, J. A. Hoyland, S. M. Richardson and A. P. Dove, A microstereolithography resin based on thiol-ene chemistry: towards biocompatible 3D extracellular constructs for tissue engineering, *Biomater. Sci.*, 2014, **2**, 472–475.
68 B. R. Spears, M. A. Marin, A. N. Chaker, M. W. Lampley and E. Harth, Precise Microscale Polymeric Networks through Piezoelectronic Inkjet Printing, *ACS Biomater. Sci. Eng.*, 2016, **2**, 1265–1272.
69 C. Liu, Y. Zou, K. Su and Z. Li, Preparation and characterization of aliphatic polycarbonate membrane for CO2 gas separation application, *J. Ind. Eng. Chem.*, 2025, **143**, 498–509.
70 Q. Zong, S. Zhou, J. Ye, X. Peng, H. Wu, M. Li, X. Ye, N. Tian, W. Sun and Y. Zhai, Aliphatic polycarbonate-based hydrogel dressing for wound healing, *J. Drug Deliv. Sci. Technol.*, 2023, **79**, 104083.
71 W. Zhang, M. Dai, Y. Zhu, S. Li, Y. Sun, X. Liu and X. Li, Imidazole functionalized photo-crosslinked aliphatic polycarbonate drug-eluting coatings on zinc alloys for osteogenesis, angiogenesis, and bacteriostasis in bone regeneration, *Bioact. Mater.*, 2024, **37**, 549–562.
72 A. K. Halvey, B. Macdonald, A. Dhyani and A. Tuteja, Design of surfaces for controlling hard and soft fouling, *Philos. Trans. R. Soc. Math. Phys. Eng. Sci.*, 2018, **377**, 20180266.
73 R. Vasudevan, Biofilms: Microbial Cities of Scientific Significance, *J. Microbiol. Exp.*, DOI:10.15406/jmen.2014.01.00014.
74 J. J. Palomares-Navarro, A. T. Bernal-Mercado, G. A. González-Aguilar, L. A. Ortega-Ramirez, M. A. Martínez-Téllez and J. F. Ayala-Zavala, Antibiofilm Action of Plant Terpenes in Salmonella Strains: Potential Inhibitors of the Synthesis of Extracellular Polymeric Substances, *Pathogens*, 2023, **12**, 35.
75 K. Sauer, P. Stoodley, D. M. Goeres, L. Hall-Stoodley, M. Burmølle, P. S. Stewart and T. Bjarnsholt, The biofilm life cycle– expanding the conceptual model of biofilm formation, *Nat. Rev. Microbiol.*, 2022, **20**, 608–620.
76 K. Sauer, A. K. Camper, G. D. Ehrlich, J. W. Costerton and D. G. Davies, Pseudomonas aeruginosa Displays Multiple Phenotypes during Development as a Biofilm, *J. Bacteriol.*, 2002, **184**, 1140–1154.
77 E. C. Rodríguez-Merchán, D. J. Davidson and A. D. Liddle, Recent Strategies to Combat Infections from Biofilm-Forming Bacteria on Orthopaedic Implants, *Int. J. Mol. Sci.*, 2021, **22**, 10243.
78 E. J. Nisenbaum, J. T. Roland, S. Waltzman and D. R. Friedmann, Risk Factors and Management of Postoperative Infection Following Cochlear Implantation, *Otol. Neurotol. Off. Publ. Am. Otol. Soc. Am. Neurotol. Soc. Eur. Acad. Otol. Neurotol.*, 2020, **41**, e823–e828.
79 M. Metais, A. Hebrard, A. Duparc, P. Mondoly, M. Delay, B. Lepage and S. Malavaud, Cardiac implantable devices: surveillance of surgical site infections and assessment of professional practices, *Arch. Cardiovasc. Dis.*, 2011, **104**, 325–331.
80 G. D. Bixler and B. Bhushan, Biofouling: lessons from nature, *Philos. Transact. A Math. Phys. Eng. Sci.*, 2012, **370**, 2381–2417.

81 Surgical Site Infections, https://www.hopkinsmedicine.org/health/conditions-and-diseases/surgical-site-infections, (accessed 28 October 2025).
82 M. Ribeiro, F. J. Monteiro and M. P. Ferraz, Infection of orthopedic implants with emphasis on bacterial adhesion process and techniques used in studying bacterial-material interactions, *Biomatter*, 2012, **2**, 176–194.
83 L. M. Baddour, Z. Esquer Garrigos, M. Rizwan Sohail, E. Havers-Borgersen, A. D. Krahn, V. H. Chu, C. S. Radke, J. Avari-Silva, M. F. El-Chami, J. M. Miro, D. C. DeSimone, and on behalf of the American Heart Association Council on Lifelong Congenital Heart Disease and Heart Health in the Young (Young Hearts); and Council on Clinical Cardiology, Update on Cardiovascular Implantable Electronic Device Infections and Their Prevention, Diagnosis, and Management: A Scientific Statement From the American Heart Association, *Circulation*, 2024, **149**, 201–216.
84 N. Bölükbaşı, T. Özdemir, L. Öksüz and N. Gürler, Bacteremia following dental implant surgery: Preliminary results, *Med. Oral Patol. Oral Cir. Bucal*, 2012, **17**, 69–75.
85 H. Alghamdi, M. Leventis and T. Deliberador, Management of Infected Tissues Around Dental Implants: A Short Narrative Review, *Braz. Dent. J.*, **35**, e24-6160.
86 M. R. Sohail, D. Z. Uslan, A. H. Khan, P. A. Friedman, D. L. Hayes, W. R. Wilson, J. M. Steckelberg, S. Stoner and L. M. Baddour, Management and Outcome of Permanent Pacemaker and Implantable Cardioverter-Defibrillator Infections, *JACC*, 2007, **49**, 1851–1859.
87 M. Chawada, Role of antibiotics in elective clean surgeries: limiting its use to single shot preoperative dose, *Int. Surg. J.*, DOI:10.18203/2349-2902.ISJ20201394.
88 A. Fay, N. Nallasamy, F. Bernardini, E. J. Wladis, M. L. Durand, M. H. Devoto, D. Meyer, M. Hartstein, S. Honavar, M. H. Osaki, T. H. Osaki, Y. M. Santiago, M. Sales-Sanz, G. Vadala and D. Verity, Multinational Comparison of Prophylactic Antibiotic Use for Eyelid Surgery, *JAMA Ophthalmol.*, 2015, **133**, 778–784.
89 L. G. Harris and R. G. Richards, Staphylococcus aureus adhesion to different treated titanium surfaces, *J. Mater. Sci. Mater. Med.*, 2004, **15**, 311–314.
90 R. C. Costa, V. L. Abdo, P. H. C. Mendes, I. Mota-Veloso, M. Bertolini, M. T. Mathew, V. A. R. Barão and J. G. S. Souza, Microbial Corrosion in Titanium-Based Dental Implants: How Tiny Bacteria Can Create a Big Problem?, *J. Bio-Tribo-Corros.*, 2021, **7**, 136.
91 J. D. C. Tardelli, V. S. Bagnato and A. C. dos Reis, Bacterial Adhesion Strength on Titanium Surfaces Quantified by Atomic Force Microscopy: A Systematic Review, *Antibiotics*, 2023, **12**, 994.
92 M. Villegas, F. Bayat, T. Kramer, E. Schwarz, D. Wilson, Z. Hosseinidoust and T. F. Didar, Emerging Strategies to Prevent Bacterial Infections on Titanium-Based Implants, *Small*, 2024, **20**, 2404351.
93 M. Wang and T. Tang, Surface treatment strategies to combat implant-related infection from the beginning, *J. Orthop. Transl.*, 2018, **17**, 42–54.
94 H. Y. Liu, E. L. Prentice and M. A. Webber, Mechanisms of antimicrobial resistance in biofilms, *Npj Antimicrob. Resist.*, 2024, **2**, 27.
95 Z. Khatoon, C. D. McTiernan, E. J. Suuronen, T.-F. Mah and E. I. Alarcon, Bacterial biofilm formation on implantable devices and approaches to its treatment and prevention, *Heliyon*, 2018, **4**, e01067.

96 H. Durand, A. Whiteley, P. Mailley and G. Nonglaton, Combining Topography and Chemistry to Produce Antibiofouling Surfaces: A Review, *ACS Appl. Bio Mater.*, DOI:10.1021/acsabm.2c00586.
97 Combining Topography and Chemistry to Produce Antibiofouling Surfaces: A Review | ACS Applied Bio Materials, https://pubs.acs.org/doi/10.1021/acsabm.2c00586, (accessed 28 October 2025).
98 A. Rai, S. Senapati, S. K. Saraf and P. Maiti, Biodegradable poly(ε-caprolactone) as a controlled drug delivery vehicle of vancomycin for the treatment of MRSA infection, *J. Mater. Chem. B*, 2016, **4**, 5151–5160.
99 WHO warns of widespread resistance to common antibiotics worldwide, https://www.who.int/news/item/13-10-2025-who-warns-of-widespread-resistance-to-common-antibiotics-worldwide, (accessed 28 October 2025).
100 M. J. Wilhelm, M. Sharifian Gh., T. Wu, Y. Li, C.-M. Chang, J. Ma and H.-L. Dai, Determination of bacterial surface charge density via saturation of adsorbed ions, *Biophys. J.*, 2021, **120**, 2461–2470.
101 M. Li and C. W. Pester, Mixed Polymer Brushes for “Smart” Surfaces, *Polymers*, 2020, **12**, 1553.
102 Y. Yang, Z. Cai, Z. Huang, X. Tang and X. Zhang, Antimicrobial cationic polymers: from structural design to functional control, *Polym. J.*, 2018, **50**, 33–44.
103 I. Francolini, C. Vuotto, A. Piozzi and G. Donelli, Antifouling and antimicrobial biomaterials: an overview, *APMIS*, 2017, **125**, 392–417.
104 A. Banerjee, A. Ghosh, B. Saha, P. Bhadury and P. De, Surface Charge-Switchable Antifouling Block Copolymer with Bacteriostatic Properties, *Langmuir*, 2024, **40**, 5314–5325.
105 J. Zhang, R. Zhou, H. Wang, X. Jiang, H. Wang, S. Yan, J. Yin and S. Luan, Bacterial activation of surface-tethered antimicrobial peptides for the facile construction of a surface with self-defense, *Appl. Surf. Sci.*, 2019, **497**, 143480.
106 W. W. Wilson, M. M. Wade, S. C. Holman and F. R. Champlin, Status of methods for assessing bacterial cell surface charge properties based on zeta potential measurements, *J. Microbiol. Methods*, 2001, **43**, 153–164.
107 A. Aguilar-Sanchez, B. Jalvo, A. Mautner, S. Nameer, T. Pöhler, T. Tammelin and A. P. Mathew, Waterborne nanocellulose coatings for improving the antifouling and antibacterial properties of polyethersulfone membranes, *J. Membr. Sci.*, 2021, **620**, 118842.
108 O. Rzhepishevska, S. Hakobyan, R. Ruhal, J. Gautrot, D. Barbero and M. Ramstedt, The surface charge of anti-bacterial coatings alters motility and biofilm architecture, *Biomater. Sci.*, 2013, **1**, 589–602.
109 D. Montag, M. Frant, H. Horn and K. Liefeith, Dependence of the initial adhesion of biofilm forming Pseudomonas putida mt2 on physico-chemical material properties, *Biofouling*.
110 E. Lebaudy, C. Guilbaud-Chéreau, B. Frisch, N. E. Vrana and P. Lavalle, The High Potential of ε-Poly-l-Lysine for the Development of Antimicrobial Biomaterials, *Adv. NanoBiomed Res.*, 2023, **3**, 2300080.
111 V. W. L. Ng, J. P. K. Tan, J. Leong, Z. X. Voo, J. L. Hedrick and Y. Y. Yang, Antimicrobial Polycarbonates: Investigating the Impact of Nitrogen-Containing Heterocycles as Quaternizing Agents, *Macromolecules*, 2014, **47**, 1285–1291.
112 G. Xu, P. Liu, D. Pranantyo, L. Xu, K.-G. Neoh and E.-T. Kang, Antifouling and Antimicrobial Coatings from Zwitterionic and Cationic Binary Polymer Brushes Assembled via “Click” Reactions, *Ind. Eng. Chem. Res.*, 2017, **56**, 14479–14488.

113 E. P. Ivanova, J. Hasan, H. K. Webb, V. K. Truong, G. S. Watson, J. A. Watson, V. A. Baulin, S. Pogodin, J. Y. Wang, M. J. Tobin, C. Löbbe and R. J. Crawford, Natural Bactericidal Surfaces: Mechanical Rupture of Pseudomonas aeruginosa Cells by Cicada Wings, *Small*, 2012, **8**, 2489–2494.
114 E. P. Ivanova, D. P. Linklater, A. Aburto-Medina, P. Le, V. A. Baulin, H. Khuong Duy Nguyen, R. Curtain, E. Hanssen, G. Gervinskas, S. Hock Ng, V. Khanh Truong, P. Luque, G. Ramm, H. A. B. Wösten, R. J. Crawford, S. Juodkazis and S. Maclaughlin, Antifungal versus antibacterial defence of insect wings, *J. Colloid Interface Sci.*, 2021, **603**, 886–897.
115 S. Pogodin, J. Hasan, V. A. Baulin, H. K. Webb, V. K. Truong, T. H. Phong Nguyen, V. Boshkovikj, C. J. Fluke, G. S. Watson, J. A. Watson, R. J. Crawford and E. P. Ivanova, Biophysical model of bacterial cell interactions with nanopatterned cicada wing surfaces, *Biophys. J.*, 2013, **104**, 835–840.
116 J. Hasan, H. K. Webb, V. K. Truong, S. Pogodin, V. A. Baulin, G. S. Watson, J. A. Watson, R. J. Crawford and E. P. Ivanova, Selective bactericidal activity of nanopatterned superhydrophobic cicada Psaltoda claripennis wing surfaces, *Appl. Microbiol. Biotechnol.*, 2013, **97**, 9257–9262.
117 D. E. Mainwaring, S. H. Nguyen, H. Webb, T. Jakubov, M. Tobin, R. N. Lamb, A. H.-F. Wu, R. Marchant, R. J. Crawford and E. P. Ivanova, The nature of inherent bactericidal activity: insights from the nanotopology of three species of dragonfly, *Nanoscale*, 2016, **8**, 6527–6534.
118 S. Rostami and B. Garipcan, Evolution of antibacterial and antibiofouling properties of sharkskin-patterned surfaces, *Surf. Innov.*, 2022, **10**, 165–190.
119 Nano and Microscale Topographies for the Prevention of Bacterial Surface Fouling, https://www.mdpi.com/2079-6412/4/1/37, (accessed 29 October 2025).
120 J. Jenkins, J. Mantell, C. Neal, A. Gholinia, P. Verkade, A. H. Nobbs and B. Su, Antibacterial effects of nanopillar surfaces are mediated by cell impedance, penetration and induction of oxidative stress, *Nat. Commun.*, 2020, **11**, 1626.
121 B. J. Privett, J. Youn, S. A. Hong, J. Lee, J. Han, J. H. Shin and M. H. Schoenfisch, Antibacterial Fluorinated Silica Colloid Superhydrophobic Surfaces, *Langmuir ACS J. Surf. Colloids*, 2011, **27**, 9597–9601.
122 R. I. Garcia-Gonzalez, C. R. Crick, R. I. Garcia-Gonzalez and C. R. Crick, in *Superhydrophobic Coating - Recent Advances in Theory and Applications*, IntechOpen, 2023.
123 S. H. Ibrahim, T. Wejrzanowski, B. Przybyszewski, R. Kozera, X. García-Casas and A. Barranco, Role of Surface Topography in the Superhydrophobic Effect—Experimental and Numerical Studies, *Materials*, 2022, **15**, 3112.
124 J. Hasan and K. Chatterjee, Recent advances in engineering topography mediated antibacterial surfaces, *Nanoscale*, 2015, **7**, 15568–15575.
125 E. A. Cuello, L. E. Mulko, C. A. Barbero, D. F. Acevedo and E. I. Yslas, Development of micropatterning polyimide films for enhanced antifouling and antibacterial properties, *Colloids Surf. B Biointerfaces*, 2020, **188**, 110801.
126 A. Francone, S. Merino, A. Retolaza, J. Ramiro, S. A. Alves, J. V. de Castro, N. M. Neves, A. Arana, J. M. Marimon, C. M. S. Torres and N. Kehagias, Impact of surface topography on the bacterial attachment to micro- and nano-patterned polymer films, *Surf. Interfaces*, 2021, **27**, 101494.
127 M. Asadi Tokmedash, C. Kim, A. P. Chavda, A. Li, J. Robins and J. Min, Engineering multifunctional surface topography to regulate multiple biological responses, *Biomaterials*, 2025, **319**, 123136.

128 M. A. Rose, J. J. Bowen and S. A. Morin, Emergent Soft Lithographic Tools for the Fabrication of Functional Polymeric Microstructures, *ChemPhysChem*, 2019, **20**, 909–925.
129 Y. Xia, J. J. McClelland, R. Gupta, D. Qin, X.-M. Zhao, L. L. Sohn, R. J. Celotta and G. M. Whitesides, Replica molding using polymeric materials: A practical step toward nanomanufacturing, *Adv. Mater.*, 1997, **9**, 147–149.
130 M. O Loughlin, University College Dublin, 2022.
131 G. Tian, G. Zhu, T. Ren, Y. Liu, K. Wei and Y. X. Liu, The effects of PCL diol molecular weight on properties of shape memory poly(ε-caprolactone) networks, *J. Appl. Polym. Sci.*, 2019, **136**, 47055.
132 N. Geoghegan, M. O'Loughlin, C. Delaney, K. D. Rochfort, M. Kennedy, S. Kolagatla, L. Podhorska, B. J. Rodriguez, L. Florea and S. M. Kelleher, Controlled degradation of polycaprolactone-based micropillar arrays, *Biomater. Sci.*, 2023, **11**, 3077–3091.
133 H. Bayraktutan, R. J. Kopiasz, A. Elsherbeny, M. M. Espuga, N. Gumus, U. Can Oz, K. Polra, P. F. McKay, R. J. Shattock, P. Ordóñez-Morán, A. Mata, C. Alexander and P. Gurnani, Polysarcosine functionalised cationic polyesters efficiently deliver self-amplifying mRNA, *Polym. Chem.*, 2024, **15**, 1862–1876.
134 M.-O. Christen and F. Vercesi, Polycaprolactone: How a Well-Known and Futuristic Polymer Has Become an Innovative Collagen-Stimulator in Esthetics, *Clin. Cosmet. Investig. Dermatol.*, 2020, **13**, 31–48.
135 V. Guarino, G. Gentile, L. Sorrentino and L. Ambrosio, in *Encyclopedia of Polymer Science and Technology*, ed. H. F. Mark, Wiley, 3rd edn., 2017, pp. 1–36.
136 V. Guarino, A. Guaccio and L. Ambrosio, Manipulating co-continuous polymer blends to create PCL scaffolds with fully interconnected and anisotropic pore architecture, *J. Appl. Biomater. Biomech. JABB*, 2011, **9**, 34–39.
137 V. Guarino, P. Taddei, M. D. Foggia, C. Fagnano, G. Ciapetti and L. Ambrosio, The Influence of Hydroxyapatite Particles on In Vitro Degradation Behavior of Poly ε-Caprolactone–Based Composite Scaffolds, *Tissue Eng. Part A*, 2009, **15**, 3655–3668.
138 S. Ghaedamini, S. Karbasi, B. Hashemibeni, A. Honarvar and A. Rabiei, PCL/Agarose 3D-printed scaffold for tissue engineering applications: fabrication, characterization, and cellular activities, *Res. Pharm. Sci.*, 2023, **18**, 566–579.
139 P. Grossen, D. Witzigmann, S. Sieber and J. Huwyler, PEG-PCL-based nanomedicines: A biodegradable drug delivery system and its application, *J. Control. Release Off. J. Control. Release Soc.*, 2017, **260**, 46–60.
140 B. Gedik and M. A. Erdem, Electrospun PCL membranes for localized drug delivery and bone regeneration, *BMC Biotechnol.*, 2025, **25**, 31.
141 K. I. Matumba, T. C. Mokhena, V. Ojijo, E. R. Sadiku and S. S. Ray, Morphological Characteristics, Properties, and Applications of Polylactide/Poly(ε-caprolactone) Blends and Their Composites—A Review, *Macromol. Mater. Eng.*, 2024, **309**, 2400056.
142 S. Tshepelevitsh, A. Kütt, M. Lõkov, I. Kaljurand, J. Saame, A. Heering, P. G. Plieger, R. Vianello and I. Leito, On the Basicity of Organic Bases in Different Media, *Eur. J. Org. Chem.*, 2019, **2019**, 6735–6748.
143 P. P. T. Nguyen, S. An and H.-H. Jeong, Microfluidic formation of biodegradable PCLDA microparticles as sustainable sorbents for treatment of organic contaminants in wastewater, *Colloids Surf. Physicochem. Eng. Asp.*, 2023, **656**, 130409.

144 L. Cai and S. Wang, Poly(ε-caprolactone) acrylates synthesized using a facile method for fabricating networks to achieve controllable physicochemical properties and tunable cell responses, *Polymer*, 2010, **51**, 164–177.
145 J. Warneke, Z. Wang, M. Zeller, D. Leibfritz, M. Plaumann and V. A. Azov, Methacryloyl chloride dimers: from structure elucidation to a manifold of chemical transformations, *Tetrahedron*, 2014, **70**, 6515–6521.
146 Methacryloyl chloride, 95%, contains 200 ppm MEHQ as stabilizer, AcroSeal , Thermo Scientific 100 mL | Buy Online | Thermo Scientific Acros | Fisher Scientific, https://www.fishersci.co.uk/shop/products/methacryloyl-chloride-95-contains-200-ppm-mehq-as-stabilizer-acroseal-thermo-scientific/10347730, (accessed 18 August 2025).
147 C. Shi, M. Wang, Z. Wang, G. Qu, W. Jiang, X. Pan and M. Fang, Oligomers from the Synthetic Polymers: Another Potential Iceberg of New Pollutants, *Environ. Health*, 2023, **1**, 228–235.
148 Oligomers - Knowledge and References, https://taylorandfrancis.com/knowledge/Engineering_and_technology/Chemical_engineering/Oligomers/, (accessed 18 August 2025).
149 T. I. U. of P. and A. Chemistry (IUPAC), IUPAC - oligomer molecule (O04286), https://goldbook.iupac.org/terms/view/O04286, (accessed 25 June 2024).
150 Differential Scanning Calorimetry – Thermal Fractionation Techniques for Polymer Characterization – Faster Throughput with the Discovery X3 DSC - TA Instruments, https://www.tainstruments.com/applications-notes/differential-scanning-calorimetry-thermal-fractionation-techniques-for-polymer-characterization-faster-throughput-with-the-discovery-x3-dsc/, (accessed 7 November 2025).
151 Z. Wang, Y. He and A. J. Müller, Using PCL oligomers to study the differences in melting behavior between polymers and small molecules crystals, *Polymer*, 2023, **271**, 125783.
152 J. Mathias, What a DSC Test of a Polymer Can Discover, https://www.innovatechlabs.com/newsroom/2267/what-a-dsc-analysis-of-a-polymer-can-discover/, (accessed 26 June 2024).
153 E. Zhuravlev, J. W. P. Schmelzer, B. Wunderlich and C. Schick, Kinetics of nucleation and crystallization in poly(ε-caprolactone) (PCL), *Polymer*, 2011, **52**, 1983–1997.
154 S. P. Rogalsky, O. V. Moshynets, L. G. Lyoshina and O. P. Tarasyuk, Antimicrobial polycarbonates for biomedical applications, *EPMA J.*, 2014, **5**, A133.
155 J. T. Bendler, Ed., *Handbook of Polycarbonate Science and Technology*, CRC Press, Boca Raton, 1999.
156 T. Rodima, I. Kaljurand, A. Pihl, V. Mäemets, I. Leito and I. A. Koppel, Acid−Base Equilibria in Nonpolar Media. 2.1 Self-Consistent Basicity Scale in THF Solution Ranging from 2-Methoxypyridine to EtP1(pyrr) Phosphazene, *J. Org. Chem.*, 2002, **67**, 1873–1881.
157 R. C. Pratt, B. G. G. Lohmeijer, D. A. Long, P. N. P. Lundberg, A. P. Dove, H. Li, C. G. Wade, R. M. Waymouth and J. L. Hedrick, Exploration, Optimization, and Application of Supramolecular Thiourea−Amine Catalysts for the Synthesis of Lactide (Co)polymers, *Macromolecules*, 2006, **39**, 7863–7871.
158 1-[3,5-Bis(trifluoromethyl)phenyl]-3-cyclohexylthiourea 454203-57-7 | TCI EUROPE N.V., https://www.tcichemicals.com/IE/en/p/B6332, (accessed 19 August 2025).

159 S. Tempelaar, L. Mespouille, P. Dubois and A. P. Dove, Organocatalytic Synthesis and Postpolymerization Functionalization of Allyl-Functional Poly(carbonate)s, *Macromolecules*, 2011, **44**, 2084–2091.
160 A. P. Dove, R. C. Pratt, B. G. G. Lohmeijer, R. M. Waymouth and J. L. Hedrick, Thiourea-Based Bifunctional Organocatalysis: Supramolecular Recognition for Living Polymerization, *J. Am. Chem. Soc.*, 2005, **127**, 13798–13799.
161 A. W. Thomas, P. K. Kuroishi, M. M. Pérez-Madrigal, A. K. Whittaker and A. P. Dove, Synthesis of aliphatic polycarbonates with a tuneable thermal response, *Polym. Chem.*, 2017, **8**, 5082–5090.
162 A. P. Dove, Organic Catalysis for Ring-Opening Polymerization, *ACS Macro Lett.*, 2012, **1**, 1409–1412.
163 2.3F: Visualizing TLC Plates, https://chem.libretexts.org/Bookshelves/Organic_Chemistry/Organic_Chemistry_Lab_Techniques_(Nichols)/02%3A_Chromatography/2.03%3A_Thin_Layer_Chromatography_(TLC)/2.3F%3A_Visualizing_TLC_Plates, (accessed 25 August 2025).
164 Infrared Spectroscopy Absorption Table, https://chem.libretexts.org/Ancillary_Materials/Reference/Reference_Tables/Spectroscopic_Reference_Tables/Infrared_Spectroscopy_Absorption_Table, (accessed 9 May 2024).
165 IR Absorption Frequencies - NIU - Department of Chemistry and Biochemistry, https://www.niu.edu/chembio/research/analytical-lab/ftir/ir-frequencies-table.shtml, (accessed 13 November 2025).
166 B. Arora, R. Tandon, P. Attri and R. Bhatia, Chemical Crosslinking: Role in Protein and Peptide Science, *Curr. Protein Pept. Sci.*, 2017, **18**, 946–955.
167 B. Husár, M. Hatzenbichler, V. Mironov, R. Liska, J. Stampfl and A. Ovsianikov, in *Biomaterials for Bone Regeneration*, eds P. Dubruel and S. Van Vlierberghe, Woodhead Publishing, 2014, pp. 149–201.
168 S. M. Müller, S. Schlögl, T. Wiesner, M. Haas and T. Griesser, Recent Advances in Type I Photoinitiators for Visible Light Induced Photopolymerization, *ChemPhotoChem*, 2022, **6**, e202200091.
169 C. E. Hoyle, T. Y. Lee and T. Roper, Thiol–enes: Chemistry of the past with promise for the future, *J. Polym. Sci. Part Polym. Chem.*, 2004, **42**, 5301–5338.
170 K. S. Lim, J. H. Galarraga, X. Cui, G. C. J. Lindberg, J. A. Burdick and T. B. F. Woodfield, Fundamentals and Applications of Photo-Cross-Linking in Bioprinting, *Chem. Rev.*, 2020, **120**, 10662–10694.
171 C. E. Hoyle and C. N. Bowman, Thiol–Ene Click Chemistry, *Angew. Chem. Int. Ed.*, 2010, **49**, 1540–1573.
172 Z. Wang, X. Jin, R. Dai, J. F. Holzman and K. Kim, An ultrafast hydrogel photocrosslinking method for direct laser bioprinting, *RSC Adv.*, 2016, **6**, 21099–21104.
173 B. Zeng, Z. Cai, J. Lalevée, Q. Yang, H. Lai, P. Xiao, J. Liu and F. Xing, Cytotoxic and cytocompatible comparison among seven photoinitiators-triggered polymers in different tissue cells, *Toxicol. In Vitro*, 2021, **72**, 105103.
174 G.-T. Kim, H.-B. Go, J.-H. Yu, S.-Y. Yang, K.-M. Kim, S.-H. Choi and J.-S. Kwon, Cytotoxicity, Colour Stability and Dimensional Accuracy of 3D Printing Resin with Three Different Photoinitiators, *Polymers*, 2022, **14**, 979.
175 C. G. Williams, A. N. Malik, T. K. Kim, P. N. Manson and J. H. Elisseeff, Variable cytocompatibility of six cell lines with photoinitiators used for

polymerizing hydrogels and cell encapsulation, *Biomaterials*, 2005, **26**, 1211–1218.
176 W. Tomal and J. Ortyl, Water-Soluble Photoinitiators in Biomedical Applications, *Polymers*, 2020, **12**, 1073.
177 A. Gavish Moscovitz, H. Simaan Yameen, O. Bar-Am and D. Seliktar, Evaluating Cross-Linking Efficiency and Cytocompatibility of Three Commonly Used Photoinitiators across Different Cell-Compatible Hydrogel Platforms, *Biomacromolecules*, DOI:10.1021/acs.biomac.5c01142.
178 I. Miranda, A. Souza, P. Sousa, J. Ribeiro, E. M. S. Castanheira, R. Lima and G. Minas, Properties and Applications of PDMS for Biomedical Engineering: A Review, *J. Funct. Biomater.*, 2021, **13**, 2.
179 S. Kumar, K. Khare and M. K. Singh, Controlling adhesion of PDMS elastomer through process parameters, *Tribol. Int.*, 2025, **209**, 110724.
180 E. Kim, Y. Xia and G. M. Whitesides, Polymer microstructures formed by moulding in capillaries, *Nature*, 1995, **376**, 581–584.
181 K. Y. Suh, Y. S. Kim and H. H. Lee, Capillary Force Lithography, *Adv. Mater.*, 2001, **13**, 1386–1389.
182 J. Autian, Structure-toxicity relationships of acrylic monomers., *Environ. Health Perspect.*, 1975, **11**, 141–152.
183 Frank A. Patty, *Industrial Hygiene And Toxicology Volume 2*, Interscience Publishers, 1963.
184 1,6-Hexanediol diacrylate technical grade, 80 Hexamethylene glycol diacrylate, https://www.sigmaaldrich.com/IE/en/product/aldrich/246816?srsltid=AfmBOopr6CwYAZ71gf4HCTFg7AaI4Y3VS6vPgEkm_3RjT_sinwftW34Z, (accessed 14 November 2025).
185 F. Rey García, PhD Thesis, Universidade de Santiago de Compostela, 2012.
186 UV Transmissibility Comparison, https://topas.com/tech-center/performance-data/uv-transmission/, (accessed 8 October 2025).
187 UV Microscopy – Slides and coverslips | JMC Scientific Consulting Ltd, https://jmcscientificconsulting.com/uv-microscopy-slides-and-coverslips/, (accessed 26 June 2024).
188 K. Van Canneyt and P. Verdonck, in *Comprehensive Biomedical Physics*, ed. A. Brahme, Elsevier, Oxford, 2014, pp. 39–53.
189 J. Jeon, H. Choi, W. Cho, J. Hong, J. H. Youk and J. J. Wie, Height-Tunable Replica Molding Using Viscous Polymeric Resins, *ACS Macro Lett.*, 2022, **11**, 428–433.
190 T. Huhtamäki, X. Tian, J. T. Korhonen and R. H. A. Ras, Surface-wetting characterization using contact-angle measurements, *Nat. Protoc.*, 2018, **13**, 1521–1538.
191 J. C. McCormack, L. Podhorska, C. Delaney, F. Zhang, B. J. Rodriguez and S. M. Kelleher, High Aspect Ratio Polymeric Nanoneedle Arrays, *Macromol. Mater. Eng.*, 2021, **306**, 2000754.
192 C. Delaney, N. Geoghegan, H. Ibrahim, M. O'Loughlin, B. J. Rodriguez, L. Florea and S. M. Kelleher, Direct Laser Writing to Generate Molds for Polymer Nanopillar Replication, *ACS Appl. Polym. Mater.*, 2020, **2**, 3632–3641.
193 S. P. Flynn, S. Daniels, B. J. Rodriguez and S. M. Kelleher, Replica molding of cicada wings: The role of water at point of synthesis on nanostructure feature size, *Biointerphases*, 2020, **15**, 061017.

194 What is Difference between SEM, TEM, FESEM?, https://www.vpi2004.com/faq/what-is-difference-between-sem%2C-tem%2C-fesem%3F, (accessed 13 October 2025).
195 T. J. Shaffner and R. D. V. Veld, 'Charging' effects in the scanning electron microscope, *J. Phys. [E]*, 1971, **4**, 633.
196 R. Flatabø, A. Coste and M. m. Greve, A systematic investigation of the charging effect in scanning electron microscopy for metal nanostructures on insulating substrates, *J. Microsc.*, 2017, **265**, 287–297.
197 Nanoimprint Lithography | Laboratory for Nano and Quantum Technologies | PSI, https://www.psi.ch/en/lnq/nanoimprint-lithography, (accessed 10 October 2025).
198 H. Gu, A. Chen, X. Song, M. E. Brasch, J. H. Henderson and D. Ren, How Escherichia coli lands and forms cell clusters on a surface: a new role of surface topography, *Sci. Rep.*, 2016, **6**, 29516.
199 S. Hou, H. Gu, C. Smith and D. Ren, Microtopographic Patterns Affect Escherichia coli Biofilm Formation on Poly(dimethylsiloxane) Surfaces, https://pubs.acs.org/doi/full/10.1021/la1046194, (accessed 12 October 2025).
200 Atomic Force Microscopes for Materials Research, https://www.bruker.com/en/products-and-solutions/microscopes/materials-afm.html, (accessed 13 October 2025).
201 What is AFM?, https://www.nanoandmore.com/what-is-atomic-force-microscopy?gad_campaignid=1370796205&gad_source=1&gbraid=0AAAAAD-XR36Uny0g2WkXPbeIE7H7oexRY&gclid=Cj0KCQiA5uDIBhDAARIsAOxj0CEUat4hwmBsbk9Q7QKocEntfo7iOi2vpjhEOwA-J16T2-Ca0Gm-e74aAg8jEALw_wcB, (accessed 15 November 2025).
202 R. B. Price, A. S. Rizkalla and G. C. Hall, Effect of stepped light exposure on the volumetric polymerization shrinkage and bulk modulus of dental composites and an unfilled resin, *Am. J. Dent.*, 2000, **13**, 176–180.
203 M. Topa-Skwarczyńska and J. Ortyl, Photopolymerization shrinkage: strategies for reduction, measurement methods and future insights, *Polym. Chem.*, 2023, **14**, 2145–2158.
204 J. A. Rogers and H. H. Lee, *Unconventional Nanopatterning Techniques and Applications*, John Wiley & Sons, 2008.
205 Effect of different tip shapes on AFM measurement - NanoAndMore, https://www.nanoandmore.com/eu/afm-tip-shape-effects?srsltid=AfmBOopQYjZmiN-XlI57HASr6nh2OdbP-ySzrD9H-x-KJ5KMgdTLik36, (accessed 13 October 2025).
206 i2i - Product (I.S. EN ISO 10993-13), https://eu-i2-saiglobal-com.dcu.idm.oclc.org/management/display/index/0/295482/-/6a3a0070d31168a2e2dbcd7decabb4c6, (accessed 13 October 2025).
207 Standard Test Method for in vitro Degradation Testing of Hydrolytically Degradable Polymer Resins and Fabricated Forms for Surgical Implants, https://store.astm.org/f1635-16.html, (accessed 13 October 2025).
208 E. Malikmammadov, T. E. Tanir, A. Kiziltay, V. Hasirci and N. Hasirci, PCL and PCL-based materials in biomedical applications, *J. Biomater. Sci. Polym. Ed.*, 2018, **29**, 863–893.
209 N. S. Allen, M. Edge and S. Hussain, Perspectives on yellowing in the degradation of polymer materials: inter-relationship of structure, mechanisms and modes of stabilisation, *Polym. Degrad. Stab.*, 2022, **201**, 109977.

210 S. Venkatachalam, S. G. Nayak, J. V. Labde, P. R. Gharal, K. Rao, A. K. Kelkar, S. Venkatachalam, S. G. Nayak, J. V. Labde, P. R. Gharal, K. Rao and A. K. Kelkar, in *Polyester*, IntechOpen, 2012.
211 K. Moraczewski, M. Stepczyńska, R. Malinowski, T. Karasiewicz, B. Jagodziński and P. Rytlewski, Modification of Polycaprolactone with Plant Extracts to Improve the Aging Resistance, *Materials*, 2023, **16**, 5154.
212 A. S. Luyt, A. Antunes, A. Popelka, A. Mahmoud, M. K. Hassan and P. Kasak, Effect of poly(ε-caprolactone) and titanium (IV) dioxide content on the UV and hydrolytic degradation of poly(lactic acid)/poly(ε-caprolactone) blends, *J. Appl. Polym. Sci.*, 2021, **138**, 51266.
213 A. Aguilar-Sanchez, B. Jalvo, A. Mautner, S. Nameer, T. Pöhler, T. Tammelin and A. P. Mathew, Waterborne nanocellulose coatings for improving the antifouling and antibacterial properties of polyethersulfone membranes, *J. Membr. Sci.*, 2021, **620**, 118842.
214 H. Murata, R. R. Koepsel, K. Matyjaszewski and A. J. Russell, Permanent, non-leaching antibacterial surfaces—2: How high density cationic surfaces kill bacterial cells, *Biomaterials*, 2007, **28**, 4870–4879.
215 B. Fang, Y. Jiang, K. Nüsslein, V. M. Rotello and M. M. Santore, Antimicrobial Surfaces Containing Cationic Nanoparticles: How Immobilized, Clustered, and Protruding Cationic Charge Presentation Affects Killing Activity and Kinetics, *Colloids Surf. B Biointerfaces*, 2015, **125**, 255–263.
216 B. D. Fairbanks, S. P. Singh, C. N. Bowman and K. S. Anseth, Photodegradable, Photoadaptable Hydrogels via Radical-Mediated Disulfide Fragmentation Reaction, *Macromolecules*, 2011, **44**, 2444–2450.
217 G. T. Hermanson, in *Bioconjugate Techniques (Third Edition)*, ed. G. T. Hermanson, Academic Press, Boston, 2013, pp. 229–258.
218 T. Soderberg, 15.7 Redox Reactions of Thiols and Disulfides, https://chem.libretexts.org/Bookshelves/Organic_Chemistry/Book%3A_Organic_Chemistry_with_a_Biological_Emphasis_v2.0_(Soderberg)/15%3A_Oxidation_and_Reduction_Reactions/15.07%3A_Redox_Reactions_of_Thiols_and_Disulfides, (accessed 14 October 2025).
219 W. A. Davis, L. N. Zakharov and D. W. Johnson, Pnictogen-Assisted Self-Assembly as a Means to Study Mediated Thiol/Disulfide Exchange in Supramolecular Dynamic Covalent Assemblies, *Chem. – Eur. J.*, 2024, **30**, e202402702.
220 PubChem, Acetone, https://pubchem.ncbi.nlm.nih.gov/compound/180, (accessed 20 October 2025).
221 S. D. Bruck, Extension of the Flory-Rehner Theory of Swelling to an Anisotropic Polymer System, *J. Res. Natl. Bur. Stand. Sect. Phys. Chem.*, 1961, **65A**, 485–487.
222 F. K. Metze, S. Sant, Z. Meng, H.-A. Klok and K. Kaur, Swelling-Activated, Soft Mechanochemistry in Polymer Materials, *Langmuir*, DOI:10.1021/acs.langmuir.2c02801.
223 E. Fennell, J. Kamphus and J. M. Huyghe, The Importance of the Mixing Energy in Ionized Superabsorbent Polymer Swelling Models, *Polymers*, 2020, **12**, 609.
224 M. Selva, M. Fabris, V. Lucchini, A. Perosa and M. Noè, The reaction of primary aromatic amines with alkylene carbonates for the selective synthesis of bis-N-(2-hydroxy)alkylanilines: the catalytic effect of phosphonium-based ionic liquids, *Org. Biomol. Chem.*, 2010, **8**, 5187–5198.

225 Clementine, Cyclic carbonates, https://specificpolymers.com/cyclic-carbonates-a-sustainable-and-greener-alternative-to-toxic-compounds-used-in-polymer-synthesis/, (accessed 14 October 2025).
226 A. Cornille, M. Blain, R. Auvergne, B. Andrioletti, B. Boutevin and S. Caillol, A study of cyclic carbonate aminolysis at room temperature: effect of cyclic carbonate structures and solvents on polyhydroxyurethane synthesis, *Polym. Chem.*, 2017, **8**, 592–604.
227 P. G. M. Wuts and T. W. Greene, *Greene's Protective Groups in Organic Synthesis*, Wiley, 1st edn., 2006.
228 G. Haeger, J. Bongaerts and P. Siegert, A convenient ninhydrin assay in 96-well format for amino acid-releasing enzymes using an air-stable reagent, *Anal. Biochem.*, 2022, **654**, 114819.
229 A. C. Stauß, C. Fuchs, P. Jansen, S. Repert, K. Alcock, S. Ludewig and W. Rozhon, The Ninhydrin Reaction Revisited: Optimisation and Application for Quantification of Free Amino Acids, *Molecules*, 2024, **29**, 3262.
230 X. Tao, B. Zheng, T. Bai, M.-H. Li and J. Ling, Polymerization of N-Substituted Glycine N-Thiocarboxyanhydride through Regioselective Initiation of Cysteamine: A Direct Way toward Thiol-Capped Polypeptoids, *Macromolecules*, 2018, **51**, 4494–4501.
231 S. S. Abbas, N. L. Kelly, G. Patias, J. V. Hanna and T. McNally, Cysteamine functionalised reduced graphene oxide modification of maleated poly(propylene), *Polymer*, 2020, **203**, 122750.
232 S. O'Halloran, A. Pandit, A. Heise and A. Kellett, Two-Photon Polymerization: Fundamentals, Materials, and Chemical Modification Strategies, *Adv. Sci.*, 2023, **10**, 2204072.
233 L. Chen, Q. Wu, G. Wei, R. Liu and Z. Li, Highly stable thiol–ene systems: from their structure–property relationship to DLP 3D printing, *J. Mater. Chem. C*, 2018, **6**, 11561–11568.
234 P. Guo, Y. Tu, J. Yang, C. Wang, N. Sheng and H. Fang, Water-COOH Composite Structure with Enhanced Hydrophobicity Formed by Water Molecules Embedded into Carboxyl-Terminated Self-Assembled Monolayers, *Phys. Rev. Lett.*, 2015, **115**, 186101.
235 S. R. Gomari, F. Amrouche, R. G. Santos, H. C. Greenwell and P. Cubillas, A New Framework to Quantify the Wetting Behaviour of Carbonate Rock Surfaces Based on the Relationship between Zeta Potential and Contact Angle, *Energies*, DOI:10.3390/en13040993.
236 C. Werner, U. König, A. Augsburg, C. Arnhold, H. Körber, R. Zimmermann and H.-J. Jacobasch, Electrokinetic surface characterization of biomedical polymers — a survey, *Colloids Surf. Physicochem. Eng. Asp.*, 1999, **159**, 519–529.
237 N. Kuehn, H.-J. Jacobasch and K. Lunkenheimer, Zum Zusammenhang zwischen dem Kontaktwinkel zwischen Wasser und festen Polymeren und ihrem Zeta-Potential gegenüber wäßrigen Lösungen, *Acta Polym.*, 1986, **37**, 394–396.
238 Beyond surface charge to wettability, https://www.anton-paar.com/corp-en/services-support/document-finder/application-reports/beyond-surface-charge-to-wettability-the-extra-gear-of-the-zeta-potential/, (accessed 9 March 2026).
239 S. R. Holmes-Farley, R. H. Reamey, T. J. McCarthy, J. Deutch and G. M. Whitesides, Acid-base behavior of carboxylic acid groups covalently attached at the surface of polyethylene: The usefulness of contact angle in following the ionization of surface functionality, *Langmuir*, 1985, **1**, 725–740.

240 Nanoindentation | Nanoscience Instruments, https://www.nanoscience.com/techniques/nanoindentation/, (accessed 17 October 2025).
241 Mechanical Properties | Nanoindentation | Nanoscience Instruments, https://www.nanoscience.com/techniques/nanoindentation/mechanical-properties/, (accessed 17 October 2025).
242 Confusion of moduli - 2017 - Wiley Analytical Science, https://analyticalscience.wiley.com/content/news-do/confusion-moduli, (accessed 19 October 2025).
243 H. Belyadi, E. Fathi and F. Belyadi, in *Hydraulic Fracturing in Unconventional Reservoirs*, eds H. Belyadi, E. Fathi and F. Belyadi, Gulf Professional Publishing, Boston, 2017, pp. 207–224.
244 An improved technique for determining hardness and elastic modulus using load and displacement sensing indentation experiments | Journal of Materials Research | Cambridge Core, https://www.cambridge.org/core/journals/journal-of-materials-research/article/an-improved-technique-for-determining-hardness-and-elastic-modulus-using-load-and-displacement-sensing-indentation-experiments/A53D45298E14F73B86495BBC056E16DC, (accessed 10 July 2025).
245 In *Mechanical Properties of Solid Polymers*, John Wiley & Sons, Ltd, 2012, pp. 19–29.
246 J. E. Mark and J. E. Mark, *The Polymer Data Handbook*, Oxford University Press, Oxford, New York, Second Edition, Second Edition., 2009.
247 D. Hoffman, Measuring the elastic modulus of polymers using the atomic force microscope, *Diss. Masters Theses Masters Rep. - Open*, DOI:10.37099/mtu.dc.etds/27.
248 An improved technique for determining hardness and elastic modulus using load and displacement sensing indentation experiments | Journal of Materials Research, https://link.springer.com/article/10.1557/JMR.1992.1564, (accessed 19 October 2025).
249 Introducing Nanoindentation ‘Sinus Mode’ for Dynamic Mechanical Analysis on Polymer Coatings, https://covalentmetrology.com/blog/introducing-nanoindentation-sinus-mode-for-thermomechanical-analysis-on-polymer-coatings/, (accessed 21 October 2025).
250 W. A. Glaeser, Ed., in *Tribology Series*, Elsevier, 1992, vol. 20, pp. 177–210.
251 W. Xu, Z. Xiao and T. Zhang, Mechanical properties of silicone elastomer on temperature in biomaterial application, *Mater. Lett.*, 2005, **59**, 2153–2155.
252 Z. Wang, A. A. Volinsky and N. D. Gallant, Nanoindentation study of polydimethylsiloxane elastic modulus using Berkovich and flat punch tips, *J. Appl. Polym. Sci.*, DOI:10.1002/app.41384.
253 M. Sahin, S. Ayalur-Karunakaran, J. Manhart, M. Wolfahrt, W. Kern and S. Schlögl, Thiol-Ene versus Binary Thiol–Acrylate Chemistry: Material Properties and Network Characteristics of Photopolymers, *Adv. Eng. Mater.*, 2017, **19**, 1600620.
254 H. Kaczmarek, M. Nowicki, I. Vuković-Kwiatkowska and S. Nowakowska, Crosslinked blends of poly(lactic acid) and polyacrylates: AFM, DSC and XRD studies, *J. Polym. Res.*, 2013, **20**, 91.
255 E. Baştürk, D. Y. Deniz and M. V. Kahraman, Preparation of thiol-ene based photo-crosslinked polymer as a potential phase change material, *Mater. Chem. Phys.*, 2016, **177**, 521–528.

256 S. Montserrat, Effect of crosslinking density on Δ*C*p(*T*g) in an epoxy network, *Polymer*, 1995, **36**, 435–436.
257 M. A. Sharaf and J. E. Mark, The Effects of Cross-Linking and Strain on the Glass Transition Temperature of a Polymer Network, *Rubber Chem. Technol.*, 1980, **53**, 982–987.
258 Y. Bai, G. Kikugawa and N. Kishimoto, Hydrolytic degradation and property aging in highly crosslinked cyanate ester resins: A computational study, *Polym. Degrad. Stab.*, 2025, **242**, 111685.
259 K. Mishra and A. Singh, Time-dependant degradation of highly cross-linked epoxy due to hygrothermal ageing at three different temperatures, *Polym. Degrad. Stab.*, 2023, **215**, 110448.
260 J. L. Gómez Ribelles, M. M. Pradas, J. M. M. Dueñas and C. T. Cabanilles, Glass transition in homogeneous and heterogeneous interpenetrating polymer networks and its relation to concentration fluctuations, *J. Non-Cryst. Solids*, 2002, **307–310**, 731–737.
261 F. Dai, Q. Zhuang, G. Huang, H. Deng and X. Zhang, Infrared Spectrum Characteristics and Quantification of OH Groups in Coal, *ACS Omega*, 2023, **8**, 17064–17076.
262 N. Vyas, R. L. Sammons, O. Addison, H. Dehghani and A. D. Walmsley, A quantitative method to measure biofilm removal efficiency from complex biomaterial surfaces using SEM and image analysis, *Sci. Rep.*, 2016, **6**, 32694.
263 A. Han and S.-Y. Lee, An overview of various methods for in vitro biofilm formation: a review, *Food Sci. Biotechnol.*, 2023, **32**, 1617–1629.
264 M. Puges, F. M'Zali, S. Pereyre, C. Bébéar, C. Cazanave and X. Bérard, A Narrative Review of Experimental Assessment to Study Vascular Biomaterials Infections and Infectability, *EJVES Vasc. Forum*, 2023, **59**, 49–55.
265 Z. Cao, C. Ma, L. Xiang and L. Cao, A main chain biodegradable polyurethane with anti-protein adsorption and anti-bacterial adhesion performances, *Soft Matter*, 2023, **20**, 192–200.
266 LIVE/DEAD™ BacLight™ Bacterial Viability Kits Microscopy, Quantitative Assays, https://www.thermofisher.com/order/catalog/product/L7012, (accessed 30 October 2025).
267 Y. Deng, L. Wang, Y. Chen and Y. Long, Optimization of Staining with SYTO 9/Propidium Iodide: Interplay, Kinetics and Impact on Brevibacillus Brevis, *BioTechniques*, 2020, **69**, 88–98.
268 H.-H. Park, K. Sun, M. Seong, M. Kang, S. Park, S. Hong, H. Jung, J. Jang, J. Kim and H. E. Jeong, Lipid-Hydrogel-Nanostructure Hybrids as Robust Biofilm-Resistant Polymeric Materials, *ACS Macro Lett.*, 2019, **8**, 64–69.
269 H.-H. Park, K. Sun, D. Lee, M. Seong, C. Cha and H. E. Jeong, Cellulose acetate nanoneedle array covered with phosphorylcholine moiety as a biocompatible and sustainable antifouling material, *Cellulose*, 2019, **26**, 8775–8788.
270 A. Dolid, L. C. Gomes, F. J. Mergulhão and M. Reches, Combining chemistry and topography to fight biofilm formation: Fabrication of micropatterned surfaces with a peptide-based coating, *Colloids Surf. B Biointerfaces*, 2020, **196**, 111365.
271 L. Song, L. Sun, J. Zhao, X. Wang, J. Yin, S. Luan and W. Ming, Synergistic Superhydrophobic and Photodynamic Cotton Textiles with Remarkable Antibacterial Activities, *ACS Appl. Bio Mater.*, 2019, **2**, 2756–2765.

272 S. Sieuwerts, F. a. m. De Bok, E. Mols, W. m. De Vos and J. e. t. Van Hylckama Vlieg, A simple and fast method for determining colony forming units, *Lett. Appl. Microbiol.*, 2008, **47**, 275–278.
273 M. Rosenberg, N. F. Azevedo and A. Ivask, Propidium iodide staining underestimates viability of adherent bacterial cells, *Sci. Rep.*, 2019, **9**, 6483.
274 T. Cundell, The limitations of the colony-forming unit in microbiology, *Eur. Pharm. Rev.*, 2015, **20**, 11–13.
275 M. Magana, C. Sereti, A. Ioannidis, C. A. Mitchell, A. R. Ball, E. Magiorkinis, S. Chatzipanagiotou, M. R. Hamblin, M. Hadjifrangiskou and G. P. Tegos, Options and Limitations in Clinical Investigation of Bacterial Biofilms, *Clin. Microbiol. Rev.*, 2018, **31**, e00084-16.
276 R. Wang, K. G. Neoh, Z. Shi, E.-T. Kang, P. A. Tambyah and E. Chiong, Inhibition of escherichia coli and proteus mirabilis adhesion and biofilm formation on medical grade silicone surface, *Biotechnol. Bioeng.*, 2012, **109**, 336–345.
277 A. K. Epstein, T.-S. Wong, R. A. Belisle, E. M. Boggs and J. Aizenberg, Liquid-infused structured surfaces with exceptional anti-biofouling performance, *Proc. Natl. Acad. Sci.*, 2012, **109**, 13182–13187.
278 A. W. Bauer, W. M. Kirby, J. C. Sherris and M. Turck, Antibiotic susceptibility testing by a standardized single disk method, *Am. J. Clin. Pathol.*, 1966, **45**, 493–496.
279 J. Hudzicki, ASM.org, https://asm.org:443/protocols/kirby-bauer-disk-diffusion-susceptibility-test-pro, (accessed 15 September 2025).
280 Z. A. Khan, M. F. Siddiqui and S. Park, Current and Emerging Methods of Antibiotic Susceptibility Testing, *Diagnostics*, 2019, **9**, 49.
281 H. Schiller, C. Young, S. Schulze, M. Tripepi and M. Pohlschroder, A Twist to the Kirby-Bauer Disk Diffusion Susceptibility Test: an Accessible Laboratory Experiment Comparing Haloferax volcanii and Escherichia coli Antibiotic Susceptibility to Highlight the Unique Cell Biology of Archaea, *J. Microbiol. Biol. Educ.*, 2022, **23**, e00234-21.
282 D. M. Webber, M. A. Wallace and C.-A. D. Burnham, Stop Waiting for Tomorrow: Disk Diffusion Performed on Early Growth Is an Accurate Method for Antimicrobial Susceptibility Testing with Reduced Turnaround Time, *J. Clin. Microbiol.*, DOI:10.1128/jcm.03007-20.
283 S. Arullappan, Z. Zakaria and D. F. Basri, Preliminary Screening of Antibacterial Activity Using Crude Extracts of Hibiscus rosa sinensis, *Trop. Life Sci. Res.*, 2009, **20**, 109–118.
284 P. Krishnamurthy, R. Shetty, K. P. Isaac, S. N. Unni, S. S. Rao and K. Parthasarathy, Differentiation of Bacterial Species in Liquid Culture Using Laser Speckle Contrast Imaging, *J. Biophotonics*, 2025, **18**, e202400565.
285 J. Shin, A. Naskar, D. Ko, S. Kim and K. Kim, Bioconjugated Thymol-Zinc Oxide Nanocomposite as a Selective and Biocompatible Antibacterial Agent against Staphylococcus Species, *Int. J. Mol. Sci.*, 2022, **23**, 6770.
286 T. L. Riss, R. A. Moravec, A. L. Niles, S. Duellman, H. A. Benink, T. J. Worzella and L. Minor, in *Assay Guidance Manual*, eds S. Markossian, A. Grossman, H. Baskir, M. Arkin, D. Auld, C. Austin, J. Baell, K. Brimacombe, T. D. Y. Chung, N. P. Coussens, J. L. Dahlin, V. Devanarayan, T. L. Foley, M. Glicksman, K. Gorshkov, S. Grotegut, M. D. Hall, S. Hoare, J. Inglese, P. W. Iversen, M. Lal-Nag, Z. Li, J. R. Manro, J. McGee, A. Norvil, M. Pearson, T. Riss, P. Saradjian, G. S. Sittampalam, M. A. Tarselli, O. J. Trask, J. R. Weidner, M. J. Wildey, K. Wilson,

M. Xia and X. Xu, Eli Lilly & Company and the National Center for Advancing Translational Sciences, Bethesda (MD), 2004.
287 Luria Broth (LB) and Luria Agar (LA) Media and Their Uses, https://asm.org:443/protocols/luria-broth-lb-and-luria-agar-la-media-and-their-u, (accessed 2 October 2025).
288 S.-W. Lim, H.-S. Loh, K.-N. Ting, T. D. Bradshaw and Z. N. Allaudin, Reduction of MTT to Purple Formazan by Vitamin E Isomers in the Absence of Cells, *Trop. Life Sci. Res.*, 2015, **26**, 111–120.
289 T. Kim, S. Kwon, J. Lee, J. S. Lee and S. Kang, A metallic anti-biofouling surface with a hierarchical topography containing nanostructures on curved micro-riblets, *Microsyst. Nanoeng.*, 2022, **8**, 6.
290 S. Stepanović, D. Vuković, I. Dakić, B. Savić and M. Švabić-Vlahović, A modified microtiter-plate test for quantification of staphylococcal biofilm formation, *J. Microbiol. Methods*, 2000, **40**, 175–179.
291 B. Mole, Bacteria staining method has long been misexplained, https://www.sciencenews.org/article/bacteria-staining-method-has-long-been-misexplained, (accessed 2 October 2025).
292 H. Ding, Y. Yang, X. Li, G. S.-P. Cheung, J. P. Matinlinna, M. Burrow and J. K.-H. Tsoi, A simple AI-enabled method for quantifying bacterial adhesion on dental materials, *Biomater. Investig. Dent.*, **9**, 75–83.
293 C. Richards, A. D. Ollero, P. Daly, Y. Delauré and F. Regan, Disruption of diatom attachment on marine bioinspired antifouling materials based on Brill (*Scophthalmus rhombus*), *Sci. Total Environ.*, 2024, **912**, 169348.
294 Trainable Weka Segmentation, https://imagej.github.io/plugins/tws/index, (accessed 19 September 2025).
295 G. A. O'Toole and R. Kolter, Initiation of biofilm formation in Pseudomonas fluorescens WCS365 proceeds via multiple, convergent signalling pathways: a genetic analysis, *Mol. Microbiol.*, 1998, **28**, 449–461.
296 J. Jara, F. Alarcón, A. K. Monnappa, J. I. Santos, V. Bianco, P. Nie, M. P. Ciamarra, Á. Canales, L. Dinis, I. López-Montero, C. Valeriani and B. Orgaz, Self-Adaptation of Pseudomonas fluorescens Biofilms to Hydrodynamic Stress, *Front. Microbiol.*, 2021, **11**, 588884.
297 H. F. Culler, C. M. Mota, C. M. Abe, W. P. Elias, M. P. Sircili and M. R. Franzolin, Atypical Enteropathogenic Escherichia coli Strains form Biofilm on Abiotic Surfaces Regardless of Their Adherence Pattern on Cultured Epithelial Cells, *BioMed Res. Int.*, 2014, **2014**, 845147.
298 I. S. Gómez-Alonso, G. Betanzos-Cabrera, M. C. Moreno-Lafont, M. E. Cancino-Diaz, B. E. García-Pérez and J. C. Cancino-Diaz, Non-biofilm-forming Staphylococcus epidermidis planktonic cell supernatant induces alterations in osteoblast biological function, *Sci. Rep.*, 2024, **14**, 1807.
299 Coefficient of Variation, https://corporatefinanceinstitute.com/resources/data-science/coefficient-of-variation/, (accessed 3 October 2025).
300 J. Jiao, L. Sun, Z. Guo, S. Hou, R. Holyst, Y. Lu and X. Feng, Antibacterial and anticancer PDMS surface for mammalian cell growth using the Chinese herb extract paeonol(4-methoxy-2-hydroxyacetophenone), *Sci. Rep.*, 2016, **6**, 38973.
301 A. Jagannath, M. Yu, J. Li, N. Zhang and M. D. Gilchrist, Improving assay feasibility and biocompatibility of 3D cyclic olefin copolymer microwells by superhydrophilic modification via ultrasonic spray deposition of polyvinyl alcohol, *Biomater. Adv.*, 2024, **163**, 213934.

302 A. Chapalain, G. Rossignol, O. Lesouhaitier, A. Merieau, C. Gruffaz, J. Guerillon, J.-M. Meyer, N. Orange and M. G. J. Feuilloley, Comparative study of 7 fluorescent pseudomonad clinical isolates, *Can. J. Microbiol.*, 2008, **54**, 19–27.
303 B. S. Scales, R. P. Dickson, J. J. LiPuma and G. B. Huffnagle, Microbiology, Genomics, and Clinical Significance of the Pseudomonas fluorescens Species Complex, an Unappreciated Colonizer of Humans, *Clin. Microbiol. Rev.*, 2014, **27**, 927–948.
304 S. M. Hinsa, M. Espinosa-Urgel, J. L. Ramos and G. A. O'Toole, Transition from reversible to irreversible attachment during biofilm formation by Pseudomonas fluorescens WCS365 requires an ABC transporter and a large secreted protein, *Mol. Microbiol.*, 2003, **49**, 905–918.
305 S. M. Hinsa and G. A. O'Toole, Biofilm formation by Pseudomonas fluorescens WCS365: a role for LapD, *Microbiology*, 2006, **152**, 1375–1383.
306 K. E. Rasmussen and J. Albrechtsen, Glutaraldehyde. The influence of pH, temperature, and buffering on the polymerization rate, *Histochemistry*, 1974, **38**, 19–26.
307 A. Sharma, N. Anup and R. K. Tekade, in *The Future of Pharmaceutical Product Development and Research*, ed. R. K. Tekade, Academic Press, 2020, pp. 695–788.
308 Testing for Normality using SPSS Statistics when you have only one independent variable., https://statistics.laerd.com/spss-tutorials/testing-for-normality-using-spss-statistics.php, (accessed 30 September 2025).
309 ImagineArt Image Studio, https://www.imagine.art/ai-image-generator, (accessed 11 November 2025).
310 A. Rajesh, A Post-hoc Test for Kruskal-Wallis, https://www.theanalysisfactor.com/dunns-test-post-hoc-test-after-kruskal-wallis/, (accessed 4 November 2025).
311 Nonparametric Pairwise Multiple Comparisons in Independent Groups using Dunn's Test - Alexis Dinno, 2015, https://journals.sagepub.com/doi/10.1177/1536867X1501500117, (accessed 4 November 2025).
312 A. Khursheed, L.-C. Xu and C. A. Siedlecki, The Effects of Submicron Textured Surface Topography on Antibiotic Efficacy against Biofilms, *J. Biomed. Mater. Res. B Appl. Biomater.*, 2024, **112**, e35436.
313 R. Hugh, L. Guarraia and H. Hatt, The proposed neotype strains of Pseudomonas fluorescens (Trevisan) Migula 1895, *Int. Bull. Bacteriol. Nomencl. Taxon.*, 1964, **14**, 145–156.
314 P. M. Martínez-García, D. Ruano-Rosa, E. Schilirò, P. Prieto, C. Ramos, P. Rodríguez-Palenzuela and J. Mercado-Blanco, Complete genome sequence of Pseudomonas fluorescens strain PICF7, an indigenous root endophyte from olive (Olea europaea L.) and effective biocontrol agent against Verticillium dahliae, *Stand. Genomic Sci.*, 2015, **10**, 10.
315 M. M. Baum, A. Kainović, T. O'Keeffe, R. Pandita, K. McDonald, S. Wu and P. Webster, Characterization of structures in biofilms formed by a Pseudomonas fluorescens isolated from soil, *BMC Microbiol.*, 2009, **9**, 103.
316 G. V. Bloemberg, A. H. M. Wijfjes, G. E. M. Lamers, N. Stuurman and B. J. J. Lugtenberg, Simultaneous Imaging of Pseudomonas fluorescens WCS365 Populations Expressing Three Different Autofluorescent Proteins in the Rhizosphere: New Perspectives for Studying Microbial Communities, *Mol. Plant-Microbe Interactions*®, 2000, **13**, 1170–1176.

317 L. Tian, E. Jin, J. Wang, X. Wang, W. Bing, H. Jin, J. Zhao and L. Ren, Exploring the antifouling effect of elastic deformation by DEM–CFD coupling simulation, *RSC Adv.*, 2019, **9**, 40855–40862.
318 K. K. Chung, J. F. Schumacher, E. M. Sampson, R. A. Burne, P. J. Antonelli and A. B. Brennan, Impact of engineered surface microtopography on biofilm formation of Staphylococcus aureus, *Biointerphases*, 2007, **2**, 89–94.
319 H. Pingle, P.-Y. Wang, H. Thissen and P. Kingshott, Controlled Attachment of Pseudomonas aeruginosa with Binary Colloidal Crystal-Based Topographies, *Small*, 2018, **14**, 1703574.
320 A. Konig-Peter, F. Kilar and T. Pernyeszi, Copper(ii) biosorption characteristics of lyophilized and thermally treated pseudomonas cells, *Environ. Eng. Manag. J.*, 2019, **18**, 455–464.
321 M. Lemos, A. Borges, J. Teodósio, P. Araújo, F. Mergulhão, L. Melo and M. Simões, The effects of ferulic and salicylic acids on *Bacillus cereus* and *Pseudomonas fluorescens* single- and dual-species biofilms, *Int. Biodeterior. Biodegrad.*, 2014, **86**, 42–51.
322 R. S. Roth, L. Birnhack, M. Avidar, E. A. Hjelvik, A. P. Straub and R. Epsztein, Effect of solution ions on the charge and performance of nanofiltration membranes, *Npj Clean Water*, 2024, **7**, 25.
323 Debye screening - how it affects zeta potential - 3 points, https://www.malvernpanalytical.com/en/learn/knowledge-center/insights/debye-screening-how-it-affects-zeta, (accessed 11 March 2026).
324 O. Frost, Automating Zeta Potential Measurements for Liposomes in High and Low Salt Environments, https://www.azonano.com/article.aspx?ArticleID=6962, (accessed 11 March 2026).
325 T. Velnar and L. Gradisnik, Tissue Augmentation in Wound Healing: the Role of Endothelial and Epithelial Cells, *Med. Arch.*, 2018, **72**, 444–448.
326 N. Mirhosseini, L. Li, Z. Liu, M. Mamas, D. Fraser and T. Wang, A comparison of endothelial cell growth on commercial coronary stents with and without laser surface texturing, *Heliyon*, 2024, **10**, e26425.
327 A. M. Almonacid Suarez, I. van der Ham, M. G. L. Brinker, P. van Rijn and M. C. Harmsen, Topography-driven alterations in endothelial cell phenotype and contact guidance, *Heliyon*, 2020, **6**, e04329.
328 P. Formentín, Ú. Catalán, M. Alba, S. Fernández-Castillejo, R. Solà, J. Pallarès and L. F. Marsal, Effects of SiO2 micropillar arrays on endothelial cells' morphology, *New Biotechnol.*, 2016, **33**, 781–789.
329 C. Lutter, M. Nothhaft, A. Rzany, C. D. Garlichs and I. Cicha, Effect of specific surface microstructures on substrate endothelialisation and thrombogenicity: Importance for stent design, *Clin. Hemorheol. Microcirc.*, 2015, **59**, 219–233.
330 C. Gu, H. Wu, G. Ge, X. Li, Z. Guo, Z. Bian, J. Xu, H. Lu, X. Chen and D. Yang, In Vitro Effects of Hollow Gold Nanoshells on Human Aortic Endothelial Cells, *Nanoscale Res. Lett.*, 2016, **11**, 397.
331 Primary Aortic Endothelial Cells; Normal, Human (HAEC) - PCS-100-011 | ATCC, https://www.atcc.org/products/pcs-100-011, (accessed 21 November 2025).
332 W. Zhu, R. Zhang, S. Liu, J. Tian, X. Lv, F. Yu and H. Xin, The effect of nanoparticles of cobalt–chromium on human aortic endothelial cells in vitro, *J. Appl. Toxicol.*, 2021, **41**, 1966–1979.

333 A. Choubey, D. Marton and E. A. Sprague, Human aortic endothelial cell response to 316L stainless steel material microstructure, *J. Mater. Sci. Mater. Med.*, 2009, **20**, 2105–2116.
334 L. Khalef, R. Lydia, K. Filicia and B. Moussa, Cell viability and cytotoxicity assays: Biochemical elements and cellular compartments, *Cell Biochem. Funct.*, 2024, **42**, e4007.
335 Two-way ANOVA in SPSS Statistics - Step-by-step procedure including testing of assumptions | Laerd Statistics, https://statistics.laerd.com/spss-tutorials/two-way-anova-using-spss-statistics.php, (accessed 22 November 2025).
336 D. M. Lane, in *Encyclopedia of Research Design*, SAGE Publications, Inc., 2010, pp. 1566–1570.
337 C. Korzeniewski and D. M. Callewaert, An enzyme-release assay for natural cytotoxicity, *J. Immunol. Methods*, 1983, **64**, 313–320.
338 V. PeŠŠková, D. Kubies, H. Hulejová and L. Himmlová, The influence of implant surface properties on cell adhesion and proliferation, *J. Mater. Sci. Mater. Med.*, 2007, **18**, 465–473.
339 S.-H. Lee, S. Yoo, S. H. Kim, Y.-M. Kim, S. I. Han and H. Lee, Nature-inspired surface modification strategies for implantable devices, *Mater. Today Bio*, 2025, **31**, 101615.
340 D. Guo, Q. Wang, C. Li, Y. Wang and X. Chen, VEGF stimulated the angiogenesis by promoting the mitochondrial functions, *Oncotarget*, 2017, **8**, 77020–77027.
341 N. O. Monteiro, C. Oliveira, T. H. Silva, A. Martins, J. F. Fangueiro, R. L. Reis and N. M. Neves, Biomimetic Surface Topography from the Rubus fruticosus Leaf as a Guidance of Angiogenesis in Tissue Engineering Applications, *ACS Biomater. Sci. Eng.*, 2022, **8**, 2943–2953.

Appendices

Appendix A

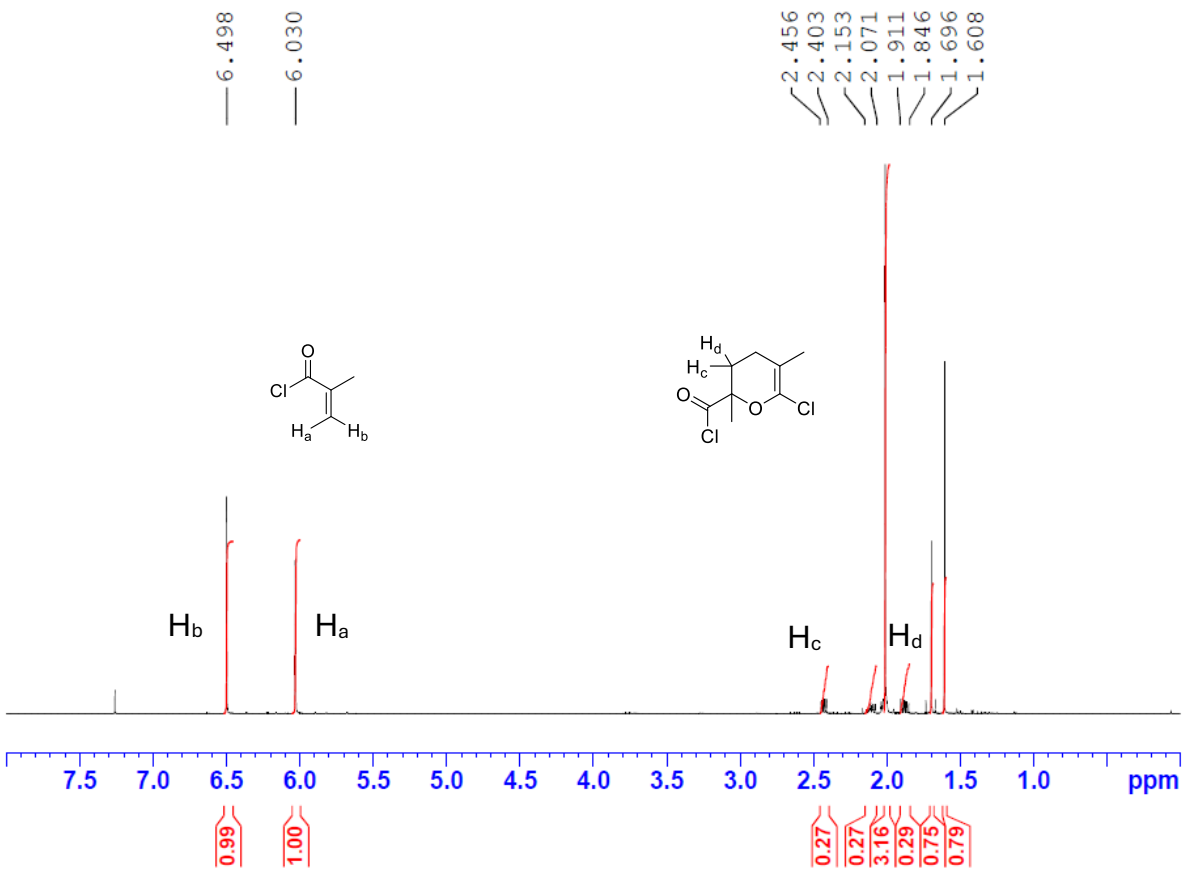
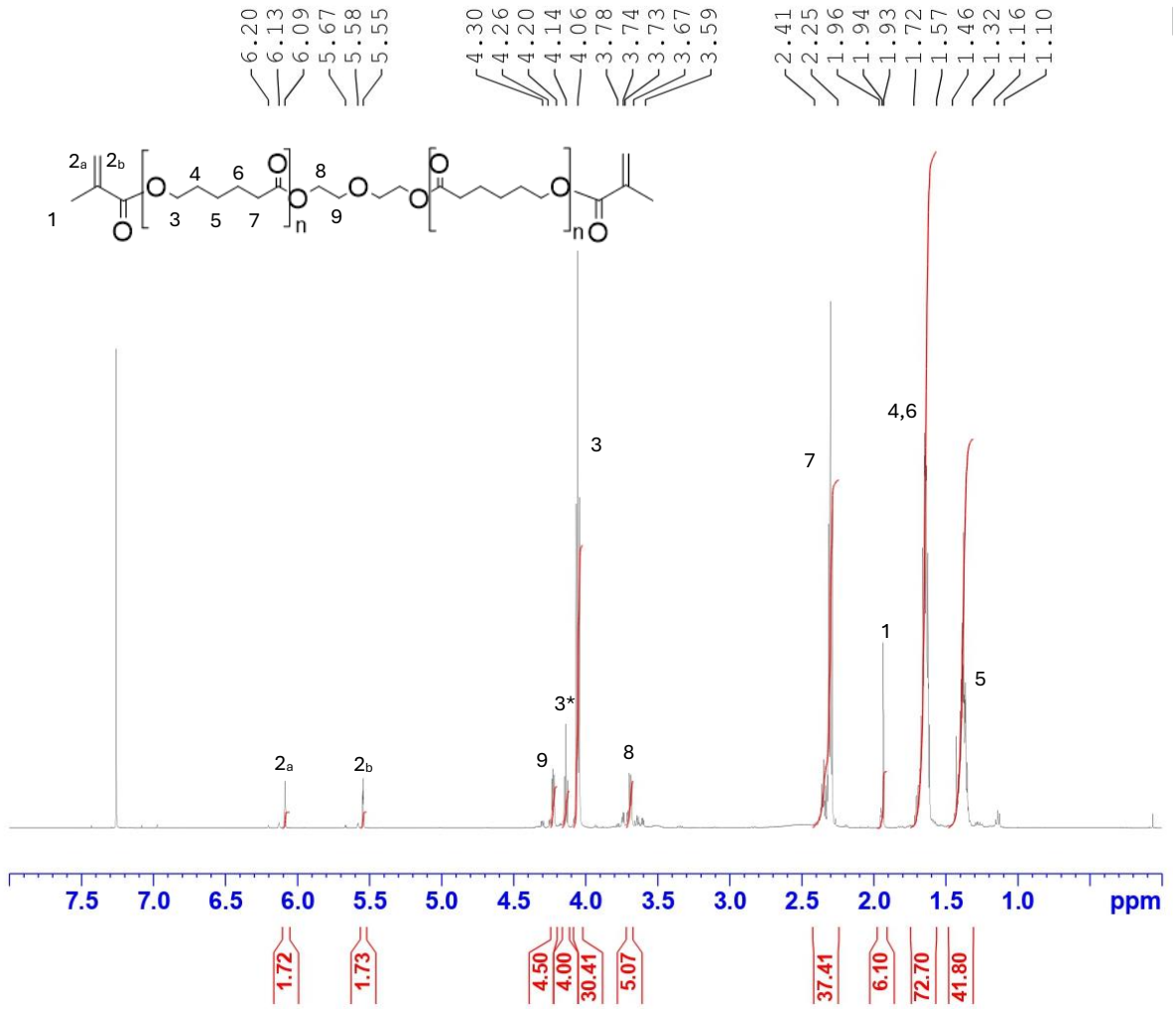


Figure A.1: ^{1}H NMR (600 MHz, $CDCl_3$) spectrum of MAC with most common impurity. Protons H_a and H_c utilised to find the percentage of impurity present.



* chain end unit

Figure A.2: ^{1}H NMR (600 MHz, $CDCl_3$) spectrum of PCLDMA-1350 with labels denoting each proton on the PCLDMA structure.

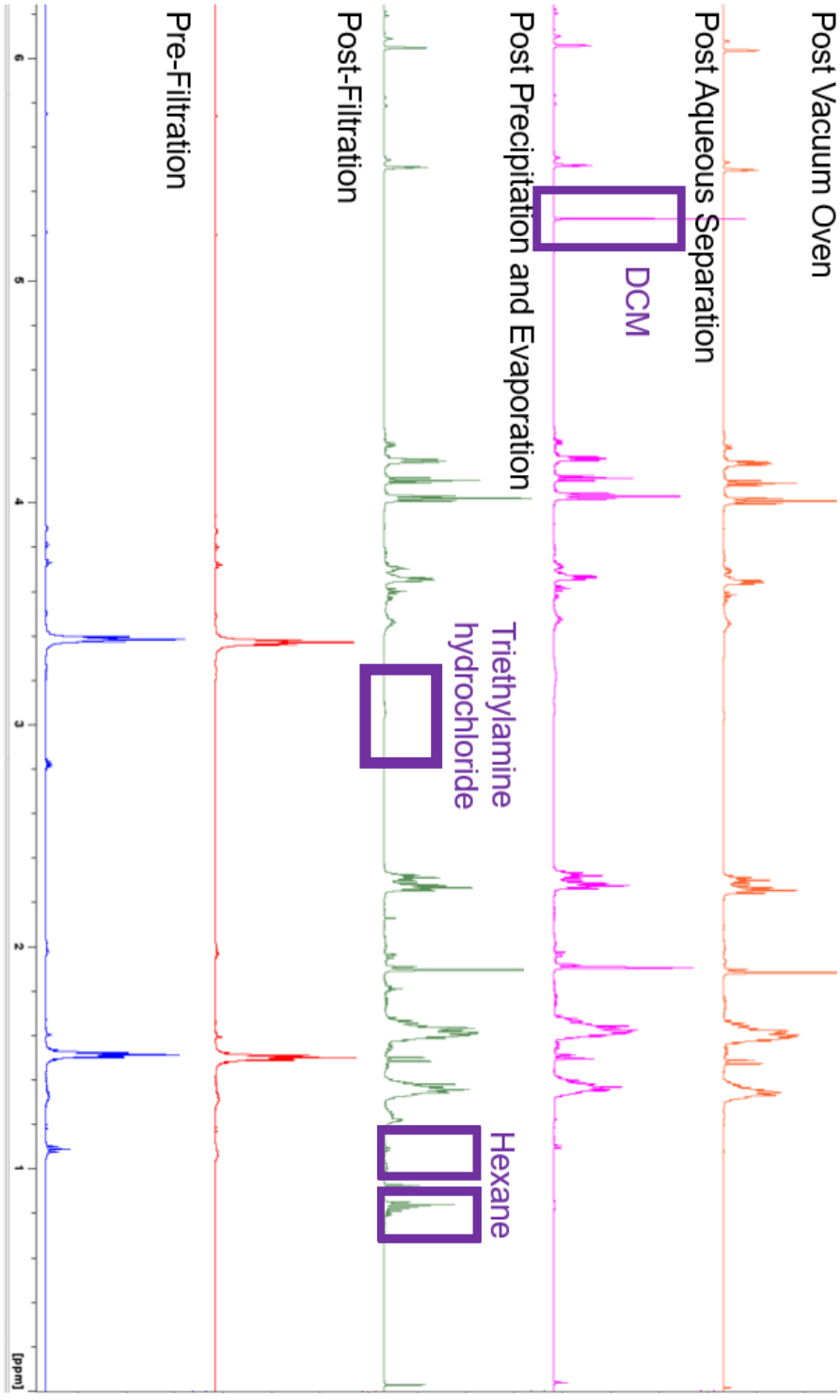
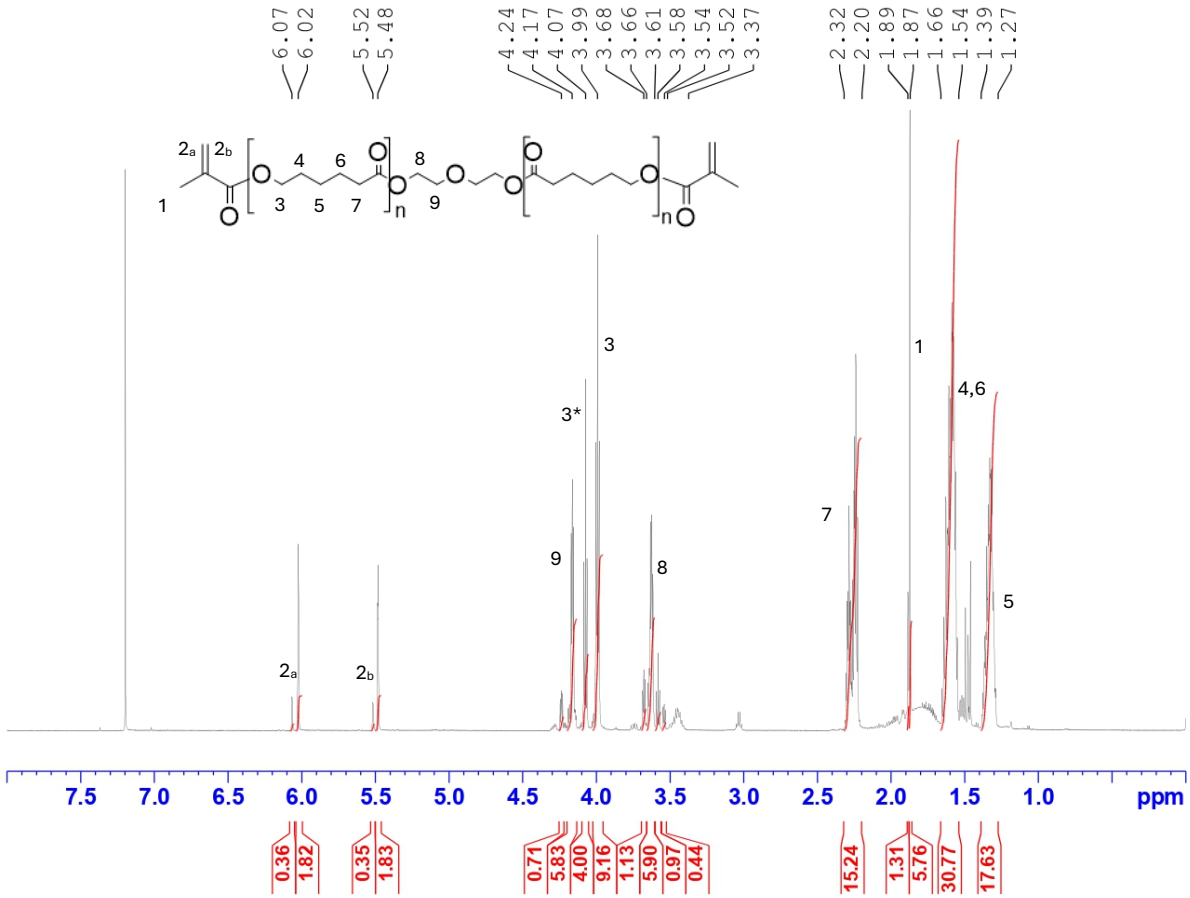


Figure A.3: Stacked ^{1}H NMR (600 MHz, $CDCl_3$) spectra of each stage of the purification process (left to right) to give purified PCLDMA-630.



* chain end unit

Figure A.4: Annotated ^{1}H NMR (600 MHz, $CDCl_3$) spectrum of PCLDMA-630.

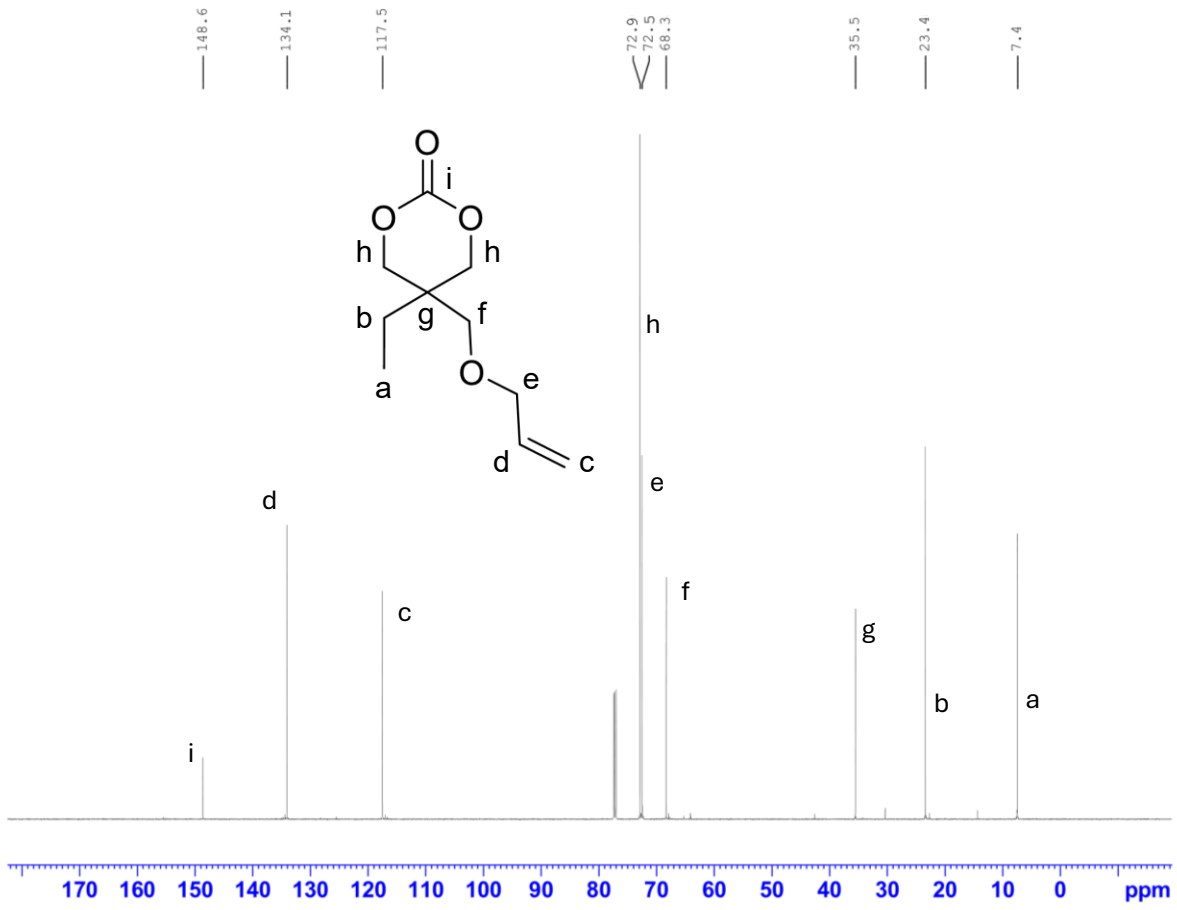


Figure A.5: Annotated ^{13}C NMR (150 MHz, $CDCl_3$) spectrum of AOMEC post-distillation under vacuum.

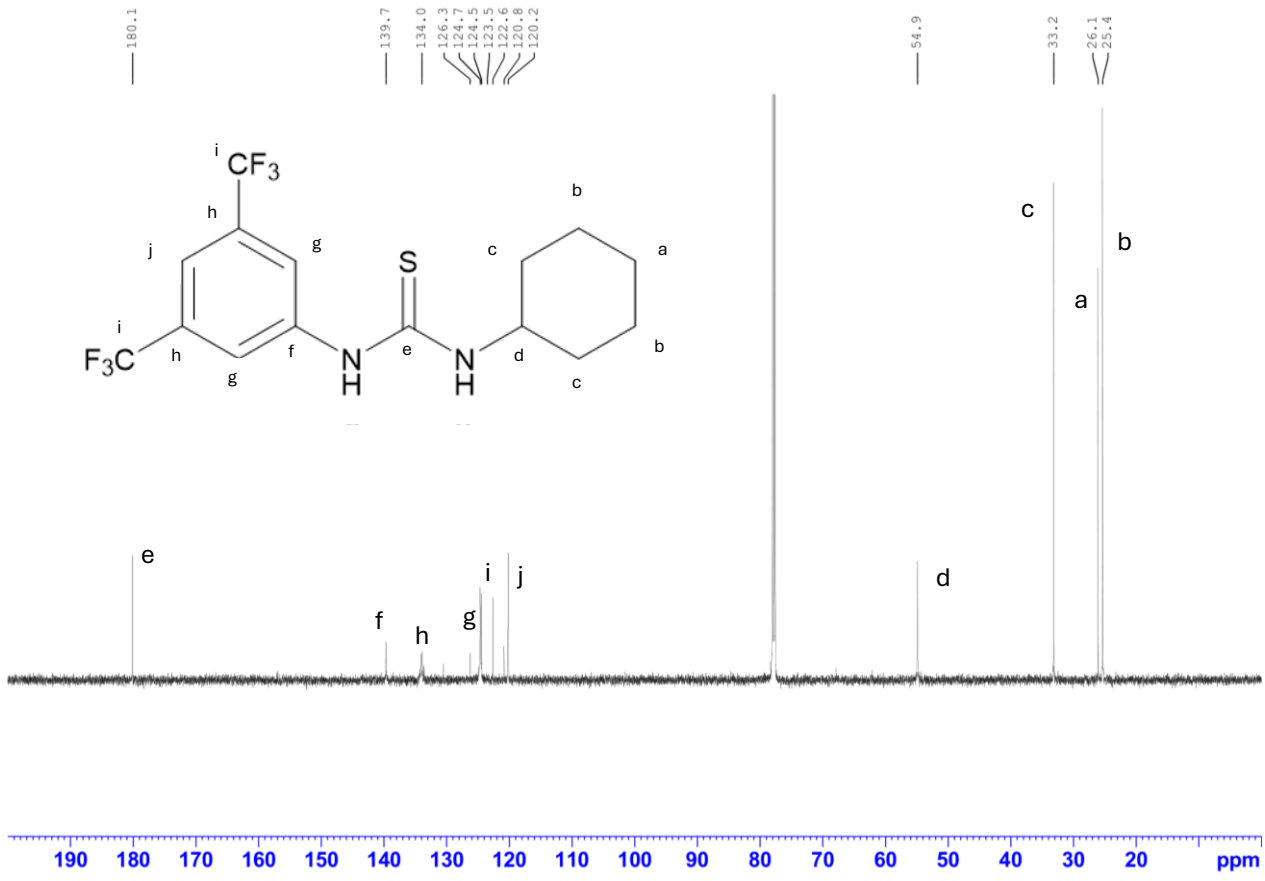
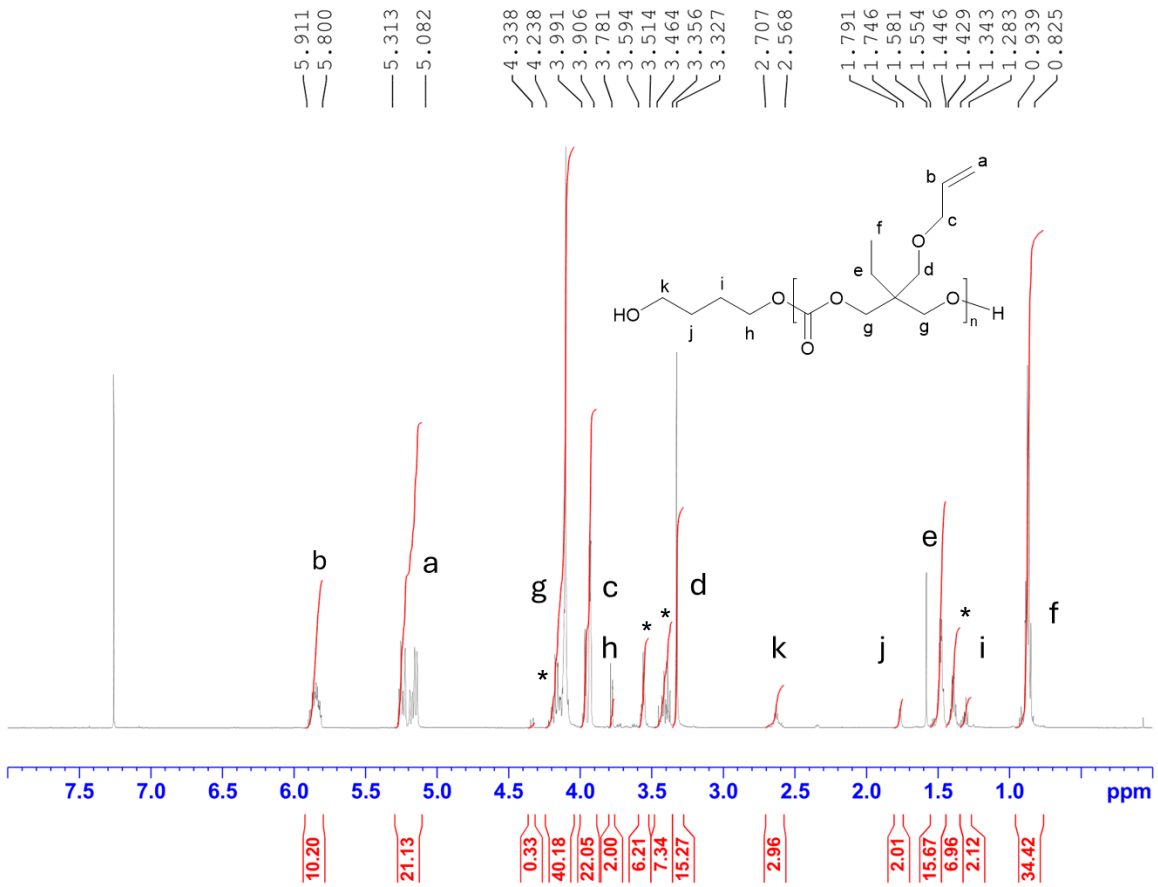


Figure A.6: Annotated ^{13}C NMR (150 MHz, $CDCl_3$) spectrum of TU cocatalyst.



* chain end unit for c, d, e and g

Figure A.7: Annotated ^{1}H NMR (600 MHz, $CDCl_3$) spectrum of fully purified PAOMEC.

Appendix B

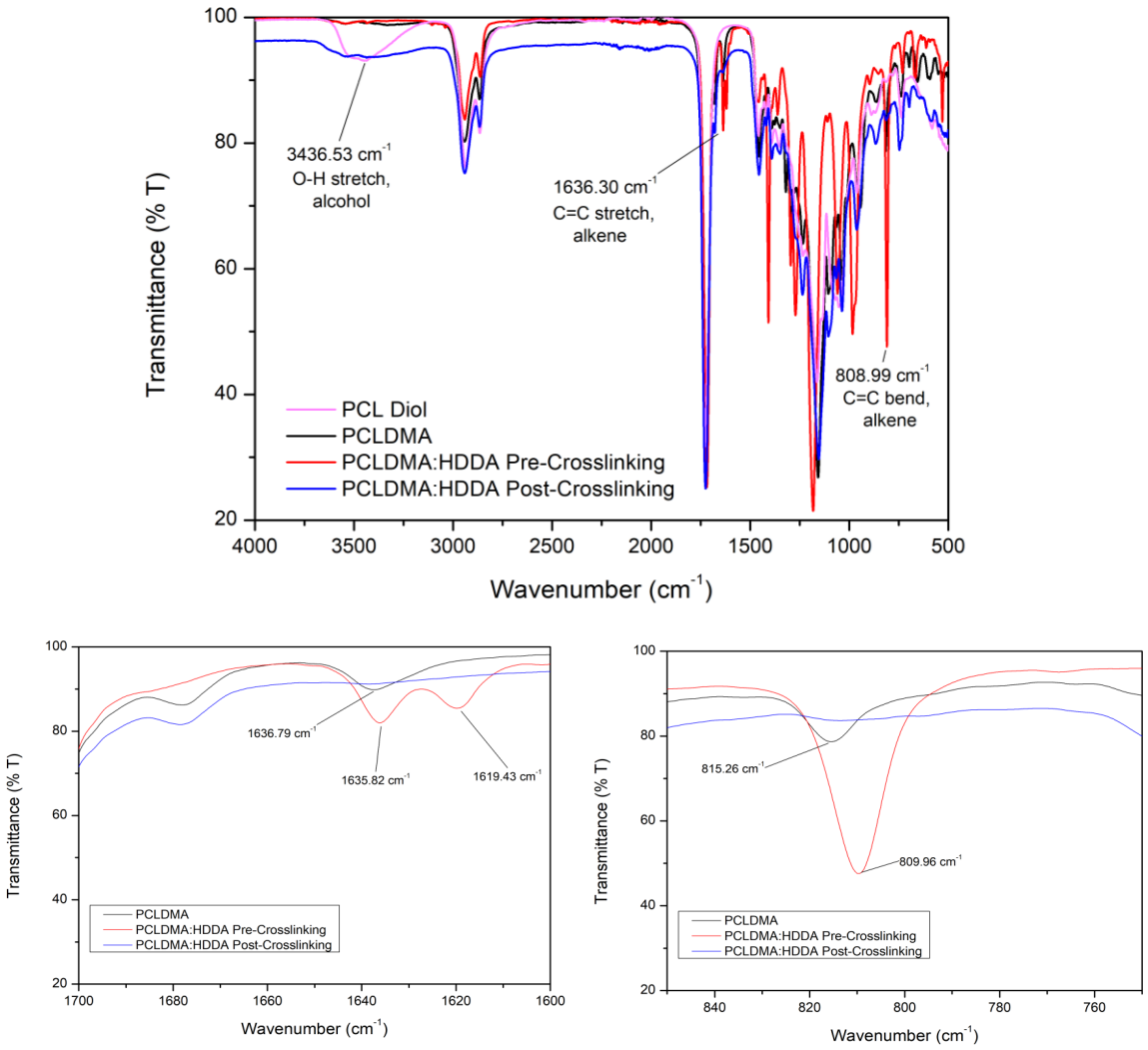


Figure B.1: Comparative FTIR spectra of PCL diol-530, PCLDMA-630 and PCLDMA-630:HDDA (1:4 ratio) pre- and post-crosslinking for 60 minutes (top). Peaks representing the alkene stretch (bottom left) and bend (bottom right) of the terminal alkene groups on pure PCLDMA_630 and PCLDMA:HDDA (1:4) pre- and post-crosslinking.

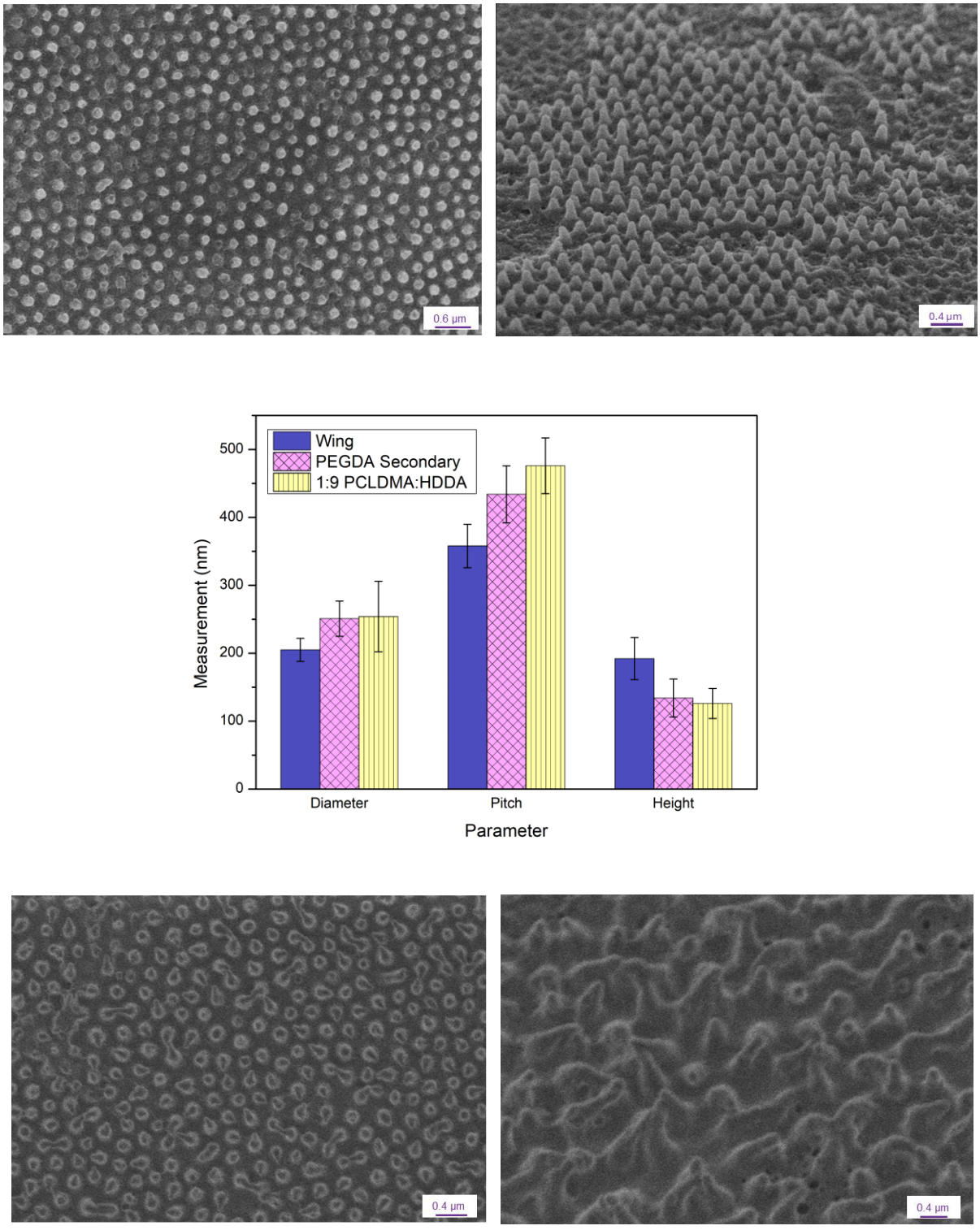


Figure B.2: FESEM image of PCLDMA:HDDA 1:9 secondary mould top down (top left) and tilted (top right) with nanopillars. Column chart of height, pitch and diameter measurements made comparing fidelity of 1:9 and PEGDA secondary moulds. Error bars represent the standard deviation. FESEM image of PCLDMA:HDDA 1:4 secondary mould top down (bottom left) and tilted (bottom right) showing collapse of nanopillars. All tilted FESEM images were taken at 40 º.

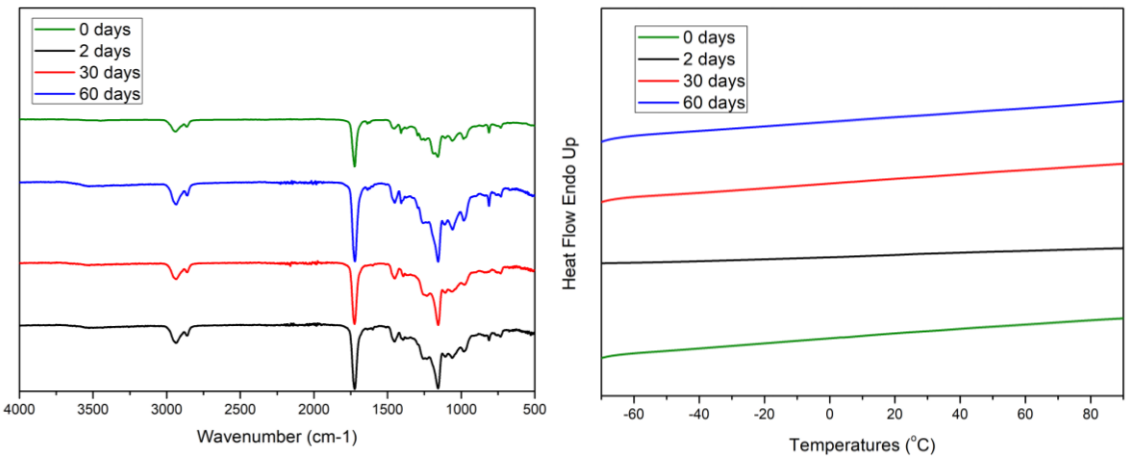


Figure B.3: FTIR (left) and DSC (right) spectra from degraded samples at each time point displayed in the spectra.

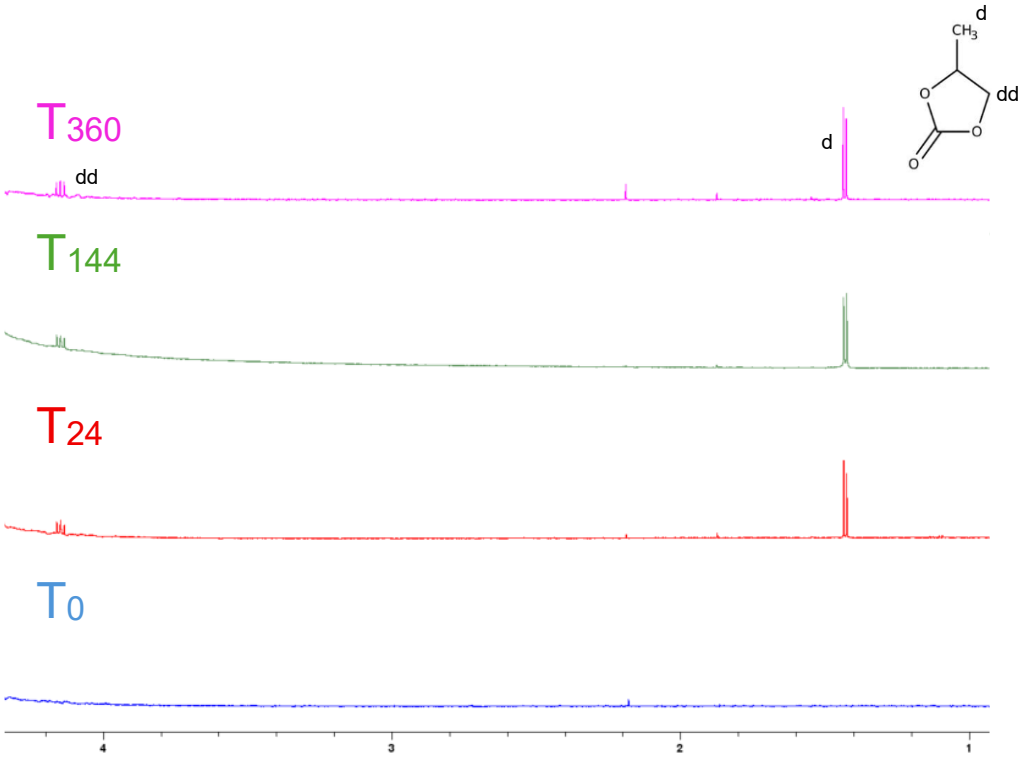


Figure B.41 ^{1}H NMR (600 MHz, $CDCl_3$) spectra of swelling studies of PAO_X samples at four timepoints soaked in deionised water showing the leaching of propylene carbonate from PAO_X sample.

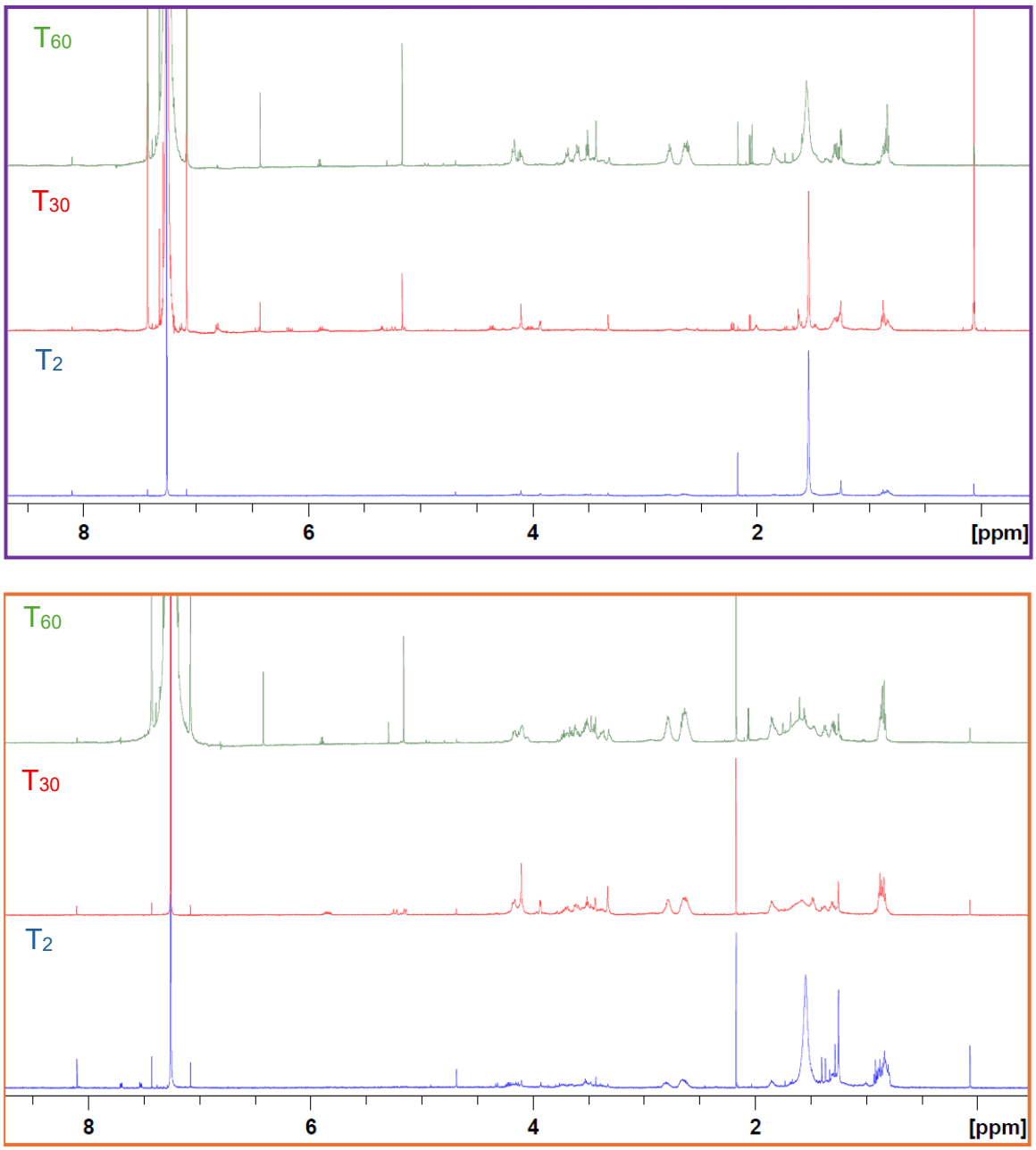


Figure B.5: ^{1}H NMR (600 MHz, $CDCl_3$) spectra of PAO_X (a) and PAO_COOH (b) samples post soaking in PBS buffer at three time points.

Appendix C

Table C.1: Data from Ray-Scheirer statistical test showing the degrees of freedom (Df), sum of the squares (Sum Sq) H and p-values. The statistically significant data are outlined in green using results collected from planar, uncharged as samples, PAO_X, as the baseline for comparison.

Source	Df	Sum Sq	H	p.value
Charge	1	1033	0.853	0.35561
Structure	1	91191	75.364	0
Charge: Structure	1	258	0.213	0.64417
Residuals	116	51059		

Table C.2: Results from Dunn post-hoc test with a Bonferroni correction with the statistically significant results outlined in green.

Comparison	Z	P.unadj	P.adj
PAO_COOH.Planar - PAO_COOH.Structured	6.465168	1.01E-10	6.07E-10
PAO_COOH.Planar - PAO_X.Planar	0.326599	7.44E-01	1.00E+00
PAO_COOH.Structured - PAO_X.Planar	6.791767	1.11E-11	6.65E-11
PAO_COOH.Planar - PAO_X.Structured	4.853753	4.13E-08	2.48E-07
PAO_COOH.Structured - PAO_X.Structured	0.979796	3.27E-01	1.00E+00
PAO_X.Planar - PAO_X.Structured	5.811971	6.17E-09	3.70E-08